Fragmentation of Carbon-bearing Projectiles and the Effects on their Raman Spectra due to Hypervelocity Impacts

A thesis submitted for the degree of
Doctor of Philosophy

by

Jamie E Wickham-Eade

School of Physical Sciences

University of Kent
Canterbury
U.K

September 2017

Declaration

The content of this thesis has been composed by the author, and has not been submitted for a further degree at any other higher educational institute.

The content comprising Chapter 5 was adapted and extended from Wickham-Eade et al. (in review) and Chapter 9 was adapted from Wickham-Eade et al. (2017).

I give permission for the Library to lend or copy this thesis upon request.

SIGNED:

Acknowledgements

Firstly, I am very grateful to Prof. Mark Burchell for his continued support and superb supervision for the duration of my PhD. I have learned a lot and definitely would never have made it this far without him.

I also wish to thank my secondary supervisor, Dr. Mark Price, and my colleague, Dr. Kathryn Harriss, for their help and support over the last three years. Additionally, I would like to thank our Experimental Officer, Mike Cole, for his assistance down in the Impact Lab and putting up with my singing! Thanks to all my fellow PhD students for their continual support and interesting conversations.

I would also like to thank my parents, Sandy and Dave, for their support and encouragement throughout the whole of my education. Without them, I would definitely have never got to this point. I would like to thank my grandfather, Ted, for igniting my interests in astronomy and space. Finally, I would like to thank my wife, Mya, for her continued support throughout my PhD.

I am very grateful to the University of Kent's Opportunity Fund and the Alumni for bestowing me the honour of holding the 2014 Alumni Postgraduate Research Scholarship and for STFC for funding the gun.

My only regret is that my time at the University of Kent went by so fast. One thing is for certain, whatever the future holds, I will always have fond memories of the School of Physical Science.

Summary

The term hypervelocity refers to something that is travelling at speeds in excess of a few km s^{-1}. Impacts within the Solar System generally occur at these speeds, hence they are referred to as Hypervelocity Impacts.

Typical impact speeds in the Solar System depends on their location. Within the main asteroid belt, the average impact speed is generally considered to be 5 km s^{-1}. Moving to impacts on Earth, the Moon and Mars, an asteroid average impact speed is approximately 22, 19 and 9 km s^{-1} respectively. Move to the outer Solar System and the average impact speed on Pluto is thought to be approximately 2 km s^{-1}.

Generally, research into hypervelocity impacts looks into cratering and the ejecta from these craters. However, the fate of the projectile is relatively neglected. Hence, this topic was explored in this thesis. To achieve this, experiments were performed using the University of Kent's two-stage light gas gun.

Along with a mechanical effect on the projectile material, the propagating shock wave can cause effects on the molecular structure. This can be investigated using Raman Spectroscopy, which is an inelastic scattering effect resulting from the laser light interaction with the molecules of the sample. By comparing a before and after spectrum of an impacted material, it is possible to determine the effects of shock pressure.

An important biomarker is carbon. The Raman spectra of carbon often contain a D (disorder) and G (graphite/order) band. The amplitude and area ratios of these two bands denote the structural organisation of the carbon-bearing materials. Impacting these materials can affect the Raman spectra. Changes in the spectra can reflect the effect shock pressures have had on the molecular structure of the material.

Firstly, the mechanical effect of a hypervelocity impact was investigated for basalt and shale. The materials were filed into 1.5 mm cubes. These cubes were then fired into water at speeds up to 6.13 km s^{-1} (peak shock pressure of 30.9 GPa). The water was then filtered through a 0.1 μm filter membrane and a scanning electron microscope used to image the entire filter paper. ImageJ was then used to analyse

the fragments. From this, information on the morphology, cumulative fragment size distribution, survival percentage and the energy density at the catastrophic disruption threshold are obtained. Catastrophic disruption is where the shock wave of an impact is sufficiently intense that the largest fragment is equal to or less than 50% of the original mass of the body (exactly 50% is the threshold limit). Over 400,000 fragments were measured per shot, providing fragment sizes down to 10^{-3} of the original projectile size. When excluding the partially disrupted projectiles (impacts not sufficient enough to surpass the catastrophic disruption threshold limit), the average semi-minor to semi-major axis ratio (b/a) for basalt and shale were 0.58 ± 0.16 and 0.59 ± 0.14 respectively. This suggests that the difference in morphology does not have an effect on this ratio at higher impact speeds. From the results an estimate of percentage survival at Pluto, the Moon, in the asteroid belt and on Mars is 76 ± 11%, 39 ± 8%, 17 ± 5% and 10 ± 4% respectively. It was found that for basalt and shale the catastrophic disruption energy density was $(24.0 \pm 2.1) \times 10^4$ and $(9.4 \pm 5.0) \times 10^4$ J kg^{-1} respectively.

The work then moved on to investigating the effect of the shock upon the fragments of the projectile. An additional material (graphite) was used with basalt and shale. The materials were shot using the same method used to investigate the mechanical effect of the hypervelocity impact. Pre-shot the projectile was mapped using a 532 nm laser in a Raman spectrometer. These spectra were then compared to the spectra of 40 separate randomly chosen fragments in each shot. From this, it is possible to determine the shock pressure effects of the impact. Although no trends were identified positive shifts were observed for the D band peak position for basalt and shale, the G band peak position of basalt experienced a positive shift while graphite experienced both a positive and negative shift. Additionally, the G band width for basalt and shale experienced an absolute narrowing of 12.2% and 8.1% respectively, while graphite exhibited an absolute broadening of 17.6%. Overall, all the materials displayed an increased structural disorder after impact, as suggested by plotting the Raman spectra R1 and R2 values. These are ratios of the D and G band amplitudes (R1) and the bands' areas (R2). Furthermore, it was found from this work that there is a possibility of misinterpreting a sample when attempting to determine whether it is biotic carbon if from a shocked environment.

The samples were also subjected to static pressure up to a maximum pressure of 3.59 GPa using a diamond anvil cell, and heating/cooling (temperature range 173 to 773 K) using a Linkam temperature stage. This was done in order to ascertain the effects of flash heating upon Raman spectra during hypervelocity impacts. It was found that the effects of temperature are mostly opposite to the effect of shock and static pressure on a carbon Raman spectrum. Increasing static pressure led to the G band peak position for shale and graphite shifting a total of 19.2 and 15.0 cm^{-1}, at

3.48 and 3.23 GPa respectively. In contrast, for shale and graphite the D and G band peak position were shifted to lower wavenumbers at high temperature (>300 K), and to higher wavenumbers at low temperature (<300 K).

Finally, the capture effect upon olivine as a constituent of a mineral assemblage was also investigated. These capture effects are shock pressures ≤300 MPa (Trigo-Rodriguez et al. 2008) and heating to over 1,000 °C for a brief period of a microsecond (Naguchi et al. 2007, Leroux 2012, see). Ground carbonaceous chondrite (CR2) was fired at approximately 6.1 km s^{-1} (Stardust collection speeds) into aerogel in order to investigate the capture effects. Three examples of shifted olivine spectra were observed. An estimate of the shift for the peaks P1 and P2 (the main two peaks seen in olivine spectra) for the three spectra are 1.21, 1.56 and 1.48 cm^{-1} and 1.81, 3.40 and 3.21 cm^{-1}, both to lower wavenumbers, respectively. The capture effects exhibited by olivine when contained within a mineral assemblage were found to be less than those when the olivine was a single grain.

In summary, the work in this thesis was undertaken in order to understand the hypervelocity impact effects upon the projectile. This is reasonably straight forward for the mechanical effects, however, the shock effects upon the carbon Raman bands were more complex. The most significant is the natural variation in the raw sample spectra. Despite this, it is possible to observe the effects of shock pressure upon the carbon D and G bands.

Contents

List of Tables

List of Figures

Publications

A list of publications resulting from work presented in this thesis is given below.

Refereed Publications

Jamie E. Wickham-Eade, Mark J. Burchell, Mark C. Price, Leon J. Hicks, Jane L. MacArthur and John C. Bridges. Raman identification of olivine grains in fine grained mineral assemblages fired into aerogel. *Procedia Engineering* (2017).
(Based on Chapter 9 of this thesis)

L. J. Hicks, J. L. MacArthur, J. C. Bridges, M. C. Price, J. E. Wickham-Eade, M. J. Burchell, G. M. Hansford, A. L. Butterworth, S. J. Gurman, and S. H. Baker. Magnetite in Comet Wild 2: Evidence for parent body aqueous alteration. *Meteoritics and Planetary Science* (2017).
(Shots from Chapter 9 of this thesis)

In Preparation

Wickham-Eade, J. E. and Burchell, M. J. and Price, M. C. and Harriss, K. H. Hypervelocity impact fragmentation of basalt and shale projectiles. (*in review*).
(Based on Chapter 5 of this thesis)

Conference Abstracts

For all abstracts written by thesis author see Appendix C.

Burchell, M. J. and Wickham-Eade, J. E. Fragmentation of basalt projectiles in hypervelocity impacts in the laboratory. *Bridging the Gap III* (2015) Abstract Number 1034.
(Based on Chapter 5 of this thesis)

Wickham-Eade, J. E. and Burchell, M. J. Can micrometeorites survive impact on the Moor or Vesta? Fragmentation of basalt projectiles in hypervelocity impacts in

the laboratory. *Royal Astronomical Society Cosmic Dust Meeting* (2015).
(Based on Chapter 5 of this thesis)

Wickham-Eade, J. E. and Burchell, M. J. Fragmentation of basalt and shale projectiles in hypervelocity impacts in the laboratory. *LPSC XLVII* (2016) Abstract Number: 1235.
(Based on Chapter 5 of this thesis)

Wickham-Eade, J. E. and Burchell, M. J. Shock pressure and temperature effects on carbon D and G bands in Raman Spectroscopy for basalt, shale and graphite. *LPSC XLVIII* (2017) Abstract Number: 1405, Poster.
(Based on Chapter 6 and 8 of this thesis)

Hicks L. J., Bridges J. C., MacArthur J. L., Wickham-Eade J. E., Price M. C., Burchell M. J., Butterworth A. L. and Baker S. H. Analogues for Wild2: carbonaceous chondrites shot into aerogel. *MetSoc 2016* (2016) Abstract Number: 6428, Poster.
(Shots from Chapter 9 of this thesis)

Wickham-Eade, J. E. and Burchell, M. J. and Price, M. C. and Hicks, L. J. and MacArthur, J. L. and Bridges, J. C. Raman identification of olivine grains in fine grained mineral assemblages fired into aerogel. *14th Hypervelocity Impact Symposium* (2017), Talk.
(Based on Chapter 9 of this thesis)

Chapter 1

Impacts

Observing the moon in the night sky, it is evident today that it has been subjected to a punishing life of impacts from other bodies. Moreover, the existence of the moon itself is thought to be as a result of an impact with an early Earth (Canup & Asphaug 2001, and references within). Equally looking at other rocky bodies we can observe the evidence of a brutal past with varying sized craters. Recent space missions, such as Dawn (NASA-JPL 2016), have returned highly detailed images of the pitted surfaces of these distant worlds. For example, the images returned by Dawn of the surface of Vesta showed an abundance of impact craters with some having preserved ejecta blankets, large troughs and enigmatic dark material (Jaumann et al. 2012). All these images revealed a collision-dominated history (Marchi et al. 2012). This continual process in the evolution of our solar system is something that needs to be understood in order to comprehend the future of our solar system and the development of others. This latter point is of ever increasing importance as the human race discovers that there are planets like Earth in other solar systems and look to investigate the potential habitability of these distant worlds.

The field of Planetary Science has concentrated heavily on the craters themselves and the ejecta from these craters. However, the fate of the projectile is relatively neglected. The fate of projectiles in different scenarios is, therefore, one topic explored

in this thesis. As well as fragmentation of projectiles during impact there can be shock heating which can change the composition or nature of the impactor material. Pasek (2015) investigated the origin of the moderately volatile mineral schreibersite (a phosphide, (Fe,Ni)3P) on the moon. He proposes that it has an origin from impact volatilization of phosphates followed by a reaction of phosphorus gases with metal to form metal phosphides. Amongst the volatilization, there would be other shock effects experienced by the impacted materials on the surface of the moon. Phosphorus is the 11th most common element on the Earth and it is essential for DNA, cell membranes and bones. Another important volatile to life is carbon, but the effects of high shock pressures on carbon bearing impactors has not been extensively explored. Fries et al. (2009) fired different coals into aerogel at 6.1 km s^{-1} as a Stardust analogue study but work investigating shock effects from impacts not into aerogel (peak shock pressure in excess of 1 GPa) have not been investigated. Furthermore, with the introduction of Raman spectrometers to space missions, such as ExoMars (Courreges-Lacoste et al. 2007) and Mars2020 (NASA 2014*b*), research using Raman spectroscopy to study planetary materials is highly timely.

The rest of this chapter shall look at the theory of shock physics, types of impactors, impact speeds and probability in the Solar System, cratering, catastrophic disruption and fracture mechanics.

1.1 Shock Physics

A shock or shock wave is generated when a wave moves faster than the local speed of sound in the material (Isbell 2005). These shocks can be generated for example by the detonation of explosives, the explosion of supernovae or impacts from impactors travelling at hypervelocities (speeds in excess of a few km s^{-1}). Figure 1.1 shows an above and side view of the particles within an infinite plate and how they react to a propagating shock front induced by a rigid impactor. A shock front will propagate

through a material with a shock velocity of U_s which increases the density (ρ), particle velocity (u_p) and internal energy (E) in the shocked part of the material. The particle velocity is the velocity of the particles as they are caught up in the flow of the passing shock wave (Boslough & Asay 1992).

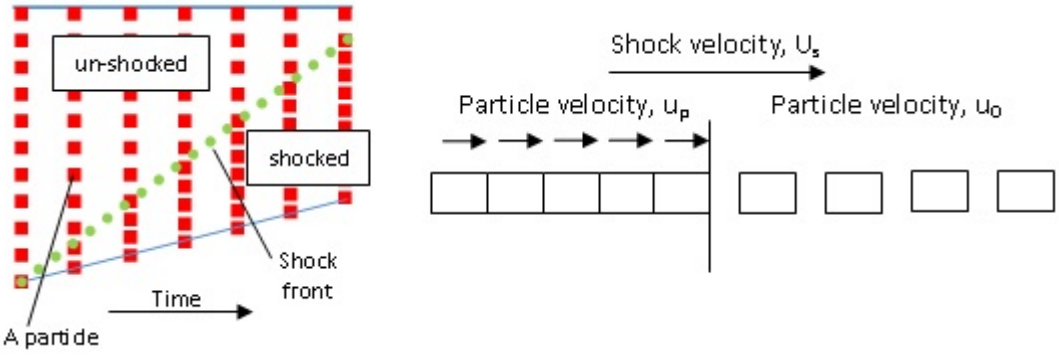

Figure 1.1: Visual representation of shock wave propagating through material. *Left:* from above and *Right:* side view. Image from Winter (2009).

For a short time, there can be said to be two regions; shocked (where the shock front has already propagated through) and un-shocked (where the shock front has yet to propagate). In between these two regions, there is a discontinuity. As already stated the shock velocity is in the order of kilometres per second (km s^{-1}) or, as is conventional in shock physics, millimetres per microsecond (mm μs^{-1}). The shock velocity is always greater than the particle velocity from a stationary frame of reference (Boslough & Asay 1992).

1.1.1 Conservation Equations

Mass, momentum and energy are all conserved across the shock discontinuity. From this, three conservation equations can be deduced on the assumption that there is no lateral movement of material. In Figure 1.2, the upper block of material is shown at the instance of impact and the lower block at some time (Δt) after it has been shocked. The laws of conservation (for mass, momentum, pressure and energy) can be applied to the material that originally lies to the left of the dashed line in the top block of

material.

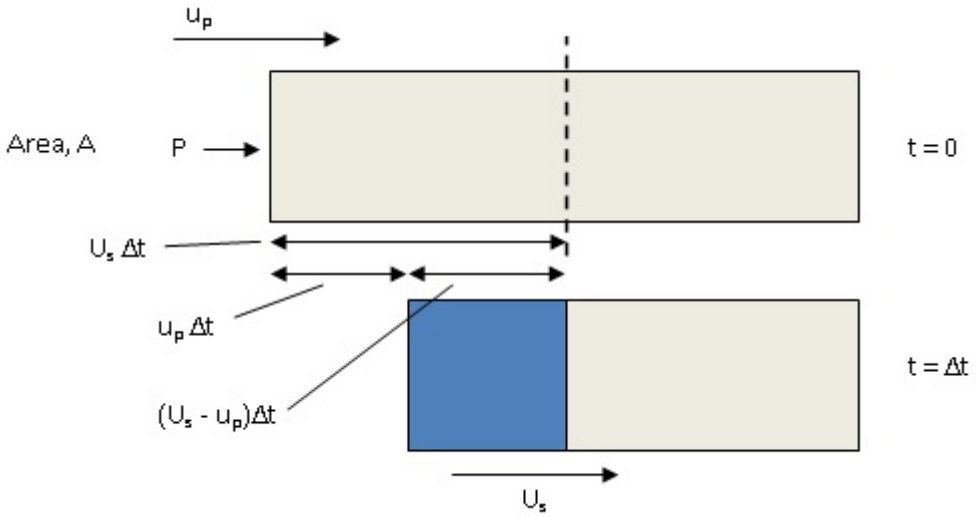

Figure 1.2: Depiction of material being shocked from the left. *Upper block:* At the instance of impact. *Lower block:* At time (Δt) after shock. The compression of the material can be determined by using the particle speed and the time elapsed. *Note:* u_p is the particle velocity, U_s is the shock velocityand P is the impact pressure. Image from Winter (2009).

From Figure 1.2 and the conservation of mass we can deduce:

$$\rho_0 U_s A \Delta t = \rho A (U_s - u_p) \Delta t, \tag{1.1}$$

where A is the surface area. This gives, after eliminating common term,

$$\rho_0 U_s = \rho (U_s - u_p), \tag{1.2}$$

and which finally after rearranging yields,

$$\frac{U_s - u_p}{V} = \frac{U_s}{V_0}, \tag{1.3}$$

where V is the specific volume (volume per unit mass).

The pressure which induced the shock discontinuity, can be determined using the

conservation of momentum. Using the fundamental physical equations for force,

$$F = ma, \tag{1.4}$$

for pressure,

$$P = \frac{F}{A}, \tag{1.5}$$

for acceleration,

$$a = \frac{v}{\Delta t}, \tag{1.6}$$

and momentum,

$$p = mv, \tag{1.7}$$

where F is force, m is mass of material, a is acceleration, P is pressure which induced the shock wave, A is area of impacting surface, v is velocity of impact and p is momentum. These equations can be combined to give:

$$P = \frac{p}{A\Delta t}. \tag{1.8}$$

Since the initial momentum of the element under consideration is zero the total momentum is:

$$p = \rho_0 U_s A \Delta t u_p, \tag{1.9}$$

where $A\Delta t u_p$ gives the volume of the material, and this with the combination of ρ_0 gives the mass of the material. Substituting Equation 1.9 into Equation 1.8, and assuming that there is an initial pressure (P_0), gives the shock pressure which causes the shock discontinuity:

$$P - P_0 = \rho_0 U_s u_p. \tag{1.10}$$

Using the conservation of energy we can deduce another useful equation in shock physics. We start with the principle that work done by a force is the force applied multiplied by the distance moved, that the specific energy is energy per unit mass, and

the specific energy gained by particles is equal to the sum of the specific internal energy and the specific kinetic energy (Boslough & Asay 1992). We can then show that:

$$Work\,done = PAu_p\Delta t, \tag{1.11}$$

$$Total\,Energy\,Gain = \rho_0 U_s A\Delta t((E - E_0) + \frac{1}{2}u_p^2). \tag{1.12}$$

Where E is the internal energy and E_o is the initial internal energy. Combining these two equations gives:

$$pu_p = \rho_0 U_s((E - E_0) + \frac{1}{2}u_p^2). \tag{1.13}$$

This can be reduced further by introducing Equation 1.10 and assuming P_0 is negligible:

$$E = \frac{1}{2}u_p^2. \tag{1.14}$$

Equations 1.3, 1.10 and 1.13 can be combined to eliminate velocities, yielding the Rankine-Hugoniot equation (Equation 1.15) for the internal energy jump, in terms of pressures and specific volumes (Boslough & Asay 1992).

$$E - E_0 = \frac{1}{2}(V_0 - V)(P + P_0). \tag{1.15}$$

Furthermore, Equation 1.3 and 1.10 can be rewritten to include initial conditions:

$$\frac{\rho_0}{\rho} = 1 - \frac{(u_p - u_{p0})}{(U_s - u_{p0})}, \tag{1.16}$$

$$P - P_0 = \rho_0(u_p - u_{p0})(U_s - u_{p0}). \tag{1.17}$$

These three equations (Equation 1.15, 1.16 and 1.17) are known as the Rankine-Hugoniot relations and are referred to as 'jump conditions' due to initial values jumping to final values as the shock wave passes by (Boslough & Asay 1992).

1.1.2 The Hugoniot and Rayleigh Line

During a hypervelocity impact, the applied stress far exceeds the yield stress of the solid, meaning that the materials impacting can be treated as fluids implying there is no material shear strength. In these circumstances, the process is deemed to be 'hydrodynamic' (Boslough & Asay 1992). To determine further information about the state of the shocked material, a Mie-Grüneisen equation of state is used (Equation 1.18). An equation of state is an equation which describes the relationship between volume, temperature and pressure of a quantity of a particular material.

$$P - P_0 = \frac{\Gamma}{v}(E - E_0), \tag{1.18}$$

where Γ (known as Grüneisen gamma) can be expressed in terms of measurable quantities determined by non-shock methods as:

$$\Gamma = \frac{3\alpha c^2}{JC_p}, \tag{1.19}$$

where α is volume coefficient of expansion, c is the sound speed, J is the mechanical equivalent of heat and C_p is the specific heat at constant pressure.

The combination of this equation of state, and the Rankine-Hugoniot relations give four equations with five variables: P, V, E, U_s and u_p. Therefore there is only one independent variable and a curve that is defined in a five-dimensional variable space. This is called the 'Rankine-Hugoniot curve', or more commonly as the 'Hugoniot' (Boslough & Asay 1992). The Hugoniot can be represented in any two-dimensional plane, however, it's most useful representations are in the $P-V$, $P-u_p$ and U_s-u_p planes. There is a family of Hugoniots for a given material with each focused on the initial state defined by P_0 and V_0. It must be noted that the Hugoniot is not a path that is followed during the propagation of the shock wave, but a locus that describes potential end states that can occur after the propagation of a single shock wave (given a certain initial state). The path followed by the steady shock compression is a chord which connects the initial

and final states of the material; this is known as the 'Rayleigh Line' (Boslough & Asay 1992).

From gas gun experiments the shock velocity and particle velocity can be determined for a material, and by plotting these on a $U_s - u_p$ plane the result is a Hugoniot. By taking the equation of the line of best fit it is possible to determine the constants which describe that material (see Figure 1.3 and Equation 1.20).

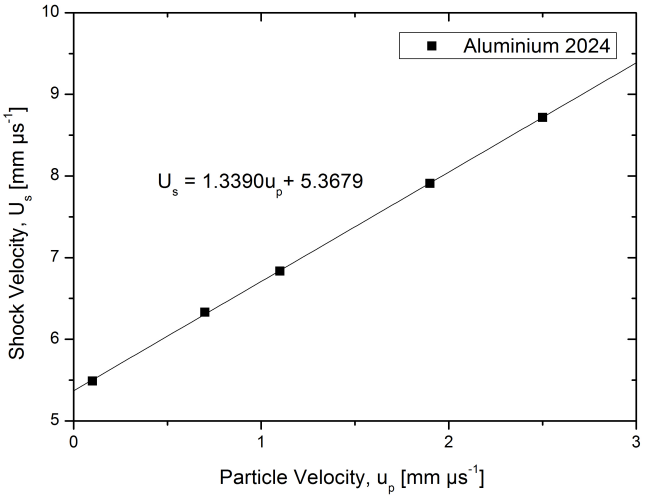

Figure 1.3: Hugoniot in $U_s - u_p$ plane of impact experiments on Aluminium 2024 Alloy (density 2.785 g cc^{-1}). Example taken from Winter (2009).

$$U_s = c + Su_p. \tag{1.20}$$

In the case of Aluminium 2024 (Figure 1.3), the coefficient c is 5.37 km s^{-1} and S is 1.34 (where U_s and u_p are in km s^{-1}). Each material will have different c and S constants, and these can be used to determine other information about the material being shocked.

The constants of a material and Equation 1.20 can be used in conjunction with Equation 1.10 to give an expression for the pressure that is solely dependent on the

particle velocity. With the assumption that P_o is negligible.

$$P = \rho_0(c + Su_p)u_p. \tag{1.21}$$

Equation 1.21 can be used to plot the Hugoniot in the $P-u_p$ plane. However, in order to determine the pressure at a certain shock velocity, the Rayleigh line is required, which is given by plotting Equation 1.10, as shown for Aluminium 2024 in Figure 1.4. Where the Rayleigh line first intersects the Hugoniot is the initial pressure, and the second intersection is the peak shock pressure. In this example (Figure 1.4), the pressure at this state would be 54.4 GPa.

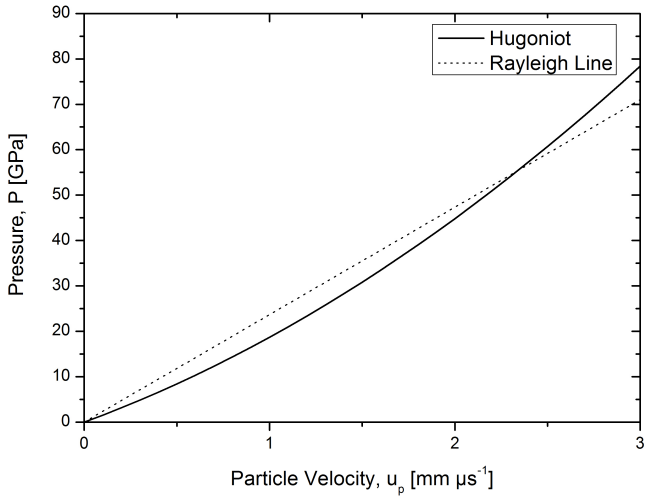

Figure 1.4: Hugoniot and Rayleigh line plotted in the $P - u_p$ plane for Aluminium 2024. The shock velocity is at 8.5 km s^{-1}. Example calculated from Winter (2009).

The $P - u_p$ plane is very useful. For example, knowing the Hugoniots for two impacting materials it is easy to determine the states generated by the collision. This method makes use of the fact that, following an impact, the normal stress and the particle velocity must be the same on both sides of the interface between impactor and target (Winter 2009). The method simply consists of plotting one Hugoniot in reverse (using Equation 1.22, where V is impact velocity) to the other material's Hugoniot and

where they intersect is the pressure at that state (see Figure 1.5) (Melosh 1989):

$$P = \rho_0(c + S(V - u_p))(V - u_p). \tag{1.22}$$

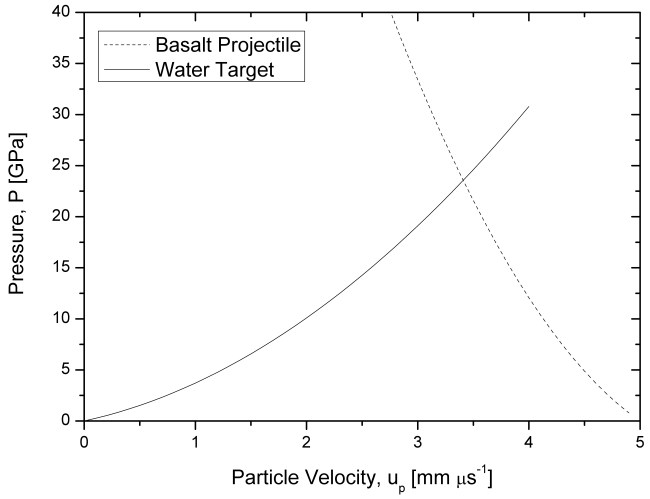

Figure 1.5: The Hugoniots of a basalt projectile impacting a water target. The water target pressures are determined using Equation 1.21. The basalt projectile is plotted in reverse using Equation 1.22 at an impact speed of 5 km s^{-1}. The intersection of the two lines is the peak shock pressure, which is 23.6 GPa.

Figure 1.5 is an example of this, using Equation 1.21 for a water target ($c = 2.393$ km s^{-1}, $S = 1.33$ and $\rho_0 = 997.9$ kg m^{-3}) and Equation 1.22 for a basalt projectile (with $c = 2.60$ km s^{-1}, $S = 1.62$ and $\rho_0 = 2860$ kg m^{-3} all values from Melosh 2013) impacting at 5 km s^{-1} would give a peak shock pressure of 23.6 GPa. Fundamentally, it is solving Equation 1.21 and 1.22 as simultaneous equations where they have the same particle velocity.

1.1.3 The Planar Impact Approximation

The Planar Impact Approximation (PIA) is a rough estimate of the quantities determined by the Hugoniot and Rayleigh line in the $P - u_p$ plane. It is only valid as long as

the lateral dimensions of the projectile are small compared with the distance the shock has propagated (Melosh 1989, 2013). This makes it valid for the contact and most of the projectile/target compression stages.

The idea behind the PIA is that two infinitely wide plates of material representative of both the projectile and the target, impact one another face-on at the given impact speed. The infinitely wide plates avoids the effects of the lateral edges of both the projectile and target. Furthermore, oblique impacts can also be approximated by using the vertical component of the impact velocity. Further assumptions of the PIA are that, after impact the pressure in the projectile and target are both equal, and that the projectile material cannot interpenetrate the target. By combining the Rankine-Hugoniot equations (Equation 1.15, 1.16 and 1.17) with the equation of the state for both the projectile and target, and applying the appropriate assumptions, results in two sets of equations which are linked. This results in unique solutions which can be obtained numerically (Melosh 2013).

For materials which both have linear $U_s - u_p$ relations (Equation 1.20) and adding subscripts p for projectile and t for target materials, the particle velocity for the target is given by (for u_{pp} in the projectile use $v_i - u_{pt}$):

$$u_{pt} = \frac{-B + \sqrt{B^2 - 4AC}}{2A}, \tag{1.23}$$

where:

$$A = \rho_{0t} S_t - \rho_{0p} S_p, \tag{1.24}$$

$$B = \rho_{0t} c_t + \rho_{0p} c_p + 2\rho_{0p} S_p v_i, \tag{1.25}$$

$$C = -\rho_{0p} v_i (c_p + S_p v_i). \tag{1.26}$$

The value of u_t can then be used in Equation 1.10 to determine the peak shock pressure (the pressure just behind a shock wave). Table 1.1 gives some example peak shock pressures for vertical impacts using the PIA (Melosh 2013). If we calculate the

PIA for the example at the end of Section 1.1.2, we again get a peak pressure of 23.6 GPa, showing the equivalence of the two calculation methods.

Table 1.1: Maximum shock pressures in vertical impacts (from Melosh 2013).

Impact velocity [km s^{-1}]	Pressure [GPa]		
	Iron on basalt	Basalt on basalt	Serpentinite (Carbonaceous chondrite) on ice
5	78	48	22
7.5	150	93	44
10	250	150	73
15	500	320	160
30	1800	1200	580
45	3900	2500	1300

It must be noted that using the PIA in the scenario where both the projectile and target are the same material, results in u_{pt} equalling zero from Equation 1.23. Hence in this case, u_{pt} equals half of the impact velocity (Melosh 1989, 2013). This is then substituted into Equation 1.10. For the work in this thesis, the PIA was used to determine all peak shock pressures.

An issue with using the PIA to determine shock pressures for a projectile and target is that it only applies to regions just behind the contact plane and falls off in the interior of a projectile. Similarly, it decreases with depth into a target. Therefore, the peak shock pressure only represents an extreme value for materials in an impact.

1.2 Types of Impactors

The peak shock pressure has a strong influence on the fate of both the target and projectile, and, as Section 1.1 suggested, the material properties strongly affect the shock waves propagation and hence the magnitude of the pressure. The solar system is populated with a range of different potential impacting materials from the micrometre-sized micrometeorites to kilometre-sized comet nuclei and up to the hundreds of kilometre sized asteroids. This section discusses some of the different types of impacts within the

Solar System and their characteristics.

1.2.1 Asteroids and Meteorites

The formal definition of an asteroid is a metallic or rocky body without an atmosphere, that orbits around the sun but is too small (approximately less than 900 km in diameter) to be classified as a planet (Elkins-Tanton 2006). In contrast the definition of a planet is a body which is big enough to be a sphere under its gravity and to be in a permanent bound orbit around the Sun, meaning it won't be perturbed by an encounter with another body over its lifetime. Asteroids are predominantly detected in orbit around the Sun between Mars and Jupiter, at approximately 2-4 AU. They are thought to be primordial material denied any further accretion by interactions with Jupiter's strong gravitational field (Elkins-Tanton 2006). Currently, there have been approximately 700,000 asteroids found residing within these orbital distances and is termed the main belt.

Asteroids are classified based on their composition determined from the surface reflectivity spectra. The Bus-DeMeo taxonomy was devised to categorise the observable asteroids. The most numerous complex are the C-types, thought to make up 75% of the asteroid population. C-type asteroids are carbonaceous and consist of clay and silicate rocks. They exist furthest from the Sun, as a result they are at low temperatures meaning that these asteroids could have water on them in the form of ice (Fornasier et al. 2014). The infrared spectra of C-type asteroids suggest they are similar in composition to carbonaceous chondrite meteorites (see below). The fragments of multiple carbonaceous chondrite impacts are thought to have been detected upon the surface of Vesta (Reddy et al. 2012). Another complex is the S-type which are asteroids consisting of stony and nickel-iron material. These asteroids inhabit the inner asteroid belt and are thought to account for 17% of known asteroids. Finally, there are the X-type which are a range of materials from carbonaceous (P-type), enstatite rich (E-type) to

metallic (M-type). These are thought to account for 8% of the known asteroid population. There are some spectra that do not fit into any of these complexes and which are known as the End Members (DeMeo et al. 2009).

In addition to these asteroids in the asteroid belt, there are also Near Earth Asteroids (NEAs) such as the Aten, Amor and Apollo groups which are defined by their orbits. The Atens are asteroids which cross Earth's orbit with a period less than 1 year. The Amors are asteroids which cross Mars' orbit but do not quite reach the orbital path of the Earth. Finally, the Apollos are a group of asteroids which cross Earth's orbit with a period greater than 1 year.

Meteorites are categorised differently to asteroids. They are split into three groups Stony, Stony-iron and Iron meteorites. These groups consist of multiple subgroups, of particular interest to the work in this thesis are the subgroups Chondrites and Achondrites from the Stony Meteorite group.

Chondrites have not been modified due to melting or differentiation of the parent body. Therefore, they are primitive objects formed by accretion. These are also the most common meteorites that fall on the Earth. The study of these is important for understanding the origin and age of the Solar System and the synthesis of organic compounds. Chondrites are so-called because they contain chondrules - 150 to 900 μm sized spherules thought to have formed by the rapid cooling of a silicate melt. Subgroups of the chondrite group are; Carbonaceous Chondrites (which have subgroups: CI, CM, CO, CV, CK, CR, CH, CB), Ordinary Chondrites (which have subgroups: H, L, LL), Enstatite Chondrites (which have subgroups: EH, EL) and R and K chondrites (Weisberg et al. 2006). The primary minerals in Chondrites are Olivine, Pyroxene, Iron-Nickel minerals, Troilite, Iron Oxide and Plagioclase Feldspar.

Achondrites do not contain chondrules. These meteorites have been differentiated and reprocessed due to melting and recrystallization on or within the meteorite's parent body. Hence, they have distinctive textures and mineralogies indicative of igneous processes. Therefore, these materials are similar to basalt or plutonic rocks. A sub-

group of Achondrites are HED (Howardite-Eucrite-Diogenite) meteorites. These have experienced extensive igneous processing similar to terrestrial magmatic rocks. The origin of HED meteorites are thought to be from the crust of the asteroid Vesta. The differences are thought to be due to the different geologic histories of their parent body. The method that these meteorites reach Earth are thought to be via an impact on Vesta ejecting debris. In particular, Eucrites are particularly basalt-like. These consist of clinopyroxenes.

From Section 1.1, the composition of each asteroid/meteorite would strongly affect the peak shock pressure upon impact and hence the fate of both the target and projectile.

1.2.2 Comets

Comets are small icy Solar System bodies, that heat up and begin to outgas, displaying a visible atmosphere (coma) and sometimes a tail, when passing near the sun. There are two types of tails produced by comets, a dust tail and an ion tail. These tails are not indicative of the direction of travel but rather the direction of the solar wind. There can be more than two tails as it depends on the differing ions in the ion tail. Within the coma, there is the comet's nucleus which is the solid part of a comet. The nucleus is typically up to a few tens of kilometres in size.

Comets are classified by their orbits as either long-period comets or short-period comets (orbit of less than 200 years). Short-period comets are split into two subcategories; Jupiter Family Comets (JFCs) and Halley-Type Comets (HTCs) (Lardner 1853). An example of a short period comet is Halley's comet which has an orbital period of 75–76 years. Long-period comets are split into two subcategories called; New (semi-major axis greater than 10,000 AU) and Returning (semi-major axis less than 10,000 AU).

The orbits can also be defined in terms of the invariant Tisserand with respect to

Jupiter (T_J) and the inverse of the semi-major axis (Burchell & Kearsley 2009). A Tisserand is a dynamical quantity which is approximately conserved during an interaction between a planet and a smaller interplanetary body (Burchell & Kearsley 2009). The equation for this is given by:

$$T_J = \frac{a_J}{a} + 2cos(i)\sqrt{(1-e^2)\frac{a_J}{a}}, \tag{1.27}$$

where a is the semi-major axis, e is the eccentricity, i the inclination of the comet's orbit and a_J the semi-major axis of Jupiter. The plotting of this splits the comets into Oort cloud comets and JFCs.

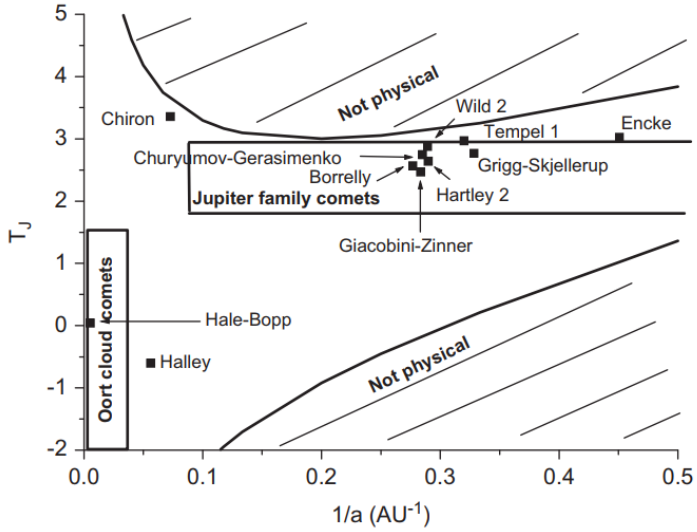

Figure 1.6: Comet classification via Tisserand (with respects to Jupiter) and semi-major axis, from Burchell & Kearsley (2009). The majority of comets lie in the regions labelled Oort cloud comets or Jupiter family comets. The exact boundaries of these regions are approximate.

Comet nuclei are thought to have formed in either the region beyond Neptune (the Kuiper belt and the scattered disk) or the space between the giant planets (Lamy et al. 2004). The latter is thought to be the origin of the majority of the ecliptic and long-period comets, which now reside in the Oort cloud. Their composition is a combination of rock, water ice, frozen CO_2, CO, CH_4 and organic material (Bockelée-Morvan et al. 2004). The average density of known comets is 0.6 g cm^{-3}, indicating that they are

highly porous bodies (Weissman et al. 2004).

With these compositions, it was thought that comets brought volatiles, water and organics to Earth (e.g. Morbidelli et al. 2000). This theory was supported by the discovery that comet 103P/Hartley 2 has a deuterium-to-hydrogen ratio (D/H) similar to that of Earth (Hartogh et al. 2011). However, the Rosetta mission contradicted this by showing that the comet 67P/Churyumov-Gerasimenko has a higher D/H ratio than the Earth (Altwegg et al. 2015) throwing this idea into ambiguity. It was also shown that the measured D/H ratio on bulk Earth and on studied asteroids differed significantly (Morbidelli et al. 2000). However, again there was contradicting evidence in the discovery that D/H ratio of carbonaceous chondrites is similar to Earth's ratio (Robert 2003). This could suggest that some but not all asteroids and comets could be deliverers of water to Earth.

1.2.3 Cosmic Dust and Micrometeorites

Cosmic dust permeates throughout the Solar System and is generally less than a few millimetres in size. Another group of small particles are micrometeorites, these are cosmic dust particles that arrive on the Earth's surface. A further group is the interplanetary dust particles (IDPs). The main source of cosmic dust particles are comets, asteroids and minor bodies which have volcanic activity on, such as Enceladus which produces material for Saturn's E-ring. Additionally, magnetic fields can accelerate dust (if charged) to the required escape velocities, i.e. dust from around Jupiter can be ejected into the rest of the Solar System (Flandes & Maravilla 2004). Dust doesn't only have to originate from within the solar system it can also be from interstellar sources (e.g. neighbouring stars) which can penetrate even into the inner heliosphere (Grün et al. 1993). The masses of these objects range between 10^{-16} and 10^{-4} kg (Zook 2002). The NASA Stardust mission returned with likely interstellar dust grains in-situ in the Solar System (Westphal et al. 2014).

1.3 Impact Speeds and Probability in the Solar System

Another important factor related to the peak shock pressure and the effects on both the target and impactor is the impact velocity. This is heavily influenced by where in the solar system the impact occurs. In addition, the size of the target body also influences the impact speed due to gravitational attraction. The range of resulting impacts speeds are from a few km s^{-1} to tens of km s^{-1}. This section shall discuss the impacts speeds within the asteroid belt, on Earth, Mars and in the outer Solar System.

1.3.1 Main Asteroid Belt

O'Brien & Sykes (2011) calculated the collision velocity distribution for Vesta, Ceres and the entire main belt using an algorithm from Bottke et al. (1994). Figure 1.7 shows the impact velocity distributions from O'Brien & Sykes (2011). In addition to this, in Table 1.2 we show the mean, root mean squared (RMS) and median impact velocities in these three scenarios. As O'Brien & Sykes (2011) noted that whilst the average impact velocities are often quoted and used (approximately 5 km s^{-1}), asteroids within the belt actually experience a significant fraction of impacts at velocities both smaller and larger than this, with an impact velocity range of approximately 14 km s^{-1}.

As seen in Figure 1.7, both Vesta and Ceres have a slightly smaller average impact velocity than the asteroids in the main belt. This is due to their orbital eccentricities and inclinations which are not particularly large. Furthermore, Ceres has a larger impact probability than Vesta due to its more central location within the belt which results in it crossing more orbits of potential impactors (O'Brien & Sykes 2011). A more significant difference between Vesta and Ceres and the main-belt asteroids is seen at velocities over approximately 8 to 10 km s^{-1}, where their probability of being impacted is roughly half that of those in the main-belt (O'Brien & Sykes 2011). O'Brien & Sykes (2011) suggest that this could result in a significant difference in the surfaces of both Vesta and Ceres and the asteroids in the main-belt, as at these speeds significant

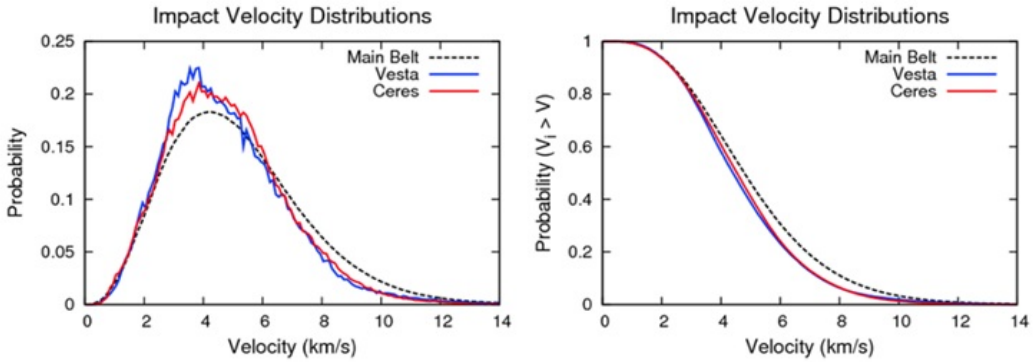

Figure 1.7: Collision velocity distribution for Vesta, Ceres and the entire main-belt, calculated using the algorithm of Bottke et al. (1994) (O'Brien & Sykes 2011). All asteroids with $H < 11$ (roughly 30 km in diameter) are included in the calculation. The figure on the right is a cumulative version of the figure on the left. The images are from Figure 6 in O'Brien & Sykes (2011).

impact melt is produced. However, it should be noted that Wünneman et al. (2008) have predicted from modelling, that even an impact at 6 km s^{-1} can result in substantial melt depending on target porosity.

Table 1.2: Collision velocities (V) and probabilities (P_i) for impacts on Vesta, Ceres and the entire main-belt, calculated using the algorithm of Bottke et al. (1994) by O'Brien & Sykes (2011). All asteroids with $H < 11$ (roughly 30 km in diameter) are included in the calculation

	P_i [10^{-18} km^{-2} yr^{-1}]	V_{mean} [km s^{-1}]	V_{RMS} [km s^{-1}]	V_{median} [km s^{-1}]
Vesta	2.72	4.75	5.18	4.41
Ceres	3.43	4.79	5.19	4.54
Main Belt	2.79	5.14	5.64	4.79

O'Brien & Sykes (2011) also calculated the impact frequency using the intrinsic collision probability, P_i, the sum of the mean target and projectile radii, r, and the number of projectiles, N_p (for example, the number of bodies of a given size). Vesta has a mean radius of 258 km (Thomas et al. 1997), and for an average intrinsic collision probability of 2.72 $\times 10^{-18}$ km^{-2} yr^{-1}, this implies that a random asteroid from the main-belt has a 1.81 $\times 10^{-13}$ yr^{-1} chance of hitting Vesta (O'Brien & Sykes 2011). Given the 1.3 million asteroids larger than 1 km in diameter (Jedicke et al. 2002, Bottke et al. 2005), this suggests that an asteroid larger than 1 km should impact

Vesta approximately every 4.2 Myr. For Ceres, this value falls to approximately every 1.0 Myr due to its larger size (O'Brien & Sykes 2011).

Finally, O'Brien & Sykes (2011) suggest that due to the Vestoids being clustered in orbital element space, their intrinsic collision probability and mean velocity of impact will be different to those impacting from the main-belt asteroids. The authors suggest that these values would be $P_i = 14.2 \times 10^{-18}$ km^{-2} yr^{-1} and $V_{mean} = 3.37$ km s^{-1} which is more probable and slower than asteroids from the main belt (O'Brien & Sykes 2011).

1.3.2 Earth, Moon and Mars

Early determinations of the impact velocities for Earth Crossing Asteroids (ECAs) were based on the method used by Öpik (1976), which requires the assumption of a circular heliocentric orbit of the planet. Steel (1998) argues that this is adequate for situations such as the Earth (with an eccentricity $e = 0.0167$). However, this can lead to misleading results for Mars. Instead, Steel (1998) favours the technique of Kessler (1981), which takes into account finite eccentricities such as Mars' of $e = 0.0933$.

Steel (1998) calculated the mean impact probability and speed for 116 ECAs (the number of known ECAs as of June 1996), and for near-parabolic comets (NPCs) impacting Earth shown in Table 1.3. Additionally, Steel (1998) calculates the maximum and minimum speeds for both situations (ECAs and NPCs) as 40.7 km s^{-1} and 12.6 km s^{-1}, and 73 km s^{-1} and 16 km s^{-1} respectively. For Mars, Steel (1998) determined the mean impact probability and speed for 646 asteroids near Mars (numbers as of November 1993) and near-parabolic comets shown in Table 1.3. Again calculating the maximum and minimum speeds for both situations (ECAs and NPCs) as 34.4 km s^{-1} and 5.7 km s^{-1} and 59 km s^{-1} and 11 km s^{-1} respectively. The minimum speeds are determined by the gravity of the body and are the in-fall speed against gravity (or the escape velocity). For the Earth, the Moon and Mars this is 11.2, 2.38 and 5.03 km s^{-1}

respectively.

Table 1.3: Table of different impactors mean impact speed and probability on the Earth, Mars and Moon. Abbreviations mean: ECAs - Earth Crossing Asteroids, NEAs - Near Earth Asteroids, NPCs - Near-parabolic Comets, SPCs - Short Period Comets, LPCs - Long Period Comets, HTCs - Halley-Type Comets and APCs - All Period Comets. In some cases only mean speeds are reported in the literature.

Type of Impactor	Impacting	Mean Speed [km s^{-1}]	Probability [yr^{-1}]	Reference
ECAs	Earth	17.7	5.08×10^{-9}	Steel (1998)
NEAs	Earth	21.7	1.85×10^{-9}	Jeffers (2001)
NPCs	Earth	55.0	2.22×10^{-9}	Steel (1998)
SPCs	Earth	19.9	1.81×10^{-9}	Jeffers (2001)
SPCs	Earth	24.3	-	Hughes (2000)
SPCs	Earth	29.0	-	Weissman (1982)
SPCs	Earth	41.0	-	Schultz (1988)
LPCs	Earth	54.2	2.18×10^{-9}	Jeffers (2001)
LPCs	Earth	53.0	-	Schultz (1988)
HTCs	Earth	57.1	1.02×10^{-9}	Jeffers (2001)
APCs	Earth	33.7	-	Hughes (2000)
Asteroid	Mars	9.30	3.14×10^{-10}	Steel (1998)
NPCs	Mars	45.0	2.44×10^{-10}	Steel (1998)
NEAs	Moon	19.4	1.15×10^{-10}	Jeffers (2001)
SPCs	Moon	18.1	8.25×10^{-11}	Jeffers (2001)
HTCs	Moon	57.9	6.79×10^{-12}	Jeffers (2001)
LPCs	Moon	52.4	1.48×10^{-10}	Jeffers (2001)

In comparison to this, Jeffers et al. (2001) calculated a synthetic distribution of orbital elements for 20,000 asteroids using a probability distribution of Rabinowitz et al. (1994) and applied a Monte Carlo (MC) numerical method to determine the impact velocities on the Earth and Moon. The mean values are also shown in Table 1.3. In comparison with Steel (1998), the value for mean impact probability is lower and the mean impact velocity is higher. This is most probably due to the number of asteroids they are using to attain their values (20,000 v.s. 116). Jeffers et al. (2001) went on to calculated the mean impact probabilities and speeds for Short Period Comets (SPCs), Long Period Comets (LPC) and Halley-Type Comets (HTCs) on the Earth and Moon (again shown in Table 1.3). The probabilities for impacts on the Moon are lower than that of Earth's, especially for slower impacting bodies (NEAs) due to

the strong interaction with the Earth's gravitational field. In addition, 10% of NEAs impacts are less than 10 km s^{-1} on the Moon, whereas there are no impacts at this velocity on Earth due to the in-fall speeds being different (Jeffers et al. 2001).

Hughes & Williams (2000) found the mean impact velocity of 14 SPCs on the Earth (Table 1.3) as 24.3 km s^{-1}. In comparison to prior work by Weissman (1982), this value is nearly 5 km s^{-1} slower. However, upon comparison with Schultz (1988) both these results are considerably different. This is thought to be due to the definition of short-period comets that Schultz (1988) is using. Such change in nomenclature alters the range of possible orbits and hence the impact speeds.

Another scenario for impacts on the Moon is one where it is impacted by ejecta from a large impact on Earth. However, the probability of this scenario occurring is very low. Armstrong (2010) used numerical modelling to investigate the transfer of terrestrial material to the Moon during a giant impact. Armstrong (2010) simulated 1.4 million particles over a range of launch velocities and ejecta angles deriving probable impact velocities, angles and sites on the Moon. He found a bimodal distribution, indicating that nearly 20% of the impacts occur nearly head on and almost 50% hit at oblique angles ($<20°$). Taking into account the angles of impacts, he found that approximately 10% of all impacts have vertical speeds of 0.1 km s^{-1} or less (Armstrong 2010). Additionally, 71% of impacts would have vertical velocities less than 2.5 km s^{-1} (Armstrong 2010) and the mean impact velocity would be approximately 2.6 km s^{-1}.

1.3.3 The Outer Solar System

Zahnle et al. (2003) used a Monte Carlo algorithm (Zahnle et al. 1998, 2001) which accounts for the different orbits of bodies, to determine the average impact velocities and other impacting parameters on satellites of bodies from Jupiter out to Pluto. The impacting bodies considered were ecliptic comets (as these dominate impact cratering in the outer solar system), long-period comets, Halley-type comets and Trojan asteroids.

The average impact velocities for all major satellites from Jupiter outwards are shown in Table 1.4.

Table 1.4: Average impact velocities on stated bodies. Table taken from Table 1 in Zahnle et al. (2003).

Body	Mean Impact Velocity [km s^{-1}]
Jupiter	
Io	32.0
Europa	26.0
Ganymede	20.0
Callisto	15.0
Saturn	
Prometheus	32.0
Pandora	31.0
Enceladus	30.0
Titan	10.5
Uranus	
Puck	15.0
Titania	6.80
Neptune	
Triton	8.20
Pluto	1.90
Charon	1.80

1.4 Impact Cratering

As stated, different impact speeds and types of impactors result in a variety of outcomes for both the target body and projectile. During a hypervelocity impact, there are three main stages (Gault et al. 1968): 1) Contact and compression; 2) Excavation; and 3) Modification. Additionally, a further stage of 'hydrothermal and chemical alteration' can be included as a separate final stage (Kieffer & Simonds 1980). These stages are discussed in turn below.

1.4.1 Contact and Compression Stage

The Contact and Compression Stage begins when the projectile first contacts the surface of the target (Figure 1.8). From modelling it is thought that the projectile can penetrate up to one or two times its diameter (Kieffer & Simonds 1980, O'Keefe & Ahrens 1982) during this stage. The intense kinetic energy of the projectile is transferred into the target in the form of shock waves which propagate into the target (and also back into the projectile). Once the shock wave reaches the back of the projectile it is reflected back in the form of a rarefaction or tensional wave (Ahrens & O'Keefe 1972). This, in turn, causes the projectile to unload from high shock pressures (>10 GPa) leading to melting and/or vaporisation of the projectile (Gault et al. 1968, Melosh 1989). The shock wave in the target results in an increase in internal energy leading to metamorphism, melting and/or vaporisation of a volume of target material close to the point of impact (Ahrens & O'Keefe 1972, Grieve et al. 1977). This highly shocked, isobaric volume in the target is often taken to be similar in size to the projectile. The end of the contact and compression phase is when the projectile is fully unloaded (Melosh 1989). The time (τ) for this is given by:

$$\tau = \frac{L}{v_i}, \tag{1.28}$$

where L is the projectile diameter and v_i is the impact velocity. Generally, this stage lasts for less than a second for all but the largest impacts.

1.4.2 Excavation Stage

This is the stage where the crater opens up into a much larger shape (Figure 1.8). The projectile plays little to no role in this stage as it has already unloaded, broken apart or melted and/or vaporised. The stage begins with a roughly hemispherical shock wave propagating out into the target. The centre of this hemisphere is often taken

as the depth to which the projectile has penetrated (Osinski & Pierazzo 2013). The propagation of the shock waves causes the target material to be set in motion, with an initial outward radial trajectory. Simultaneously the shock wave that initially travelled upwards meets the ground surface boundary and generates a rarefaction wave which propagates back down into the target body (Melosh 1989). In the near-surface region an 'interference zone' is formed in which the maximum pressure is reduced due to the interaction between the shock and rarefaction waves (Melosh 1989).

This combination of the shock and rarefaction wave causes an 'excavation flow-field' and generates a 'transient cavity' (Dense 1968). Due to the variety of trajectories of the material in the different regions of the excavation flow field, there is a splitting of the transient cavity into an upper 'excavated zone' and a lower 'displaced zone' (Osinski & Pierazzo 2013). The material in the upper zone is ejected past the cavity walls as an ejecta blanket. The material in the lower zone is thought to remain in the transient cavity (Stöffler et al. 1975) as it is displaced downwards. However, there is evidence that some material can be displaced out of the transient cavity by a second episode of ejecta emplacement (Osinski et al. 2011).

During this stage, the shock waves cause the creation of the cavity rim which rises above the initial ground level. The produced crater is many times larger than the projectile. On Earth, this is typically estimated to be 20 times the impactor diameter. This stage of cratering can take seconds to minutes to reach completion.

1.4.3 Modification Stage

This stage is determined by the size of the transient cavity and the properties of the target rock lithologies (Melosh & Ivanov 1999). For transient craters less than 2-4 km on Earth, the transient cavity undergoes minor modification which leads to the creation of a simple bowl shape crater (Figure 1.8a). For transient craters larger than this there is increased instability and the crater is modified heavily by gravitational

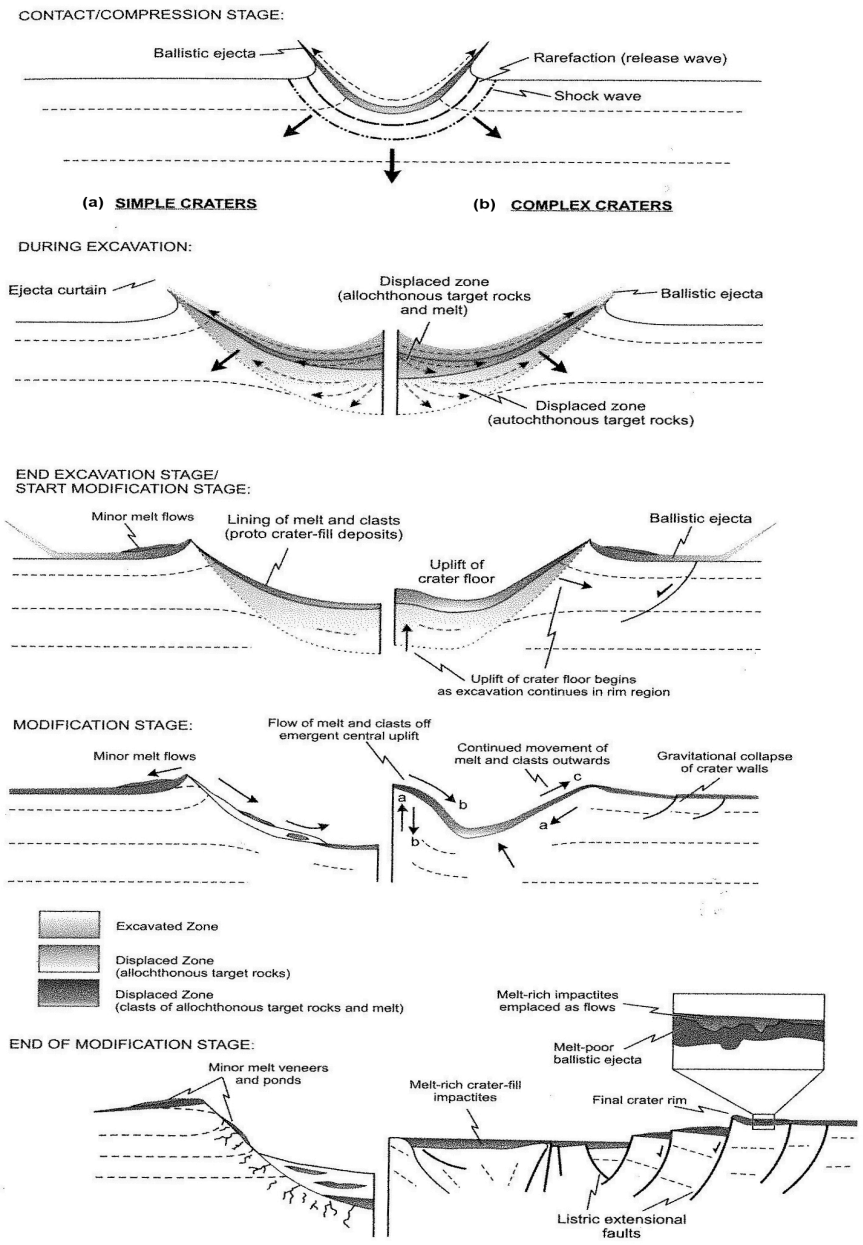

Figure 1.8: The cross-sections of the formation of a crater covering the three main stages. The left side shows the formation of a simple crater and the right the formation of a complex crater. Schematic from Osinski & Pierazzo (2013).

forces which result in a complex crater (Figure 1.8b). In a complex crater, a uplift effect occurs which causes the floor of the transient cavity to develop a central mound. This is due to the compressed material initially forced downwards, rebounding up at the centre - this is known as a lithostatic rebound. This inward and upwards movement of material also results in the steepening of the crater walls. The walls either collapse

and fall back into the crater basin (Osinski & Pierazzo 2013) or can remain causing slump terraces. Vertically ejected material can also fall back into the crater floor. The modification stage has no clear end point as it merges into more familiar geological processes such as mass movement and erosion. As well as slightly changing the overall crater diameter, this period can see in filling of the transient crater floor, leading to an apparent shallower crater.

1.5 Catastrophic Disruption

If the crater produced by an impact is large in comparison to the target body, then an impact disruption event can occur. The term catastrophic disruption refers to a form of impact where the shock pressures are so intense that they cause the body to disrupt into pieces where the largest piece's mass is equal to or less than 50% of the original body. An important parameter in catastrophic disruption is the impact energy density Q. If this exceeds a critical value (Q^*) then catastrophic disruption has occurred. This point is commonly defined as being when the mass of the largest single target fragment is half the initial target mass. The impact energy density for the combined projectile and target system is defined as the input energy per unit mass (Equation 1.29).

$$Q = \frac{0.5 M_p V_i^2}{M_p + M_t}, \tag{1.29}$$

where the $M_{p/t}$ is for the mass of the projectile or target and V_i is the vertical component of the impact velocity.

Although Q was originally introduced to study target disruption, it is also possible to consider the disruption of the projectile. Gault & Wedekind (1978) and Schultz & Gault (1990*b*) proposed that for just the projectile, the impact energy density, Equation 1.29, can be rewritten as:

$$Q_p = 0.5V_i^2, \tag{1.30}$$

or to include impact angles other than that of normal incidence:

$$Q_p = 0.5V_i^2 \sin^2(\theta), \tag{1.31}$$

where θ is the angle of impact with respect to the plane of the target.

Similar to Q^*, we can define Q_p^* as the threshold value of Q for the projectile when the largest intact projectile fragment is half the projectile's original mass.

Figure 1.9 is a schematic taken from Leliwa-Kopystynski et al. (2009) showing the full range of outcomes for a target body from an impact. For a projectile in a hypervelocity impact the catastrophic disruption threshold is reached at relatively low impact velocities. This is influenced by the ratio of the projectile to target mass.

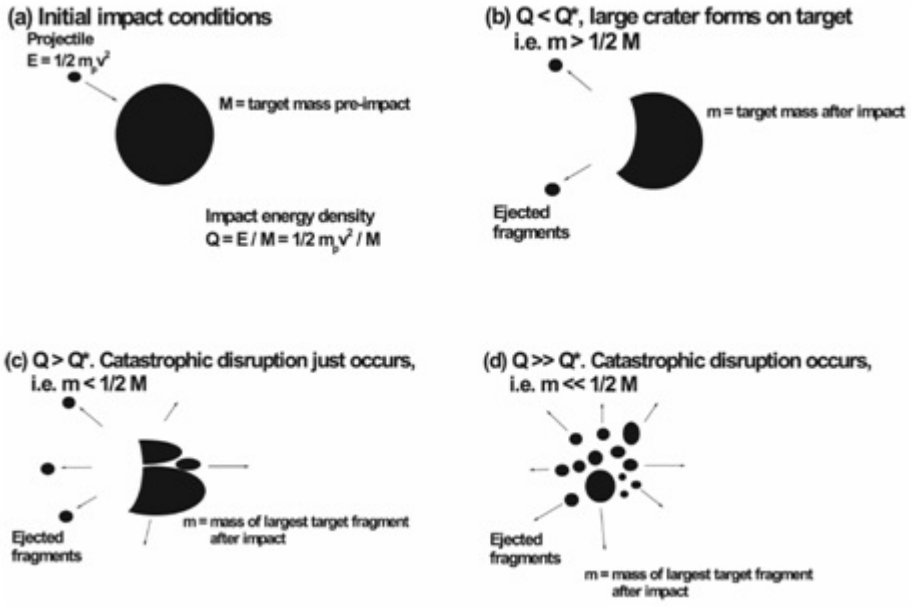

Figure 1.9: Schematic of possible outcomes from hypervelocity impacts on a body. a) shows the initial impact conditions, b) the outcome where the impact energy density is less than the threshold resulting in a crater, c) the result where the impact energy density is greater than the threshold resulting in catastrophic disruption just occurring and d) where the impact energy density is far greater than the threshold resulting in catastrophic disruption occurring. Schematic from Leliwa-Kopystynski et al. (2009).

Research into catastrophic disruption has been conducted both in the laboratory and using computer simulations. The majority of this research has extensively studied the fate of the target body in order to further our understanding of large-scale asteroid impacts (e.g. Holsapple et al. 2002). More recently, attention has turned to the ejecta from such impacts by studying their mass and velocities (e.g. Michikami et al. 2007, Housen & Holsapple 2011). However, there is a gap for research to be conducted into the fate of the projectile as the full extent of the projectile survivability is poorly understood. It is still often assumed that the projectile is vaporised upon impact and that little to none survives. With recent discoveries of foreign bodies on surfaces of solar system bodies, such as carbonaceous material on Vesta (Reddy et al. 2012) and the possibility of a 'Black Boulder' on (25143) Itokawa (Hirata & Ishiguro 2011), it would seem that a considerable quantity of impactor is surviving impacts. Indeed there is evidence of projectile material survival at terrestrial impact sites, e.g. the 25 cm sized fragment in cores from the Morokweng crater (Maier et al. 2006). For the remainder of this section, current research from laboratory experiments and computer simulations on the disruption, implantation and fate of the projectile shall be discussed.

1.5.1 Laboratory Experiments

One of the earliest discussions into the fate of the projectile was conducted by Gault & Heitowit (1963), where they investigated how the kinetic energy of the projectile was partitioned during an impact. They estimated that the projectile internal energy (the waste heat) was approximately 6% of the projectile's kinetic energy for sand, and between 4 and 12% for basalt targets. Later, Gault & Wedekind (1978) investigated projectile ricochet in shallow angle impacts in the laboratory, as well as the projectile energy density (Q_p^*) needed to fragment aluminium and basalt projectiles during an impact.

Shallow angle impacts were investigated further by Schultz & Gault (1990*b*) in which

they considered in detail the break-up of projectiles in such impacts. In this work, they fired aluminium and basalt spheres at predominantly steel targets, but with some examples of water and aluminium as well. The speed range the experiments were conducted over was from 0.4 to 5.3 km s^{-1}, at angles less than 30° (and as low as 2.5°) from the horizontal. In addition to the projectile fragmenting, a significant amount of the impactor was recovered post-shot (over 50% in some cases). In cases where the projectile ricocheted it was effectively intact. Additionally, Burchell et al. (2010, 2015) fired aluminium spheres at angles of approximately 1° incidence onto sand targets at 2 km s^{-1} in order to determine features of the SMART-1 crater. They concluded that the spacecraft body would not be present in the main crater (Burchell et al. 2015).

Schultz & Gault (1984) also investigated how the projectile fragmentation can influence crater morphology. They found that when the impact induced shock pressures exceeded the dynamic strength of the projectile, cratering efficiency was reduced. However, since this occurs at modest impact speeds, extrapolation of low speed data to higher speed examples in the Solar System may not be effective.

Separate studies have also considered projectile fragmentation during penetration of thin plates (Piekutowski 1995). In that work spherical aluminium projectiles, approximately 9.53 mm in diameter, were fired at thin sheets from 1.98 km s^{-1} to 7.38 km s^{-1}. They found that the projectile made up the dominant feature in the debris cloud by capturing images of it using radiography. Piekutowski (1995) determined the components of the front, middle and back of the debris cloud.

Nagaoka et al. (2014) fired millimetre-sized pyrophyllite and basalt projectiles onto regolith-like sand targets at velocities up to 960 m s^{-1}. They determined Q_p^* to be $(4.5 \pm 1.1) \times 10^4$ for pyrophyllite and $(9.0 \pm 1.9) \times 10^4$ J kg^{-1} for basalt projectiles (Nagaoka et al. 2014). Furthermore, they determined that destruction of rock projectiles occurred when the peak pressure was about ten times the tensile strength of the rocks (Nagaoka et al. 2014). Additionally, Avdellidou et al. (2016) fired forsterite olivine and synthetic basalt sphere projectiles onto low porosity (<10%) pure water-ice targets at speeds

ranging from 0.38 to 3.50 km s^{-1}. They found that approximately a few percent of the initial projectile mass survived as implanted mass on the target body. Moreover, they found an order of magnitude difference for Q_p^* between olivine ($Q_p^* = 7.07 \times 10^5$ J kg^{-1}) and basalt ($Q_p^* = 2.31 \times 10^6$ J kg^{-1}). This may reflect different shock pressures corresponding to the different target types. They also found that the two materials had very similar fragment size frequency distributions (Avdellidou et al. 2016).

In relation to the observations of the exogenic material upon the surface of Vesta (Reddy et al. 2012), Daly & Schultz (2013, 2014, 2015*a*,*b*, 2016) conducted hypervelocity impact experiments, using the NASA AMES Vertical Gun range. In their work, they investigated possible impacts of materials onto Vesta and Ceres. They fired basalt and aluminium projectiles, approximately 6.35 mm in diameter, onto pumice and highly porous ice targets, at speeds between 4.5 to 5 km s^{-1}, and inferred that both Vesta and Ceres should have significant levels of exogenic material delivered to them via impacts. Averaged over the probability distribution of impact angles, approximately 17% of the mass will remain in or near the crater (Daly & Schultz 2016).

Separate studies have looked into the survival of projectiles with an emphasis upon the survival of biomarkers within them (e.g. see Bowden et al. 2008, Parnell et al. 2010, Burchell, Bowden, Cole, Price & Parnell 2014). In addition to these Burchell, McDermott, Price & Yolland (2014), Burchell et al. (2017) showed that even diatom fossils can survive impacts.

Finally, we note that McDermott et al. (2016) fired copper projectiles into ice at speeds up to 7.05 km s^{-1} and found that they could survive with relatively low impact alteration at speeds up to 1.50 km s^{-1}, and with significant retention after fragmentation at speeds up to 6.30 km s^{-1}. This work suggested four classes of disruption for metallic projectiles as a function of impact speed and peak shock pressure; 1) minimal damage, 2) ductile deformation, 3) increasing fragmentation and 4) complete fragmentation. McDermott et al. (2016) aimed to estimate the percentage of survival for the Deep Impact Mission impacting on comet 9P/Tempel 1. This mission consisted of a

363 kg impactor (of which 49% was porous copper) impacting the comet nucleus at 10.3 km s^{-1} (A'Hearn et al. 2005, Veverka et al. 2013). McDermott et al. (2016) predicted a survival of between 8 and 15% of the copper projectile at the impact site.

1.5.2 Computer Simulations

There is a significant problem with interpretations from experimental data determined using Two-stage Light Gas Guns. Generally, the projectiles fired are no larger than a few centimetres due to the extreme mechanical difficulties in accelerating larger objects to such velocities as 5 km s^{-1}. Furthermore, to accelerate a projectile in excess of 10 km s^{-1} is very difficult, with guns tending to be less efficient when above 8 or 9 km s^{-1} as fewer projectiles hit their targets. In comparison, computer modellers are able to simulate scenarios where kilometre sized objects are impacting at a wide range of speeds. However, given that they tend to look at the large scale behaviour, they often neglect the projectile.

One of the most significant issues is that for smaller objects the fragmentation is governed by the material strength. In contrast, for larger objects, the body's own gravitational attraction has a strong effect on how the crater grows or if a disrupted body reassembles under self-gravity. In an effort to define the threshold for catastrophic disruption (Q^*), Benz & Asphaug (1999) used a smooth particle hydrodynamic (SPH) model to simulate collisions between basalt and icy bodies from centimetre to hundreds of kilometres in diameter. Their model differs from its predecessors as it incorporated the combined effects of the material strength (using a brittle fragmentation model) and the self-gravitation. The results show three regimes: material strength dominated (small sizes), self-gravitation dominated (large sizes) and a mixture of the two at intermediate size.

Figure 1.10 is a plot of the mean catastrophic disruption threshold ($\bar{Q}^*$) against target radius in centimetres from Benz & Asphaug (1999). The results from Benz &

Asphaug (1999) correspond to their basalt targets being impacted at 3 km s^{-1}. As seen in Figure 1.10 the value for $\bar{Q}^*$ in the small size strength regime decreases with increasing target size. This is due to larger targets being weaker than smaller ones. Furthermore, in the gravitational regime, the value for $\bar{Q}^*$ increases considerably with target size. This is due to the gravitational forces being larger with increasing mass/size. In Figure 1.10 the only other paper to consider both the gravitational and strength regime in the same model was Durda et al. (1998). Interestingly, both found that the weakest rocky bodies in the Solar System are in the order of 100-200 m in diameter. However, this is the only result the two papers agreed on with overall Q^* values lower in Durda et al. (1998). The origin of these discrepancies could be due to how the two calculate Q^*. Durda et al. (1998) determined Q^* by using an underlying collisional model which could be predicting inaccurate outcomes, whereas Benz & Asphaug (1999) determined Q^* by fitting to observed sizes from past experimental work. On the other hand, it could be due to material parameter differences.

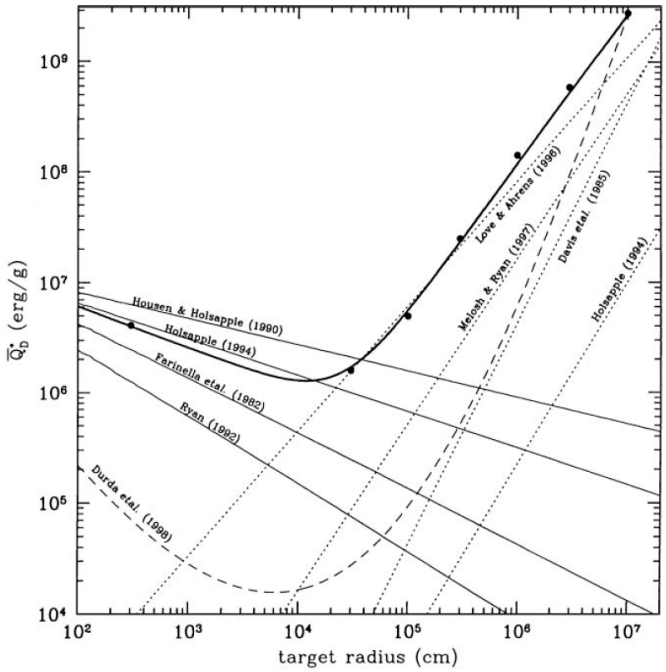

Figure 1.10: Prediction of the mean catastrophic disruption threshold ($\bar{Q}^*$) versus target body radius (r). The plot is from Benz & Asphaug (1999) and shows the prediction from their own (heavy line - corresponding to impact on basalt at 3 km s^{-1}) and other models.

As seen in Figure 1.10 larger bodies are dominated by self-gravitational forces, rather than material strength. This enhanced role of gravity is due to the difficulty of the fragments escaping their mutual gravitational attraction. Due to the low efficiency of momentum transfer in collisions, the velocity of larger fragments tends to be small, and more energetic collisions are needed to disperse them. The efficiency of momentum transfer is found to be larger for larger projectiles (Benz & Asphaug 1999). Therefore, at fixed impact energy, a low-velocity high-mass projectile will lead to a higher fragment velocity than a small-mass high-speed projectile. Thus predicting Q^* may not be dependent on a single parameter like impactor size.

Benz & Asphaug (1999) also consider how non-normal incidence changed Q^*. They found that it increased Q^* (at any r value) because the projectile coupled less well with the target. This raises the issue of what happens to the projectile in non-normal incidence. Pierazzo & Melosh (2000) used a hydrocode simulation to model oblique impacts in order to determine the fate of the projectile. The impact angles investigated were at 90, 60, 45, 30 and 15° from the horizontal. The impactor size (5 km in radius), type (dunite) and impact velocity (20 km s^{-1}) were all kept constant. Pierazzo & Melosh (2000) found that the projectile material was focused downrange for oblique impacts. From angles, less than 30° the majority of the projectile was ejected from the opening of the crater downrange. Furthermore, at very oblique impacts (30 and 15°) a significant amount of the projectile material was ejected at speeds in excess of Earth's escape velocity. The shock inside the projectile was also found to decrease as angles of impact decreased from the horizontal. Finally, Pierazzo & Melosh (2000) showed that shock melting and vaporization occurred in all their projectiles, except for the most oblique at 15°. This work agrees with the experimental work at smaller scales of Gault & Wedekind (1978) and Schultz & Gault (1990*b*).

The distribution of projectile material after impact has also been considered by other modellers. For example, Bland et al. (2008) investigated slower impacts at varying angles on the Moon. Like Pierazzo & Melosh (2000) they looked at impact angles

of 90, 60, 45, 30 and 15° from the horizontal but also varied the speed, using 3, 5 and 7 km s^{-1}. They found that for impact angles between 45 and 90°, over 50% of the projectile material could be found within the crater. Whereas at angles lower than this, the majority of the projectile was expelled from the crater at each speed, matching the findings of Pierazzo & Melosh (2000). Yue et al. (2013) investigated projectile survivability in lunar impacts in order to determine if observed minerals on the central peaks of lunar craters were exogenic. Using numerical models they found that the projectile may survive vertical impacts at velocities less than 12 km s^{-1}, and fragments may well be swept back into the central peak of the final crater as it collapses.

There is physical evidence of survival of microscopic fragments of high speed impactors in craters. For example, the Morokweng crater is located in the Kalahari Desert near the town of Morokweng in South Africa's North West province. The minimum crater diameter is approximately 80 km and drill cores into the crater floor were found to contain projectile material in clasts up to 25 cm in size (Maier et al. 2006). This shows that asteroids can survive impacts on Earth. Potter & Collins (2013) used numerical modelling to determine the survivability of asteroid impacting Earth in order to determine possible scenarios for the Morokweng crater. An impactor was deemed surviving should parts remain solid (i.e. did not melt or vaporise). Potter & Collins' (2013) model demonstrated that survivability decreases with increasing impact velocity, impact angle (with respect to the horizontal), and target density as shown earlier by other numerical simulations and laboratory experiments (Pierazzo & Melosh 2000, Bland et al. 2008, Schultz & Gault 1990*b*, Gault & Wedekind 1978). However, their model went on further to investigate the effects of porosity and shape of the impactor. It was found that increasing impactor porosity decreased survivability. Meanwhile, prolate-shaped (polar axis > equatorial axis) impactors have a higher survivability than spherical and oblate-shaped (polar axis < equatorial axis) impactors. From this, Potter & Collins (2013) went on to determine a relatively simple equation to determine the fraction of shocked material within the impactor. In addition to previous suggestions of a low-velocity and/or high-angles of impact, Potter & Collins (2013) suggests

an elongated and/or low porosity impactor is the cause of the high meteoritic content in the Morokweng crater.

1.6 Fracture Mechanics

To understand what is happening to an impactor during an impact it is necessary to go into fracture mechanics. Fracture mechanics is the study of crack propagation in a material. There are three ways to apply a force to enable a crack to propagate (Figure 1.11).

- Mode I fracture - A tensile stress normal to the plane of the crack creates an *Opening Mode*,
- Mode II fracture - A shear stress acting parallel to the plane of the crack and perpendicular to the crack front creates a *Sliding Mode*, and
- Mode III fracture - A shear stress acting parallel to the plane of the crack and parallel to the crack front creates a *Tearing Mode*.

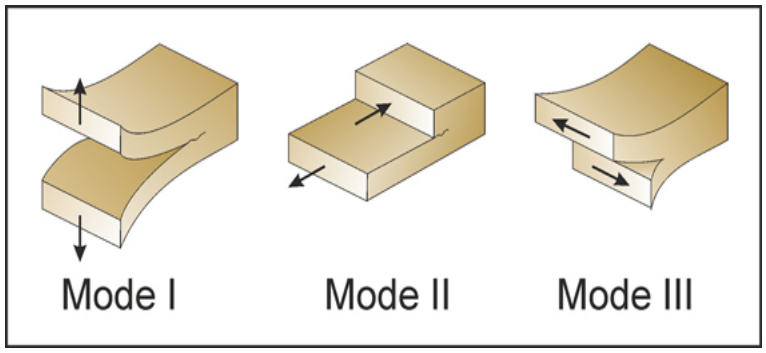

Figure 1.11: The three different crack modes. Diagram taken from Philipp et al. (2013).

1.6.1 Griffith Crack Theory

To counter previous issues with the studies of cracks, Griffith (1921) employed an energy balance approach which revolutionised material science. The strain energy per unit volume of stressed material is given by:

$$U^* = \frac{1}{V}\int F dx = \int \frac{F}{A}\frac{dx}{L} = \int \sigma d\epsilon. \tag{1.32}$$

where A is the cross sectional area, F is the force and L is the length.

If the material is linear it means that the stress, σ, is proportional to the strain, ϵ, where the constant of proportionality is Youngs Modulus, E. Hence, the strain per unit volume can now be written as:

$$U^* = \frac{E\epsilon^2}{2} = \frac{\sigma^2}{2E}. \tag{1.33}$$

As a crack propagates into a material it creates two free surfaces either side. For these surfaces, the strain energy is released. This is easily visualised by having two triangles either side of the crack with a height of βa and a crack depth of a. The material in each triangle is fully unloaded whilst the remaining material continues to feel the full stress (σ) (Anderson 1991). This is represented in Figure 1.12.

The value of β for plane stress loading is $\beta = \pi$ (Anderson 1991). The total strain energy U released is the strain energy per unit volume multiplied by the volume of both triangular regions:

$$U = -\frac{\sigma^2}{2E} \cdot \pi a^2. \tag{1.34}$$

This is the energy that is liberated by the crack propagation. However, bonds between molecules need to be broken in order for the crack to grow. This means that the bond energy is in effect absorbed by the material (Anderson 1991). However, this is not the same for a rock, where breaking occurs along grain boundaries and requires

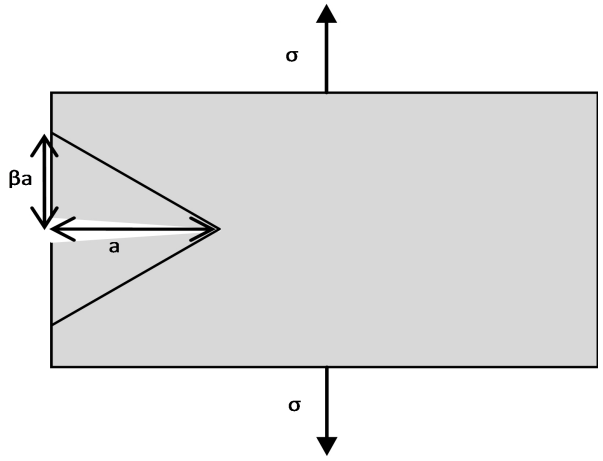

Figure 1.12: Diagram of crack propagation. Showing the length of the crack a and stress (σ) being applied. The material within the two triangles experiences no stress.

less energy. The surface energy S associated with a crack is:

$$S = 2\gamma a, \tag{1.35}$$

where γ is the surface energy (Joules per meters squared) and the factor of 2 is needed as two new surfaces have been formed.

As the crack grows, the quadratic dependence of strain energy on the crack length eventually dominates the surface energy. Beyond a critical crack length a_c the system can lower its energy by letting the crack grow still longer. As long as the stress is increased the crack will continue to grow until $a = a_c$. Beyond this point the crack growth is spontaneous and catastrophic (Anderson 1991).

The critical crack length can be determined by setting the derivative of the total energy $S + U$ to zero:

$$\frac{\partial(S+U)}{\partial a} = 2\gamma - \frac{\sigma_f^2}{E}\pi a = 0, \tag{1.36}$$

where σ_f is the fracture stress. Equation 1.36 can be rearranged to give:

$$\sigma_f = \sqrt{\frac{2E\gamma}{\pi a}}. \tag{1.37}$$

Equation 1.37 describes the crack propagation in a brittle material. However, for ductile materials this equation is altered to:

$$\sigma_f = \sqrt{\frac{E\mathcal{G}_c}{\pi a}}, \tag{1.38}$$

where $\mathcal{G}_c$ is a parameter which refers to the critical strain energy release rate.

Although none of this theory is used in the work in this thesis, it is important to consider how a projectile will fragment upon impact. The projectile upon impact is most likely to be dominated by Mode I fracture during the release of pressure. This release causes the materials to expand away from one another (creating an opening mode) producing cracks.

1.7 Chapter Summary

This chapter has discussed the physics behind a hypervelocity impact, the types of impactors in the Solar System, the average impact speeds and probabilities of these impactors, the effect of an impact on the target (larger body) and the projectile in both experimental and computational studies, the catastrophic disruption of the impactor and fracture mechanics. These topics lead to the specific questions being addressed in this thesis:

- How fragile are multi-mineralic samples/basaltic impactors compared to metallic impactors? Basalt will be studied as it is readily available and easy to use. In addition, what is the fraction of original projectile mass retained at increasing shock pressures?
- Is basalt typical for rocks or is there variation between different types of rocky material. To this end, two projectile types will be studied, basalt and shale.
- Of the potential fragments on the surfaces of other bodies what is the most

probable shape? And can the size of the largest fragment on another body be linked with the impact speed?

- For possible implanted material on other bodies, what is the cumulative fragment size distribution? And how does this compare from the laboratory to real solar system bodies such as Vesta?

Chapter 2

Impact Effects on Materials

We have seen the physics behind impacts, what types or impactors there are and their speeds, what happens to the projectile and target during an impact event. In this chapter, we shall discuss the molecular effects of pressure and temperature. The following sections cover examples of impactor survival in nature, shock states of materials, the ExoMars Rover, Raman spectroscopy of carbonaceous materials and the pressure and temperature effects on Raman spectra.

2.1 Impactor Survival in Nature

The Morokweng impact crater is significant evidence for the survival of stony asteroidal material which impacted the Earth forming a large crater. What was found was a large (25 cm), unaltered, fossil fragment and several smaller fragments within the impact melt of the crater (Maier et al. 2006). Finding large fragments of stony meteorites in craters is a rare scenario. However, projectile fragments have been recovered at 13 terrestrial impact sites (Table 15.1, Goderis et al. (2013)). In Table 2.1 details of 13 impactor fragments recovered from terrestrial craters are shown (taken from Table 15.1 in Goderis et al. 2013). It must be noted that this table excludes impact craters smaller than 0.1 km in diameter. Table 2.1 suggests that iron meteorites are probably

the only type of small meteorite[1] to survive atmospheric passage (larger fragments of iron meteorites have been found, for example the Holsinger meteorite, weighing 639 kg), as there are no small chondrite fragments found in small impact craters. This suggests that for impacts on Earth there is a lower limit on size for chondritic impactor survival. Bodies can also enter and slow down in the Earth's atmosphere for a relatively soft landing. Generally, exposed meteorite fragments are altered and/or destroyed by weathering quickly after a few thousand years. However, such materials can survive for a prolonged time within the impactites and buried in an impact crater. For example, both the Chicxulub and Morokweng meteorite fragments were found within drill cores (Goderis et al. 2013).

Survival also occurs on other bodies. For example, on the Moon projectile fragments from impacts early in its history can be found within the lunar regolith (e.g. Joy et al. 2012, and earlier references therein). Furthermore, the Curiosity rover found an iron meteorite (NASA 2014*a*). Additionally, recent observations by NASA's Dawn mission of the asteroid (4) Vesta showed it was littered with low albedo dark material (DM) objects (Reddy et al. 2012). These DM objects are associated with impact craters, being in the ejecta blanket and/or on the crater walls or rims (Reddy et al. 2012). Reddy et al. (2012) considered whether the DM was a result of volcanic activity or were exogenic in origin. The authors reported that the majority of the spectra of DM object were similar to carbonaceous chondrite meteorites mixed with materials indigenous to Vesta, suggesting that they are exogenic in origin. Also looking at Vesta, Palomba et al. (2014) used spectral data provided by the VIR-Dawn imaging spectrometer, to identify definite DM objects and catalogue them, finding 123 in total.

Finally, the JAXA mission Hayabusa to asteroid (25143) Itokawa revealed a surprising lack of craters but an abundance of boulders on the surface (Fujiwara et al.

[1]Based on the earlier discussion, the projectile diameter is likely to be a $\frac{1}{20}^{th}$ of the crater diameter, hence most of the craters in Table 2.1 arise from impacts by objects $\leqslant 50$ m in diameter. Given that the minimum size for an object to pass intact through the atmosphere to strike the Earth at high speed is in the range of 10 – 50 m depending on composition (iron meteorites being more likely to survive than rocky ones), there may be a selection bias effect here.

Table 2.1: Table of the craters where 13 meteorite fragments were recovered. Only craters larger than 0.1 km in diameter are listed. The data in the table is extracted from Table 15.1 in Goderis et al. (2013).

Crater Name	Location	Age [Ma]	Diameter [km]	Impactor Type	Reference
Morasko	Poland	<0.010	0.1	IIIC - iron	Koblitz (2000)
Kaalijarvi	Estonia	0.004	0.11	IA - iron	Buchwald (1975); Koblitz (2000)
Wabar	Saudi Arabia	0.006	0.12	IIIA - iron	Morgan et al. (1975); Mittlefehldt et al. (1992*a*)
Henbury	Australia	<0.005	0.16	IIIA - iron	Taylor (1967); Koblitz (2000)
Odessa	USA	<0.050	0.17	IA - iron	Buchwald (1975); Koblitz (2000)
Boxhole	Australia	0.03	0.17	IIIA - iron	Buchwald (1975); Koblitz (2000)
Macha	Russia	<0.007	0.3	Iron	Gurov (1998)
Monturaqui	Chile	<1.000	0.46	IA? - iron	Bunch & Cassidy (1972); Buchwald (1975)
Wolfe Creek	Australia	<0.300	0.88	IIIB - iron	Attrep et al. (1991); Koblitz (2000)
Barringer	USA	0.049	1.19	IA - iron	Morgan et al. (1975); Mittlefehldt et al. (1992*b*)
Rio Cuarto	Argentina	<0.100	4.5	Chrondrite (H?)	Schultz et al. (1994)
Morokweng	South Africa	145	70	Ordinary Chondrite; type LL	Maier et al. (2006)
Chicxulub	Mexico	64.98	170	CC (CM2)	Kyte (1998)

2006). One of the most interesting finds was the 'Black Boulder', which is a unique rock with a low brightness (Fujiwara et al. 2006). The location of this is where the gravitational potential is strongest, suggesting that the boulder has not moved (Hirata & Ishiguro 2011). Since space weathering (which can alter brightness) is a global effect, i.e. wouldn't just affect one rock, it would suggest that the boulder arrived in its location by an asteroid collision.

All the individual meteorites that have reached the surface of Earth have one significant difference between them and indigenous rocks - a fusion crust. During the atmospheric passage, these meteorites have experienced temperatures up to 1800 °C

causing significant changes to their external layer (Norton & Chitwood 2008). The creation of the fusion crust occurs only in the last few seconds after molten chunks have ceased to break away and ablation is reduced (Norton & Chitwood 2008). The components of some chondritic stony meteorites are olivines, orthopyroxenes and grains of elemental iron. During melting the olivines and orthopyroxenes create a structureless light brown glass. The grains of iron oxidise and form the iron oxide magnetite, which mixes with the light brown glass to form a dark brown to black fusion crust approximately 1 mm thick (Norton & Chitwood 2008). Differences in the mineralogy of the meteorite result in changes in the colour and composition of the fusion crust. Additionally, there is the presence of contraction cracks. These are shallow fine cracks which are created by the rapid cooling of the fusion crust (Norton & Chitwood 2008).

2.2 Shock States of Materials

To recap, in Section 1.1 the physics of shocks was discussed. A major difference between nature and laboratory impact events is the time scale for the shock loading and unloading and the shock heating and cooling due to the size of impact (small vs. large). To be discussed in this section are the mechanically formed phenomena, phase effects and other effects to minerals that can occur as a result of a hypervelocity impact.

2.2.1 Mechanical Effects

Whilst the shock passes through a material it can deform, twist and compress the material. This leads to a variety of different effects remaining when the shock has dissipated. This section shall discuss the resultant mechanically formed phenomena of shatter cones, planar microscopic features and diaplectic glasses.

Shatter Cones

Shatter cones form in the bedrock beneath meteorite impact craters (see Burchell 2015, for a relevant review). They are evidence that the rock has been subjected to a shock pressure of at least 2 GPa (Baratoux & Reimold 2016). These features are cone shaped with striated surfaces (Figure 2.1). These are known to form in many types of rocks (including igneous and metamorphic) but are best formed in fine-grained sedimentary rocks such as limestone (Burchell 2015, Deuysch et al. 2015).

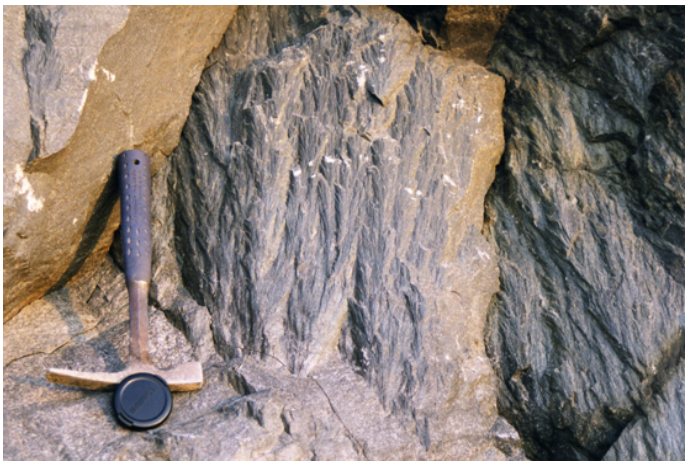

Figure 2.1: Image of shatter cones taken from (Burchell 2015). These shatter cones are in quartzite in the Sudbury impact structure in Canada. The image was taken by L. Ferrière (Natural History Museum Vienna; www.meteorimpactonearth.com).

Shatter cones from several millimetres to half a centimetre have been produced experimentally with impacts at around 7 km s^{-1} and peak shock pressure up to 70 GPa (Kenkmann et al. 2012, Wilk & Kenkmann 2016). Attempts have been made to use the apex of shatter cones to point to the impact point, however, this has had mixed results due to the cones often pointing in a wide variation of directions. The variation in directions is due to the folding of the strata containing the shatter cones. Despite this, studies have shown that shatter cones can be formed by shock waves propagating from impact loci (Kenkmann et al. 2012, Wilk & Kenkmann 2016).

Planar Microscopic Features

There are two types of planar microscopic features: planar fractures (PFs) and planar deformation features (PDFs).

- *Planar Fractures (PFs)* - These are a fracture/breakage that occurs along a single plane in a sample. The occurrence of PFs in minerals can be from a variety of different origins including shock. Hence, they are not used as a diagnostic of a shock history of a sample (French & Koeberl 2010). They appear at low shock pressures of approximately 5 to 8 GPa and parallel to crystallographic planes. In quartz, they are typically approximately 10 μm wide and 20 μm or more apart (Stöffler & Langenhorst 1994).
- *Planar Deformation Features (PDFs)* - These appear as thin parallel planes of deformation, e.g. see Figure 2.2. These only occur in shocked minerals such as quartz or feldspar. As a lot of rocks on Earth contain these minerals, these features are a good tool for determining the shock history of a sample.

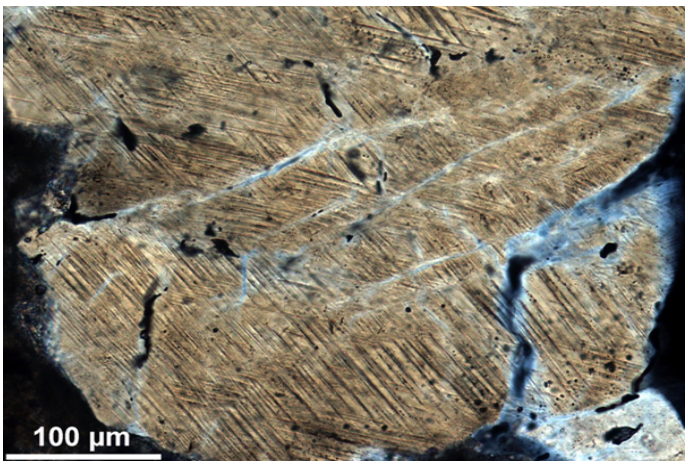

Figure 2.2: Image (in crossed polariszers) of a quartz grain with two sets of planar deformation features. This sample is from the Bosumtwi impact structure in Canada (Sample KR8-006). Image taken from (Burchell 2015) and taken by L. Ferrière (Natural History Museum Vienna; www.meteorimpactonearth.com).

Due to Planar Deformation Features forming after PFs, the PFs can act as grain boundaries to the formation of PDFs. Typically PDFs are 2 – 3 μm wide, and are

regularly spaced (roughly 2 - 10 μm apart) lamellae (Burchell 2015). For quartz, the orientation of the PDFs are typically aligned to one of the main crystallographic axes. However, they can be aligned to different crystallographic axes in contrasting regions of the grain. The minimum formation pressure of these features is approximately 5 - 10 GPa (see review by Burchell 2015). With increasing shock pressure, PDFs are found to be aligned with more of the crystallographic axes of the sample. The frequency of PDFs increases around 25 - 30 GPa.

Diaplectic Glasses

Diaplectic glasses form as a result of a shock, by solid-state transformation, and involves no melting. For quartz, this occurs at approximately 35 GPa but for porous rocks, it forms at lower pressures (Burchell 2015). Although these glasses are amorphous the pre-shock morphology of the mineral is present, but flow features or vesicles are absent (Stöffler & Langenhorst 1994). These glasses are metastable meaning that they don't always survive at impact sites. The most commonly mentioned diaplectic glasses are diaplectic quartz glass and maskelynite, which is diaplectic feldspar glass. In addition, Wozniakiewicz et al. (2012) observed diaplectic olivine glasses after firing olivine into aluminium foils representing an analogue for Stardust capture. The peak shock pressures obtained were up to 79 GPa (Wozniakiewicz et al. 2012), in excess of the minimum known pressure to form diaplectic olvine glasses of 56 GPa (Jeanloz et al. 1977, Schneider & Hornemann 1977).

2.2.2 Additional Effects

Additional effects that can occur to minerals and rocks are the formation of high-pressure polymorphs and melting, which are both discussed in this section.

High-pressure Polymorphs

When a mineral is shocked to a particular pressure it can transform into a different mineral exhibiting the same composition but different atomic structure. An early example of this was that quartz was shown to transform into coesite by static pressure (Coes 1953). This transformed mineral, coesite, was later found in Barringer meteor crater (Chao et al. 1960). Its presence was thought to be as a result of extreme shock pressures. It was determined that the transition of quartz to coesite occurs at shock pressures of approximately 35 GPa in dense non-porous crystalline rocks. As with diaplectic glass, in the presence of pores, the shock pressure required for this is reduced to around 5.5 GPa (example for porous sandstone) (Osinski 2007). The pressure difference is thought to be as a result of pressure concentration effects at the pore/crystal interfaces (Burchell 2015).

Another high-pressure polymorph is diamond from graphite. These form under static pressures of 80 GPa, but have been known to form at around 20 GPa in shock experiments. Diamonds found in impact craters are known as impact diamonds (Gurov et al. 1995) and can be of mm in size.

Other high-pressure polymorph transformations that have been observed from impacts are wadsleyite and ringwoodite from olivine, jadeite from pyroxene, majorite from enstatite and reidite from zircon (Burchell 2015).

Melt

At high shock pressures of around 50 GPa individual minerals begin to melt. If the pressure increases to around 60 GPa, in the case of non-porous crystalline rocks, the whole rock tends to melt. For highly porous rocks, such as sandstone, the melting of individual quartz mineral grains begins at approximately 20 GPa and the whole rock at pressures above 30 - 35 GPa (Kieffler et al. 1976). At around 50 GPa post-shock temperatures begin to exceed 1000 °C. This leads to melting along fractures and other

features (Burchell 2015). Increasing the shock pressure leads to a wider melt region.

Rocks consist of a variety of different minerals each having different melting temperatures. This can result in selective melting in regions throughout the rock (partial melting). The melt can then quench as a glass or recrystallize in rock form. When this occurs the outcome is a rock with a variety of textures across the sample. When the whole sample melts, it can be homogeneous at large scales, due to mixing effects, but be extremely heterogeneous at small scales. This generally occurs at shock pressures of 60 - 80 GPa, where post shock temperatures are in excess of 2000 °C (Burchell 2015).

2.3 ExoMars

Knowing that fragments of impactors have been found on Earth, the Moon and various asteroids there is also a possibility for them to be on the surface of Mars. Indeed there have been cases where meteorites have been found on the Martian surface by NASA's Opportunity and Curiosity Rovers (both in Meridiani Planum) (Arvidson et al. 2011, Fairen et al. 2011, NASA 2014*a*). Looking ahead, the joint ESA and Roscomos mission ExoMars consists of an orbiter (launched in 2016) and a rover (to be launched 2020). The primary candidate for the rovers landing site is Oxia Planum with other sites being Aram Dorsum, Hypanis Vallis and Mawrth Vallis (ESA 2016*b*). Should Oxia Planum be chosen, it is geographically described as a plain with an elevation of more than 3,000 metres below the Martian mean elevation. This plain is rich in clay-bearing rocks and is thought to have once had water in the area (ESA 2016*b*). The ExoMars rover will analyse the rocks on the surface and subsurface at any of these locations with its suite of onboard equipment. Some of the rocks analysed may well be of exogenic origin (projectile fragments).

On board the ExoMars rover will be a panoramic camera (PanCam), an infrared spectrometer (ISEM), a close-up imager (CLUPI), ground penetrating radar (WISDOM), a multi-spectral imager for the subsurface (Ma_MISS), a visible plus infrared

imaging spectrometer (MicrOmega), an organic molecule analyser (MOMA), a drill to reach subsurface samples down to a depth of 2 m and a Raman Laser spectrometer (RLS) (ESA 2016*a*). The RLS is of particular interest to the work covered in this thesis and will, therefore, be discussed further here.

The RLS onboard the ExoMars Rover will use a 532 nm laser excitation and have a spot size of 50 μm with an autofocus in the range of $\pm$ 1 mm (Rull et al. 2013). The laser produces an irradiance between 0.8 and 1.2 kW cm^{-2} on the target. This upper threshold is used in order to remain below the level of thermal damage a powdered grain could sustain (Rull et al. 2013).

The theory of Raman spectroscopy and its application to characterisation for various materials is discussed in the next three sections of this chapter. We particularly look into the theory of Raman Spectroscopy, the spectra for carbonaceous materials and the effects on these spectra when heated and put under pressure.

2.4 Raman Spectroscopy

In 1923 the theoretical physicist Adolf Smekal was the first to postulate an inelastic scattering of light (Smekal 1923). Five years later, Chandrasekhara Venkata Raman and Kariamanickam Srinivasa Krishnan observed experimentally the inelastic scattering of light, which is now known as Raman scattering (Raman & Krishnan 1928). In the original experiment, sunlight was focused using a telescope onto a sample of either purified liquid or a dust-free vapour. A second lens was placed by the sample to collect the scattered light. Finally, optical filters were used to show the existence of scattered radiation with an altered frequency from the incident light (Raman & Krishnan 1928). It is this shift in frequency (now known as the Raman shift) which underpins what is commonly known as Raman Spectroscopy.

2.4.1 Absorption and Scattering of Light

When light interacts with a target material there are one of two outcomes; absorption or scattering. The absorption of light occurs only when the energy of the incoming photon is precisely equal to the energy gap between two electron energy levels. If this is the case the energy is transferred to the electron which is excited up to the relevant energy level and then cascades down in a variety of steps to re-release photons of specific frequencies corresponding to the energy level steps. The scattering of light is a very different process where it does not matter what the energy of the incident photon is (Smith & Dent 2005).

Considering light as a propagating oscillating dipole, when it interacts with the sample it transfers energy to the electrons in the electron cloud which results in it being distorted. This interaction causes the electrons to polarise and go to higher energy states. In effect, a short lived 'complex' between the light and electron is created (Smith & Dent 2005). Although this causes a different electron geometry, the time scale is too short to cause the nuclei to move appreciably. Due to instabilities the 'complex' immediately releases the light as scattered radiation (Smith & Dent 2005). It is important to note that the electron states do not describe the electron arrangement during this process as the electrons are scattered to 'virtual states'. The energy of these virtual states is totally dependent on the frequency of light source being used. This also means that the extent of the electron cloud distortion is also limited by the illumination (Smith & Dent 2005). Modern Raman Spectrometers use monochromatic laser light in order to observe the effect.

There are two forms of scattering: Rayleigh and Raman. Rayleigh scattering is where the energy transferred from the light to the electron cloud is almost immediately scattered resulting in no nuclear movement (Smith & Dent 2005). Therefore, this is an elastic scattering process and is the most intense of the two effects. Raman scattering is a rare event (one in 10^6 - 10^8 photons), where the light and electron interaction

cause nuclear movement at the same time (Smith & Dent 2005). Due to the fact that the nuclei are far heavier than the electrons, the movement results in an appreciable change in energy of the molecule, making this an inelastic scattering process. Whether the change is to a higher or lower energy depends on the initial conditions of the molecule. Should the molecule be at rest in the ground state then the interaction is most likely to result in a Stokes shift (i.e. upwards), whereas if the molecule is already at a higher vibrational state this will result in an anti-Stokes shift (downwards) (Smith & Dent 2005). At room temperature the molecule is typically in the ground state, meaning it is more likely to result in a Stokes shift (Smith & Dent 2005). This means that the Stokes shift is the more intense of the two. In Figure 2.3 we show a simple diagram illustrating the two scattering events. The states m and n are two different vibrational states of the ground electron state dictated by the energy of the laser.

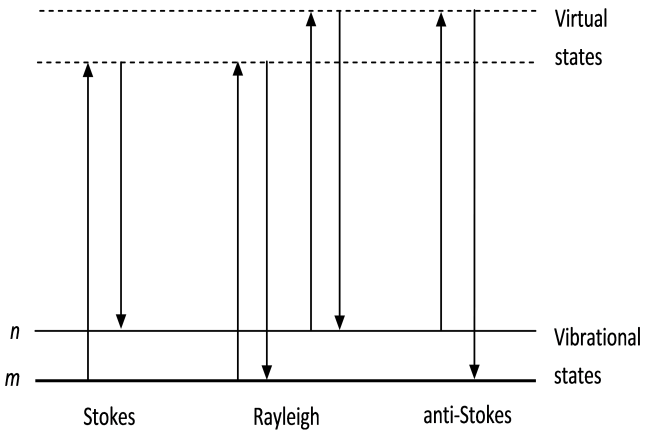

Figure 2.3: Diagram of the Rayleigh and Raman scattering processes. Re-drawn from Smith & Dent (2005).

The ease with which the electron cloud around the molecule can be distorted is equivalent to the molecular polarisability, α (Smith & Dent 2005). The interaction between the light and molecule induces a molecular electric dipole ($\overrightarrow{p}$), which is given by:

$$\overrightarrow{p} = \alpha \overrightarrow{E}, \tag{2.1}$$

where:

$$E_i = E_0 cos(2\pi f_i t), \tag{2.2}$$

with E being the electric field of the incident light oscillating with a frequency of f (Siebert & Hildebrant 2008). In Raman scattering the resulting polarisation results in nuclear displacement, given by (Siebert & Hildebrant 2008):

$$q = q_0 cos(2\pi v_R t), \tag{2.3}$$

where q refers the total displacement, q_0 the initial displacement, v_m the molecular vibration and t the time.

For small distortions, polarisability is linearly proportional to the displacement, given by (Siebert & Hildebrant 2008):

$$\alpha = \alpha_0 + (\frac{\partial \alpha}{\partial q})_0 q_0 + \ldots. \tag{2.4}$$

The resultant dipole is (Siebert & Hildebrant 2008):

$$\overrightarrow{p} = \alpha \overrightarrow{E} = \alpha_0 E_0 cos(2\pi v_i t) + \frac{1}{2} E_0 q_0 (\frac{\partial \alpha}{\partial q})_0 [cos(2\pi(v_i + v_R)t) + cos(2\pi(v_i - v_R)t)], \tag{2.5}$$

where the first term in Equation 2.5 refers to the Rayleigh scattered light, the second to anti-Stokes scattering and final term to the Stokes scattered light (Siebert & Hildebrant 2008). Therefore, and very importantly, Raman scattering only occurs when a molecule is polarisable (Siebert & Hildebrant 2008, Smith & Dent 2005).

2.4.2 Molecular Vibrations

Providing that no absorption of photon energy is occurring, the energy of a molecule can be split into multiple parts known as the degrees of freedom. These are split into three types; translation, rotation and vibration. There are three translational and three

(two if the molecule is linear) rotational degrees of freedom (Smith & Dent 2005). The number of vibrational degrees of freedom is thus given by:

$$DoF_{vib} = 3N - 6, \tag{2.6}$$

$$DoF_{lin,vib} = 3N - 5, \tag{2.7}$$

with N being the number of atoms in the molecule and where Equation 2.7 is for a linear molecule. This means that for a diatomic molecule there will only be one vibration (Smith & Dent 2005). For a molecule such as oxygen or nitrogen, this is a simple stretch in the O - O or N - N bond respectively.

For a triatomic molecule, there are three modes of vibration. These are a symmetrical stretch, bending or deforming, and an asymmetrical stretch. Figure 2.4 is taken from Smith & Dent (2005) and demonstrates the three vibrational modes of water (H_2O) and carbon dioxide (CO_2). This type of diagram is referred to as a 'spring and ball' model, where the spring is the bond and the ball is the nucleus. The relation for the vibrational frequency is determined by Hooke's law. This indicates that an atom with heavy nuclei and weak bonds would have a low frequency and one with strong bonds and light nuclei have high frequencies (Smith & Dent 2005). It must be noted that not all vibrational modes are 'Raman active' (produce a Raman spectra), because as stated it relies on there being a change in polarizability.

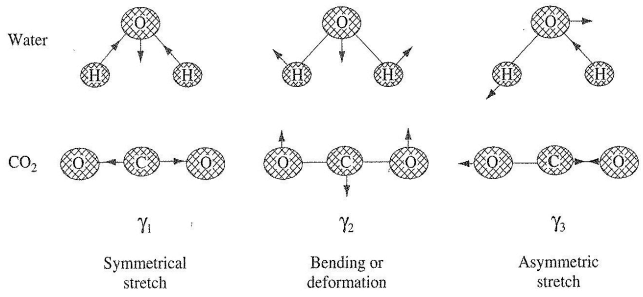

Figure 2.4: Spring and ball model showing the three modes of vibration for water (H_2O) and carbon dioxide (CO_2). Figure from Smith & Dent (2005).

The 'spring and ball' method of interpreting vibrational spectra is widely used, how-

ever, it is not the most accurate. More accurate models are ones which take into account the electron density differences in the clouds around the nuclei. For considerably more complicated molecules the analysis of what is vibrating is determined theoretically using density functional theory (DFT) (Smith & Dent 2005). Furthermore, in order to assign vibrations to certain spectral peaks, it is important to realise that two or more bonds can interact and vibrations of the linked group of atoms can lead to being observed in the spectra (Smith & Dent 2005). For example, the CH_2 group has both a symmetrical and asymmetrical stretch, rather than two separate CH stretches.

2.5 Raman Spectroscopy of Carbon Bearing Materials

Carbon is the fourth most abundant element in the universe, and for life on Earth, it is one of the most important. From animals' and plants' respiration cycle to carbohydrates, lipids, proteins and nucleic acids (DNA, RNA), to carbon of long dead organic material in rocks (petroleum, coal etc.) the need to understand carbon is very important when investigating life in the Solar System. Carbon can be simply detected by Raman spectrometry, and rovers, like ExoMars, will be using Raman spectrometry to look for such biomarkers.

Figure 2.5 is a Raman spectrum of graphite taken as part of this thesis work. The two main bands evident are the carbon bands known as the D1/D band or disordered band ($\sim$1350 cm^{-1}) and the G band or graphite (or ordered) band ($\sim$1580 cm^{-1}). The locations of these bands vary from sample to sample. Additionally, there is the D2 band ($\sim$1620 cm^{-1}), D3 band ($\sim$1510 cm^{-1}), S1 band ($\sim$2700 cm^{-1}) and S2 band ($\sim$2950 cm^{-1}). However, the most prominent are D1 and G and these are widely referred to as the D and G bands of carbon.

The carbon motions which produce these bands are shown in Figure 2.6. The G mode has E_{2g} symmetry. E_{2g} refers to the point groups of the atoms, where E means that the molecule returns to the same position it started from. Figure 2.6a shows the

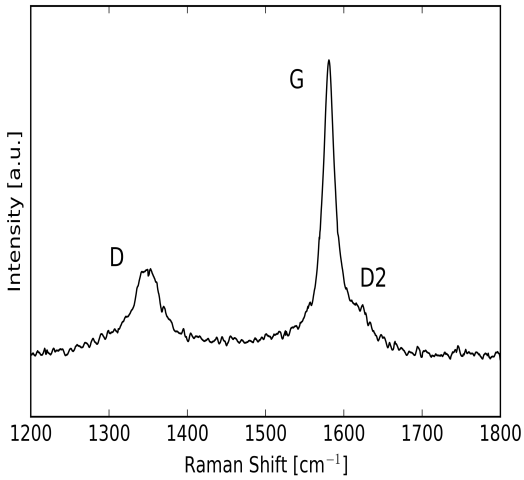

Figure 2.5: Spectrum of the D1 (at ∼1346 cm^{-1}), G (at ∼1575 cm^{-1}) and D2 (at ∼1615 cm^{-1}) bands of the standard commercial graphite used in this thesis (further information on this material shall be discussed later). This spectrum has been unprocessed and is the authors own work.

in-plane bond-stretching motion of pairs of C sp^2 atoms. This mode doesn't require the presence of a sixfold ring system and can occur in chains as well (Ferrari & Robertson 2000).

The D peak is produced as a result of a breathing mode of A_{1g} symmetry (Figure 2.6b). This mode is forbidden in perfect graphite and is only active in the presence of disorder (Ferrari & Robertson 2000). The presence of a D2 band is due to randomly distributed impurities or surface charges on the graphite which split the G band.

Extensive work has gone into understanding the carbon bands produced by graphite. A review by Reich & Thomsen (2004) looked through the past 30 years of literature researching the carbon bands. For highly ordered graphite there is no D band. However, Tuinstra & Koenig (1970) reported observations of the carbon D band by using a 488 nm Argon-ion laser on pyrolytic graphite, commercial graphite and carbon black. They found that the D band increased in intensity with an increase in the amount of unorganised carbon in the sample and with a decrease in graphite crystal size (Tuinstra & Koenig 1970, Reich & Thomsen 2004). It was later shown that the D band was

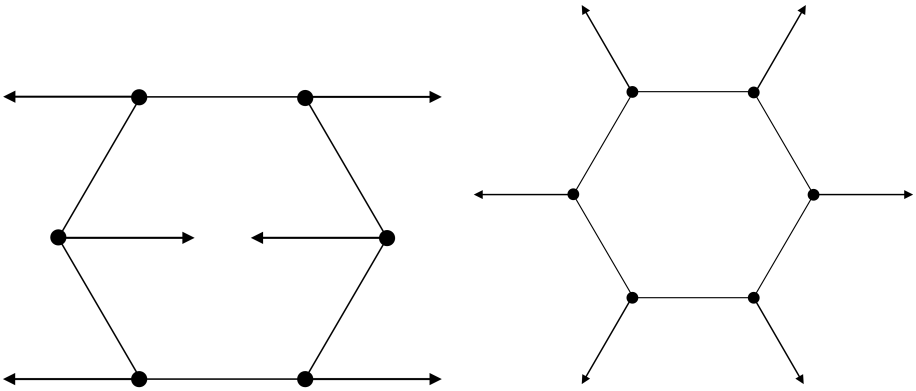

(a) E_{2g} G mode (b) A_{1g} D breathing mode

Figure 2.6: The motion of carbon atoms in the (a) G and (b) D modes. These diagrams are reproduced from Ferrari & Robertson (2000)

not affected by the type of disorder (Wang et al. 1990, Reich & Thomsen 2004). By far the most perplexing work to be published was that of Vidano et al. (1981) who employed different lasers and found that the location of the D band shifts to higher wavenumbers with increasing laser wavelength (Reich & Thomsen 2004, and references therein). Finally, it was found that the anti-Stokes positions of the carbon bands differed to the Stokes positions, contradicting the fundamental understanding of Raman spectroscopy (Tan et al. 1998, Reich & Thomsen 2004). The answer to the origin of the D band is suggested by Reich & Thomsen (2004), and echoed in a later review by Ferrari (2007), as double-resonant Raman scattering. This explains the D band by the double-resonant Raman process, which for a given laser wavelength and phonon (quantum mechanical description of an elementary vibrational motion) branch, selectively enhances a particular phonon wave vector and phonon frequency (Reich & Thomsen 2004). The activation process for the D peak starts with a laser induced excitation of an electron/hole pair, followed by an electron-phonon scattering with an exchanged momentum. Next occurs defect scattering and, finally, electron/hole recombination. The double resonance condition occurs when the energy is conserved in all of these transitions (Ferrari 2007).

A review by Ferrari & Basko (2013) looked into the use of Raman spectroscopy as a tool to study the properties of graphene. Graphene is a two-dimensional sheet of carbon

rings. Ferrari & Basko (2013) mentions the difference between the Raman spectrum of graphite and single layered graphene (SLG) as consisting of two fundamentally different sets of peaks. They both have the D and G bands present, however, the SLG has the absence of a peak at approximately 42 cm^{-1}, known as the C peak. The C peak is sensitive to the interlayer coupling, therefore the absence of this could suggest the presence of SLG (Ferrari & Basko 2013).

In rocks on Earth, the origin of the carbon results from either the break down of organic components during metamorphism, leaving the resultant carbon to be incorporated in the newly forming minerals (Konhauser 1998), or by an abiotic precipitation of graphite from carbon rich fluid (Luque et al. 1998). There is significant difficulty in determining whether the source of the carbon in rocks is biotic or abiotic. Bower et al. (2013) attempted to improve the understanding of Raman spectroscopy as a method for life detection, by comparing the carbon D and G bands present in meteorites and those for microfossils in rocks. The author found that G band peak positions greater than 1600 cm^{-1} were associated with metamorphic temperatures up to 200 °C (Bower et al. 2013). Additionally, the younger microfossils and Murchison meteorite displayed an increased D band width relative to the G band width, whereas the older microfossils and high-temperature processed meteorites do not. This is thought to be as a result of thermal maturity (Bower et al. 2013). Bower et al. (2013) conceded that they were unable to unambiguously identify biogenic carbon from abiogenic carbon, but their work appears promising. Furthermore, there is added difficulty in identifying biogenic carbon from oxidising environments as this could lead to misinterpretations due to a band in the spectrum of haematite overlaying the carbon D band (Brolly et al. 2016).

2.6 Pressure and Temperature Effects on Raman Spectra

As indicated in the previous section, the Raman spectra for a material are not fixed, environmental influences can change them. When an external factor (such as pressure

or temperature) is applied to a material it can affect the structure and bonds of the crystals and this, in turn, leads to a change in the Raman spectra. Conversely, conditions that a material has been exposed to can be inferred by comparing the change in the Raman spectrum from an original unaltered spectrum. Three major influences on Raman spectra are shock pressure, static pressure and temperature. The static pressures needed to alter spectra are often in the GPa range. Shock pressures in the same range are rarely observed during processes occurring on Earth, but are generated during hypervelocity impacts. Therefore shock pressure effects on minerals and biomarkers' Raman spectra are often studied as part of hypervelocity impact events, either in the laboratory or in samples taken from impact sites. The effects of static pressure and temperature are usually investigated in order to develop and understand processes such as graphitisation during metamorphism.

2.6.1 Shock Pressure Effects

Foster et al. (2014) investigated the effects of peak shock pressure on olivine captured at high speed in aerogel[2] and on aluminium foils. This work was performed to aid interpretation of the returned samples of NASA's Stardust mission in 2006 (Brownlee et al. 2006). The Stardust spacecraft collected samples from the comet 81P/Wild 2 in blocks of aerogel and aluminium foils whilst flying past the comet at a relative speed of 6.1 km s^{-1}. Aerogel captures materials in a low pressure impact spread along the length of a track formed as the projectile decelerates in the aerogel. This process can involve low shock pressures ($\leqslant$300 MPa according to Trigo-Rodriguez et al. 2008) but can also heat the samples to over 1000 °C for brief periods of a microsecond (Naguchi et al. 2007, Leroux 2012). Prior to sample return it was unclear if particles captured after such a process would give Raman spectra, but this was demonstrated by Burchell et al. (2001). Impacts onto metals such as aluminium involve much greater shock

[2]Aerogel is a low density, highly porous medium. In NASA's Stardust Mission it was a SiO_2 aerogel, transparent in nature and has a density gradient of 5 mg cc^{-1} at the front face and rising to 50 mg cc^{-1} at the rear.

pressures (60 – 90 GPa, Burchell & Kearsley 2009) with extensive fragmentation and melting of the projectile. Again it was unclear if the projectile residue in a crater would provide Raman spectra. However, Burchell et al. (2008) showed that this was the case. Hence, Foster et al. (2014) fired a suite of different olivine samples at aluminium plates and aerogel at approximately 6.1 km s^{-1}. After capture, both the aerogel blocks and aluminium craters were analysed using Raman spectroscopy. One of the most significant results of Foster et al. (2014) was the permanent shift of the olivine doublet peaks in comparison to the original un-shocked sample. It was concluded that this was as a result of the strain on the olivine crystal lattice caused by the impact. Conversely, work by Farrell-Turner et al. (2005) found no systematic shifts in Raman spectra of the olivine doublet with shock pressures reaching 59 GPa, compared to the 85–90 GPa in Foster et al. (2014).

Xie et al. (2001) also conducted shock experiments on olivine-rich samples. They found that at peak shock pressure of 83 GPa there was a broadening of the olivine doublet and sometimes a shift. In order to clarify the situation, Harriss & Burchell (2016) fired powdered San Carlos olivine (grain size 1 - 10 μm) into aluminium foils at a speed range of 0.6 to 6.1 km s^{-1} (corresponding peak shock pressure of 5 to 86 GPa). They found a permanent shift in peak position in the Raman spectra of the olivine at impacts speeds in excess of 5 km s^{-1}, equivalent to peak shock pressures of 65 GPa. This is compatible with the previous results (Xie et al. 2001, Farrell-Turner et al. 2005, Foster et al. 2014), suggesting a minimum threshold for lasting effects on the spectra of approximately 65 GPa. The observed shift of the olivine doublet peak positions was twice the magnitude of previous work (Harriss & Burchell 2016).

As well as changes to Raman spectra suggesting changes in the structure of a given material, phase changes can also occur via shocks. Bucio et al. (2015) conducted a series of shock experiments on gypsum using a one stage light gas gun, to determine the effects of shock compression on the mineral. Their maximum attained velocity was 829 m s^{-1}, which corresponded to a shock pressure of 14 GPa. Using micro-Raman

analysis, amongst other techniques, they determined a transformation of gypsum to bassanite with a possibility of bassanite being transformed to anhydrite (Bucio et al. 2015).

2.6.2 Static Pressure and Temperature Effects

To separate out shock effects from other influences, it is important to consider the effects of other environmental conditions on Raman spectra. The effects of static pressure on carbon spectra are generally conducted with a diamond anvil cell. Static loading experiments on carbon bearing rocks are typically concerned with investigating the graphitisation of rocks. Zerda et al. (2000) investigated the structural changes observed in carbon black particles and, as a comparison, highly oriented pyrolytic graphite (HOPG), with increasing static pressure. Carbon black is a material produced as a result of the imperfect combustion of heavy petroleum products and is used as a filler to modify mechanical, electrical and optical properties of the medium it is being used with (Zerda et al. 2000). In their work, a ruby was used as a reference material to determine the amount of pressure being applied. Zerda et al. (2000) found that with increasing static pressure from 0 to 5 GPa, there was a shift in the G band from approximately 1570 to 1595 cm^{-1} for the HOPG. Furthermore, this investigation on a single crystal of HOPG suggested that when it is broken into multiple crystallites the D band appears. Additionally, the authors found a higher peak shift at lower pressures for fragmented HOPG than for the single crystal HOPG. Zerda et al. (2000) speculated that for pressure less than 1 GPa the shift is caused by a reduction of crystal size whereas for greater pressures the shift was caused by changes in the intermolecular potentials. For the carbon black there was a shift of approximately 25 cm^{-1} in the Raman spectra as pressure was applied up to 3.5 GPa, however, this varied depending on which carbon black sample was used. Zerda et al. (2000) speculated that for carbon black the shift is due to the pressure modifying the intermolecular potential and there was no effect from the size of the crystallites. It was reported that the effects of the

pressure were fully reversible after it was released. Further work on single wall carbon tubes (SWCT) has suggested the same effect on the G band and has also suggested a broadening in the same pressure range (Lu et al. 2012).

Kerogen, a carbonaceous material, is commonly used to determine the thermal history of the metamorphic rock it was extracted from. During metamorphism, the carbonaceous material is broken down and loses its volatiles. Of the three relevant factors (pressure, temperature and time scale), temperature is deemed to be the most important for graphitisation (Beyssac, Goffe, Chopin & Rouzaud 2002, Beyssac, Rouzaud, Goffe, Brunet & Chopin 2002). Huang et al. (2010) investigated the structural changes of kerogen extracted from mudstone under varying pressures and temperatures. Instead of a diamond anvil cell, Huang et al. (2010) used a sapphire anvil cell which allows for the observation of the D band during compression where the widely used diamond anvil cell does not due to it being masked by the stronger diamond peak (Zerda et al. 2000). Huang et al. (2010) found that both the D and G bands shifted to higher wavenumbers with increasing pressure whereas, for increasing temperatures both are shifted to lower, suggesting that these effects can counter each other to some degree. Furthermore, the intensities of each band decreased with increasing pressure, and there was an irreversible effect on the peak positions of the carbon bands at temperatures above 600 °C. Additionally, Huang et al. (2010) also reported that of the two bands the G band appeared more sensitive to pressure and that graphitisation could not be caused solely by added pressure.

Huang et al. (2010) estimated the relative effect of temperature and pressure on the shift of each band by determining a coefficient (dT/dP). This value was found to be 3.9 $\times 10^{-3}$ and 6.8 $\times 10^{-3}$ °C GPa^{-1} for D and G bands respectively. The interpretation of this suggests that for the maximum pressure at which a metamorphic rock is formed (1 GPa), the relative shift of the D and G band caused is countered by temperatures of 256 and 147 °C for the D and G band respectively (Huang et al. 2010). Finally, Huang et al. (2010) suggest that instead of the carbon bands being used to determine thermal

history, it could be used as a geothermobarometer.

2.7 Summary of Chapter

This chapter started by discussing examples of impactors being retained in impact craters on Earth and the effect of hypervelocity impacts on materials. It has gone on to discuss the detectable crystal effects of shock pressure, temperature and static pressure by Raman spectroscopy with a specific interest in carbon. This is of particular interest to missions such as ESA's ExoMars Rover and NASA's Mars 2020 Rover which are both fitted with Raman spectrometers. These topics lead that will more questions to be explored in the rest of this thesis:

- Shock pressure has been shown to cause an effect to the crystalline structure of some minerals. What is the effect on the carbon D and G bands in Raman spectroscopy?
- How does shock pressure compare with static pressure and temperature as factors affecting crystalline structure?

Chapter 3

Method I - Impact Simulation

This chapter discusses the impact simulation equipment and software that has been used during the duration of the research. It starts by going into the operation and components of the University of Kent's Two-stage Light Gas Gun and continues on to discuss the software ANSYS Autodyn.

3.1 University of Kent's Two-Stage Light Gas Gun

Gas and powder guns in general were developed in order to investigate millimetre- and centimetre-size projectile impacts. Two-stage light gas guns (LGGs) were introduced to reach velocity regimes exceeding that of gas and powder guns (Crozier & Hume 1957). Two-stage LGGs can reach peak velocities in the 7 - 8 km s^{-1} range, considerably higher than the maximum for powder guns of approximately 2.3 km s^{-1} (Asay & Shahinpoor 1993). Furthermore, for high impedance materials, the peak shock pressures generated can be approaching 1 TPa (Asay & Shahinpoor 1993).

The basic principle of operation for a two-Stage Light Gas Gun is that, a light gas is compressed in the first stage in a chamber (known as the pump tube) between a piston and a diaphragm/burst disc. Behind a piston is a cartridge which when struck with

sufficient force ignites the primer, driving the piston forward compressing the light gas. This in turn ruptures the burst disc which propels the sabot, positioned just behind the burst disc, and which contains the projectile/s.

The University of Kent's Two-stage Light Gas Gun (Burchell et al. 1999) has been in operation since the late 1990s and has had significant modifications and improvements since then. Figure 3.1 is an image of the set up of the gun for the majority of the work in this thesis. For this section of the chapter the operation and components of the gun shall be discussed along with the gun's further capabilities.

Figure 3.1: Image of the University of Kent's Two-Stage Light Gas Gun as used for majority of the work in this thesis.

3.1.1 Operation and Components of the Two-Stage Light Gas Gun

Figure 3.2 is a schematic of the University of Kent's Two-stage Light Gas Gun. The set up consists of a firing pin, powder chamber, cartridge, pump tube, piston, central break, collar, burst disc, sabot, launch tube, blast tank, laser curtain and target chamber. Each component shall be discussed further in the following two sections. The discussion is split depending on whether the components are in the first stage or second stage.

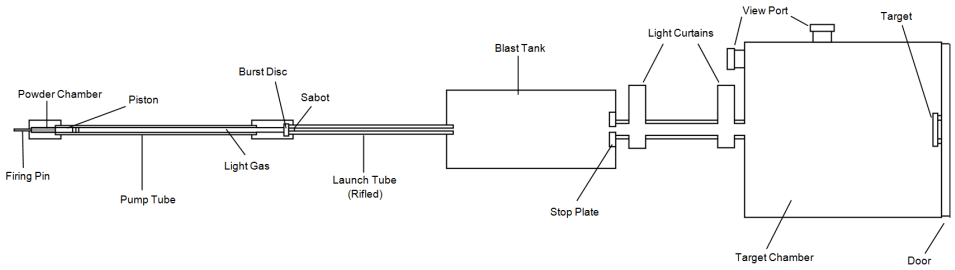

Figure 3.2: Schematic of the University of Kent's Two-Stage Light Gas Gun.

First Stage

Two-stage LGGs require a mechanism with sufficient force to ignite the primer in the base of a cartridge. For this a brass pendulum is used, which can be triggered by the gun operator outside the laboratory (ensuring no one is in the room when the gun is operating for safety purposes). The brass pendulum is suspended at 50° from the vertical and upon triggering swings down to the vertical hitting the horizontal striking rod into the firing pin and subsequently into the cartridge primer which ignites the powder (Burchell et al. 1999).

The cartridge is held in the powder chamber. The cartridges are produced on-site and consist of a shotgun cartridge, primer and rifle powder. Firstly, the blank cartridges are fired so their original primers can be removed and replaced with a Magnum 209 primer. The cartridge is then filled with between 10.00 and 10.05 grams of rifle powder, and stuffed with wadding before being sealed by crimping the cartridge.

The type of powder used in the cartridge depends on the required shot speed. In the laboratory three types of rifle powder are used; Reloader 7, 19 and 22. The higher speeds are attained by powder which burns quickly, as this relates to the pressure profile and ultimately the speed of which the piston is propelled.

The light gas is held and compressed in the pump tube. The gas is fed into the tube through a connection hole in the tube. This same connection is used to evacuate the pump tube if necessary. The pump tube is sealed by the presence of the burst disc at

one end and the piston at the other. Once the tube is initially evacuated the light gas is fed in. The gas used and the pressure of the gas is determined by what shot speed is required. Table 3.1 shows the different gases and their pressure ranges used in the impact lab, and their resulting speeds.

Table 3.1: Table of different light gases used in the University of Kent's Two-Stage Light Gas Gun and the speeds attainable.

Gas	Pressure [bar]	Velocity [km s^{-1}]
Hydrogen	35 – 66	>4
Helium	38 – 111	2.8 – 4.5
Nitrogen	43 – 82	<3
Krypton and Nitrogen	55 – 90	≈ 1

Table 3.1 shows that a lighter gas can obtain a higher speed. This is due to the gas's low molecular weight. Equation 3.1 shows that the maximum possible speed of a projectile ($U_{p,max}$) is related to the speed of sound in an ideal driver gas (Moritoh et al. 2003, Doolan 2001).

$$U_{p,max} = \frac{2C}{\gamma - 1}, \tag{3.1}$$

and

$$C = \sqrt{\frac{\gamma RT}{m}}, \tag{3.2}$$

where, C is the speed of sound (m s^{-1}), γ is the specific heat ratio, R is the gas constant, T is the gas temperature and m is the molecular weight of the driver gas (g). Therefore, lighter gases such as Hydrogen and Helium are widely used to attain high speed shots.

There are two types of pistons used in the Light Gas Gun, one 6.0 cm long and the other 8.2 cm long and both are 1.3 cm in diameter. Towards the front end of the piston both have two circular grooves in which there is a rubber 'O' ring in each. These help ensure that there is a gas-tight seal in the pump tube.

The central breach is placed in between the pump tube and launch tube. The bore inside is funnelled shaped allowing for an increased pressure at the end in contact with

the launch tube and to connect between two bore sizes. A further purpose is to stop the piston hitting the launch tube. At shot speeds greater than 5 km s^{-1}, an additional piece of circular soft aluminium (known as Central Breach Gasket) is used to lower strain on the central breach. As the central breach takes the majority of the stress from the built up pressure and impact of the piston, it has a metal collar surrounding it. This ensures that there are no safety issues should the central breach fail.

The burst disc is an aluminium disc diaphragm with a diameter of 12.7 mm, secured with double sided tape to the end of the launch tube. The burst disc is used to ensure the correct pressure is reached in order to propel the projectile at the desired speed. Hence, the burst disc has been calibrated to burst at certain pressures. For shot speeds between 1 and 5 km s^{-1} the disc is scored using a press in the tensometer, held at 7 kN. This scoring creates fault lines allowing the disc to burst along them. For shot speeds great than 5 km s^{-1}, no scoring is added to the disc.

Behind the burst disc, the sabot is placed containing the projectile. The sabot is approximately the same width as the bore of the launch tube meaning minimal pressure is lost from propelling the sabot. There are two types of sabot used in the University of Kent's Two-stage Light Gas Gun. One sabot consists of 4 pieces of isoplast and the other is a solid sabot of nylon. For the 4-split sabot each piece is serrated allowing the pieces to lock together, meaning that whilst being accelerated down the launch tube they do not move independently. The solid sabot can be made to have a cavity in order to hold a projectile.

Currently the light gas gun can fire single projectiles and multiple smaller projectiles (buckshot). Objects between 0.8 and 3 mm in diameter can be shot as a single shot (Burchell et al. 1999). As a buckshot, objects down to 5 μm can be fired, however, this will result in multiple small impacts on the target.

Second Stage

The second stage of the light gas gun comprises of a launch tube, blast tank, laser curtain and target chamber. The launch tube is where the projectile is accelerated. It consists of a rifled barrel (rifling is constant at 1 turn in 0.76 m) approximately 0.76 m long. Due to the spin generated from the rifling the split sabot acquires a rotational component to its motion when it leaves the launch tube. The Kent gun has a variety of different launch tubes depending on the requirements of the shots (Table 3.2).

Table 3.2: Table of the different launch tubes used for each projectile being fired.

Projectile Type	Velocity [km s^{-1}]	Launch tube/type of rifling
Frozen	1-7	$0.22''$ smooth or $0.170''$ 4 bit external
Large or awkwardly shaped	1-7	$0.22''$ 6 bit shallow
Single/buckshot	7 and above	$0.170''$ 4 bit external
Single/buckshot	up to 7	$0.177''$ 4 bit internal

The differences in each launch tube is the bore size and the style of the rifling. For the larger launch tube with a bore size of $0.22''$ (5.558 mm) there are two types of rifling. One has a shallow rifling and the other has no rifling. The launch tube with the shallow rifling is used for firing large awkwardly shaped projectiles. The other, with no rifling, is used to shoot ice projectiles as the smooth surface means the brittle ice projectiles are not broken apart by rough rifling.

A further set of launch tubes have a bore size of $0.170''$ (4.318 mm), with one having a 4 bit external square rifling and the other a 6 bit wedge rifling (Figure 3.3). The former launch tube is used for high velocity shots (greater than 7 km s^{-1}) and the latter for medium reliability shots. The final launch tube used, is one with a bore of $0.177''$ (4.450 mm) and a 4 bit internal square rifling (Figure 3.3) for slow speed shots. The type of rifling will determine the type of shot; a smooth rifling will be for higher speed shots as there will be less friction slowing the acceleration of the sabot. However, the absence of a significant rifling could result in a poor split of the sabot allowing the sabot to continue on to hit the target material.

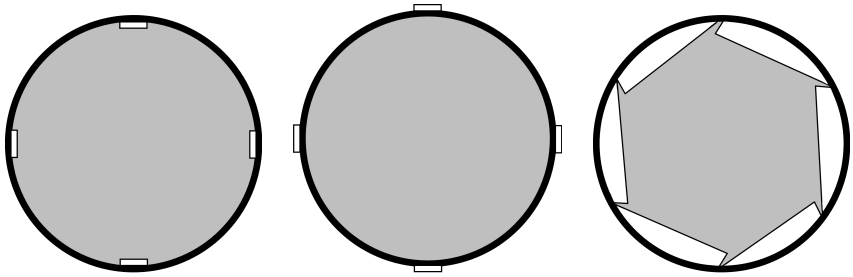

Figure 3.3: Schematic of rifling.

After the launch tube, the sabot passes into a larger diameter blast tank, where it is no longer laterally confined. The rotational component, now on the sabot from the rifling of the launch tube, causes the sabot components to separate from the direct path on to the target material passing through the stop plate which has a central hole of 1 cm in diameter (Burchell et al. 1999). This stop plate is impacted by the split sabot parts which have now travelled off the main axis of the gun (at an angle of typically 6°) (Burchell et al. 1999) meaning they will not impact and contaminate the target and not damage the blast tank. The stop plate, located at the exit of the blast tank, is fitted with the impact sensor made of polyvinylidene difluoride (PVDF). This sensor is flexed by the shock wave generated from the impacting sabot producing an electrical signal which can be monitored on an oscilloscope (Burchell et al. 1999). After adjusting for the transit time of the shock wave through the stop plate this signal combined with the signal given by the muzzle detector at the entrance to the blast tank can give the sabot speed to an accuracy of ±4%.

The projectile/s, now travelling without the sabot, pass through two 3R lasers curtains emitting at a wavelength of 633 nm. The laser curtain is generated by the beam being passed through a barrel lens, broadening the beam, and then a slit, generating a curtain. At the end of the laser curtain the beam is passed through a slit and a barrel lens (in reverse) to narrow the beam onto a photo-diode which is connected to an oscilloscope for monitoring. Using the known separation between the two lasers (0.499 m) and the time difference between the triggering of the two oscilloscopes the speed of

the projectile can be determined to an accuracy of approximately ±1% (Burchell et al. 1999).

The University of Kent has two target chambers for the gun, a small chamber and a larger main chamber (used here and shown as a cube at the far end of the image in Figure 3.1). The large chamber (1.14 × 1.14 × 1.15 m) was lent to the University in March 2012 by NASA. Targets can either be securely mounted on the door of the chamber or free standing in the middle. The chamber is fitted with two view ports in order to make observations of the impact and has the capability to have analytical equipment deployed on the target.

3.1.2 Single Stage Gun

For shot speeds less than 1 km s^{-1}, the gun is used just as a singular stage gun. To achieve these speeds a light gas is fed into the pump tube much like in the two-stage gun. However, instead of compressing the gas with rifle powder and a piston, the pressure of the gas inside the pump tube is increased just by adding more gas until the burst disc ruptures. The expanding gas then propels the projectile. The material used for the burst disc is either Acetate, Mylar or Aluminium foil with a thickness of 100 μm or 0.5 mm. The pressure needed to burst the disc is calibrated from past shot data. Table 3.3 is a summary of the configurations of the single stage gun used for the work in this thesis.

Table 3.3: Summary of the configurations of the single stage gun used for the work in this thesis

Configuration	Pressure [bar]	Shot Speed [km s^{-1}]
H_2 and 50 μm Al Foil	50 – 85	0.30 – 0.65
H_2 and Acetate	≈ 100	0.80 – 1.10
H_2 and 100 μm Al Foil	≈ 97	≈ 1.12

3.1.3 Other Gun Capabilities

Over time, a variety of useful systems have been added to the gun. These include:

- *Rotating Target Holder* - This can be used inside the target chamber to investigate the effect of rotation on an impacted body (see Morris & Burchell 2017).
- *Variable Temperature Target* - This can be fitted to the inside of the target chamber door. It can electronically heat a cylindrical target with a diameter of approximately 60 mm and a length of 10 cm, to approximately 1,000 K. This can be used to determine the effect of a hot target on crater morphology (Morris et al. 2011).
- *The Cold Gun* - The two-stage light gas gun can fire frozen projectiles at a range of speeds. Before firing the launch tube is placed in the freezer at -140 °C over night. Additionally, the central breach and collar are placed in the fridge at 5 °C before required (see Burchell, Bowden, Cole, Price & Parnell 2014a).

Under development:

- *Electronic Burst Disc* - In order to obtain a more controlled release for the single stage gun allowing for a more sensitive and reliable speed determination an electronic burst disc can be used. Once the required pressure of the light gas is obtained behind the electronic burst disc, an electric current can be used to rupture the disc by melting it.
- *The Vertical Gun* - In order to remove the effects of gravity on all shots completed at the University of Kent a vertical gun is being constructed. This new gun can fire projectiles vertically at speeds between 0.2 and 5 km s^{-1} into the same chamber as the existing horizontal gun.

3.2 Hydrocode Modelling

A hydrocode is a computational modelling tool used to investigate the behaviour of continuous media. The 'hydro-' refers to the fluid nature of the material at such high shock pressures and the '-code' refers to the use of numerical simulations used to model these situations. Generally, the system being studied is represented by a 'mesh' of cells which can be influenced by external and internal forces. For a short period of time these forces are assumed to be constant, leading to the adjustment of the geometry of the mesh. The forces are then recalculated and the process repeats. In this section of Chapter 3 the types of hydrocode models and the software package Autodyn shall be discussed.

3.2.1 Types of Hydrocode Meshes

There are a variety of different ways in order to model and analyse the system in a hydrocode. This section shall discuss three types: Lagrangian, Eulerian and Smooth Particle Hydrodynamics (SPH).

Lagrangian

Both Lagrangian and Eulerian work use a mesh to determine the motion of a material under strain. This mesh represents the geometry, initial material parameters and appropriate boundary conditions. The material coordinates in a Lagrangian mesh move with the mesh when under external influences, see Figure 3.4. This means that the material coordinates of material points are time invariant and that no material passes between mesh elements. Furthermore, boundary nodes remain on the boundary, meaning that boundary and interface conditions are easily applied. However, this system can be hindered by severe mesh distortion as the mesh deforms with the material.

Eulerian

The significant feature of an Eulerian approach is that the mesh coordinates are fixed, meaning that the material moves through the Eulerian grid (Figure 3.4) resulting in the spatial coordinates of the material vary with time. The material points changing with time makes dealing with history-dependent material difficult. In addition to this, boundary nodes and the material boundary may not coincide, potentially making the boundary and interface conditions hard to apply. However, an Eulerian approach allows for non-symmetric deformation of a material and will not lead to uncomputable solutions unlike the Lagrangian method. Additionally, more problems are more easily expressed in Euerian coordinates.

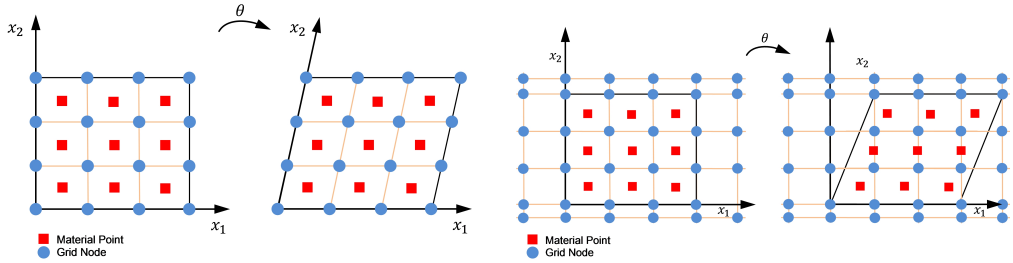

Lagrangian Mesh Eulerian Mesh

Figure 3.4: Comparison of a Lagrangian and Eulerian mesh and how the material and mesh alter under the influence of external parameters.

Smooth Particle Hydrodynamics (SPH)

Smooth particle hydrodynamics (SPH) was invented to simulate problems in astrophysics involving fluid masses moving in three dimensions in the absence of boundaries (Gingold & Monaghan 1977). SPH works by looking at the motion of a set of points. By giving these points a mass they are deemed particles. At any time the velocity and thermal energy of these points are known. For the particle to move, the force acting on it is calculated by interpolation techniques at each time step. There are some issues regarding material properties and boundary and interface conditions in an SPH code,

however this method is still used, see Kupchella et al. 2015.

3.2.2 ANSYS Autodyn

Impacts performed using the LGG can be modelled using hydrocode software such as ANSYS Autodyn (Hayhurst & Clegg 1997). Autodyn is a powerful tool to analyse impact events, versatile enough to work on personal computers and supercomputers.

Figure 3.5 is an image of the Autodyn user interface. Initially, the user has to determine the mesh type (Lagrangian, Eulerian or SPH), the units and whether the model will be in two dimensions or three. The next step involves inputting the material being modelled. For this an equation of state (EOS) and strength model is needed.

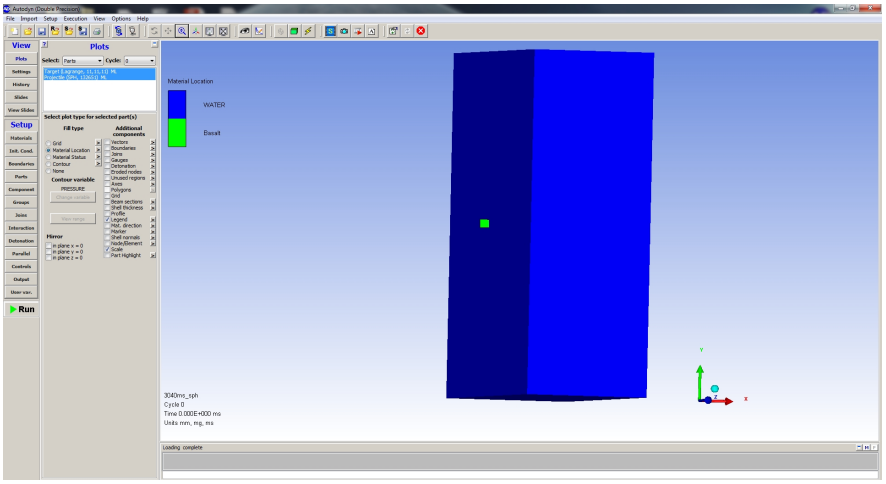

Figure 3.5: Image of the user interface for the Autodyn software.

An equation of state (EOS) is an equation describing the state of matter under certain physical conditions. Usually, the EOS relates the stress to deformation and internal energy (or temperature). Autodyn has many different EOSs available to describe the state of matter, examples are; the Bulk Modulus, Shear Modulus, Ideal Gas EOS, Polynomial EOS, Linear Shock EOS, Bilinear Shock EOS and more. The Mie-Grüneisen and Linear Shock equations of state are discussed in Section 1.1.2.

Strength models are needed in addition to an EOS to describe materials which have

strength. Strength models can be used to define the transition between elastic and plastic strain and to define the onset of fracture. They are also used to describe a material's resistance to shear distortion. There are various strength models to be implemented in Autodyn, such as, the Von Mises model, Piecewise JC model, Orthotropic Yield model or the Beam Resistance model.

The Von Mises model was used for the work in this thesis. It uses the original Von Mises premise that the yield stress has a constant value. The advantages of this is that it doesn't involve input of a lot of material parameters, which is useful when many material parameters are unknown or cannot be accurately determined. However, the model does not generally take into account the effect of strain rate sensitivity or thermal softening. The Von Mises strength model is used widely for impact modelling, for example, see Fendyke et al. (2013).

In order to overcome large cell distortion the user can define a cut off which tells Autodyn when to remove the cell. The final components needed to run a simulation are the material size and position, initial speeds and the placement of gauges. Gauges are used to record the pressure and temperature at their location during the impact.

Autodyn and other hydrocodes are valuable tools in researching hypervelocity impacts as they allow for a wide range of investigation parameters. Whereas light gas guns are restricted by their set-up. However, it is important to use the two methods in conjunction with each other as hydrocodes may not be physically reliable.

Chapter 4

Method II - Analytical Equipment

The work presented in this thesis uses the University of Kent's Hitachi S-3400N Scanning Electron Microscope (SEM) and the Horiba LabRam-HR Raman Spectrometer. In this chapter, these pieces of equipment shall be discussed.

4.1 Scanning Electron Microscope (SEM)

The birth of electron microscopy can be traced back to 1926 when Busch studied the trajectories of charged particles in axially symmetric electric and magnetic fields. He found that such fields could act as particle lenses (e.g. for an overview see Bogner et al. (2007) and references therein). The need for scanning electron microscopy was to be able to obtain a higher magnification than in optical microscopes which are limited by diffraction effects for visible light. Currently, SEM's can have a spatial resolution better than 10 nm (Reed 2005). Moreover, the SEM's large depth of field (usually at least 100 times greater than an optical microscope) can be more relevant than just the high resolution.

A SEM works by scanning the surface of the sample with an electron beam and displaying the signals received by the electron detector on a monitor. The interaction between the electron beam and the specimen lead to different information being obtained (i.e. topography and relative composition). For example, SEMs equipped with an Energy Dispersive X-ray spectrometer (EDX) can determine the elemental characterisation of the specimen.

The University of Kent's SEM is a Hitachi S-3400N. This model of SEM has a variable-pressure mode which allows for the analysis of wet, oily and non-conductive samples without the need for a complicated sample preparation technique. Additionally, the SEM is also fitted with an EDX spectrometer. The standard configuration for SEMs are the electron gun, condenser lens, deflection coil, objective lens, secondary electron detector, display and vacuum pump (Figure 4.1).

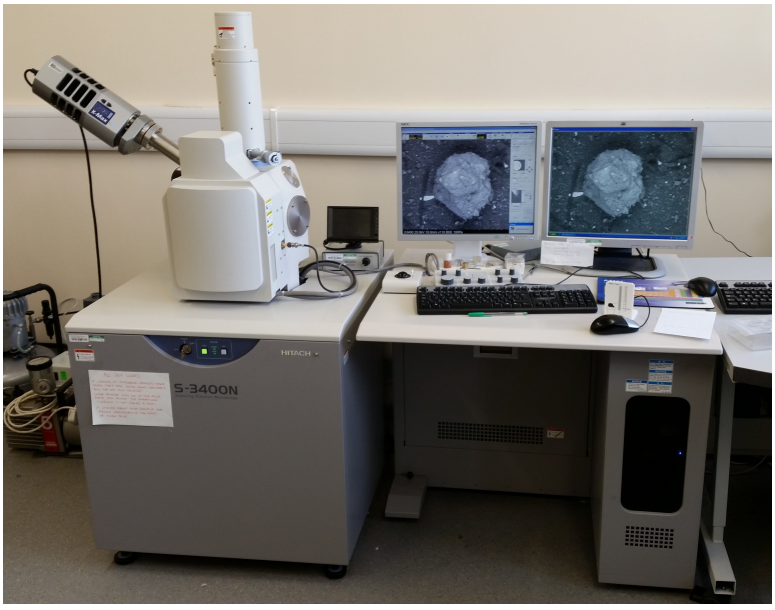

Figure 4.1: Image of the University of Kent's Hitachi S-3400N SEM

4.1.1 Electron Interactions

The types of information from specimens attainable using the University of Kent's SEM are topography, composition and elemental data. This information is obtained

via accelerating electrons at voltages up to 40 kV onto the surface of the specimen. The electrons interact by either being deflected in a process called backscattering or the incident electrons remove electrons from the specimen which in turn are detected. The elemental data is determined by these dislocated electrons being replaced by electrons in the outer shell of the atom. This transition emits an X-ray photon of energy specific to the element.

Backscattered Electrons (BSE)

The fundamental effect that backscattering relies on is elastic scattering. This is where interactions with atomic nuclei can lead to large deflections, with little transfer of energy due to the large mass difference between the nuclei and the electron. The mechanics of this interaction were derived by Ernest Rutherford, and the angular deflection γ is given by:

$$\tan(\frac{\gamma}{2}) = \frac{Z}{(1.4pE)}, \tag{4.1}$$

where E is the energy (in keV) of the electron, Z is the atomic weight and p is the minimum distance (in nm) between the undeflected electron path and the nucleus (known as the 'impact parameter') (Reed 2005).

An incident electron interacting with the surface of a sample has a finite probability of being deflected through an angle greater than 90° and re-emerging. This result can also be obtained by multiple deflections through smaller angles. The fraction of electrons which leave the sample is known as the backscattering coefficient, η. This coefficient strongly depends on the atomic number, due to an increasingly higher probability of a high angle deflection with increasing Z (see Equation 4.1) (Krinsley et al. 1998, Reed 2005).

Figure 4.2 shows the paths of electrons entering two materials, one with a high Z and the other with a low Z. Following from the likely result that the electron doesn't deflect at angles greater than 90°, the electron would take a 'zig-zag' path deflecting

at each nucleus it comes into contact with. In some cases, this results in the electron leaving the surface of the material to be detected, and in others, the electrons are 'lost' into the sample. Due to Equation 4.1, which shows the relation between nuclei size, Z, and deflection angle, larger nuclei (higher Z) will have more electrons emitted from the sample than smaller nuclei (lower Z), due to the larger deflection angles leading to more electrons making their way back to the surface.

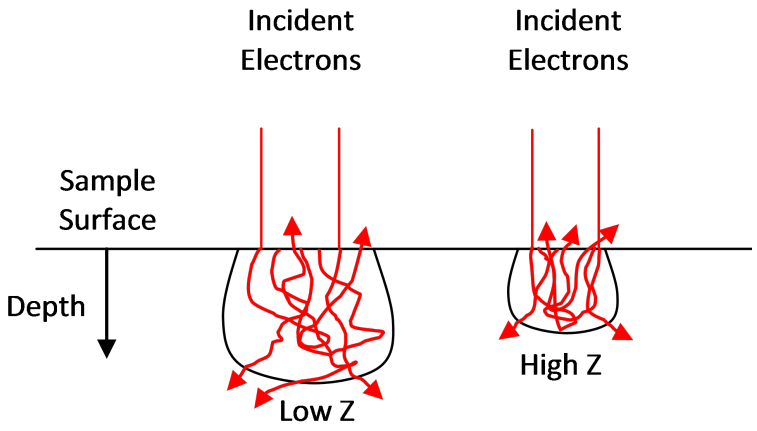

Figure 4.2: Backscattered electron interaction with different atomic weights, Z. Redrawn from Krinsley et al. (1998).

This means that materials that appear brighter in the Backscattering mode are ones with a denser/heavier nucleus and those that are dimmer as those with less dense/lighter nucleus. This is shown in Figure 4.3 which is a Backscattering Electron image of the different mineral phases in a sample basalt, which was obtained by the author. The lighter/whiter phases are the minerals which contain significantly heavy atoms (high Z) such as Iron (Fe). The darker phases are those which have lighter atoms (low Z) such as Silicon (Si), Calcium (Ca) and Magnesium (Mg), which could suggest it is a pyroxene.

Figure 4.3: Backscattered electron image of different mineral phases in basalt from the Isle of Skye. The whiter phase refer to a material with a higher value of Z and the darker refers to a lower Z.

Secondary Electrons (SE)

Secondary electrons (SE) are ejected either by the incident electrons, or via a backscattered electron being directed back to the surface of the material, see Figure 4.4. The secondary electrons are distinguishable from backscattered electrons by their much lower energies, with the average being only a few electron volts (Reed 2005). Due to this low energy, these electrons must originate from no more than a few nanometres into the surface of the sample. Accordingly, a secondary electron image has a higher resolution (Vernon-Parry 2000).

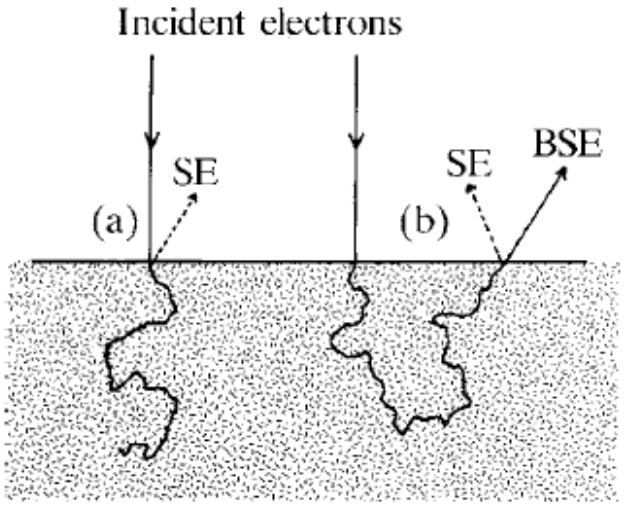

Figure 4.4: Secondary electron production by (a) incident electrons as they enter the sample, and, (b) backscattered electrons as they leave the sample. Diagram taken from Reed (2005).

The secondary electron coefficient, σ, is defined as the ratio of secondary electrons produced per incident electron. This value is approximately between 0.1 and 0.2 and does not vary smoothly with the nucleon number (Z) (Reed 2005). However, there is a relation between the incident electron energies and the secondary electron coefficient. For incident electrons with energies less than 5 keV, the secondary electron coefficient increases due to the range of the incident electrons being shorter, resulting in more energy being deposited near the surface of the sample, meaning a greater number of secondary electrons are released (Reed 2005).

X-Rays

X-rays are produced either by electrons interacting with atomic nuclei producing a smooth 'continuous' spectrum, or by transitions of electrons between different energy levels producing spectral lines specific to each element known as a 'characteristic' spectrum (Reed 2005).

The continuous X-ray spectrum is generated by an incident electron passing through a strong electric field close to the atomic nucleus, which could lead it to have a quantum jump to a lower energy state and thus emit an X-ray photon with any energy up to the initial energy of the electron, E_o (Reed 2005). This continuous spectrum (or 'continuum' or 'Bremsstrahlung') has a limiting effect on the characteristic spectrum by limiting the detectability of elements present in low concentrations. Kramers' law represents the intensity, I, of the continuum, which is:

$$I = constant \times Z(E_o - E)/E, \tag{4.2}$$

where E is the X-ray photon energy and Z is the atomic number. The intensity of the continuum falls off at the 'Duane-Hunt limit', where the X-ray energy is equal to the initial electron energy (Reed 2005).

The characteristic X-ray spectra is a transition between different energy levels within the atom. The energies of these energy levels are principally governed by the quantum number n. In an atom the closest electron shell is the K shell (n = 1), the next is the L shell (n = 2) and then M shell (n = 3), etc. Atoms always fill up from the shells closest to the nuclei meaning that for some atoms the M shell could be vacant. The number of electrons in each shell is determined by other quantum numbers relating to angular momentum. This results in the K shell having a maximum of 2 electrons, the L shell a maximum of 8 and the M shell a maximum of 18 electrons. Finally, the L, M and higher shells are split into subshells with each having different energies. The L shell consists of three subshells (L1, L2 and L3), and the M shell has five subshells

(Reed 2005).

Let us assume that an incident electron has sufficient energy to ionise an electron, this leaves a gap in the shell meaning that an electron in a higher shell will cascade down to fill the vacancy. This process will emit an X-ray photon. Spectral lines are designated K, L, etc. according to the shell containing the initial vacancy. The most intense spectral lines are labelled α, those which a next most intense, β, etc. (see Figure 4.5).

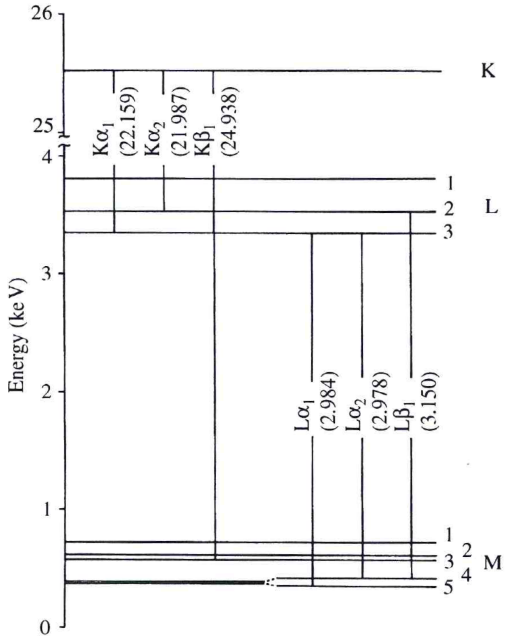

Figure 4.5: Diagram of the energy released from the transition of electrons from a higher energy state to a lower. Taken from Reed (2005).

4.1.2 Instrumentation

Electron Gun

The electrons required for the beam are generated using an electron gun. The premise of this is by heating a metal filament this increases the free electron's kinetic energy which, when this is high enough, leads to them 'escaping' the material. When this is

done in a vacuum the electrons are free to move and are easily directed by a magnetic field. The University of Kent's SEM uses a tungsten filament to produce free electrons. The temperature of this filament is at 2,600 K and it generates an electron source with a diameter of 30 μm (Hitachi 2013). The average life time of the filament is approximately 50 hours (Hitachi 2013).

Electron Column

The electron column is the section of the SEM where the electrons are generated and focused to form an image. The electrons produced by the electron gun travel through the condenser lenses, deflection coils and objective lens before finally reaching the target.

The condenser lens consists of a coil of copper wire, carrying a direct current, surrounded by an iron casing. The iron casing is shaped in a ring with a small hole in the centre, the magnetic field generated by the current within the copper wire is used to focus and demagnify the electron beam by making the electrons flow through this hole (Goldstein et al. 1981). Altering the current in the copper coil allows the user to alter the beam. After the condenser coils, there is an aperture which prevents stray off-axis electrons from travelling further down the column and potentially causing spherical aberrations Reed (2005).

The deflection coils are used to manipulate the electron beam allowing it to scan in a raster fashion over the sample. The coils are in multiples of four which have a variety of potentials across in order to change the angle of the beam (Reed 2005). The final lens in the column is the objective lens. This lens is similar to the condenser lens by using an electromagnetic field in order to manipulate the electrons travelling down the column. However, the difference is that a polepiece is used, instead of just an open hole, in order to minimise the magnetic field near the sample (Reed 2005). Figure 4.6 is a schematic for a SEM column.

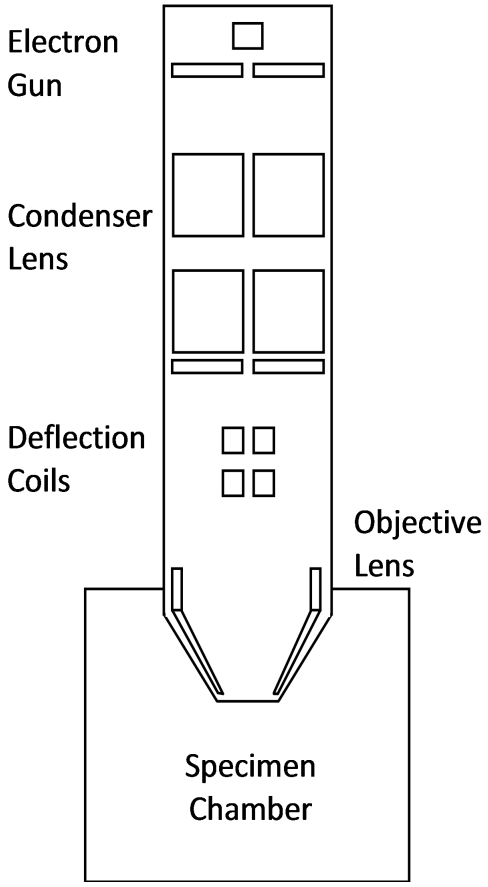

Figure 4.6: Schematic of Electron Column displaying the electron gun, condenser lens, deflection lens and objective lens.

Specimen Chamber

The specimen chamber contains the three detectors; the backscattered electron detector, the secondary electron detector and the energy dispersive X-ray spectrometer (EDX). When the SEM is in operation, the sample chamber is under vacuum or under a variable pressure. In order to change samples, the chamber has to be returned to atmospheric pressure. The samples are placed on the stage which moves in x, y and z directions. Figure 4.7 is a schematic of the equipment layout inside the specimen chamber.

The BSE detector is a solid state detector located directly above the sample. The detector uses a negative potential to avoid collecting SEs (Reed 2005). The BSE de-

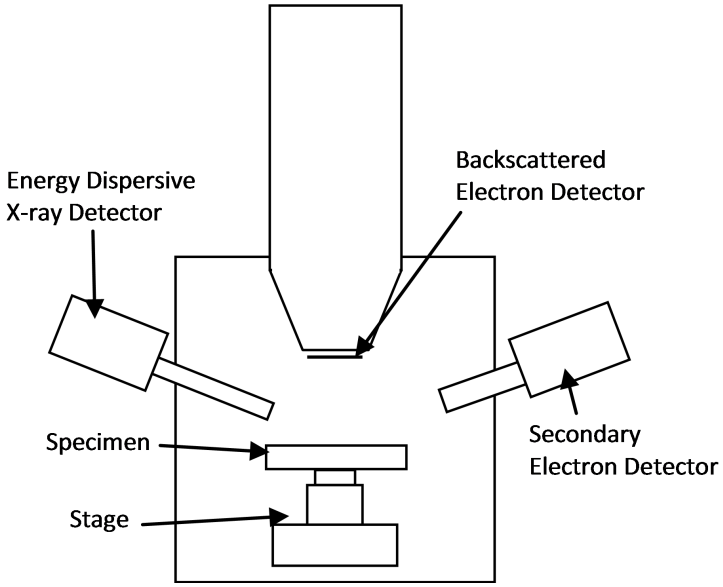

Figure 4.7: Schematic of Specimen Chamber displaying the BSE detector, SE detector and the EDX detector.

tector in the University of Kent's SEM has five segments (some have four) of which four of the segments are in a ring around a hole which allows for the electron beam to pass through. The fifth segment is used for 3D imaging. Each segment can be turned off separately allowing for different topological information to be determined (Reed 2005). One disadvantage of BSE detectors is that they are insufficient when dealing with electrons with an energy lower than 10 keV (Reed 2005).

The SE detector is a scintillator which is located at the side of the sample chamber. When an electron strikes a scintillator it results in the emission of a photon which in turn interacts with a photomultiplier changing it into an electrical signal (Reed 2005). In order to deal with low energy electrons, in front of the scintillator, there is a positive potential of 10 kV increasing the electron's energy (Reed 2005). Furthermore, in order to avoid non-SEs being detected, and interactions with the electron beam, a grid with a potential of positive 200 V is placed in front of the scintillator (Reed 2005).

The EDX spectrometer converts X-ray photons into electrical pulses by promoting the electrons orbiting the atom's nucleus (valence electrons) to leave the atom (the conduction band). With an element such as silicon or germanium, this produces electron

hole pairs (Reed 2005). The X-ray photons energy is related to the number of pairs produced and hence the number of pulses. These are then converted into a spectrum of their intensity versus energy in keV. From this, the elements can be determined (Reed 2005).

4.1.3 Issues with SEM

SEM images may be degraded by a range of factors e.g. depth of focus and limitations in resolution. However, there are further ways in which a SEM image can be degraded as discussed here.

Statistical Noise

For images produced from a quick scan rate, there are a low number of electrons per pixel, this results in the image being subjected to large statistical fluctuations resulting in noise. This is remedied by producing an image using a slow scan rate. However, this has the downsides of a slow response to moving the specimen and adjusting the focus etc. (Reed 2005).

Specimen Charging

A specimen with a surface charge causes the low energy secondary electrons to be deflected. This results in an image with bright patches where the charging is occurring. This effect is as a result of insulating samples and is managed by applying a conducting coat. This coat allows for the surface charge to flow away and reduces the charging effect. However, this method is not a practical answer for samples which are needed for other analysis. Another solution is variable pressure mode which lowers the vacuum within the sample chamber. This allows for the pool of surface electrons to be 'drained' away through the base of the sample holder which is earthed (Reed 2005). The user of

the University of Kent's SEM can select a pressure between 0.1 and 1000 Pa to use in variable pressure mode (VP-mode).

Stray Field and Vibration

Some stray alternating magnetic fields are not blocked by the screening of the column. These fields can cause straight edges in a scattering image to appear ragged. To stop this, you either need to install a field cancelling system or minimise it by using a high acceleration voltage and minimum working distance (Reed 2005).

Vibrational interference also causes a similar problem. The source of the vibrations can be anything from the mechanical vibration of the vacuum pump to traffic outside. To lower the effects you can mount the column on an anti-vibration mounting which the University of Kent's SEM is equipped with.

Astigmatism

The effects of astigmatisms lead to a blurring and elongating of the image as seen in Figure 4.8. The cause of the astigmatism is small lens imperfections or contaminations on apertures (Reed 2005). It can be remedied by adjusting the stigmator. However, if after adjustment the astigmatisms still occur, then it is necessary to clean the column apertures (Reed 2005).

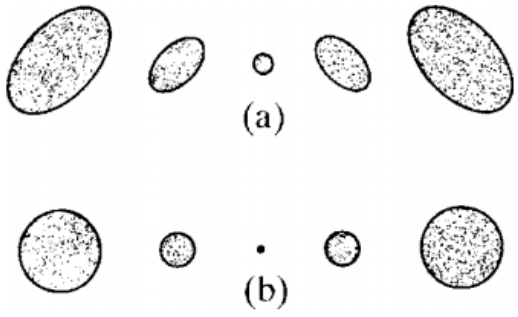

Figure 4.8: Diagram of the appearance of the electron beam (a) with and (b) without astigmatism. Taken from Reed (2005).

4.2 University of Kent's Horiba LabRam-HR

The second half of the work completed in this thesis was conducted using a Raman spectrometer. The University of Kent's Horiba LabRam-HR (Figure 4.9) is fitted with a suite of four lasers (473 nm, 532 nm, 633 nm and 714 nm) and has two temperature stages covering temperatures between -150 and 1,500 °C. The Raman effect itself is discussed in Section 2.4. This section of the Analysis Equipment chapter will discuss the instrumentation of the University of Kent's Raman spectrometer and the issue of fluorescence.

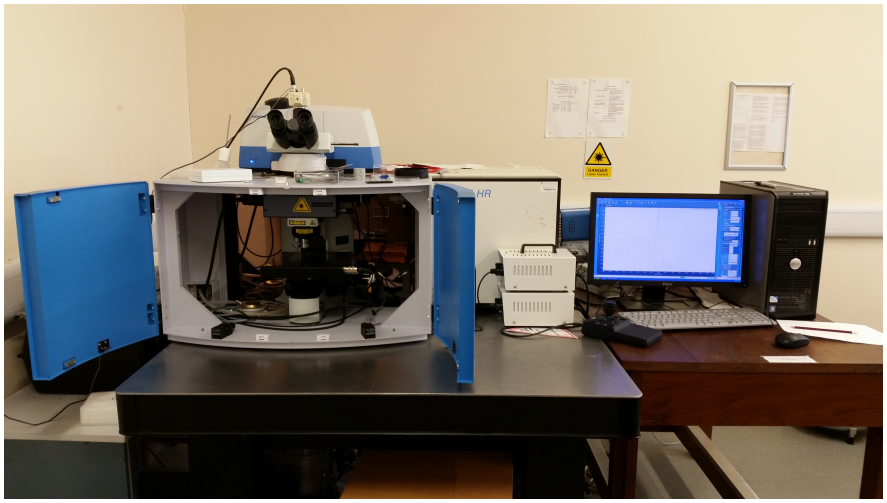

Figure 4.9: Image of the University of Kent's Raman Spectrometer.

4.2.1 Instrumentation

Raman spectroscopy is a measurement of the frequency of scattered light, hence it is important for the light source to be narrow, powerful and monochromatic. Therefore, a laser is the perfect radiation source for the task. The University of Kent's Raman spectrometer is fitted with a blue ($\lambda = 473$ nm, $f = 634$ THz), green ($\lambda = 532$ nm, $f = 564$ THz), red ($\lambda = 633$ nm, $f = 474$ THz) and infra-red ($\lambda = 714$ nm, $f = 420$ THz) lasers. The production of laser light is via the electronic transition from an excited state to a ground state by the introduction of a photon of the exact energy, known

as stimulated emission. This results in two photons of identical energies. The power produced from a laser can be from several milliwatts to a few watts, depending on the type of laser (Banwell 1983).

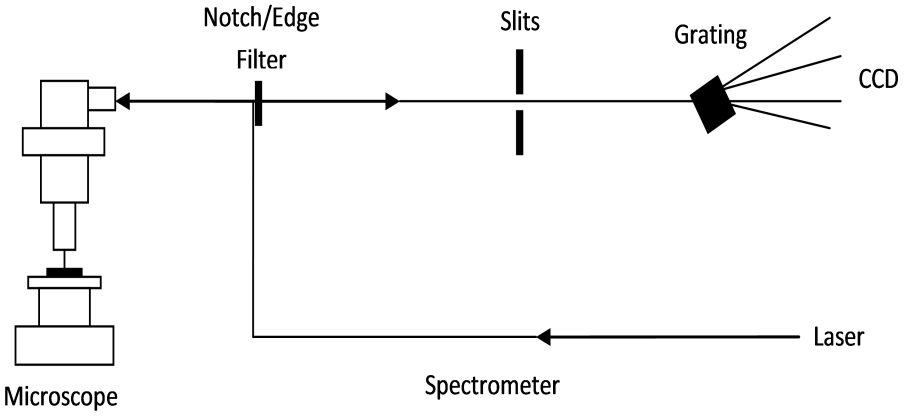

Figure 4.10: Diagram of the laser path within Raman Spectrometer. Replicated from Smith & Dent (2005).

Figure 4.10 shows a typical path of the emitted laser light within a Raman Spectrometer. After emission, the laser light is passed through a pin hole and collected as an expanded parallel beam. This is done so that the laser light can fill the optics of the microscope. Additionally, the light passes through a plasma filter in order to remove any specious radiation such as weak emission lines other than the main excitation line in the laser and background radiation from the laser. The laser light then interacts with either a notch or edge filter, depending on which is being used as the University of Kent's Raman system has both. These are both interference filters which allow different scattered light to be transmitted. The notch filter allows both Stokes and anti-Stoke scattered light whereas an edge filter only allows the Stokes scattered light. Both these filters are specially designed so that when the laser is at a certain angle to the plane of the filter it entirely reflects the laser light into the microscope and onto the surface of the sample. The scattered light returns up the microscope and interacts with the notch or edge filter at an angle perpendicular to the plane of the filter. Hence allowing the scattered light (Stokes or Stokes and anti-Stokes depending on the filter) to pass through. This light is passed onto a monochromator and onto the

CCD detector (Smith & Dent 2005).

The Raman spectrometer requires frequent calibration. This is done using a sample of silicon which has a singular, narrow Raman peak at 520.6 cm^{-1}. The calibration is completed by the computer, ensuring that both the peak of silicon and the Rayleigh (laser line) are measured to be in the correct locations. To ensure correct spectra are obtained this should be carried out before every session. Additionally, in order to not obscure the weaker Raman peaks, there is a filter blocking the Rayleigh light except for a peak at 0.0 cm^{-1}.

Fortunately, sample preparation for Raman spectroscopy is very simple. As the technique is predominantly a surface one, the sample simply needs to be on a glass slide or flat dish. This means that the sample can be analysed by other equipment post-Raman analysis. Programs such as LabSpec6 allow the user to acquire singular spectra or to map a certain area. The stage under the microscope can be automatically operated by the computer, allowing for multiple spectra to be acquired over a certain area autonomously. In addition to mapping an area, the Raman spectrometer also has the capability to acquire spectra at different temperatures autonomously with the aid of a Linkam temperature stage. This can be heated electronically to temperatures up to 500 °C for the cooler of the two or up to 1500 °C for the hot temperature stage. Furthermore, the temperature can be lowered to approximately -150 °C with the aid of liquid nitrogen. The computer can fully control the heating and spectra acquisition allowing for the experiment to be conducted without the experimenter's presence.

4.2.2 Fluorescence

Fluorescence is the most common problem encountered in Raman spectroscopy. Fluorescence is generated by the electronic excitement of the electrons in the inner shell of a fluorophore molecule by the incident radiation. As stated before in Section 2.4, when the energy of the incident radiation is equal to the difference between two electronic

energy states, the electron transitions to a higher energy level. It then returns to the original ground state by a variety of transitions emitting photons with energies corresponding to those transitions. The result is a variety of photons covering a range of wavelengths different to the incident radiation. Figure 4.11 is a diagram showing both the Raman scattering process and the emission of fluorescence.

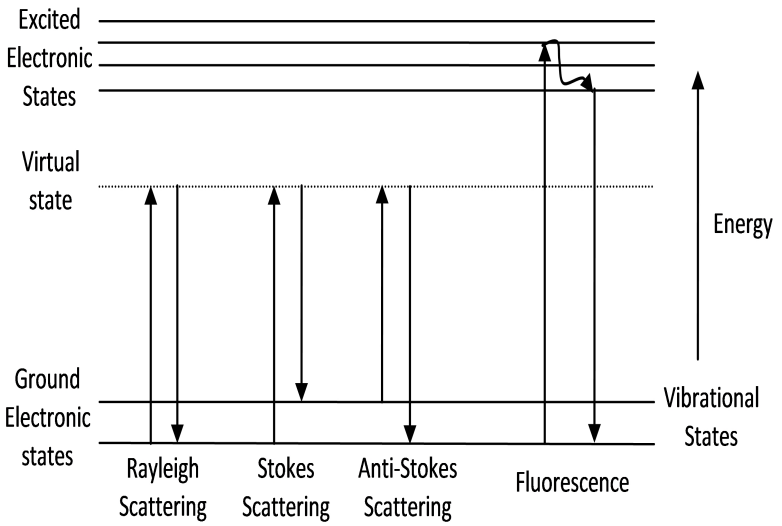

Figure 4.11: Diagram of the Raman scattering and Fluorescence process. Drawn from SCRes (2004).

In comparison to Raman scattering, fluorescence is a strong effect which can easily obscure weak Raman peaks. There are multiple things that can be done to reduce the effects of fluorescence which will be discussed in the remainder of this section.

Photobleaching

Photobleaching is a term used in optics where radiation is used to generate a photochemical alteration to dye, or in the case of Raman spectroscopy, a fluorophore molecule. This act causes the molecule to no longer be able to fluoresce due to an alteration in covalent bonds or non-specific reactions between the fluorophore and the surrounding molecules (Smith & Dent 2005). The technique involves simply irradiating the sample with the laser light for a period of time (anywhere from several minutes

to several hours) before acquiring a spectrum. In Figure 4.12 we show the spectra for paracetamol initially and three times after photobleaching. It is clear that the overall background fluorescence is decreasing with each spectrum as the intensities drop. Figure 4.12 also shows that there is a saturation point where the effects of photobleaching become minimal.

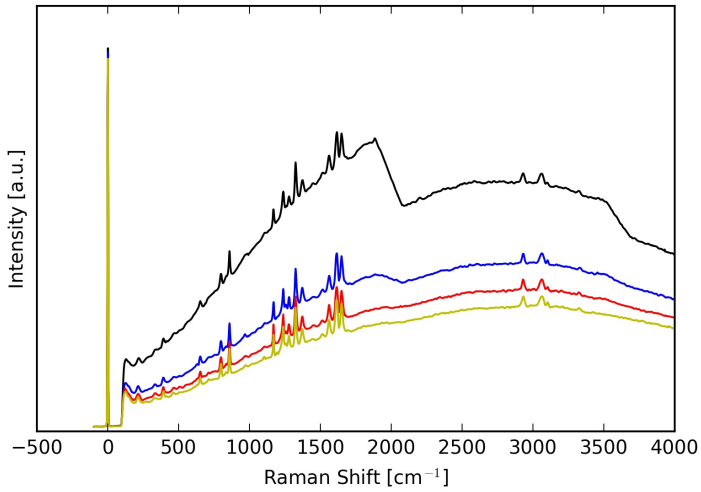

Figure 4.12: Four spectra of paracetamol acquired using the 473 nm laser with the University of Kent's Raman Spectrometer. The top spectrum is the initial and the subsequent are spectra of the same sample in the same location but after being photobleached.

Although photobleaching is a good technique for reducing fluorescence, it has been pointed out that it can cause physical and chemical changes to delicate samples if irradiated for a significant time (Macdonald & Wyeth 2006). Hence, caution must be taken when using this technique on valuable or delicate samples.

Changing Laser Wavelength

Due to fluorescence being as a result of the electronic excitement of electrons in fluorophore molecules, a simple method to reduce fluorescence is to change the wavelength of the laser being used. By using a laser with a lower energy (i.e. longer wavelength) than the electron excitation required energy fluorescence can be reduced. However,

the caveat to using a laser with a lower energy is the lower frequency, and, due to the intensity of the Raman peaks being dependent on the fourth power of frequency (Smith & Dent 2005), this could result in some weak peaks not being observable.

Resonance Raman Spectroscopy

This effect occurs when the frequency of the laser beam is close to the electronic excitation frequency of the fluorescent pigment or molecule. When this resonance occurs the Raman scattering is enhanced in the order 10^3 to 10^6, resulting in Raman scattering becoming a much more sensitive technique (Smith & Dent 2005). Additionally, when this resonance condition occurs it is possible to retrieve electronic and vibrational information about the sample (Smith & Dent 2005).

Figure 4.13 is a pictorial representation of the possible transitions occurring, highlighting the transition of the resonance scattering. The difference between the resonance Raman scattering and fluorescence is the relaxation times. For a scattering event, this relaxation time is short whereas for fluorescence it is longer. Due to the quick relaxation, the nuclei of the molecule has no time to adjust resulting in a scatter, whereas, for fluorescence, the nuclei have time to reach equilibrium resulting in the emission of a photon (Smith & Dent 2005).

One disadvantage of this technique is that significant absorption and fluorescence can occur should the frequency of the laser be the same as the energy required for an electronic transition. A further disadvantage is that this technique only works for a certain class of molecules, such as porphyrin rings which are present at the centre of a number of key enzymes (Smith & Dent 2005).

Baseline Correction

This method of removing the fluorescence involves using a computer to manipulate the spectra to appear nearly flat. This is integrated into software such as LabSpec6.

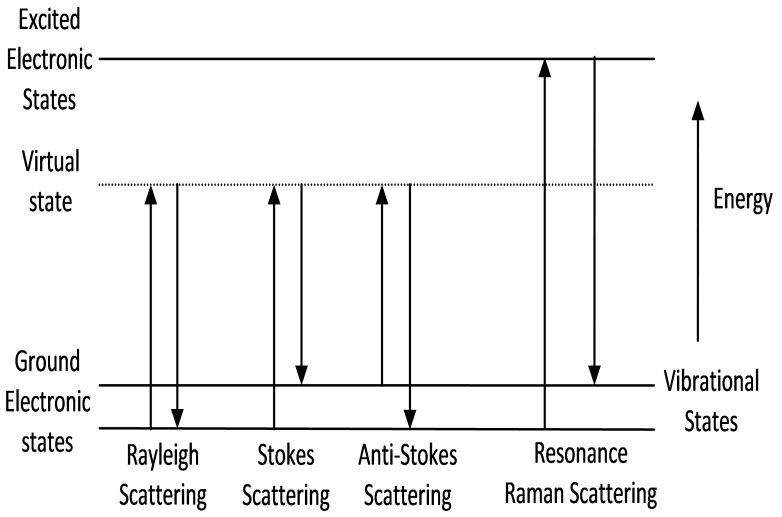

Figure 4.13: Diagram showing the transitions for all Raman scattering and Resonance Raman Scattering. Drawn from SCRes (2004).

It can either be done automatically or manually, each with their own positives and negatives. For example, setting values for an automatic correction could result in the computer performing baseline subtractions that are not optimal for the spectra. Whereas, manually fitting baselines could lead to the user's interpretation biasing the data and result in some small peaks being missed.

Chapter 5

Projectile Fragmentation

Studies of projectiles post-impact date back to the 1960s, but they are far less frequent than impact studies into cratering or the ejecta from craters. Nevertheless, projectile survival after impact is an important topic that needs to be explored as there are several examples of projectiles surviving impact in nature (Goderis et al. 2013, Yue et al. 2013, Reddy et al. 2012).

The conclusions from some prominent impact studies shall be summarised here, for further discussion see Section 1.5.1.

Schultz & Gault (1990*b*) found that a significant amount of impactor could be recovered after having ricocheted down range for angled impacts. Nagaoka et al. (2014) discovered that destruction (a material breaking into smaller fragments) of the basalt projectile occurred when the peak pressure was approximately ten times the tensile strength of the rock. In addition, they were able to determine the energy density at the catastrophic disruption threshold, Q_p^*, to be $(4.5 \pm 1.1) \times 10^4$ for pyrophyllite and $(9.0 \pm 1.9) \times 10^4$ J kg^{-1} for basalt projectiles (Nagaoka et al. 2014). Moreover, Avdellidou et al. (2016) found an order of magnitude difference between the energy density at the catastrophic disruption threshold of olivine ($Q_p^* = 7.07 \times 10^5$ J kg^{-1}) and basalt projectiles ($Q_p^* = 2.31 \times 10^6$ J kg^{-1}). Furthermore, it was established that

the two materials had very similar cumulative fragment size frequency distributions (Avdellidou et al. 2016). Daly & Schultz (2013, 2014, 2015*a*,*b*, 2016) determined that both Vesta and Ceres should have significant levels of exogenic material delivered to them by impacts. Finally, McDermott et al. (2016) found that there was relatively low impact alteration on projectiles at speeds less than 1.50 km s^{-1}. Furthermore, this work suggested four classes of disruption for metallic projectiles with increasing shock pressure; 1) minimal damage, 2) ductile deformation, 3) increasing fragmentation and 4) complete fragmentation.

This chapter discusses the first experiment in this thesis, looking into the fragmentation of basalt and shale projectiles in hypervelocity impacts in the laboratory. Beginning with a discussion of the materials used then moving onto the methodology and results.

5.1 Sample Materials

The two rocky materials chosen to investigate projectile fragmentation were basalt and shale. Basalt was chosen as it was a commonly available multi-mineralic sample which is an analogue to basaltic impactors expelled from bodies such as the Moon, Mars or the asteroid Vesta. Shale was chosen as a significantly different material to compare to basalt with the addition of having significant carbonaceous material, which is important for the experiments discussed in later chapters.

5.1.1 Basalt

Basalt is a dark-coloured fine grained igneous rock usually forming as an extrusive rock. It forms when lava reaches the Earth's surface and quickly cools (typically within a few days or a week) to form solid rock. It is one of the Earth's most abundant bed rocks and also features on other solar system bodies such as the Moon and Mars.

Figure 5.1: Google Map image of basalt outcrop on the Isle of Skye, Scotland (57°39'15.9"N, 6°14'52.1"W).

The basalt used here was collected from the Isle of Skye, Scotland (57°39'15.9"N, 6°14'52.1"W). Figure 5.1 is a Google Maps image of the outcrop where the samples were collected. It is a very fine-grained basalt with small (approximately millimetre sized) vesicles. This fine grained nature of the basalt makes it an excellent material to make millimetre-sized projectiles which can be launched in the gun without breaking up. The composition of the basalt is olivine (Fayalite 80, Forsterite 20), clinopyroxene (Enstatite 10, Ferrosilite 47, Wollastonite 43) and feldspar (Anorthite 57, Albite 32, Orthoclase 11). The phases can be seen in the EDX image in Figure 5.2. The red refers to minerals with high concentrations of magnesium, such as clinopyroxene, the area covered by these is approximately 31% of the EDX image. The green refers to high concentrations of aluminium, such as felspar, and the area covered by these is approximately 42% of the EDX image. The blue refers to high concentrations of iron, these areas also had high concentrations of Ti, and these cover an area of approximately 7% of the EDX image. The remaining area of 20% is not the sample material.

5.1.2 Shale

Shale is a fine-grained sedimentary rock which forms from compaction of silt and clay-sized mineral particulates. Shale is in the category of mudstone and is fissile and laminated. This lamina structure can be seen in Figure 5.3 as flat surfaces where

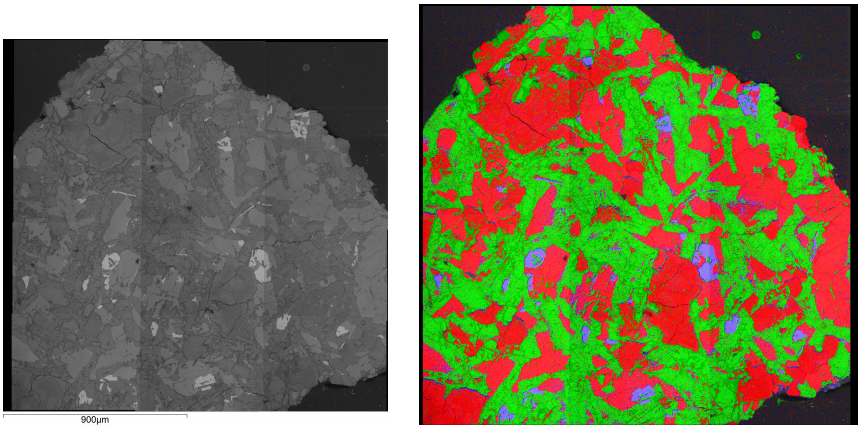

Figure 5.2: *Left:* Backscattered SEM image of basalt sample. *Right:* EDX of same basalt sample. Where red = magnesium, green = aluminium and blue = iron rich minerals.

the sample had been extracted. Its composition is mainly clay-sized minerals, such as illite, kaolinite and smectite. It also contains other minerals such as quartz, chert and feldspar.

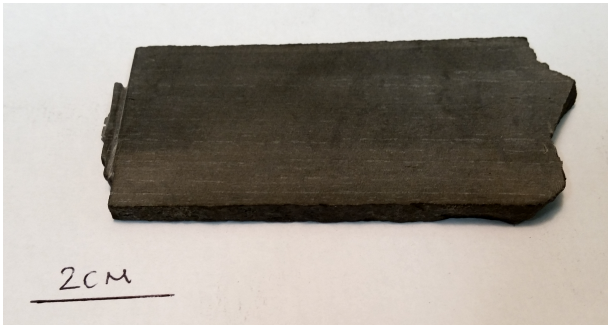

Figure 5.3: Image of shale sample used in the experiment.

The shale used in this experiment was collected in Scotland. Figure 5.4 is an SEM and EDX image of the shale. In the EDX image of the shale the red areas refer to minerals which are compositionally high in aluminium (possibly kaolinite). The green areas are compositionally high in silicon (quartz) and the blue areas are compositionally high in calcium (feldspar).

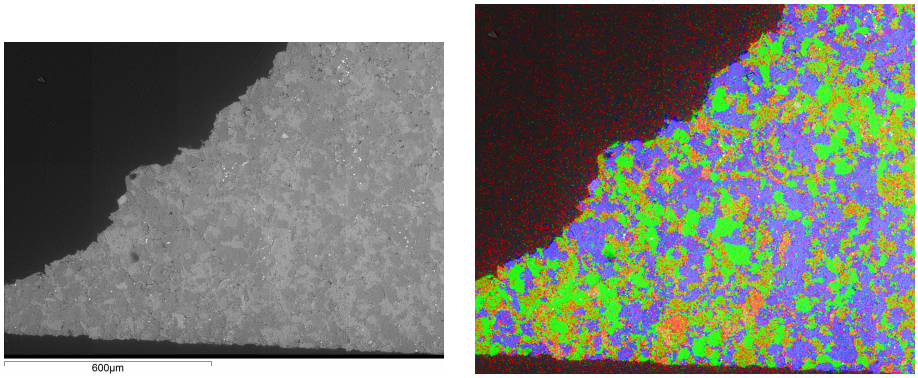

Figure 5.4: *Left:* Backscattered SEM image of shale sample. *Right:* coloured and combined elemental map over the same region produced using EDX data for aluminium (red), silicon (green) and calcium (blue) rich minerals.

5.2 Methodology

The general procedure for this experiment was that the projectiles were fired into water at varying speeds to investigate the fate of the projectile post impact. The impacts investigated were predominantly at normal angles of incidence, however, an impact angle of 15° was also investigated. After impacting, the fragmented projectile material was collected. From here the water, containing the projectile fragments, was filtered. Once dry the fragments were mapped using the scanning electron microscope, and from the individual pictures in the map, the information regarding the projectile fragment's semi-major and -minor axis were obtained. This section discusses the method used in this experiment.

5.2.1 Projectile and Target

The sample material was shaped into 1.5 mm cubes for firing in the gun. This was completed by cutting the material off of the main sample using a Dremel diamond wheel cutter and shaping using a diamond file. A cube shape was used as this is the easiest shape to make that will fly well. A sphere is an ideal shape, however, this is incredibly difficult to make. Figure 5.5 is an example of a basalt projectile. Before shooting

the projectiles were measured and weighed. As a further comparison, synthetic basalt glass spheres were used. These were obtained from 'Whitehouse Scientific' and had a composition of SiO_2 (43%), Al_2O_3 (14%), CaO (13%), Fe_2O_3 (14%), MgO (8.5%), Na_2O/K_2O (3.5%) and other (4%). These basalt glass spheres were the same as used by Avdellidou et al. (2016) and were used to enable comparisons against that work.

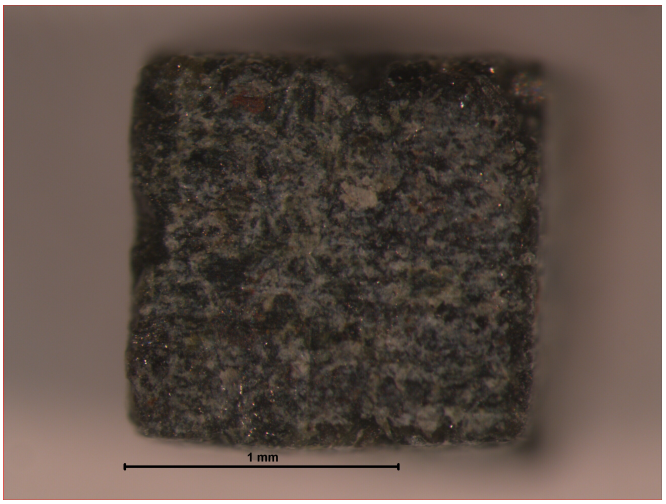

Figure 5.5: Image of basalt projectile.

In order to address the aims of this thesis, it was necessary that the projectile be retrievable after impact. In order to do this, the projectiles were fired into water. As the LGG is (at the time of shooting) horizontal, it requires a special target design. The target used for this experiment was the ocean target. This is an aluminium frame which suspends a bag of water and is covered by an aluminium box with one entry hole approximately 31.4 mm in diameter (Figure 5.6). Each bag held approximately 250 ml of water in the line of flight of the projectile, there was a water column of approximately 3 cm.

5.2.2 Impact Experiment and Filtering

As stated, the 1.5 mm cube projectiles were fired using the LGG. The speed of each shot is determined by varying the pre-pressure in the first stage of the gun. Speeds

Figure 5.6: Two images of the Ocean Target. The ruler in the right image is 30 cm long.

below 1 km s^{-1} are achieved by bursting a diaphragm between the first and second stage. In each shot, the pressure inside the chamber was held at 50 mbar in order to avoid deceleration of the projectile. For further discussion on the functionality of the LGG see Section 3.1. The basalt projectiles here were shot at speeds between 0.51 and 6.02 km s^{-1} and for the shale projectiles between 0.39 and 6.13 km s^{-1}.

After a successful shot, the water containing the fragments of the projectile was collected by washing the target chamber with RO water and collecting the water. The water was then filtered through a 0.1 μm Durapore membrane filter using a vacuum pump (Figure 5.7). The system can hold up to 300 ml of water at one time. In order to not lose any projectile fragments the beaker containing the water was rinsed thoroughly.

The introduction of the 0.1 μm Durapore membrane filter and the vacuum pump was an enhancement upon the initial procedure. Originally the water was filtered through filter paper with the use of gravity, however, this caused significant issues. One issue was that after filtering the material would need to be removed to be put on a SEM stub as the filter paper was too large and couldn't be kept flat to produce a sufficient SEM map. In this transition, it was easy for material to be lost, or the carbon sticky, which the material would be stuck to in the SEM, would obtain strands from the filter paper. This increased the amount of non-projectile material making the analysis of the fragments far more complex. Therefore, it was decided that the vacuum pump and filter membrane was the best method of extracting projectile fragments from the water.

Figure 5.7: Image of filter system used.

5.2.3 Analysis of Fragments

After filtering the water and collecting the projectile fragments, the filter paper was mapped in the SEM. The SEM was set to variable pressure (VP) mode at a pressure of 120 Pa and magnified to x95. This magnification took the map to the maximum number of images possible for a given run, approximately 1040, although only 900 of these images contained projectile fragments as the map shape was a rectangle and the filter paper was circular, meaning that the corners of the map contained no filter paper (See Figure 5.8 for example). The number of images and the minimum size of the fragments posed a significant issue. The process of measuring all the fragments on the filter paper required a computer as it was impractical to perform the task by eye on the console. ImageJ[1] was the perfect software to complete this task.

ImageJ is an image processing and analysis tool in Java. In addition to image processing, it has the capabilities to analyse particles, get the size distribution and many more functions. Before using ImageJ the empty fields of view from the SEM map

[1]Website: https://imagej.nih.gov/ij/

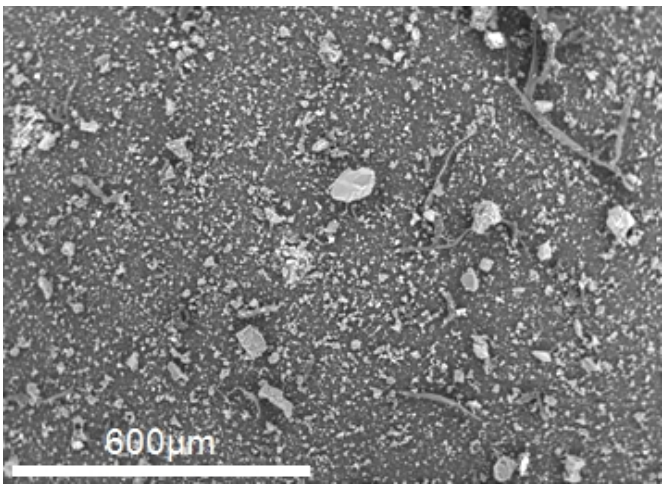

Figure 5.8: Example field of view of filter paper taken from SEM map.

were removed. The remaining images were read into ImageJ. The scale for each image was then set by drawing a line over the image scale bar and stating that the length of the scale bar refers to, for example, 600 μm. ImageJ then sets the pixel size per unit length. Each image was then cropped to remove the scale bar (as this couldn't be in the image when it was processed), their contrast enhanced by 0.4% (as this improved the image for processing) and were then converted into 8-bit images.

The next step involves auto adjusting the image threshold. This is the simplest method of image segmentation, converting a greyscale image into a binary image. ImageJ has 17 different auto threshold methods. A comparison of the three best methods, Renyi Entropy, Yen and Otsu, was conducted in order to determine the most suitable. Table 5.1 shows the statistics for each threshold method. All three methods approximately agree on the maximum sized fragment. The Otsu threshold method appears to measure approximately 100,000 more fragments than the others. Seeing as Yen and Renyi Entropy threshold methods roughly agree on the number of fragments in the shot and many of the other statistics, it seems like either of these two threshold methods would be suitable. Therefore, for this work, the Renyi Entropy method was used.

The final step is selecting the parameters for analysing the projectile fragments in ImageJ. For this analysis a minimum size of 10 μm and a circularity of 0.10 -

Table 5.1: Statistics of the three threshold methods used.

		Size [μm]				
	Total Fragments	Maximum	Minimum	Mean	Median	SD
Otsu	607,825	290.2	10.0	15.9	13.6	7.33
Renyi Entropy	501,709	290.2	10.0	15.3	13.2	6.70
Yen	509,859	290.3	10.0	15.3	13.2	6.75

1.00 was used. The reason for this minimum measured fragment size is that smaller fragments were too numerous at higher impact speeds reducing the reliability of the measurement. This circularity was used as anything with a circularity of less than 0.10 will not typically be projectile material. Figure 5.9 is an image comparing the pre processed image and the result from ImageJ. It appears to suggest a very good agreement between the two.

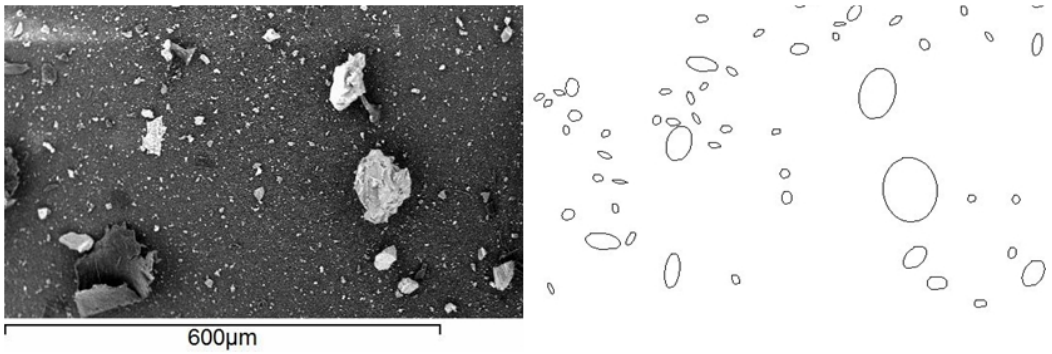

Figure 5.9: Comparison of an SEM image of projectile fragments to the ImageJ fit.

In order to determine whether ImageJ was suitable, two fields of view from the same shot were measured both by the user (by eye) and by ImageJ. Table 5.2 shows the statistics of the fragment diameters determined by both measurement techniques. It shows that ImageJ measures almost three times more fragments than the user. These fragments are of smaller diameter due to the much lower mean and median values for ImageJ. Although the user has the added benefit of being sensitive to far smaller fragments, evident from the minimum fragment size being smaller than 10 μm, ImageJ appears to have a better overall sensitivity to smaller fragments. This being the case it is important to take into account that the results generated from ImageJ have not had a control, compensating for the gun shot residue, removed. However, from just

two images the degree of contaminants from the gun shot is likely to be very low. This is discussed further below.

Table 5.2: Statistics of the two measurement techniques for the measured fragment diameters in micrometers.

		Size [μm]				
	Number	Maximum	Minimum	Mean	Median	Range
Measured by User	144	184.1	8.26	31.0	25.6	175.8
Measured by ImageJ	404	170.3	10.0	17.8	13.9	160.3

Figure 5.10 is a cumulative fragment size distribution of both measurement techniques. At the smaller end of the scale, it is clearly evident that ImageJ performs better at measuring smaller fragments than the user. For the intermediate and larger fragments, ImageJ appears to perform equally to the user. When considering the time taken by the user to accurately measure fragments in the two fields of view and consider that there are around 900, it seems like an inferior measurement technique. Therefore, ImageJ is far more suited to measuring the fragment sizes in each shot.

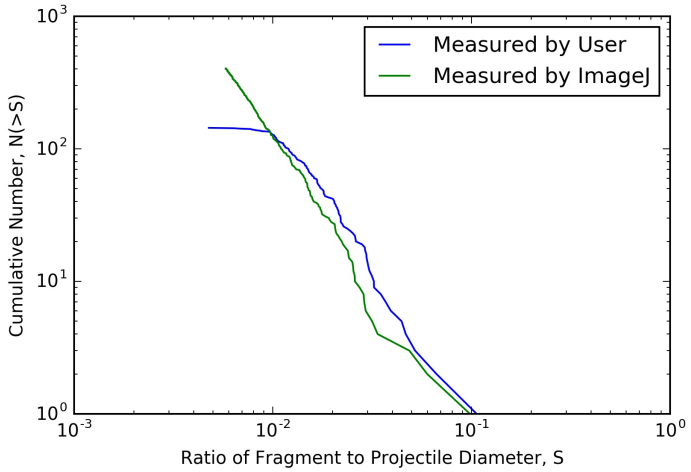

Figure 5.10: Cumulative fragment size distribution plot for two fields of view in the same shot comparing measuring the fragments by the user and by ImageJ.

Finally, to remove from each shot distribution the unwanted items on the filter paper that were not projectile related, a blank control shot was fired into ice. The ice was melted and the water filtered. The size distribution of the gunshot residue

was then obtained using ImageJ. To ensure that no material from the ice was in the final distribution the size distribution of the ice was obtained and subtracted from the control shot. Finally, this distribution was subtracted from each shot distribution in order to limit the amount of contamination in each result. The code written for this task is in Appendix D.1. Generally, the residue size was less than 10 μm and hence didn't contribute to the distributions.

Finding the Mass of the Retained Projectile

In order to determine the mass of each fragment from their two-dimensional images, an assumption had to be made. The two tested assumptions were that the shape of a fragment can be represented either by a sphere or by an ellipsoid. Using the volume of the three-dimensional shape and the density of the material it is possible to determine the mass of the fragment. Doing this for all fragments measured gives the total retained mass of the projectile (Equation 5.1 and 5.2). In Equation 5.1, it is assumed that a sphere is present, whose radius is the average of the two observed radii. In Equation 5.2 is it assumed that object is an ellipse, with the largest axis x, and the intermediate and axes are both given by y, the smaller of the two observed axes.

$$M_{tot} = \sum_{i=1}^{N} \frac{4}{3}\rho\pi \left(\frac{x_i + y_i}{2}\right)^3, \tag{5.1}$$

$$M_{tot} = \sum_{i=1}^{N} \frac{4}{3}\rho\pi x_i \times y_i^2, \tag{5.2}$$

where ρ is the density of the projectile material, x_i is the semi-major axis and y_i is the semi-minor axis.

By using Equation 5.1 the mass of a single fragment is larger than that calculated by Equation 5.2. Although the difference is not large over 400,000 fragments this difference does have a significant effect. Therefore, the assumption that each fragment can be assumed to be a sphere is over estimating the mass of the fragment. Furthermore, the

assumption that the fragment can be represented as an ellipse is more plausible due to an object falling would land with its largest axis horizontal to the plain. Therefore, for this work Equation 5.2 was used.

For materials such as basalt, which is a crystalline rock, the impact may have resulted in the projectile being fragmented into its constituent minerals. If this was the case then the value of the density used would not be most representative and lead to an incorrect mass. Although this was not undertaken due to laboratory restrictions, shots could have been imaged using X-rays to determine the fragments constituents. From here each minerals mass could have be determined with higher precision.

5.3 Results and Discussion

There was a total of 24 shots completed in this work (16 with basalt, 7 with shale and 1 control). Table 5.3 summarises each shot, giving the mass of the projectile, speed of impact, peak shock pressure, mean fragment diameter and the ratio of the mass of the largest fragment to the mass of the projectile.

Figure 5.11 is a plot of the mean fragment diameters shown in Table 5.3. The equation of the fit for the basalt data is:

$$D = (19.5 \pm 0.7)v^{(-0.19\pm0.03)}, \tag{5.3}$$

with an $R^2 = 0.79$, and for shale is:

$$D = (23.3 \pm 1.3)v^{(-0.31\pm0.07)}, \tag{5.4}$$

with an $R^2 = 0.84$, where for both equations v is the impact speed and D is the mean fragment diameter.

It would appear that there is a sharp decrease in the mean fragment diameter for

Table 5.3: Shot and projectile summary. The peak shock pressure was determined using the planar impact approximation (PIA) (Melosh 1989, 2013). Any blank entries for the mean fragment diameter are due to the projectile not fragmenting. The control shot had no projectile, therefore, has no mass and peak shock pressure. The error on the mean fragment diameter is the error on the mean.

Shot Number	Material	Mass [mg]	Speed [km s^{-1}]	Peak Shock Pressure (PIA) [GPa]	Mean Fragment Diameter [μm]	$m_{L,p}/M_p$
S290715#1	Basalt	7.2913	0.51	1.09	-	0.9960
S100615#1	Basalt	8.1406	0.64	1.41	-	0.9964
S240615#1	Basalt	8.7076	0.70	1.57	23.8 ± 0.13	0.1775
S050815#1	Basalt	7.2704	0.84	1.95	18.5 ± 0.05	0.0031
S050315#1	Basalt	11.0215	0.96	2.30	18.0 ± 0.02	0.0086
G261115#1	Basalt	8.8064	1.95	5.80	16.8 ± 0.01	0.0031
G010515#2	Basalt	8.0027	3.04	10.9	15.3 ± 0.01	0.0036
G141015#1	Basalt	7.0080	4.05	16.9	15.6 ± 0.02	0.0014
G101215#1	Basalt	7.6841	4.71	21.4	14.0 ± 0.01	0.0023
G041115#1	Basalt	7.8892	4.92	23.0	15.4 ± 0.02	0.0014
G271114#1	Basalt	7.8091	5.31	26.0	14.2 ± 0.01	0.0011
G211015#2	Basalt	7.7528	6.02	31.9	14.6 ± 0.01	0.0017
G110516#1	Basalt*	5.1432	1.98	5.93	18.0 ± 0.07	0.0108
S270416#1	Basalt**	7.2529	0.59	0.29	-	0.9980
S110316#1	Basalt**	7.4938	0.98	0.50	-	0.2338
G200416#3	Basalt**	7.4240	2.01	1.12	-	0.0318
S280116#1	Shale	7.5177	0.39	0.74	-	0.9982
S030216#1	Shale	7.1062	0.59	1.20	29.5 ± 0.49	0.2909
S181115#1	Shale	7.1359	0.95	2.12	22.7 ± 0.29	0.4133
G130116#2	Shale	7.4033	1.93	5.34	15.5 ± 0.02	0.0383
G041115#1	Shale	6.4649	3.12	10.3	15.5 ± 0.02	0.0126
G031215#2	Shale	7.4867	4.64	19.7	15.5 ± 0.01	0.0058
G211015#2	Shale	8.0830	6.13	30.9	16.0 ± 0.01	0.0022
G250315#1	Control	-	5.36	-	14.6 ± 0.02	-

* Synthetic basalt, ** Basalt cube fired at an angle of 15° into water.

both basalt and shale for the low impact speeds (<1.5 km s^{-1}). The gradient of the trend of the data appears to flatten at speeds higher than this. This could suggest that the mean fragment diameter is becoming constant at higher impact speeds (>2 km s^{-1}). However, the fits to the data suggest that as the impact speed increases the mean fragment diameter decreased but at a significantly slower rate for higher impact speeds.

Table 5.4 gives the shock pressures determined by the PIA and the Autodyn hydrocode simulation for each shot. In Autodyn the peak shock pressures were determined using 250 gauges evenly spaced over the whole volume of the projectile. This allowed

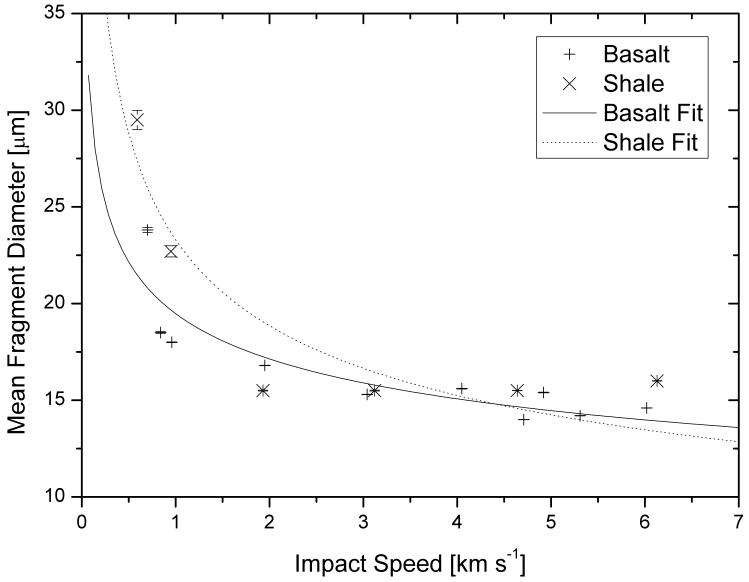

Figure 5.11: Mean fragment diameter versus the impact speed. The errors bars shown are the error on the mean value.

for the peak pressure to not be a single value across the body and permits reasonable identification of both the maximum and minimum pressure in the projectile. In addition, in Table 5.4 we also give the median peak shock pressure in the samples. This provides a complete picture of the shock pressure inside the projectile. From Table 5.4, it can be seen that the peak shock pressure calculated using the PIA lies between the maximum and median values found by Autodyn, and is typically some 50% of the maximum value at low speeds (0.5 km s^{-1}) rising to 75% at intermediate speeds (4 km s^{-1}), and finally back to 60% at 6 km s^{-1}. Hence, it is a reasonable indicator of the peak shock in a finite volume of the sample (and not just at a single point), so we use it as a measure of shock pressure in the rest of the analysis. However, it should be recalled that there are more lightly shocked regions in each impactor.

Figure 5.12 demonstrates how the pressure measured by three gauges (#234 at the front, #9 at the back of the projectile and #111 in the middle of the projectile) changed with time for the 6.02 km s^{-1} simulated basalt impact. Due to being at the front of the

Table 5.4: Comparison of peak shock pressures determined from the planar impact approximation (PIA) (Melosh 1989, 2013) and the AUTODYN-3D models.

Speed [km s^{-1}]	Material	PIA [GPa]	AUTODYN-3D [GPa]		
			Highest	Median	Lowest
0.51	Basalt	1.09	2.14	0.44	0.05
0.64	Basalt	1.41	2.71	0.60	0.05
0.70	Basalt	1.57	3.00	0.68	0.06
0.84	Basalt	1.95	3.63	0.85	0.07
0.96	Basalt	2.30	4.20	1.05	0.07
1.95	Basalt	5.80	8.96	3.07	0.23
3.04	Basalt	10.9	14.6	6.07	0.84
4.05	Basalt	16.9	20.2	9.79	1.34
4.71	Basalt	21.4	24.0	12.1	1.79
4.92	Basalt	23.0	31.0	12.6	1.66
5.31	Basalt	26.0	30.5	13.9	2.07
6.02	Basalt	31.9	48.3	21.5	3.5
0.39	Shale	0.74	1.18	0.28	0.01
0.59	Shale	1.20	1.87	0.47	0.02
0.95	Shale	2.12	3.07	0.93	0.06
1.93	Shale	5.34	6.66	2.78	0.36
3.12	Shale	10.3	11.4	5.72	0.91
4.64	Shale	19.7	33.2	9.88	1.73
6.13	Shale	30.9	53.3	20.6	4.95

projectile Gauge 234 gets destroyed. The shock wave reaches Gauge 111 and 9 later, and then leads to Gauge 111 being destroyed. After an initial compression (increase in pressure) measured by Gauge 9, there is an expansion of the material (represented by a negative pressure). This pattern is repeated for approximately 6 μs. Comparing the peak shock pressures experienced by Gauges 234 and 9 we can determine that the back of the projectile experienced considerably less shock as opposed to the front. It must be noted that these gauges did not record the highest or lowest peak shock pressure in the event. The gauges which measured the highest were positioned just behind the front impacting face.

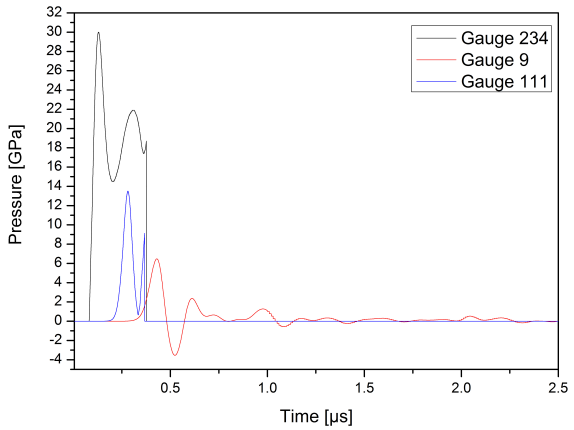

Figure 5.12: Pressure readings for three gauges at the front face (gauge 234), middle (gauge 111) and rear (gauge 9) of the basalt projectile impacting water at 6.02 km s^{-1}.

5.3.1 Morphology of Projectile Fragments

Figure 5.13 shows three typical fields of view in shots at 0.96, 3.04 and 5.31 km s^{-1}. The average size of the fragments in each field of view decreases with increasing impact speed (sizes are given in Table 5.3).

Figure 5.14 and 5.15 show the ratio of the semi-minor (b) to semi-major (a) axis for all fragments measured in each shot for basalt and shale. A ratio of 1 refers to a circular fragment and 0.1 to a bar shaped fragment.

It would appear that at lower speeds, both basalt and shale had a high mean value of b/a. However, for basalt, this rapidly reduced to b/a $\sim$ 0.55 once speeds reached 1 km s^{-1} and then becomes stable. However, for shale, the value of b/a of $\sim$ 0.55 is only reached for impact speeds of approximately 4.5 km s^{-1} and above. This suggests that initially when the projectile has been disrupted the fragments appear to be more spherical on average, but with increasing impact speed/pressure they are more elliptical. This could be an effect of constituent mineral grains. At the slower speeds the projectiles could be mostly break along grain boundaries with the constituent minerals remain mostly intact. However, at the higher impact speeds the minerals are becoming

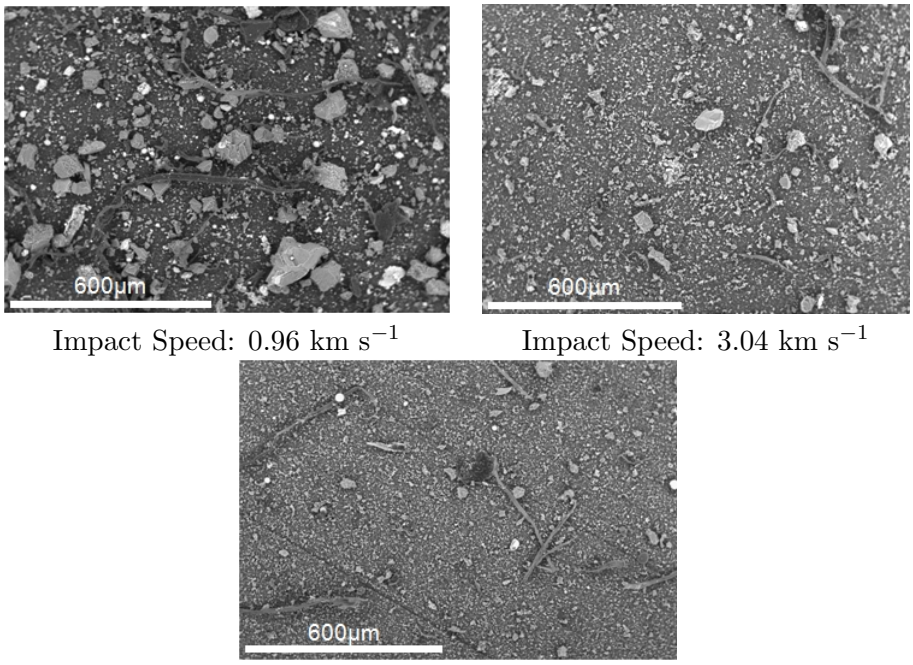

Impact Speed: 0.96 km s^{-1} Impact Speed: 3.04 km s^{-1}

Impact Speed: 5.31 km s^{-1}

Figure 5.13: SEM Images of basalt projectile fragments at 0.96, 3.04 and 5.31 km s^{-1}.

disrupted which is leading to a constant mean b/a value.

Figure 5.16 shows the mean value of each b/a plot and how it changes with impact speed. When excluding the partially disrupted shots (shots < 1 km s^{-1}) the averages are 0.58 ± 0.16, for basalt, and 0.59 ± 0.14 for shale. Therefore both basalt and shale projectiles appear to have similar morphologies upon disruption.

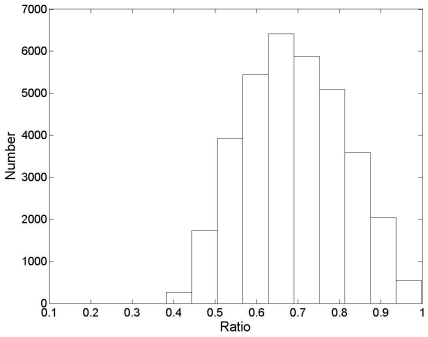

Basalt - b/a at 0.70 km s^{-1}

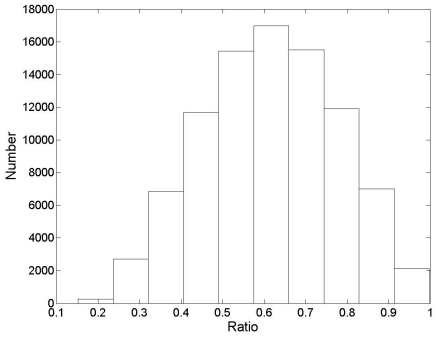

Basalt - b/a at 0.84 km s^{-1}

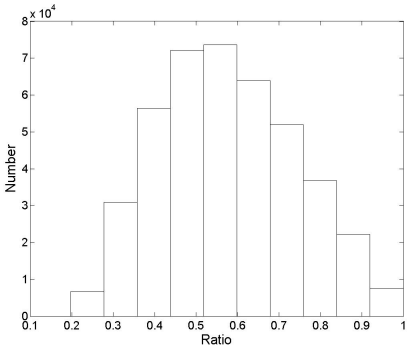

Basalt - b/a at 0.96 km s^{-1}

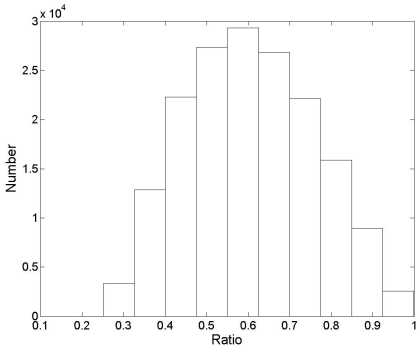

Basalt - b/a at 1.95 km s^{-1}

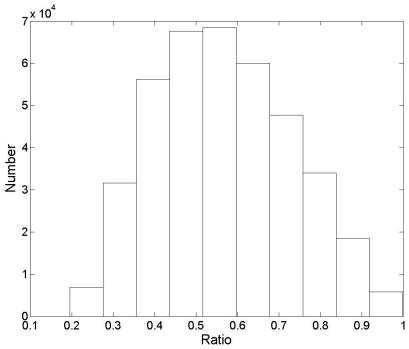

Basalt - b/a at 3.04 km s^{-1}

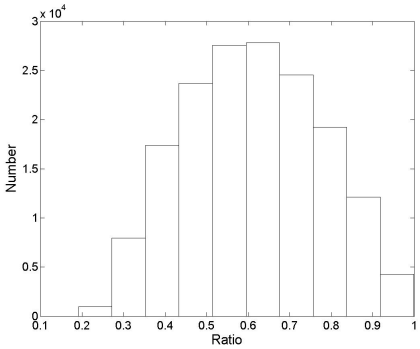

Basalt - b/a at 4.05 km s^{-1}

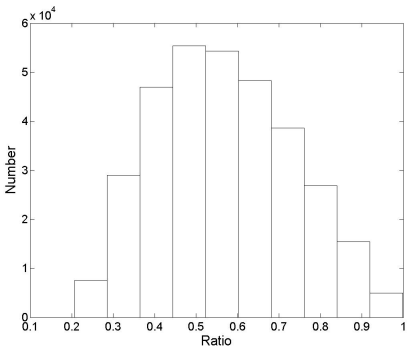

Basalt - b/a at 5.31 km s^{-1}

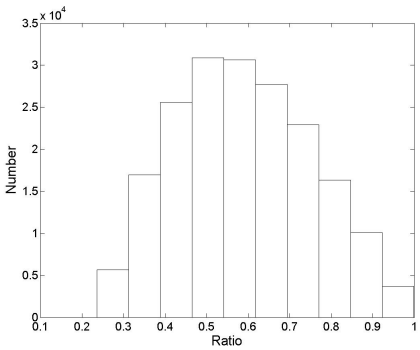

Basalt - b/a at 6.02 km s^{-1}

Figure 5.14: Ratio of the semi-minor to the semi-major axis of the basalt projectile fragments.

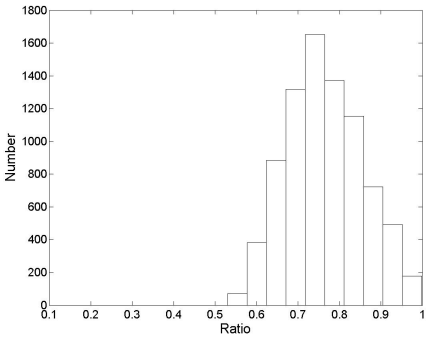

Shale - b/a at 0.59 km s^{-1}

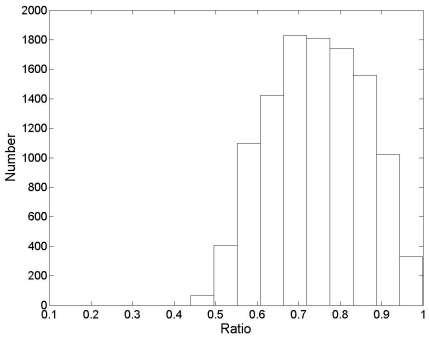

Shale - b/a at 0.95 km s^{-1}

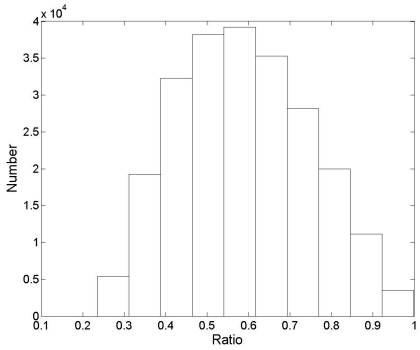

Shale - b/a at 1.93 km s^{-1}

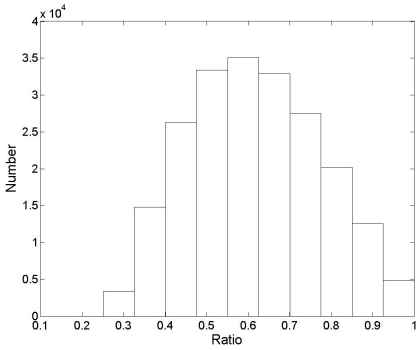

Shale - b/a at 3.12 km s^{-1}

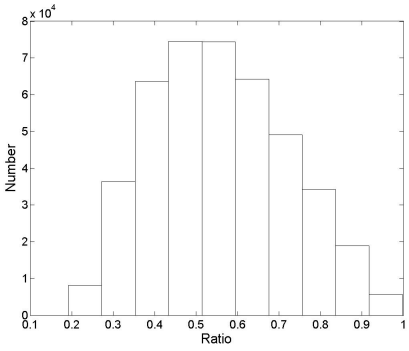

Shale - b/a at 4.64 km s^{-1}

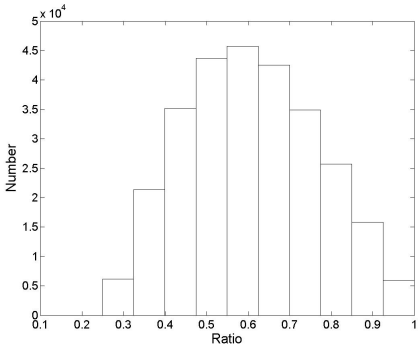

Shale - b/a at 6.13 km s^{-1}

Figure 5.15: Ratio of the semi-minor to the semi-major axis of the shale projectile fragments.

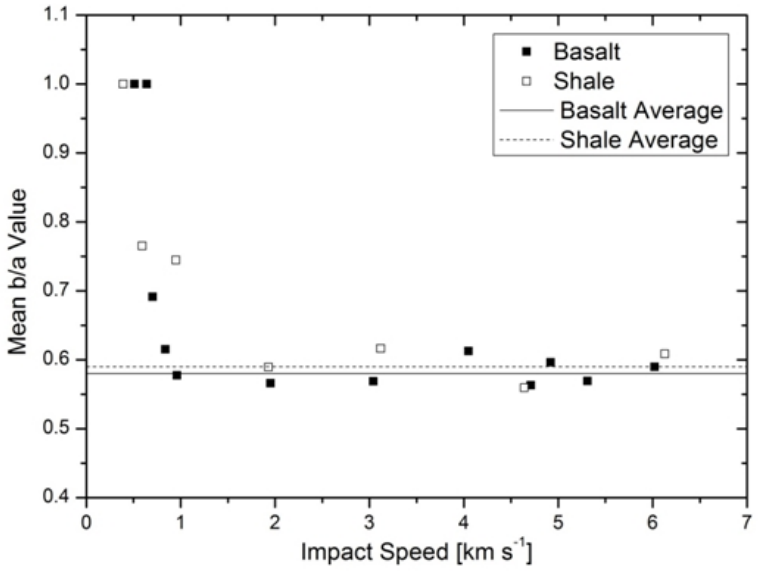

Figure 5.16: Mean b/a values for each shot. The two lines refer to the mean values excluding the slower shots for basalt (black line) and shale (red line).

5.3.2 Cumulative Fragment Size Distribution (CFSD)

Figure 5.18 and 5.19 are cumulative fragment size distributions (CFSD) for each basalt and shale cube shot. Three power laws were fit to each distribution. These were in the form $N(> S) = aS^b$, where N is the number fragments greater than a given size S. Three were fit because one did not accurately fit the whole size distribution, meaning an accurate understanding of what is happening could not be obtained. The three power law ranges refer to the large, intermediate and small sized fragments in each shot defined by the shape of the data as these lines we fit in order to describe the data as accurately as possible. The power b values for basalt and shale are given in Table 5.5.

Figure 5.17 is the 0.96 km s^{-1} plot shown in Figure 5.18 enlarged as an example in order to display the data points in Figure 5.18 and 5.19.

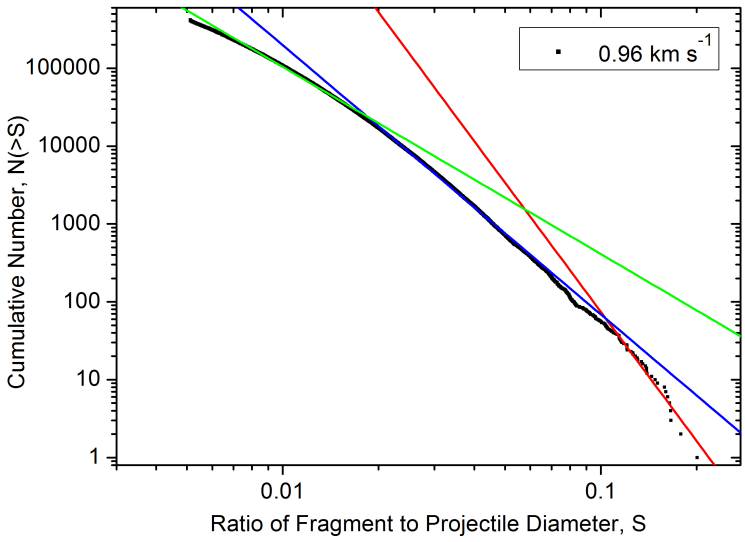

Figure 5.17: Example of 0.96 km s^{-1} plot shown in Figure 5.18 enlarged in order to display the data points more visibly.

Figure 5.20 shows how the power b changes with increasing impact speed. For slower shot speeds (the partial fragmentation domain) it would seem that the gradient of the

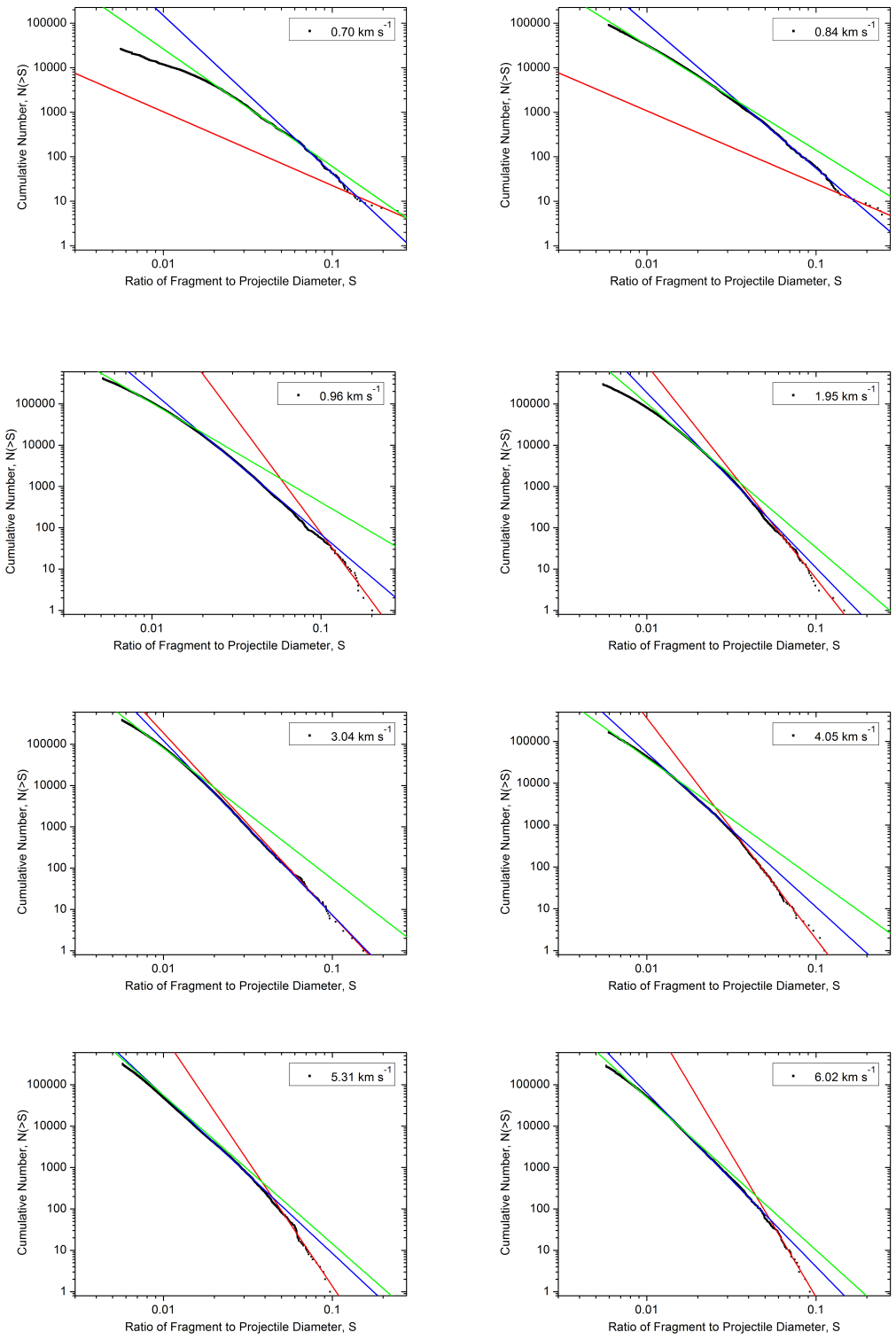

Figure 5.18: Cumulative fragment size distributions (normalised to the original projectile diameter) for each basalt shot. Red curves are fits to the larger sizes, blue to the intermediate sizes, and green to the smaller sizes in each distribution. The black 'line' is composed of data points.

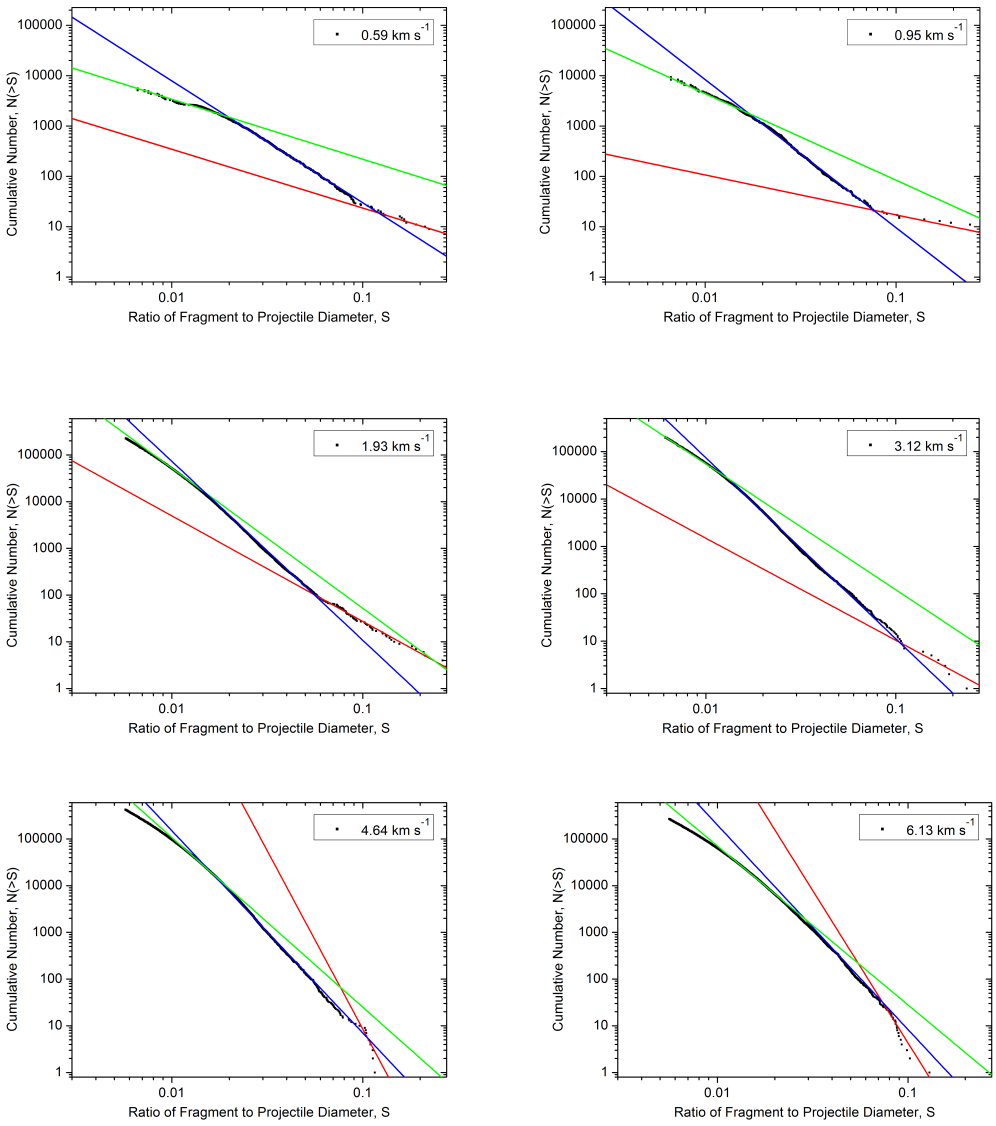

Figure 5.19: Cumulative fragment size distributions (normalised to the original projectile diameter) for each shale shot. Red curves are fits to the larger sizes, blue to the intermediate sizes, and green to the smaller sizes in each distribution. The black 'line' is composed of data points.

large fragments is shallower than the intermediate or small section. This is due to the large fragments in these shots having not been broken up into multiple smaller similarly sized fragments. This results in fewer large fragments but with significant size differences. With increasing impact speed, these larger fragments become more disrupted resulting in a greater number of smaller and similar sized fragments (steeper

Table 5.5: Summary of all fitting values for each power law and size section of the cumulative fragment size distribution. Power law in the form of $N(>S) = aS^b$, where N is the number of fragments greater than a given size S. The R^2 value is also give, the closer this value is to 1 this generally suggests a better fit to the data.

Speed	Small			Intermediate			Large		
[km s^{-1}]	a (x10^{-3})	b	R^2	a (x10^{-3})	b	R^2	a (x10^{-3})	b	R^2
Basalt Cube									
0.51	-	-	-	-	-	-	-	-	-
Error	-	-	-	-	-	-	-	-	-
0.64	-	-	-	-	-	-	-	-	-
Error	-	-	-	-	-	-	-	-	-
0.70	139.6	-2.64	0.9986	12.1	-3.54	0.9911	497.7	-1.66	0.9495
Error	± 2.1	± 0.0045	-	± 1.1	± 0.036	-	± 159	± 0.16	-
0.84	62.8	-2.36	0.9964	31.4	-3.25	0.9960	582.4	-1.63	0.9880
Error	± 3.1	± 0.0011	-	± 0.9	±0.009	-	± 72	± 0.06	-
0.96	1623.6	-2.40	0.9972	24.0	-3.46	0.9982	0.20	-5.51	0.9845
Error	± 1.0	± 0.0010	-	± 0.2	± 0.002	-	± 0.1	± 0.15	-
1.95	10.8	-3.49	0.9995	0.6	-4.24	0.9944	0.04	-5.17	0.9876
Error	± 0.04	± 0.0009	-	± 0.01	± 0.005	-	± 0.01	± 0.12	-
3.04	36.2	-3.17	0.9948	0.4	-4.22	0.9992	0.30	-4.41	0.9833
Error	± 0.1	± 0.0006	-	± 0.03	± 0.002	-	± 0.1	± 0.08	-
4.05	60.3	-2.91	0.9990	2.3	-3.68	0.9998	0.01	-5.28	0.9769
Error	± 0.04	± 0.0011	-	± 0.01	± 0.001	-	± 0.001	± 0.24	-
4.71	21	-3.13	0.9940	0.1	-4.70	0.9979	0.01	-5.02	0.9370
Error	± 0.1	± 0.0011	-	± 0.001	± 0.006	-	± 0.002	± 0.56	-
4.92	2.8	-3.62	0.9984	0.3	-4.18	0.9981	0.02	-5.06	0.9293
Error	± 0.05	± 0.0005	-	± 0.003	± 0.003	-	± 0.03	± 0.48	-
5.31	3.8	-3.58	0.9990	1.3	-3.81	0.9969	0.001	-6.05	0.9923
Error	± 0.001	± 0.0004	-	± 0.02	± 0.004	-	± 0.002	± 0.16	-
6.02	2.1	-3.69	0.9965	0.2	-4.19	0.9973	0.0001	-6.88	0.9891
Error	± 0.001	± 0.0010	-	± 0.01	± 0.007	-	± 0.00006	± 0.22	-
Basalt Sphere									
1.98	1900	-2.41	0.9791	16.7	-3.66	0.9966	0.14	-6.25	0.9351
Error	± 5.8	± 0.0009	-	± 0.2	± 0.003	-	± 0.2	± 0.91	-
Shale									
0.39	-	-	-	-	-	-	-	-	-
Error	-	-	-	-	-	-	-	-	-
0.59	14165.2	-1.19	0.9893	114	-2.42	0.9987	1595.1	-1.17	0.9466
Error	± 149	± 0.0022	-	± 1.6	± 0.004	-	± 275	± 0.10	-
0.95	1612.1	-1.72	0.9897	11	-2.94	0.9881	2772.8	-0.79	0.9216
Error	± 19	± 0.0024	-	± 0.5	± 0.011	-	± 393	± 0.07	-
1.93	52.3	-3.00	0.9992	1.6	-3.83	0.9998	150.5	-2.26	0.9927
Error	± 0.1	± 0.0004	-	± 0.005	± 0.001	-	± 12	± 0.03	-
3.12	269.2	-2.66	0.9973	1.7	-3.82	0.9990	73.5	-2.15	0.9317
Error	± 0.6	± 0.0004	-	± 0.01	± 0.001	-	± 42	± 0.27	-
4.64	5.9	-3.63	0.9992	0.3	-4.33	0.9961	0.0002	-7.63	0.8260
Error	± 0.02	± 0.0008	-	± 0.004	± 0.003	-	± 0.0006	± 1.33	-
6.13	11.2	-3.40	0.9984	0.4	-4.35	0.9987	0.001	-6.53	0.9250
Error	± 0.1	± 0.0010	-	± 0.01	± 0.007	-	± 0.002	± 0.71	-

slope).

Overall, each size section appears to get steeper (larger b) with increasing impact speed. This is due to the increasing shock pressure breaking larger fragments into multiple similar sized fragments. Hence, at the highest impact speeds (greatest shock pressure) there are fewer larger fragments. It must be noted that there are some

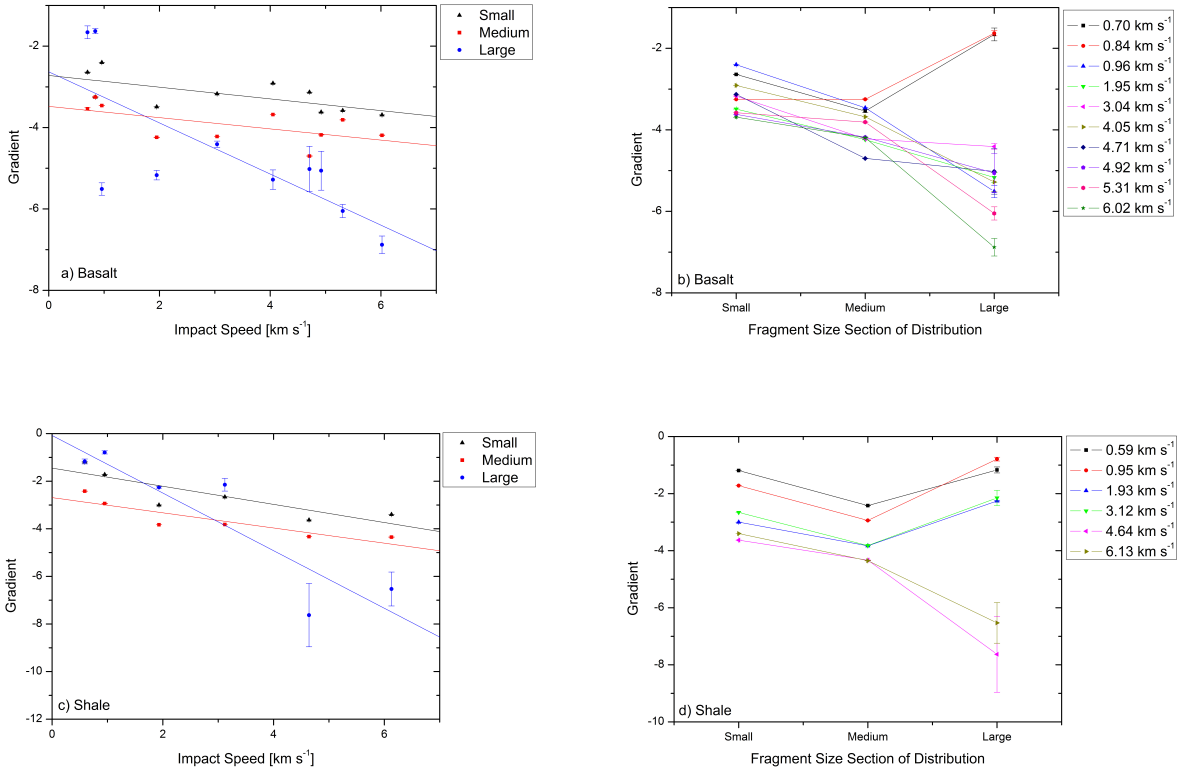

Figure 5.20: The gradients of the cumulative fragment size distribution versus (a) impact speed and (b) by size regime for basalt, and similarly (c) and (d) are for shale. The fit lines in (a) are $-0.144x^{-2.72}$, $-0.138x^{-3.48}$ and $-0.628x^{-2.63}$ for the small, medium and large fits respectively. In (c) the fits are $-0.381x^{-1.45}$, $-0.319x^{-2.69}$ and $-1.21x^{-0.08}$ for the small, medium and large fits respectively. The 'x' in these refer to a variable which is impact speed.

fluctuations in trend in Figure 5.20. This could be explained by possible fragments being lost during collection. For the smaller sizes (largest number of fragments) we expect a fairly complete collection of fragments. However, at the largest sizes where the number of fragments is small, should a fragment be lost it could easily bias the results slightly. The possibility that additional fragmentation could have occurred for samples that have a pre-existing weakness was considered. For this to occur the sample would have to survive being filed into a cube without breaking and survive acceleration during the shot. Samples did break during production and others during acceleration. An oscilloscope is used post impact to analyse the projectile as it proceeds to the

target chamber. All results were drawn from shots where the projectile was whole at this point. Therefore, it is assumed that fragmentation was solely as a result of the impact. In Figure 5.20b and 5.20d it can be seen that at largest sizes there is a sudden jump in gradient at a given speed ($\sim$1 km s^{-1} for basalt, $\sim$3 km s^{-1} for shale). This seems related to both moving well above the disruption limit and the change in mean b/a value (Figure 5.14 and 5.15).

Higher Magnification

Figure 5.21 is a CFSD plot for fragments from the 1.95 km s^{-1} shot of basalt but with a higher magnification allowing for fragments as small as 1 μm to be measured. In order to perform this, the filter paper was mapped in four quarters. The plot is fit with three power laws in the same form as in Figure 5.18 and 5.19.

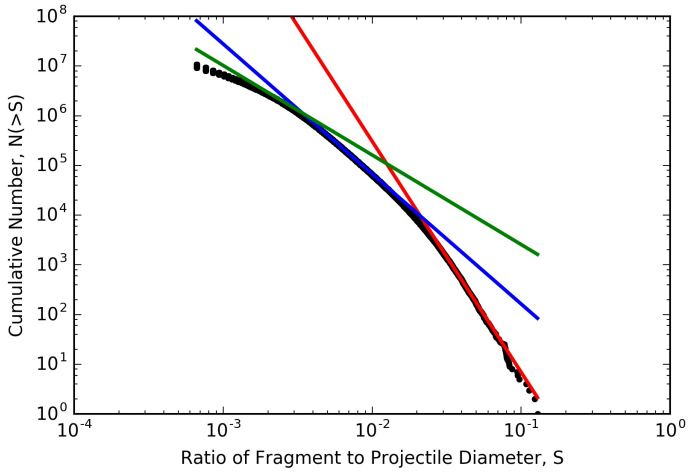

Figure 5.21: Cumulative fragment size distribution of fragments for a basalt projectile shot at 1.95 km s^{-1}. Derived from images take at a magnification of $\times$200. The black points are the data of the ratio of the fragment to projectile diameter. The coloured lines represent three different fits: red - large fragments, blue - intermediate fragments and green - small fragments.

Increasing the magnification to $\times$200, allowing the smallest fragment size to be measured to be 1 μm, led to 5,611,029 fragments being measured. When compared to the number of fragments from the same shot when imaged and analysed at $\times$95

magnification (302,871 fragments) this is a major increase.

Table 5.6 displays the comparison between the power law gradients b for the 1.95 km s^{-1} shot for basalt for the ×95 and ×200 magnification.

Table 5.6: Summary of all fitting values for each power law and size section of the cumulative fragment size distribution. Power law in the form of $N(>S) = aS^b$, where N is the number of fragments greater than a given size S.

	Small	Intermediate	Large
b x95 Magnification	-3.49	-4.24	-5.17
b x200 Magnification	-1.80	-2.62	-4.65

It appears that the increased number of smaller fragments has considerably changed the gradient of the small section. A similar effect can be seen in the intermediate sized fragments. Both the small and intermediate size sections have become shallower for the ×200 magnification, due to the more complete fragment size distribution. Whereas, for the large sized fragments, the gradients have remained similar, which was expected as there were no new fragments in this size range.

Large Fragments

Figure 5.22 displays the behaviour of fragments at the very largest sizes. These fragments are heavily dependent on impact speed. For slower speeds, the fragments produce a concave shape. At intermediate speeds (approximately 3 km s^{-1}) they flatten out. Finally, for higher speeds, they produce a convex shape. This behaviour is seen in the largest fragments of disrupted targets (Durda et al. 2007, Leliwa-Kopystynski et al. 2009) and is related to the object transitioning from a partially disrupted to a catastrophically disrupted regime. As the energy density increases, the larger fragments (which appear in the slower speed impacts) are replaced by multiple smaller fragments.

It would appear that both basalt and shale show the same effect at similar speeds, however, for shale, it appears as though the distribution for 4.64 km s^{-1} is still transitioning between a flat line and a convex line.

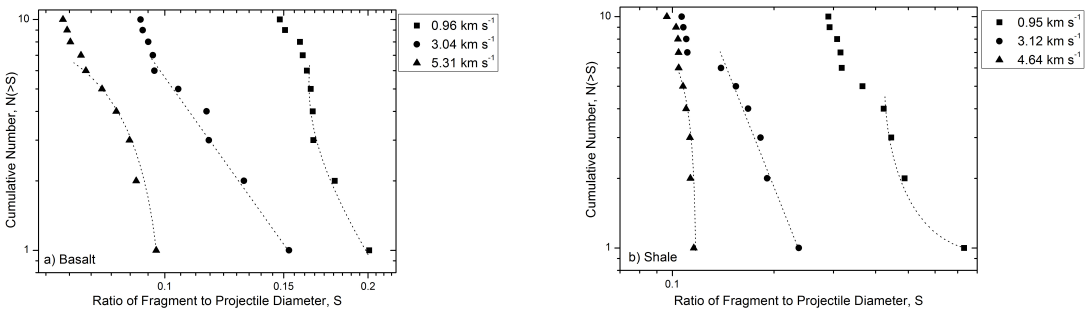

Figure 5.22: Cumulative fragment size distribution for the 10 largest fragments for basalt (a) and shale (b) at three impact speeds.

5.3.3 Retained Projectile Percentage

We assumed that each fragment's shape is approximately equal to that of an ellipsoid with a semi-major (a) and -minor (b) axis, and take the density of the projectile material. By doing this, the mass of each fragment can be determined. Summing these values for every measured fragment gives the total retained mass of the projectile (Equation 5.2) assuming complete effective scanning etc. By comparing this with the mass of the projectile pre-impact it is possible to determine the percentage retained which gives an approximation of the percentage of the projectile surviving impact.

In Figure 5.23 we show the surviving mass percentage against peak shock pressure for each shot. For basalt there appears to be a good power law fit, giving the equation:

$$Percentage = (115 \pm 11)P^{(-0.49\pm0.05)}, \tag{5.5}$$

where $Percentage$ is the percentage retained and P is the peak shock pressure in GPa. The goodness of fit for this is $R^2 = 0.9449$.

The same power law fit for the shale data gives:

$$Percentage = (100 \pm 9)P^{(-0.33\pm0.07)}, \tag{5.6}$$

with a correlation coefficient of $R^2 = 0.8444$.

Shale thus appears to have a higher surviving mass percentage at the higher shock pressures. It was considered whether this was an artefact of Equation 5.2, whereby the third axis of each fragment (the depth) is not measured but assumed to be equal to the semi-minor axis. The third axis could be smaller than the semi-minor axis due to shale being layered. However, upon further investigation of the fields of view the fragments of shale do not appear to be particularly flat 'plate' shaped compared to the basalt. This was determined as it was possible to make out textures due to the different shades around the edges of the fragments.

Looking closer at Figure 5.18 and 5.19 at a given impact speed it would seem that the largest fragment of shale is larger than the largest fragments in the equivalent basalt shot. Seeing that most of the mass is in the large fragments, this may explain why shale gives more complete mass recovery than basalt.

A mechanism to explain the mass loss in a shot includes the mass present in fragments of a size below the experimental limit. Another mechanism is the removal of projectile fragments from the impact site mixed with target material ejected at high speed. The mixing of projectile material with target ejecta has been shown by Burchell et al. (2012) for example.

Basalt is a good analogue of basaltic impacting material (for example from Mars, the Moon or HED meteorites) in the solar system. Therefore, the equation of the line of best fit (Equation 5.5) on Figure 5.23 can be used to determine an estimation of the impact survival percentage of basaltic impactors in different solar system impact scenarios. In Table 5.7 we use the average impact speed at different solar system bodies, obtained from references given in Table 5.7, and the planar impact approximation with the appropriate material values to determine the peak shock pressure from the impact. The impactors are taken as basalt and the target bodies are either regolith (sand), water ice or basalt for the Moon, Pluto and both Mars and Asteroid belt respectively. The appropriate C, S and density values for the target materials are 1.70 km s^{-1}, 1.31

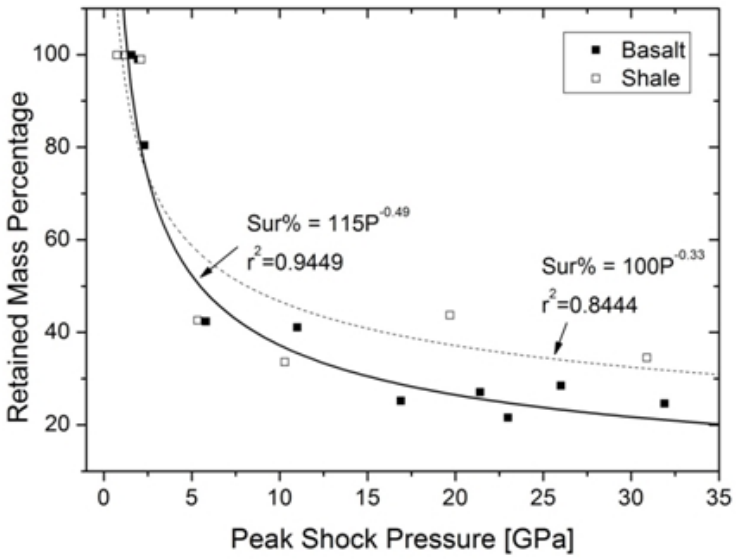

Figure 5.23: Retained projectile percentage against peak shock pressures determined using the PIA. Error bars are not shown on these data due to their size being too small.

and 1600 kg m^{-3}, 1.32 km s^{-1}, 1.53 and 915 kg m^{-3} and 2.60 km s^{-1}, 1.62 and 2860 kg m^{-3} for regolith (dry sand), water ice and basalt respectively (Melosh 2013). From these, we can deduce the approximate surviving percentage of the impactor.

Table 5.7: Approximation of impactor survival in different solar system impact scenarios. The peak shock pressure was determined using the PIA and the percentage survival was ascertained from the equation of the trend line on Figure 5.23. The reference is for the average impact speeds for all but Burchell et al. (2014a) which refers to the impact speeds on the moon by ejecta from impacts on the Earth.

Body	Speed [km s^{-1}]	Shock Pressure [GPa]	Percentage Survival	Reference for impact speed
Pluto	1.9	2.3	76 ± 11	Zahnle et al. (2003)
The Moon	2.3	8.9	39 ± 8	Burchell et al. (2014a)
Mean collision Speed in the Asteroid Belt	5.0	47.5	17 ± 5	Bottke et al. (1994)
Mars	9.3	134.8	10 ± 4	Steel (1998)

These predicted values provide only a very rough guide owing to the neglect of parameters such as: scaling to different projectile sizes, porosity in both projectile and target etc. However, they do suggest that Pluto and the Moon should have large amounts of impactor remnants on their surface or sub-surface beneath impact craters. Furthermore, although it is a slight extrapolation from the data, this work suggests that

17 ± 5% of an asteroid collision should survive. Additionally, this suggests that 10 ± 4% of the impactor could survive an impact on Mars, although again, this is a major extrapolation beyond the shock pressure regime in which the data were taken here. We note however that the curve in Figure 5.23 is not varying greatly with shock pressure at higher pressures so this is likely a reasonable estimate as an order of magnitude. These estimates also assume there is no impactor size-dependent effect which occurs between the laboratory size experiments and any other size of impactor. Despite this, this work does have direct relevance for small meteorites and micrometeorites impacting these bodies.

5.3.4 Onset of Projectile Disruption

The energy density is the energy per unit mass of an object. During a shot, the energy is determined by the kinetic energy. The projectile energy density is, therefore, energy per unit mass of the projectile and is given by (Schultz & Gault 1990*b*, Nagaoka et al. 2014):

$$Q_p(\theta) = \frac{0.5 M_p v_i^2 sin^2\theta}{M_p} = 0.5 v_i^2 sin^2\theta, \tag{5.7}$$

where M_p is the mass of the projectile, v_i is the velocity of impact and θ is the angle of impact where for normal incident impacts this is $sin^2\theta = 1$. The vertical component of the impact velocity is used as this is found to couple into the target for crater formation, the remaining energy is transferred as kinetic energy to ejecta or ricochet fragments at very low angles. It is assumed that energy lost in fragmentation greatly exceeds other internal energy losses, such as deformation. The fragmentation limit, Q_p^*, is defined as the minimum specific energy required to disrupt the projectile so that the largest fragment contains 50% of the original projectile's mass (i.e. $m_{L,p}/M_p = 0.5$).

Figure 5.24 is a plot of the $m_{L,p}/M_p$ against the projectile energy density, Q_p^*, for all basalt and shale cube shots at angles of normal incidence. In order to describe the basalt data, two power laws are fitted. By contrast, the shale has only one trend in

behaviour.

The equations for these power law fits are, for shale:

$$\frac{m_L}{m_p} = (1.05 \pm 7.39) \times 10^5 Q_p^{-1.07 \pm 0.62}, \tag{5.8}$$

and for basalt where $Q_p < 10^6$ J kg^{-1}:

$$\frac{m_L}{m_p} = (4.58 \pm 1438) \times 10^{22} Q_p^{-4.27 \pm 2.56}, \tag{5.9}$$

and where $Q_p > 10^6$ J kg^{-1}:

$$\frac{m_L}{m_p} = 2.50 \pm 7.04 Q_p^{-0.46 \pm 0.18}, \tag{5.10}$$

where Q_p is in J kg^{-1}. The uncertainties on these fits are largely due to the low number of data points. This resulted in the fitting software not being able to converge leading to very large uncertainties. Therefore these were not used to determine the uncertainties on any derived value as the results were non-physical. The error on the derived value of the catastrophic disruption energy density threshold (Q_p^*) are determined by saying that this value lies between the values above and below the threshold at $\frac{m_L}{m_p} = 0.5$. From Equation 5.8 and 5.9 the catastrophic disruption energy density thresholds are $(9.4 \pm 5.0) \times 10^4$ J Kg^{-1} and $(24.0 \pm 2.1) \times 10^4$ J Kg^{-1} for shale and basalt respectively. This is a factor of three difference between the two materials.

Schultz & Gault (1990*b*) suggest that the energy partitioned into projectile fragmentation, ΔE_{PF}, can be split into the energy partitioned into fragmentation after impact, ΔE_F, and the energy used getting to the fragmentation limit, ΔE_o, shown in Equation 5.11:

$$\left(\frac{\Delta E_{PF}}{m_p}\right) = \left(\frac{\Delta E_F}{m_p}\right) + \left(\frac{\Delta E_0}{m_p}\right). \tag{5.11}$$

Equation 5.11 can be rewritten by introducing the largest fragment mass, m_L, by

multiplying each term in Equation 5.11 and rearranging the terms by dividing by ΔE_{PF}:

$$\left(\frac{m_L}{m_p}\right) = \left(\frac{m_L}{m_p}\right)_{CD} \left(\frac{\Delta E_F}{\Delta E_{PF}}\right) + \left(\frac{m_L}{m_p}\right)_{PD} \left(\frac{\Delta E_0}{\Delta E_{PF}}\right), \tag{5.12}$$

$$\left(\frac{m_L}{m_p}\right) = a\left(\frac{\Delta E_F}{\Delta E_{PF}}\right)_{CD} + b\left(\frac{\Delta E_0}{\Delta E_{PF}}\right)_{PD}, \tag{5.13}$$

where a and b represent fractions of the original projectile mass that define partial and catastrophic disruption respectively (Schultz & Gault 1990*b*). The first term can be shown to be equivalent to the projectile strength, S (given by the tensile strength of the material) divided by the peak vertical stress, σ_θ, or equivalently when catastrophic disruption dominates failure (Schultz & Gault 1990*b*). This is given by:

$$\frac{m_L}{m_p} \sim \left(\frac{\sigma_\theta}{S}\right)^{-1} \sim \left(\frac{\rho_p Q}{S}\right)^{-1} \sim \left[Q\left(\frac{c_t \rho_t}{c_p \rho_p}\right) sin^2\theta \left(\frac{S}{\rho}\dot{\epsilon}^{0.25}\right)^{-1}\right]^{-1} = [Q_c(\theta)]^{-1}, \tag{5.14}$$

where $\dot{\epsilon}$ is the strain rate, c refers to the speed of sound and ρ to the density. When partial disruption occurs, the second term in Equation 5.13 dominates. Schultz & Gault (1990*b*) went on to demonstrate that:

$$\frac{m_L}{m_p} \sim \left[Qsin^6\theta \left(\frac{S}{\rho}\dot{\epsilon}^{0.25}\right)\right]^{-1} = [Q_o(\theta)]^{-1}. \tag{5.15}$$

Finally, Schultz & Gault (1990*b*) went on to combine these equations giving:

$$\frac{m_L}{m_p} = \left[\frac{a}{Q_c(\theta)} + \frac{b}{Q_o(\theta)}\right], \tag{5.16}$$

where Q_c is the energy density when catastrophic disruption dominates failure, Q_o is the energy density when partial disruption occurs and the values of a and b can be derived empirically. For the data in this work, a and b are not derived. However, Schultz & Gault (1990*b*) do derive a and b for their data.

Figure 5.25 shows results from four separate studies; Schultz & Gault (1990*b*), Nagaoka et al. (2014), Avdellidou et al. (2016) (which all used basalt projectiles) and the

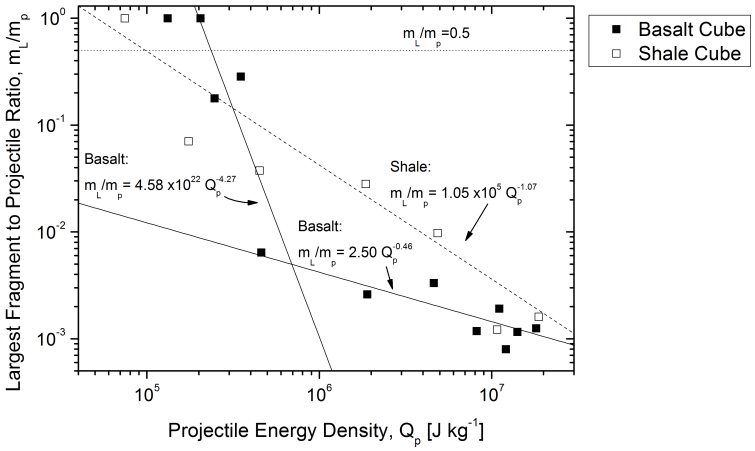

Figure 5.24: Mass ratio of largest surviving fragment of projectile versus the projectile energy density, Q_p. The horizontal dotted line refers to the catastrophic disruption threshold, $m_{L,p}/M_p$=0.5. The dashed and the solid lines are the fits to the shale and basalt respectively. The fits were fitted in log-log space.

results for basalt projectiles in this work. It also includes the data for the synthetic basalt sphere and non-normal incident impact from Table 5.3. As stated before, Schultz & Gault (1990*b*) fired basalt projectiles at inclination angles between 7.5 and 15° onto sand and one shot onto water, Nagaoka et al. (2014) fired basalt cylinders (5 mm in diameter and 5 mm in length) into sand and Avdellidou et al. (2016) fired synthetic basalt spheres (diameter 2.0 2.4 mm) into ice.

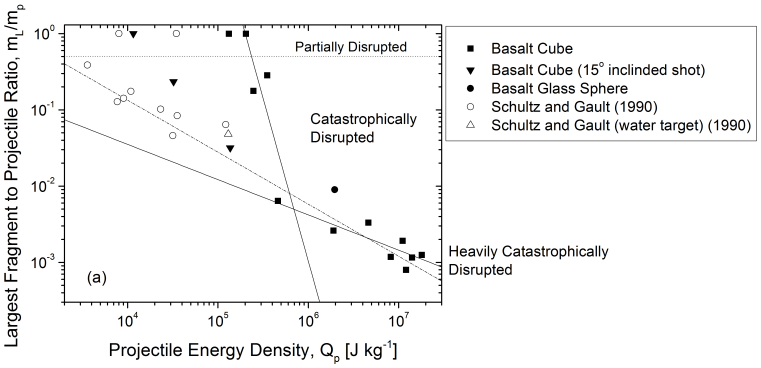

Schultz & Gault (1990*b*)

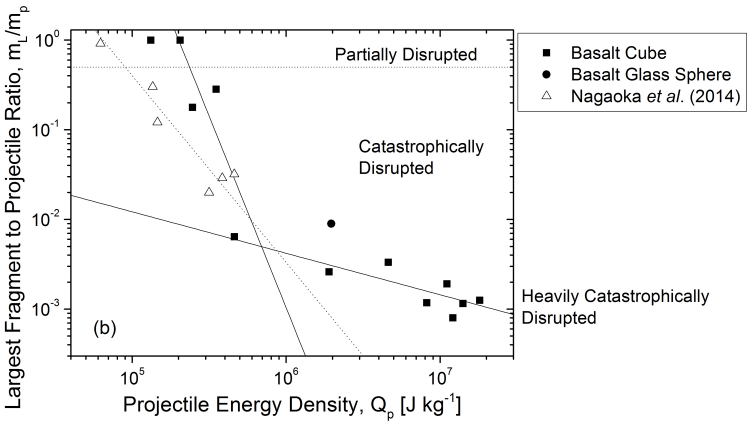

Nagaoka et al. (2014)

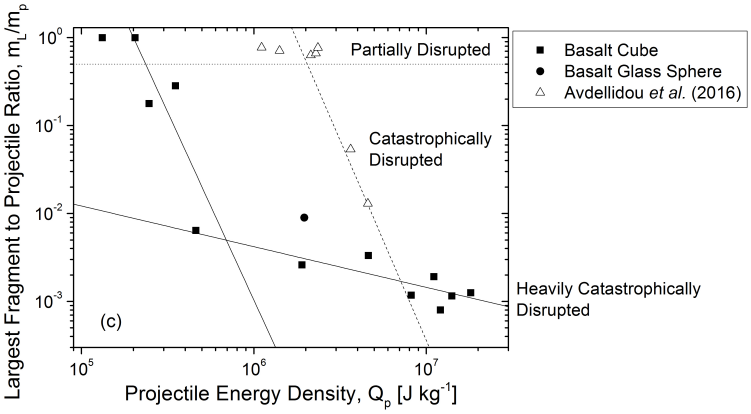

Avdellidou et al. (2016)

Figure 5.25: Mass ratio of largest surviving fragment of projectile versus the projectile energy density, Q_p, for all the basalt impacts listed in Table 5.3, compared to data from (a) Schultz & Gault (1990*b*), (b) Nagaoka et al. (2014) and (c) Avdellidou et al. (2016). The horizontal dotted line refers to the catastrophic disruption threshold, $m_{L,p}/M_p$=0.5. All other lines are lines of fit for each dataset.

The data in Figure 5.25a follows two trends Trend 1 (basalt impacts at normal incidence from this work) and Trend 2 (shots at non-normal incident: this work and work from Schultz & Gault (1990*b*) involving basalt onto sand at 7.5°). Trend 1 has almost intact projectiles recovered after the impact, until $Q \sim 10^5$ J kg^{-1}. The surviving fraction then falls off rapidly between 10^5 and 5 $\times 10^5$ J kg^{-1} as disruption occurs. Above 5 $\times 10^5$ J kg^{-1}, the projectile is fully disrupted and the gradient of the slope decreases (Trend 2).

The shots completed by Schultz & Gault (1990*b*) that were into sand were all fired at an angle of 7.5°, this means that the projectile energy density is considerably lower than that in this work, i.e. Q_p is lower due to the $\sin^2\theta$ term in Equation 5.7. Schultz & Gault (1990*b*) show that the projectile usually fragments at a much lower Q_p value than in our work at normal incidence; this is due to the shallow impact angle. The implication is that, although the non-normal incidence at a given impact speed should, according to Equation 5.7, reduce the energy density in the projectile, in fact, it is leading to disruption at a significantly lower Q_p value. It could be that in shallow angle impacts, shear effects are important (i.e. so called "impact decapitation", Schultz and Gault 1990*a*), i.e. there has been a transition to a differing physical cause of disruption of the projectile. The non-vertical component of the energy density is transferred into kinetic energy of the ejecta or the ricochet of the projectile when fired at low angles.

In Figure 5.25b we compare the work in this chapter to that of Nagaoka et al. (2014). The data could (mostly) be taken as from a single data set with the same trend versus Q_p. Whereby an initial steep fall in $m_{L,p}/M_p$ until $Q_p \sim 10^6$ J kg^{-1} (or $m_{L,p}/M_p \sim 0.01$), and then a shallower dependence on Q_p emerges. This suggests that there is no significant difference between impacts on sand (porosity 45%) and water. Target porosity is known to play a part in the impact cratering process (see Love and Ahrens 1996), but it does not appear to have significantly influenced projectile disruption here.

Finally, in Figure 5.25c we compare the results in this chapter to those of Avdellidou et al. (2016) who used the same light gas gun facility as used here, and similarly-sized

projectiles of basalt, but fired onto solid ice target (porosity < 10%). Here the choice of target has clearly influenced the outcome of the event. Catastrophic disruption on ice occurs at an increased Q_p^* (by a factor of 10). We shot a basalt sphere into our water target at a similar speed to Avdellidou et al. (2016) to see if the shape of the projectile was significant (Avdellidou et al. (2016) used spheres rather than cubes as used here). The result was close to that expected based on our data derived from cube shaped projectiles rather than that for the basalt spheres in Avdellidou et al. (2016). It therefore, appears projectile shape is not the issue.

Table 5.8: Summary of the projectile energy density at catastrophic disruption and the corresponding impact speed for shale and basalt from this work and basalt from Nagaoka et al. (2014) and Avdellidou et al. (2016).

Impactor	Q_p^* [J kg^{-1}]	Impact Speed [m s^{-1}]	Peak Shock Pressure (PIA) [GPa]	Reference
Shale	(9.4 ± 5.0) ×10^4	434 ± 120	0.84 ± 0.33	This work
Basalt	(24.0 ± 2.1) ×10^4	693 ± 30	1.55 ± 0.10	This work
Basalt	(9.0 ± 1.9) ×10^4	424 ± 45	1.00 ± 0.13	Nagaoka et al. (2014)
Basalt	2.31 ×10^6	2149	1.32	Avdellidou et al. (2016)

Finally, the peak shock pressure at the catastrophic disruption threshold, Q_p^*, is calculated for Nagaoka et al. (2014), Avdellidou et al. (2016) and this work. From Table 5.8 we take the Q_p^* values for basalt of (24.0 ± 2.1) ×10^4 J kg^{-1}, (9.0 ± 1.9) ×10^4 J kg^{-1} and 2.31 ×10^6 J kg^{-1} from this work, Nagaoka et al. (2014) and Avdellidou et al. (2016) respectively. From Equation 5.7 it can be deduced that the impact velocities are: 693 ± 30 m s^{-1}, 424 ± 45 m s^{-1} and 2149 m s^{-1}. Using the PIA with the appropriate target values for C, S and density taken from Melosh (2013), these impact speeds correspond to peak shock pressures of 1.55 ± 0.10 GPa (this work) and 1.00 ± 0.13 GPa (Nagaoka's work). Avdellidou et al. (2016) have estimated the peak shock pressure in their impacts using Autodyn as 1.32 GPa at 2149 m s^{-1}. We, therefore, find that disruption occurs at 1.55 ± 0.10, 1.00 ± 0.13 and 1.32 GPa, very similar values in all three experiments on a variety of target types. The yield strength of basalt rocks is very variable and sample specific due to each samples having different vesicles and

pre-existing fractures/weaknesses. However, the yield strength of basalt (at low strain rate) is approximately 250 MPa (Schultz 1993). Therefore the peak shock pressure at the catastrophic disruption threshold for these three works is approximately 4 to 5 times that of the compressive yield strength (at low strain rates) of basalt. For shale, however, we find the peak shock pressure at Q_p^* is some fourteen times the yield strength.

5.3.5 Solar System Implications

This work is particularly relevant to dust and small rocky impacts onto airless bodies. It can be used to describe the percentage survival of an impactor and the possible size distribution of the fragments. For example, the impact of a basalt-like small projectile on to a basalt-like airless body at the average impact speed in the asteroid belt (5 km s^{-1}) and at the most probable impact angle (45°) would experience a peak shock pressure of 28 GPa. This work would suggest that (22 ± 2)% of the impactor would survive. It would then be possible to match the cumulative fragment size distribution in this work which was produced by an impact nearest to the peak shock pressure of 28 GPa to estimate the fragment size distribution. This would be useful for topics such as mass exchange for small impacts and the mixing which has been observed on the surface of asteroids, such as the NEA 2008 TC3 (Jenniskens & et al. 2009, Bischoff et al. 2010).

For this work to be scaled up and compared to kilometre sized impactors, the effect of size need to be considered. The ratio of grain to projectile size in this experiment is greater than for kilometre sized impactors in the solar system. Looking at the strength regime in Figure 1.10, as the size of the target increases the Q_D^* decreases. This would suggest that the grain-projectile size ratio is having an effect on the fragmentation. This means that Q_p^* for kilometre sized impactor would be less than a millimetre sized impactor. However looking at Figure 1.10, the change in the Q_D^* from a millimetre

size to a metre size impactor (three orders of magnitude), reduces the Q^*_D by a factor of around five. We can expect that Q^*_p may fall by this amount as we extrapolate. This is actually less than the difference in predictions by different authors of Q^*_D at a single size. Therefore, the size ratio of the largest fragment to projectile for a solar system sized impact could be slightly lower than in this experiment. Furthermore, by adjusting this work from speeds to similar pressure ranges there is a reduction of some difficulties in scaling. Nonetheless, caution is needed in the interpretation of this work when scaling to larger impactors.

This work can be used to determine possible information regarding impacts of real bodies in the Solar System. For example, if impactor fragments were identified, and the mean b/a ratio obtained for the fragments, a crude indication of impact speed can be obtained. That is to say, a high value of the mean (b/a = 0.6 – 0.7) would indicate a lower speed impact (< 1 km s^{-1}) had occurred. Whereas, a lower mean value (b/a = $\sim$0.5 – 0.6) would suggest a higher impact speed. As suggested by, amongst others, Durda et al. (2007), and Leliwa-Kopystynski et al. (2009), if the largest fragments are observed in an asteroid family, the impact event can be labelled catastrophic or above by the convex or concave nature of the shape of the large fragments in the CFSD. Applying the same logic to projectile fragment size distribution again can indicate limits on the likely impact speeds.

The surface of the asteroid Vesta has dark material believed to be exogenous carbonaceous chondrite fragments (Reddy et al. 2012, Palomba et al. 2014). Reddy et al. (2012) state that the Veneneia crater (diameter 395 km), which is the second largest on the surface of Vesta, could have formed as the result of a 30 km diameter projectile impacting at 4.75 km s^{-1}, or a 50 km diameter projectile impacting at 2 km s^{-1}. The largest crater on Vesta, Rheasilvia (diameter 505 km), is postulated to have formed from either a 5.5 km s^{-1} impact from either a 37 km impacting at 90°, or a far larger diameter sized projectile impacting at the more probable angle of 45° (Ivanov & Melosh 2013).

Using the data from this work and this information, it is possible to make some predictions regarding the amount of impactor surviving an impact, the size of the largest fragment, the size of a typical fragment and the size of the modal fragment, see Table 5.9. In relation to this situation, although basalt is more analogous to an achondrite (or HED, basalt-like impactor) and not a chondrite (like the impactors on Vesta), basalt is used to determine this information. Daly & Schultz (2016) used basalt as a material to look into the delivery of projectile material to the Vestan regolith. Daly & Schultz (2016) states that carbonaceous chondrite-like impactors are likely less competent and more porous than the basalt projectiles used in their experiments. However, the retention of carbonaceous chondrite impactors is likely to be similar to what is observed for basalt projectiles. Daly & Schultz (2016) argues that projectiles of both types will fail in a brittle manner and that fragment sizes in both cases will be influenced by the critical flaw size of the material.

As basalt is not an analogous material to a carbonaceous chondrite it is not perfectly suited for the DM on Vesta in this work, however, this is valid for an achondrite/basalt-like impact and it has been used as a comparison material in past work (Daly & Schultz 2016). Should a similar situation be found for an basalt-like impactor then this following process can be used for more suitable results. Nonetheless, the peak shock pressure was determined using the PIA for a basalt on basalt impact. We then match that pressure to the CFSD generation in this work at a similar peak pressure. It is then possible to use Equation 5.17 to determine fragment sizes on Vesta for a basalt-like impact.

$$\frac{d_{FV}}{d_{iV}} = \frac{d_{FS}}{d_p}, \tag{5.17}$$

where d is object diameter and the subscripts FV mean fragment on Vesta, iV the impactor (on Vesta), FS meaning fragment in the relevant shot, and p the projectile in the shot.

Therefore finding the ratio for the largest, typical and modal projectile fragments,

and multiplying by the impactor size, it is possible to determine impactor fragment sizes on Vesta. The same is done with impacts on Ceres. However, due to Ceres' porosity, the peak shock pressure is modelled as a basalt on permafrost ice impact. The appropriate values needed for permafrost in the PIA are density = 1960 kg m^{-3}, C = 2.51 km s^{-1} and s = 1.29 (Melosh 2013). In addition to this, the peak shock pressure can be used in Equation 5.5 to determine the percentage total surviving of the projectile post impact.

For Rheasilvia impact scenarios of an basalt-like impactor, in the cases of normal incidence impacts, the peak shock pressure exceed those in our experiments here (maximum of 31.9 GPa). We therefore use the CFSD from the impact at 31.9 GPa in the higher pressure scenarios although they may introduce inaccuracy due to the number of smaller fragments being higher.

Table 5.9: Fragment size and percentage survived information regarding basalt-like achondrite impacts onto Vesta and Ceres. On Vesta, the Veneneia and Rheasilvia craters are considered along with similar impacts on Ceres. The peak shock pressure for each impact was determined using the planar impact approximation (Melosh 2013). By using the ratio of the diameter of the projectile fragment to the projectile from this work and the impactor size for Vesta or Ceres it is possible to determine the sizes of fragments. The percentage survival was determined using Equation 5.5.

	Impact Speed [km s^{-1}]	Impact Angle	Size of Impactor [km]	Peak Shock Pressure (PIA) [GPa]	Survival %	Size of Largest Fragment [km]	Size of Typical Mid Size Fragment [m]	Modal Size Fragment [m]
Vesta Scenarios								
Veneneia	2.00	45	50	8	43	7.64	1562	295
Veneneia	4.75	45	30	26	24	2.91	865	183
Rheasilvia	5.50	90	37	55	16	3.40	1004	233
Rheasilvia	5.50	45	90	32	21	8.28	2442	567
Ceres Scenarios								
Veneneia Conditions	2.00	45	50	6	48	7.35	1742	315
Veneneia Conditions	4.75	45	30	19	27	3.34	804	183
Rheasilvia Conditions	5.50	90	37	42	19	3.40	1004	233
Rheasilvia Conditions	5.50	45	90	24	24	11.80	2366	549

For a 50 km achondrite/basalt-like projectile impacting at 2 km s^{-1} to form the Veneneia crater, we predict the largest fragment size to be 7.6 km in diameter. A

typical and modal size would be 1.6 km and 295 m respectively. Furthermore, 43% of the impactor could survive. For the other possible impact event to form Veneneia (30 km, 4.75 km s^{-1}) we get a modal, typical and largest fragment size of 183 m, 865 m and 2.9 km and a survival percentage of 24%. For the same conditions for an impact on Ceres we find very similar fragment sizes (see Table 5.9).

For the larger impactor at the more inclined impact angle, we get larger fragments in comparison to the smaller impactor. The same is seen for the similar impact scenario on Ceres. For both scenarios on Vesta and Ceres, we see no more than 24% of the impactor surviving.

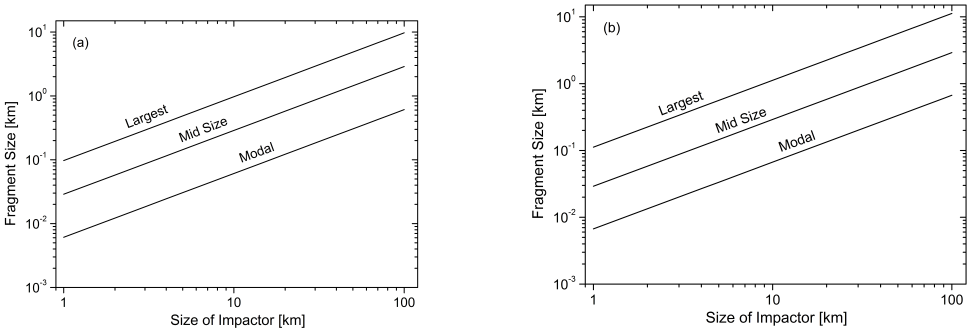

Impacts on Vesta Impacts on Ceres

Figure 5.26: Log-log plot of fragment size versus the size of a achondrite impactor for (a) Vesta and (b) Ceres. For Vesta, each impact was basalt projectile onto basalt target at 45° at the average impact speed on Vesta of 4.75 km s^{-1} (Reddy et al. 2012). For Ceres, it was a basalt projectile onto a permafrost target at 45° at the mean collision speed in the asteroid belt (Bottke et al. 1994). The peak shock pressures were determined using the planar impact approximation (Melosh 2013). The ratio of the diameter of the projectile fragment to the projectile from this work for the shot relating to the peak shock pressure of the target was used.

It is also possible to consider the fragment sizes from a range of impactor sizes on Vesta and Ceres. We assumed 45° incidence and mean impact speeds of 4.75 and 5.00 km s^{-1} respectively. Proceeding as previously, we find the model, typical and largest fragment size for impactors range in diameters from 1 to 100 km (see Figure 5.26).

5.4 Chapter Conclusion

This chapter has discussed the first experiment involving basalt and shale 1.5 mm cubed projectiles being fired onto water at speeds between 0.39 and 6.13 km s^{-1}. The water targets were then filtered through a 0.1 μm filter membrane. The filters were subsequently mapped at x95 magnification generating over 900 fields of view. From here, ImageJ software was used to analyse the fragments. The data from these images have been used to determine the morphologies of the fragments, the cumulative fragment size distributions, the possible survival at different solar systems scenarios and provided an insight into the onset of projectile disruption. The summary of the findings from this chapter are:

- At slower speeds the fragments appear more circular and become more elliptical at higher impact speeds. Excluding the partial disruption impacts, the average semi-minor axis to semi-major axis ratio (b/a) for basalt and shale were 0.58 $\pm$ 0.16 and 0.59 $\pm$ 0.14 respectively. This suggests that at higher speeds the morphology of basalt and shale are similar.

- We fit three power laws, in the form $N(> S) = aS^b$, to the cumulative fragment size distribution plots. This has shown that with increasing speed the gradient b of each section gets steeper.

- Furthermore, the behaviour of the largest fragments yield similar results to that of targets, suggesting a transition between disrupted to heavily catastrophically disrupted objects.

- The total mass retained at the impact site from each shot has been measured in this work. From this, it is possible to determine the retained percentage. Fitting the percentage retained at each peak shock pressure yields an equation which can be used to determine the percentage surviving for different Solar System impact scenarios. The estimated percentage survival at Pluto, the Moon, in the asteroid

belt and on Mars is 76 ± 11%, 39 ± 8%, 17 ± 5% and 10 ± 4% respectively. The unaccounted for mass is lost due to vaporising. Although, these approximations ignore the effects of porosity in the target and projectile and scaling issues.

- The ratio of the mass of the largest fragment to the mass of the projectile was plotted against the projectile energy density. For basalt, we find that two power laws are needed to fit the data, whereas shale only needed one. This suggests that the two materials are different The catastrophic disruption energy density of basalt and shale were found to be (24.0 ± 2.1) $\times 10^4$ J kg^{-1} and (9.4 ± 5.0) $\times 10^4$ J kg^{-1} respectively. These results have been compared to other studies in the literature.

- From this work, it is possible to determine the impactor percentage-survived and possible original impactor size applicable in many solar system impact events, with specific examples of impacts on Vesta and Ceres. The fragment sizes for a wide range of impactor sizes were predicted. For the specific cases of Venenea and Rheasilvia on Vesta, we find 16 - 24% of the impactor can survive if the impact was at the mean impact speed predicted for Vesta (around 5 km s^{-1}). This compares well with the prediction of 17% of Daly & Schultz (2016). For Ceres, we find impactor retention in the typical range of 20 - 30%, somewhat higher than Daly & Schultz (2015*b*) where they consider basalt impacting porous snow. With further work looking into the role of the angle of impact on the largest fragment diameter to projectile diameter ratio, we could constrain a better estimation of the size and mass of impactors.

Chapter 6

Shock Pressure Effects on Carbon Raman Spectra

The Raman spectrum of a material is not fixed. It can be altered by environmental factors. For example, applying an external influence to a material can alter the structure and bonds, which results in an altered Raman spectrum.

There are two types of carbon in a rock sample, abiotic and biotic. Abiotic means that the carbon is not derived from living organisms. The possible identification of biomarkers by the ExoMars 2020 rover using Raman spectroscopy will involve looking at the carbon D and G bands. The final landing location for the ExoMars rover will either be Oxia Planum or Mawrth Vallis (ESA 2016*b*). In these areas, there are could be shocked rocks present in the form of lightly shocked ejecta rocks. Unfortunately, we are yet to unambiguously identify biotic carbon using Raman spectroscopy (Bower et al. 2013). But if there is a difference, we need to be able to isolate it from other factors such as shock. It is therefore important to know if the shock history of a rock could have an effect on the carbon D and G bands.

With regards to impact work, effects upon Raman spectra have been reported by Foster et al. (2014) who noted that there was the permanent shift of the olivine doublet

peaks in comparison to the original un-shocked sample for both impacts in aerogel and on to aluminium foils. This led to the conclusion that this was as a result of the strain on the crystal lattice caused by the impact. This was confirmed by a later report (by Harriss & Burchell 2016).

In addition to peak shifts, Raman spectroscopy has been used to show a phase change of a material when shocked. Bucio et al. (2015) found that gypsum transformed to bassanite which has a possibility of turning into anhydrite. These have been discussed in greater depth in Section 2.6.1 of this thesis.

This chapter looks into the shock pressure effects on carbon bearing projectiles fired in a two-stage light gas gun. It starts by looking at the homogeneity of the carbon Raman spectra of the projectile materials. Moving on, it then presents the results and discussion of the effects of shock pressure upon the carbon D, G and D2 bands in Raman spectroscopy.

6.1 Rock Characterisation

The three materials used in this chapter are basalt, shale and graphite. In basalt, carbon can be found in the form of carbonate minerals and sometimes in the form of graphite. The carbon in the form of graphite will be non-homogeneously distributed throughout the basalt. A carbonate mineral present could be calcite.

Each material displays the D and G band of carbon in its Raman spectrum (see Chapter 2 for discussion on the Raman spectra of carbonaceous materials). However, graphite has the addition of a D2 band. Figure 6.1 shows the spectra with these bands for the three sample materials.

The exact location of the G band is not well defined in the literature, ranging from 1565 cm^{-1} (Court et al. 2007), to 1598 cm^{-1} (Marshall et al. 2010). When there are randomly distributed impurities the G band can split into two peaks, the G band and

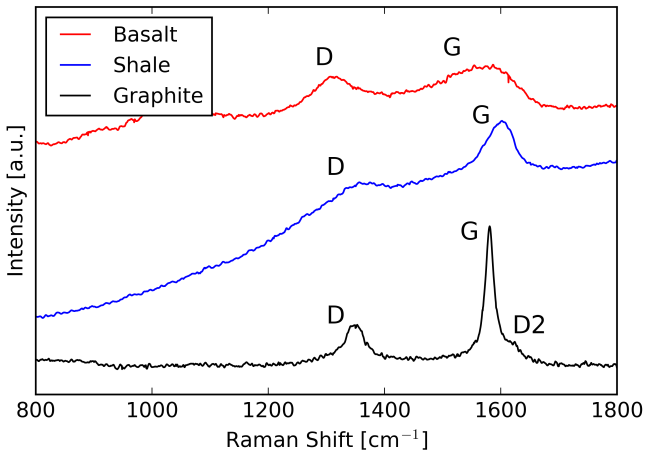

Figure 6.1: Three spectra of basalt, shale and graphite showing the carbon D, G and D2 bands. These spectra have had no background subtraction done.

the D2 band. This can lead to difficulty in interpreting spectra which have very broad G bands as they can mask the D2 band. The D2 band isn't present in every spectrum, therefore it is important to avoid inferring something that isn't there. For the basalt spectra in this work, it is clear that there is no D2 band as there are no peaks around 1620 cm^{-1}. However, for shale, this distinction is not clear due to the high wavenumber location of the larger band. Figure 6.2 shows two possible fits to a shale spectrum. The possible G and D2 bands, in this case, are very close together (Figure 6.2b), meaning it is difficult to confidently say if the D2 band is present or not. Therefore, the shale spectra were analysed as a D and G band system keeping to the minimal possible solution and to not infer something that may not be there. Hence, for this work basalt and shale shall be analysed solely as a D and G band system and graphite as a D, G and D2 band system.

Important information regarding the analysis of the D and G bands lies in the band peak positions, the band widths, and the ratio of the D to G band amplitudes (R1). R1 is given by:

$$R1 = \frac{D_{amplitude}}{G_{amplitude}}. \tag{6.1}$$

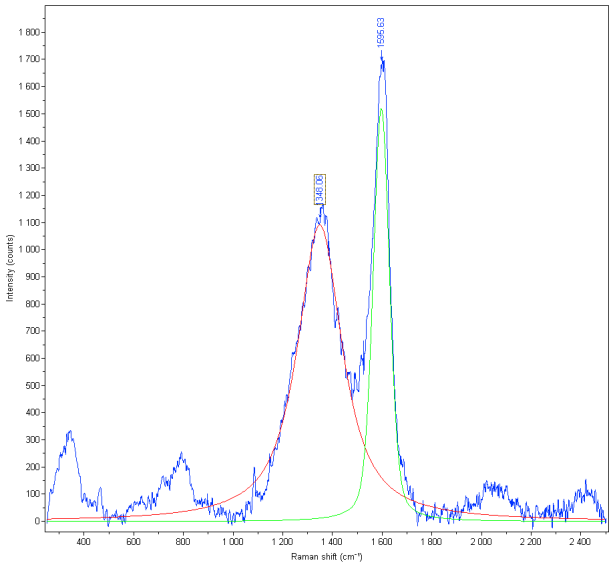

(a) D and G Band Fitting

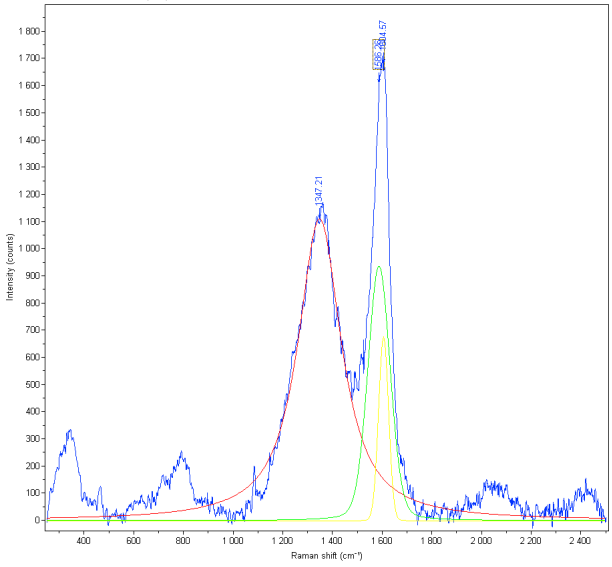

(b) D, G and D2 Band Fitting

Figure 6.2: Curve fitting of shale Raman spectrum, where the background has been subtracted. In (a) with just D and G bands, whilst in (b) the same spectrum is fit with a D, G and D2 band.

The ratio of the areas of the three bands (R2) is also of use and is given by:

$$R2 = \frac{D_{area}}{D_{area} + G_{area} + D2_{area}}. \tag{6.2}$$

The ratios R1 and R2 are used to determine the structural organisation of the

material. R2 is a better proxy for the structural organisation when R1 is less than 1. When R1 is greater than 1, it provides more useful information (Beyssac et al. 2003). The higher the R1 and R2 value, the more disorganised the structure is.

Appendix E.1 contains example Raman spectra with baseline removed for basalt, shale and graphite projectiles and fragments. For the basalt projectiles (Figure E.1) their spectral attributes are varied. Some have D band amplitudes greater than their G band's, while some do not. The majority have the G band amplitudes greater than the D band. In regards to the band width, those where the D and G band are of approximately equal amplitude have widths (FWHM) of similar sizes. For the shale projectile example spectra (Figure E.3) each appears similar. The G band amplitude is always greater than the D band amplitude and the widths are often similar between each spectrum. There is a slight variation in the signal to noise ratio (SNR) due to the spectra being acquired by mapping the non-uniform surface. Finally for the example graphite projectile spectra (Figure E.5) each appears similar. The G band amplitude is always greater than the D band, however, there is some variation in the D band amplitude and width. Furthermore, the G band width also has a slight variation.

The example spectra for the basalt fragments (Figure E.2) show some variation. The D band amplitude varies significantly, whereas the G band amplitude is reasonably constant. As the D band amplitude varies so does the D band width (FWHM). The example spectra for the shale fragments (Figure E.4) vary. The G band amplitude and width remains constant, whereas the D band is more varied. The example spectra of the graphite fragments (Figure E.6) shows greater variation than the projectile spectra. The D and D2 band amplitudes and widths, and the G band widths have been altered.

Figure 6.3 displays four example spectra of basalt with their peaks fitted. A Gaussian fit was completed using the software LabSpec6. Although the two projectile spectra (Figure 6.3a and 6.3b) are different the fits are both close to the spectra. For Figure 6.3b, the D band peak position could possibly be slightly off to the left or the peak. However, this difference doesn't appear to be large enough to suggest this method

should not be used. Equally, with the fragment spectra, both appear well fitted with no significant variations from the spectral lines.

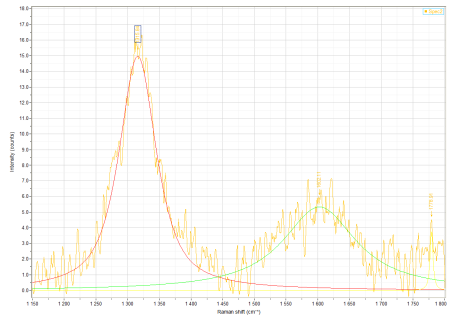

(a) Projectile Spectrum Fitting 1

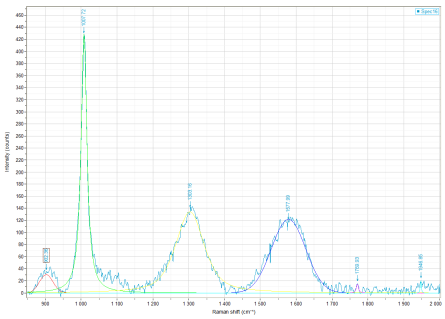

(b) Projectile Spectrum Fitting 2

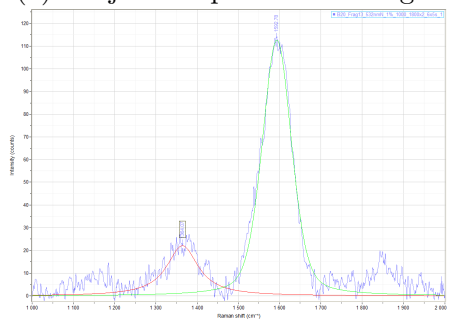

(c) Fragment Spectrum Fitting 1

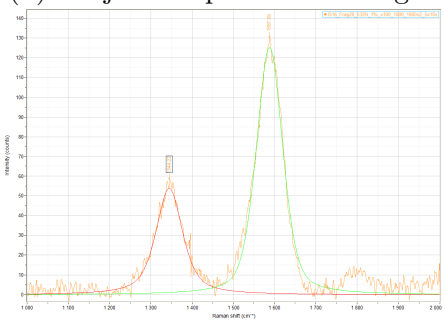

(d) Fragment Spectrum Fitting 2

Figure 6.3: Spectral fitting examples for basalt. a and b are for the projectile and c and d are for two separate fragments.

For basalt, there were multiple Raman spectral evidence for the presence of graphite in the sample material, for example Figure 6.4. This could explain possible similarities between the results of the two materials.

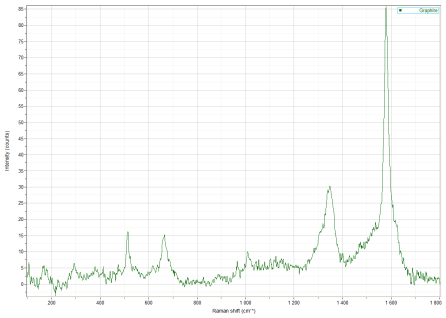

(a) Basalt Spectrum

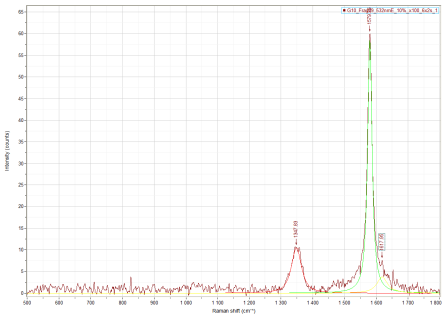

(b) Comparison Graphite Spectrum

Figure 6.4: Graphite spectrum from basalt sample (a), compared with a graphite spectrum from a graphite sample (b).

Figure 6.5 displays four example spectra of shale with their peaks fitted. Much like

the basalt spectra in Figure 6.3, both the shale projectile and fragment spectra are well fitted with limited variation in the spectra. One exception would be in Figure 6.5d, where the width of the fitted spectra is less at the base than the fitted peak. This could be an artefact of the background fluorescence (baseline) being removed. However, the width of this D band looks correct on visual comparison with the spectra.

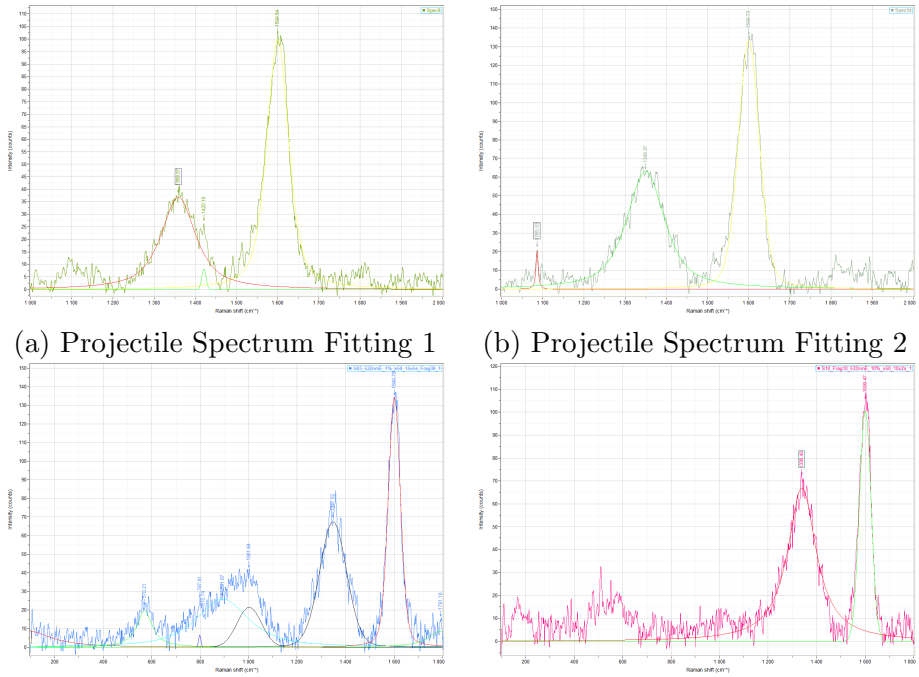

(a) Projectile Spectrum Fitting 1 (b) Projectile Spectrum Fitting 2

(c) Fragment Spectrum Fitting 1 (d) Fragment Spectrum Fitting 2

Figure 6.5: Spectral fitting examples for shale. a and b are for the projectile and c and d are for two separate fragments. The fitted curve

Finally, Figure 6.6 shows four example graphite spectra with their peaks fitted. The fits to these spectra are very good. This is most likely due to graphite having the strongest carbon bands of the three samples.

Before characterising the samples further, it is important to note the quantity of carbon in basalt. Throughout this experiment, the carbon spectra from basalt have been difficult to acquire. This is partially due to the carbon being in particular carbon-rich phases, such as graphite. These are non-homogeneously spread across the basalt which could perceivably result in certain areas being low in carbon. This leads to either a poor carbon spectrum or a non-existent spectrum. Table 6.1 displays the quantity of

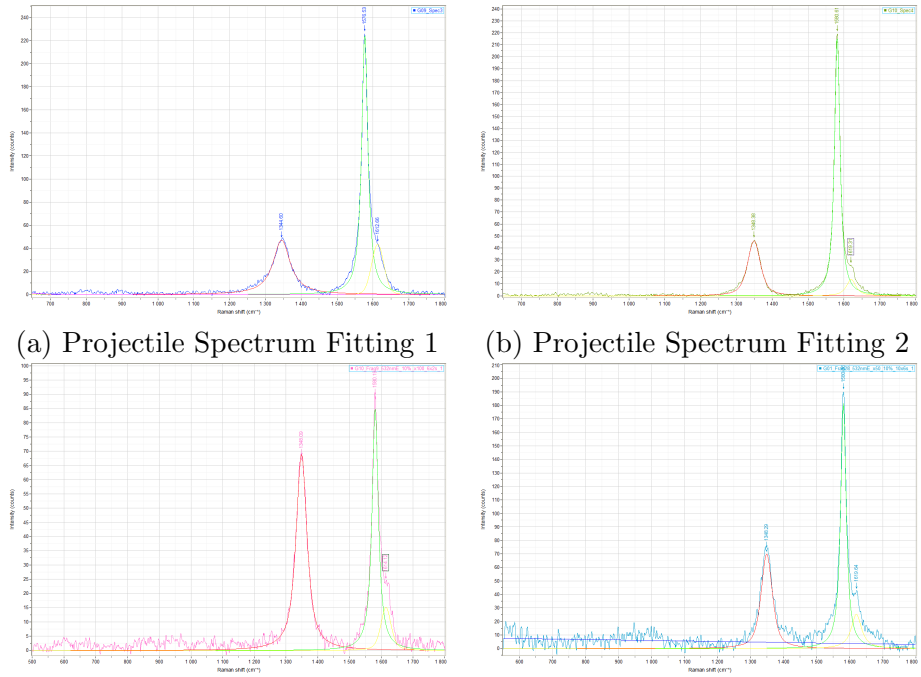

(a) Projectile Spectrum Fitting 1 (b) Projectile Spectrum Fitting 2

(c) Fragment Spectrum Fitting 1 (d) Fragment Spectrum Fitting 2

Figure 6.6: Spectral fitting examples for graphite. a and b are for the projectile and c and d are for two separate fragments.

carbon from submarine basaltic glasses, basalt from Eastern China and basaltic glass from the Mariana Trough. In addition to these, Table 6.1 also includes the carbon content for Angrites (a small group of achondrites), basaltic Martian meteorites and HED meteorites.

Table 6.1: Quantity of carbon in different samples on Earth and in meteorites. The references refer to the sources of the carbon content values quoted.

Sample	Carbon Content [ppm]	Reference
Submarine Basaltic Glass	22–160	Sakai et al. (1984)
Basalt from Eastern China	550–800	Zha et al. (2018)
Mariana Trough	8–231	MacPherson et al. (1999)
Angrites	10–140	Abernethy et al. (1928)
Basaltic Martian Meteorites	1–100	Grady et al. (2004)
HED Meteorites	10–30	Grady et al. (1997)

Based upon the contents of other terrestrial basalts, we estimate ours will contain similar abundances. Comparing this to the meteorite values in Table 6.1 it is higher.

For shale, the sample used was the same as a sample used in Hutchinson et al.

(2014). The Total Organic Carbon (TOC) concentration of the shale samples used in this work ranges between 0.5 and 3.42%. The extractable carbon fraction, which is the extract divided by the TOC, ranges between 0.018 and 0.145 (Hutchinson et al. 2014). Generally, throughout the experiment the carbon bands in the shale sample were easily acquirable. Finally, for graphite the carbon content is pure carbon.

In order to determine the homogeneity of each sample, an area of approximately 300 by 180 μm of each material was mapped using the 532 nm (green) Raman laser. A 25 or 10% neutral density (ND) filter, which blocks 75 and 90% of laser light respectively, was used. The spot size of the green laser through the x50 objective is 2 μm and the power with these ND filters was 668 and 1961 MW m^{-2} respectively. Ten accumulations with 2-5 second dwell times were used. The mapping resulted in 60 individual spectra for each material. The variation in the carbon spectra is summarised in Table 6.2.

Table 6.2: Table of the statistics arising from the characterisation samples of each material by fitting the Raman spectra. There are 60 spectra for each sample material. The band widths refer to the FWHM of the spectra.

	D Band Peak Position [cm^{-1}]	D Band Width [cm^{-1}]	G Band Peak Position [cm^{-1}]	G Band Width [cm^{-1}]	D2 Band Peak Position [cm^{-1}]	D2 Band Width [cm^{-1}]	R1	R2
Basalt								
Mean	1358.6	76.2	1583.0	83.4	-	-	0.0892	0.0753
Error	± 0.91	± 3.36	± 0.30	± 0.56	-	-	± 0.006	± 0.006
SD	7.03	26.1	2.32	4.32	-	-	0.043	0.046
Shale								
Mean	1347.5	110.8	1599.3	54.6	-	-	0.4436	0.4217
Error	± 1.06	± 4.80	± 0.28	± 0.79	-	-	± 0.024	± 0.026
SD	8.21	37.2	2.13	6.11	-	-	0.182	0.203
Graphite								
Mean	1348.4	40.6	1580.8	17.5	1619.5	31.9	0.2546	0.3349
Error	± 0.09	± 0.68	± 0.09	± 0.19	± 0.39	± 1.25	± 0.005	± 0.008
SD	0.69	5.26	0.71	1.44	2.99	9.70	0.038	0.064

The most homogeneous sample is graphite, as suggested by each band having a width and position with a low standard deviation. This is because the D and G bands for this sample are very strong and, in the case of the G band, rather narrow (see Figure 6.1). Furthermore, this does not vary greatly from spectrum to spectrum. For the D band (generally the weaker of the D and G bands) it seems that shale has more variation

than basalt. As the D band for basalt and shale were weak and poorly resolved making them hard to measure, it is unsurprising to see that they have the most variation.

The larger variation in peak characteristics for basalt is due to the significantly lower occurrence of carbon in the sample. When the D and G bands were observed they were often both broad and low in intensity. Due to the nature of the sample, more laser power would result in the laser burning material meaning that analysing the basalt represented a significant challenge.

Each material's variations are displayed in more detail in the next three figures. Figure 6.7, 6.8 and 6.9 show the peak positions, widths and R1 and R2 ratios for each point in the 300 by 180 μm area with the average over the whole area subtracted. This determines the difference in each area to the mean value over the whole area.

Figure 6.7 shows the variation in D and G bands across the 54,000 μm^2 area for basalt. The D band shows the most variation with the peak position. Note that it is not random across the sample, but is clustered in regions. The most significant of such regions, top right of the D band peak position plot, also shows up as a distinct region in the D band width and G band peak position plots. The minimum difference from the average D band peak position of this area is -10 cm^{-1} and the maximum is +25 cm^{-1} (a range of 35 cm^{-1}). The same for G is a minimum and maximum of -3 and +4.5 cm^{-1} respectively. When considering the band width, it appears the D band has the largest minimum and maximum difference of -60 and +60 cm^{-1} (range of 120 cm^{-1}) respectively. In comparison, the minimum and maximum for the G widths are -12 and +12 cm^{-1} respectively. This very broad variation in D band width is due to the low band intensities. This is evident in the R1 values, where the average is 0.0892. The range in the differences between the location value and the average of the whole area for R1 and R2 are 0.175 and 0.2 cm^{-1} respectively.

Figure 6.8 shows that variation in D and G bands for a 300 by 180 μm area of shale. As for basalt, the D band position for shale is the most variant in band peak position, with a range of 40 cm^{-1}. The minimum and maximum difference from the average over

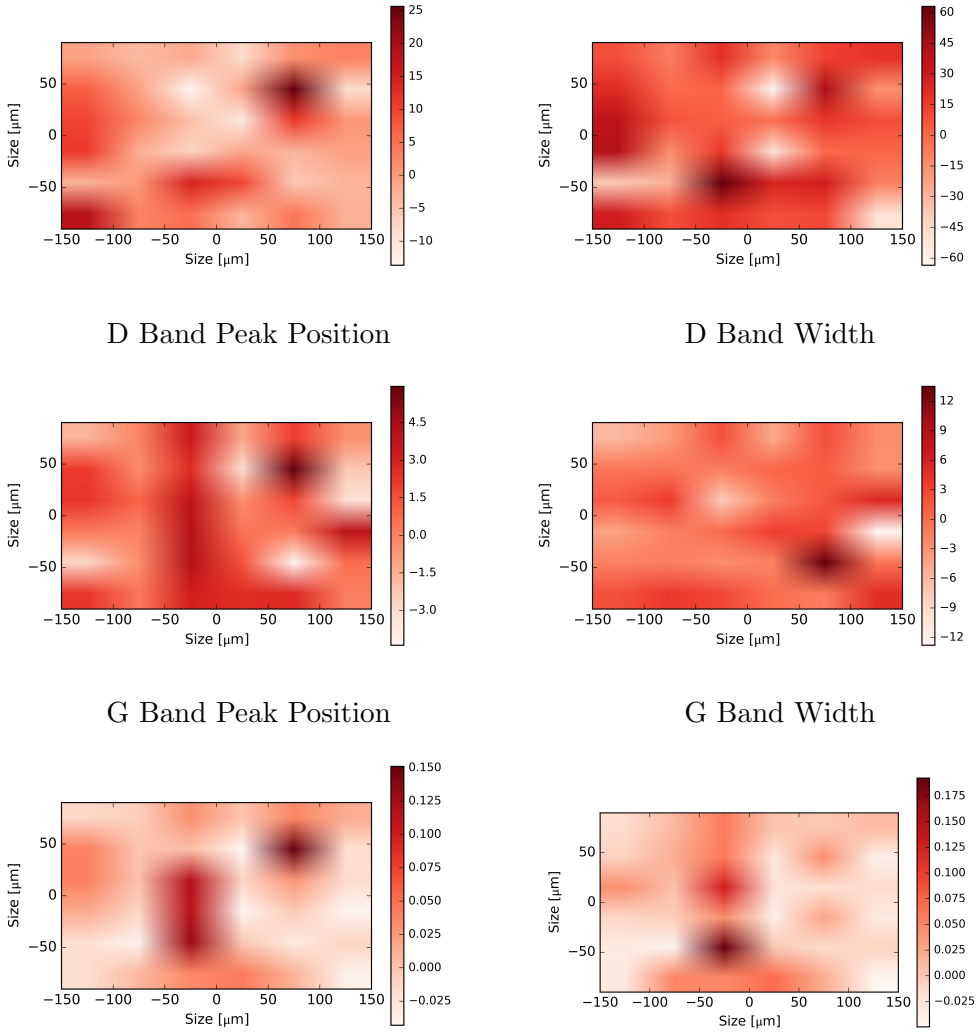

Figure 6.7: Basalt spectra over an area of 300 μm by 180 μm. In each plot, there are 60 basalt spectra and the units for the colour bars are cm^{-1}. These plots show the difference between the mean value of the area at each location. White region values are below the mean, with red being above the mean (see the scale bars to the right of each figure for more quantitative values).

the area for D and G band positions are -15 and +25, and -5 and +3 cm^{-1} respectively. This suggests that the G band peak position is the least variant. For the widths, the D band is the most variant with a range of 140 cm^{-1}. The variation for the R1 and R2 values are broad with a range of 0.8 and 0.64 respectively. The D bands were far more prominent in this sample material hence creating reliable R1 and R2 values.

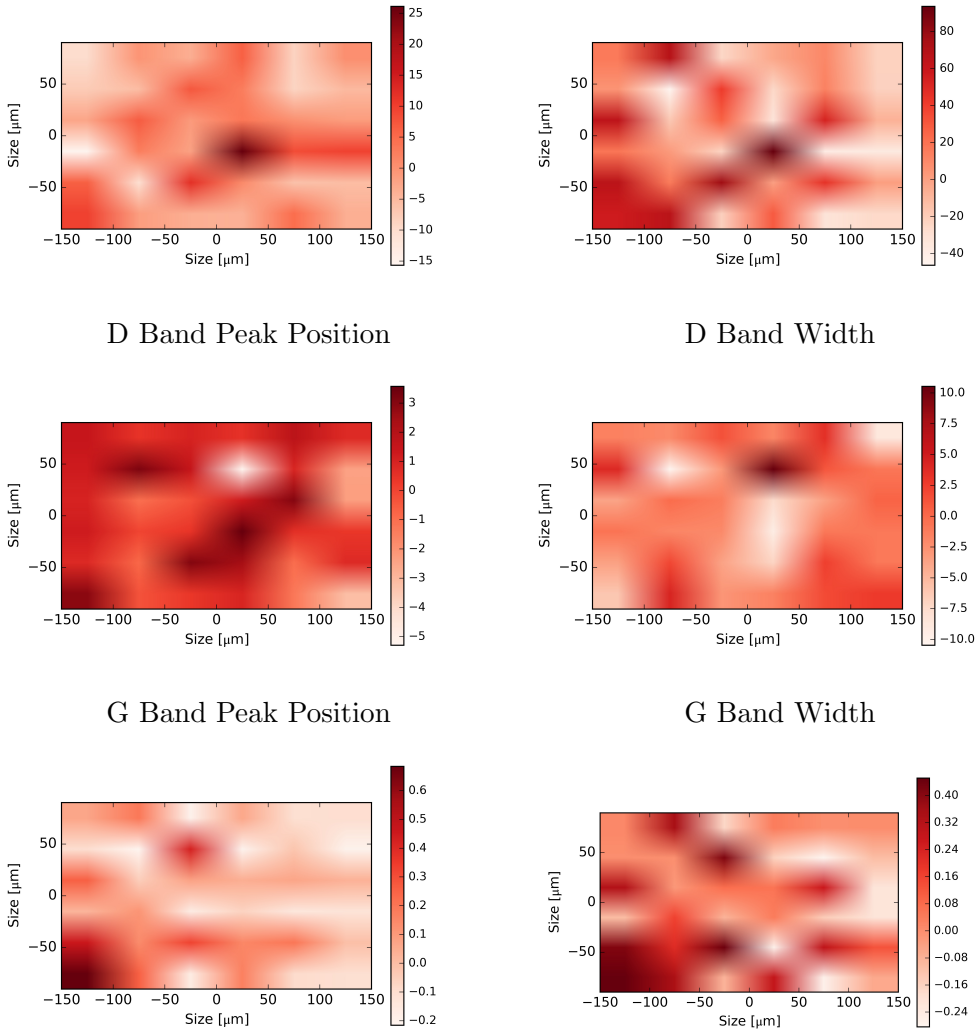

Figure 6.8: Shale spectra over an area of 300 μm by 180 μm. In each plot, there are 60 shale spectra. These plots show the difference between the mean value of the area at each location. See Figure 6.7 comments.

From Figure 6.9 the range in the D and G band peak positions are both small at 3.2 and 4 cm^{-1} respectively for graphite. The range of the D2 band peak position is 14 cm^{-1}. This is larger than for the D and G band peak position for graphite. The widths of the D and G band both have small ranges of 9 and 7 cm^{-1} respectively. This is due to the strong D and G bands in graphite. The D2 band width for graphite appears to be rather variant, with a range of 35 cm^{-1}. It appears the more defined the peaks are,

the less variant they are. The range of the R1 and R2 values which are 1.2 and 0.175 respectively.

Overall, graphite appears to be the most homogeneous of the three sample materials. Shale would be the next due to basalt's issues with acquiring a good D band. What these figures do show is that the materials have significant variation across a small area. Since the original positions of the fragments within the projectile analysed in this chapter cannot be determined, comparing the fragment spectra to the projectile spectra taken from one of the faces of the projectile is not the most appropriate method. A better method would be to take the average for all projectile spectra for each sample material and compare those averages to the fragments average in each shot. Furthermore, any apparent shifts between projectile fragments and the un-shot material, have to be compared in magnitude to the natural spread in the relevant value in the raw samples.

Natural variability for the D and G band peak position on the raw sample of basalt is 1358.6 $\pm$ 7.03 and 1583.0 $\pm$ 2.32 cm^{-1} respectively. The same for the D and G band peak position of shale is 1347.5 $\pm$ 8.21 and 1599.3 $\pm$ 2.13 cm^{-1} respectively. The D, G and D2 peak positions for graphite are 1348.4 $\pm$ 0.69, 1580.8 $\pm$ 0.71 and 1619.5 $\pm$ 2.99 cm^{-1} respectively.

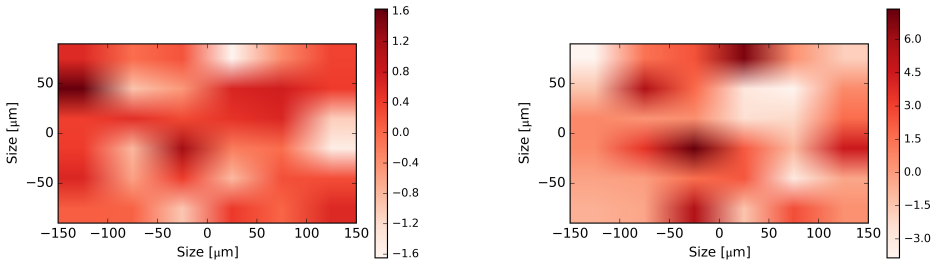

D Band Peak Position

D Band Width

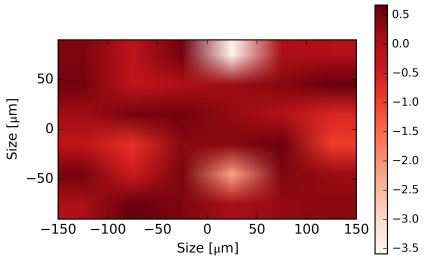

G Band Peak Position

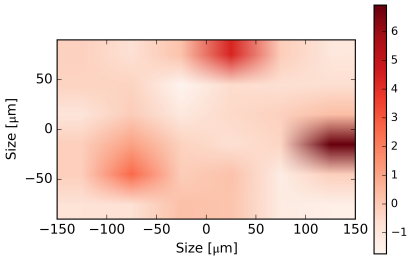

G Band Width

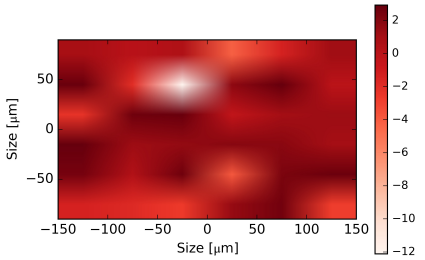

D2 Band Peak Position

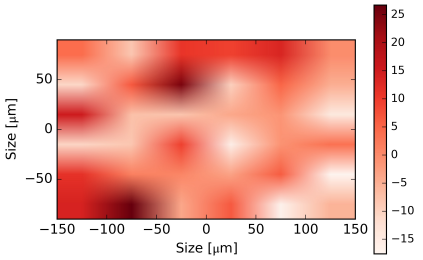

D2 Band Width

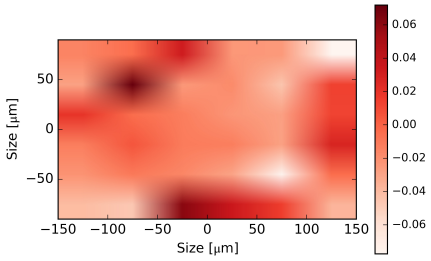

R1

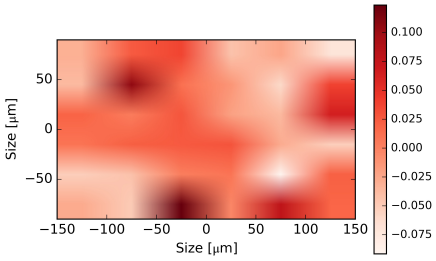

R2

Figure 6.9: Graphite spectra over an area of 300 μm by 180 μm. In each plot, there are 60 graphite spectra. These plots show the difference between the mean value of the area at each location. See Figure 6.7 comments.

6.2 Methodology

The samples were shocked by firing 1.5 mm cubes of each material into bags of water using the University of Kent's Two-stage Light Gas Gun. This was the same method used in Chapter 5. To recap, the three sample materials (basalt, shale and graphite) were filed into 1.5 mm cubes. These cubes were then impacted onto water using the gun. As the gun is horizontal the water was held in a plastic bag in a frame within a box - called the ocean target (see Figure 5.6 in Chapter 5). The water was then collected from the target and filtered through a 0.1 μm filter membrane to collect the fragments.

Before shooting, 25 spectra from each projectile were acquired. These were from a map over a small area on one of the cube's/projectile's faces for each projectile shot. Post filtering, 40 spectra were acquired - one each from 40 randomly selected fragments. All spectra were taken using the Raman spectrometer's 532 nm (green) laser. This laser was chosen due to it being similar to the proposed ESA/Roscosmos ExoMars 2020 mission's Raman spectrometer (Rull & et al. 2017).

When acquiring spectra from the surface of the projectile, care was taken to not use too much laser power as this created burning and ruined the sample spectrum. Typically a 10 or 25% effective transmission neutral density filter was used to limit the laser power at the sample. The spot size of the 532 nm laser through the x10, x50 and x100 objectives are 10, 2 and 1 μm respectively. The maximum laser power (ND filter of 25% and x100 objective) is 7.84 mW μm^{-2}. This is an equivalent of 7840 MW m^{-2}. Each sample material was sensitive to laser power, but in particular, basalt was the most sensitive as it was prone to being burnt by the laser. When acquiring spectra from the fragments, even lower laser power was used in order to not introduce any laser heating effects which can be an issue (Hibbert & Price 2014). For the spectra of the fragments a neutral density filter up to 1% transmission was used to limit laser power on each fragment.

Table 6.3: Details of shots used for the results for this chapter. Material type is given, along with the shot speed and peak shock pressure (determined using the planar impact approximation, PIA, Melosh 2013).

Shot Number	Material	Speed [km s^{-1}]	Peak Shock Pressure (PIA) [GPa]	Number of Projectile Spectra	Number of Fragment Spectra
S050315#1	Basalt	0.96	2.30	125	40
G200515#1	Basalt	1.98	5.90	125	40
G010515#2	Basalt	3.04	10.9	125	40
G141015#1	Basalt	4.05	16.9	125	40
G041115#2	Basalt	4.96	23.3	125	40
S181115#1	Shale	0.95	2.12	125	40
G130116#2	Shale	1.93	5.34	125	40
G041115#1	Shale	3.12	10.3	125	40
G031215#2	Shale	4.64	19.7	125	40
G211015#2	Shale	6.13	30.9	125	40
G130716#1	Graphite	0.86	1.60	100	40
G140916#1	Graphite	1.80	4.15	100	40
G100616#1	Graphite	3.07	8.94	100	40
G280916#1	Graphite	4.00	13.4	100	40

As shown in Section 6.1, the sample material has a natural variability in peak position and band width for the D and G bands. This assumption allows for far better statistics when analysing these results. There are 25 spectra per projectile, combined with the number of shots (see Table 6.3). This leads to the number of raw spectra for each projectile material being 125, 125 and 100 for basalt, shale and graphite respectively.

To ensure that no carbon spectra are of gun debris, the blank shot generated from the work in Chapter 5 was analysed. A range of debris sizes were analysed and it was found that any gun debris with carbon signatures were very small and appeared very different to the projectile fragments. With this in mind, caution was taken in selecting the 40 fragments to analyse to ensure that they looked like projectile fragments, thus excluding gun debris.

6.3 Results and Discussion

6.3.1 Shock Pressure Effects on Carbon D and G Bands

In this section, the shock pressure effects on band position, width and separation, and R1 and R2 values are shown and discussed.

D Band Peak Position

Figure 6.10 shows the average fragment D band peak positions with the average of all the projectile D band peak positions subtracted for each material's projectiles. Therefore, for peak position a positive value suggests a shift to higher wavenumbers, whereas a negative value indicates a shift to lower wavenumbers.

It is difficult to draw conclusions from the data shown above due to the degree of scattering. However, for basalt, it can be argued that the D band has been shifted to a higher wavenumber. At the lowest shock pressure, there appears to be a shift of approximately 7.0 cm^{-1} to a higher wavenumber. This is interesting as it suggests a sharp increase in peak position for pressures less than 2.3 GPa. At the highest peak shock pressure, there has been a relative D band shift of approximately 9.5 cm^{-1}. Overall when considering the error bars represent the error on the mean, it would appear that the D band of basalt has experienced a shift. However, there is one data point at 10.9 GPa where the error bars are large enough suggest that it possibly didn't experience a shift. If we were to consider the data having no trend, the average shift over all shots is approximately 8.3 $\pm$ 3.3 cm^{-1}.

For shale (Figure 6.10b), it appears that the D band peak position is shifted to higher wavenumbers at a low pressure, and as shock pressure increases this shift still occurs but to a lesser degree. The largest relative shift occurs for the lowest pressure shot and is 15.7 cm^{-1}. The lowest is at the highest peak shock pressure and is 7.2 cm^{-1}. If we are to assume there is no trend, the average relative shift to the pre-shot

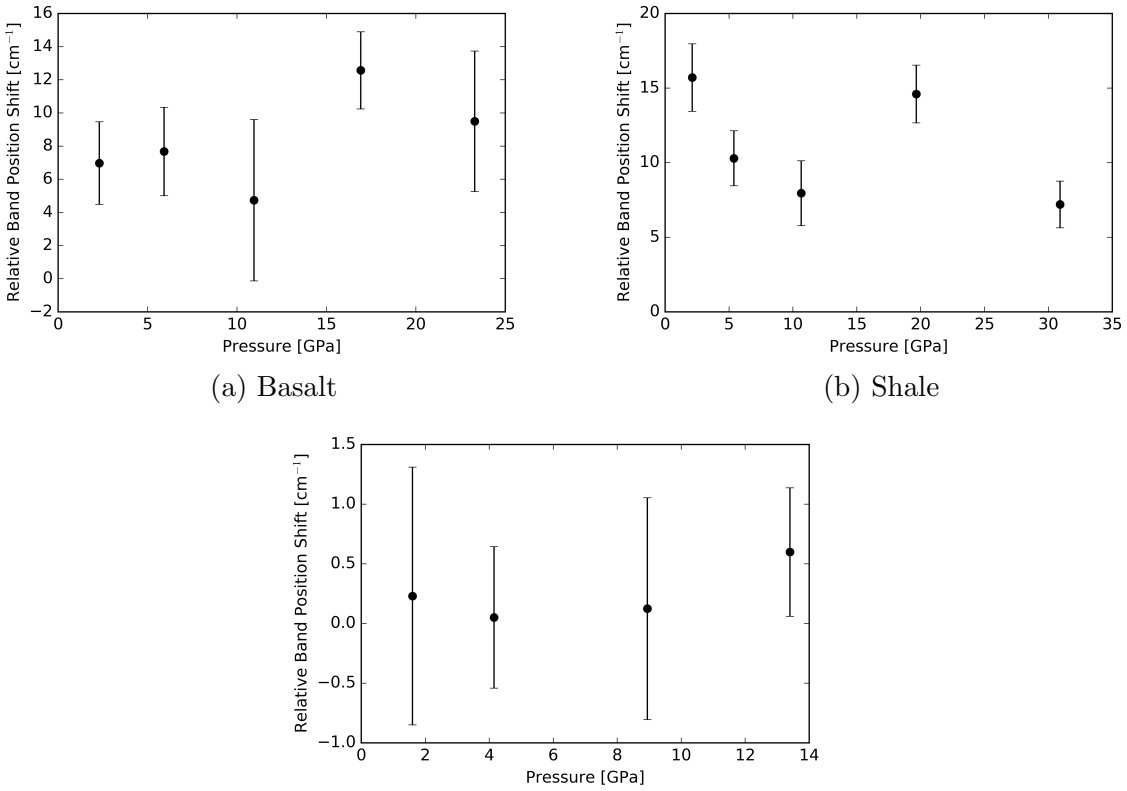

(a) Basalt

(b) Shale

(c) Graphite

Figure 6.10: D band peak position relative shift to the pre-shot spectra versus peak shock pressure determined using the planar impact approximation (PIA) (Melosh 2013).

spectra value is 11.2 ± 2.0 cm^{-1}.

Raw graphite had well-defined D band peak positions with relatively low variation, suggesting it would yield the most reliable results out of the three materials. In Figure 6.10c the D band peak position doesn't show a shift for the majority of shots. The data points have their error bars crossing/reaching zero. Possibly the fourth data point is suggesting an increase in D band shift at pressures higher than 13 GPa, but this cannot be determined as graphite could not be fired at speeds higher than 4.00 km s^{-1} Therefore, this data would suggest that graphite does not experience a shock effect.

G Band Peak Position

Figure 6.11 shows the average fragment G band peak positions with the average of all the projectile G band peak positions subtracted for each material's projectiles.

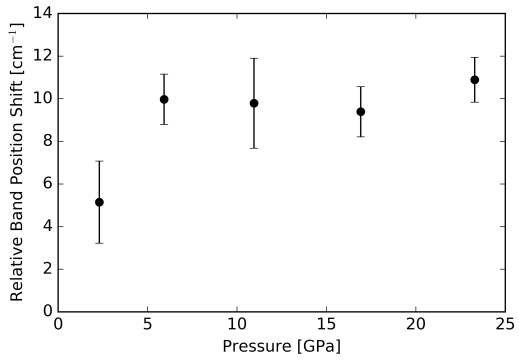

(a) Basalt

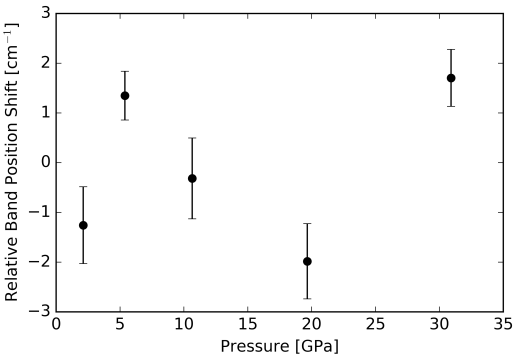

(b) Shale

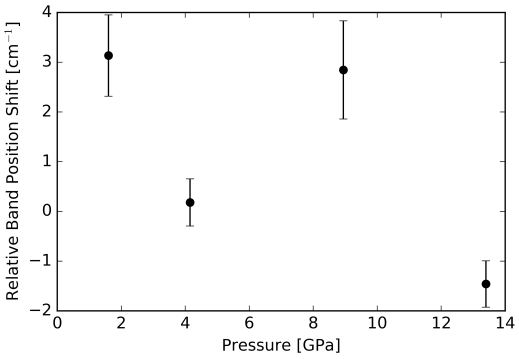

(c) Graphite

Figure 6.11: G band peak position's relative shift vs. peak shock pressure. Peak shock pressure was determined using the PIA.

For basalt (Figure 6.11a) there seems to be a positive trend with peak shock pressure. At the maximum peak shock pressure (23.3 GPa) the relative peak shift is 10.9 ± 1.0 cm^{-1}. This effect is well outside errors, even at the lowest peak shock pressure of 2.3 GPa where the relative shift is approximately 5.1 cm^{-1}. However, Figure 6.11a could be interpreted as having all data along an average shifted value (much like in Figure 6.10a) with the first data point being anomalously low. The average relative shift value for these data points is 9.0 cm^{-1}. Nonetheless, the G band peak position for basalt spectra does appear to experience a shock effect.

However, this effect of shock pressure on the G band peak position is not evident for shale (Figure 6.11b). It would appear that the data is scattered around zero shift. This scatter in the data could be as a result of acquiring the spectra of fragments that did not experience the peak shock pressure due to their initial location within the projectile upon impact. As discussed in Chapter 5, the material just behind the front face of the impacting projectile experiences the peak shock pressure and the material at the rear of the projectile experiences a considerably lower shock pressure. Ideally, a far greater number than 40 spectra would be required to mitigate this effect.

For graphite (Figure 6.11c), there again would appear to be scattered data with no underlying trend. Although, two data points suggest a positive shift and one a negative. Where no effect was found for the D band of graphite, in three shots the G band appears to have experienced a relative shift of 3.1 $\pm$ 0.8, 2.8 $\pm$ 1.0, and -1.5 $\pm$ 0.4 cm^{-1}. This scatter is possibly as a result of the magnitude of variation of the raw sample. In Figure 6.9 G band peak position, there are low areas (in white). Areas such as these were thought to average out over the whole projectile, but possibly they didn't and are masking any possible trends in the data. Given this variation, and the low magnitude of each data point, no effect can be seen.

D2 Band Peak Position

Figure 6.12 shows the relative peak shift of the D2 carbon band for the graphite samples. Arguably there could be D2 bands present in the shale spectra but it was impossible to confidently say that they were, and therefore to avoid inferring something that wasn't there it was analysed just as a G band.

In Figure 6.12 there is no trend that can be ascertained. Most of the data appear to be scattered around zero. There is just one data point which suggests an effect of shock pressure on D2 band peak position at 8.94 GPa. The relative band position shift for this data point is -4.5 $\pm$ 1.1 cm^{-1}.

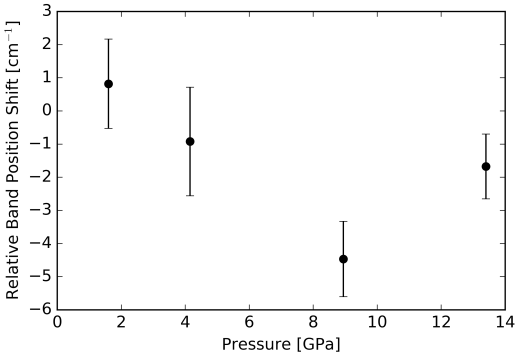

Figure 6.12: The relative shift of the D2 carbon band in graphite against peak shock pressure, determined using the PIA.

G Band Peak Position vs. Average Fragment Diameter

The next question to consider when interpreting the previous results was to see if there was a correlation of effect with fragment size. Figure 6.13, 6.14 and 6.15 show a comparison of the G band peak position with the average diameter of each fragment. The G band is shown as it was typically the stronger and better defined peak.

For basalt (Figure 6.13), it would appear that as the impact speed increases, fewer fragment's G band peak positions lay below the average projectile G band peak position (the dashed line). This suggests, as shown in Figure 6.11a, that the shock pressure is causing a positive shift in the G band peak position. This is likely due to the shock wave causing the carbon aromatic rings to experience strain and distort. From Figure 6.13, it isn't clear that there is any fragment size effect. It was thought that the smaller fragments could have experienced a greater shock than the larger, hence having a shifted G band peak position. This was assumed as smaller fragments are thought to be more disrupted by the impact than the larger fragments. However looking at the 4.96 km s^{-1} shot, there are 60 μm fragments which have the same G band peak position as the smaller fragments. From Table 5.3 in Chapter 5, a basalt shot at 4.92 km s^{-1} had a mean fragment diameter of 15.4 $\pm$ 6.6 μm. This would suggest that there are far fewer larger fragments at this speed, suggesting there may not be a fragment size effect visible in this data.

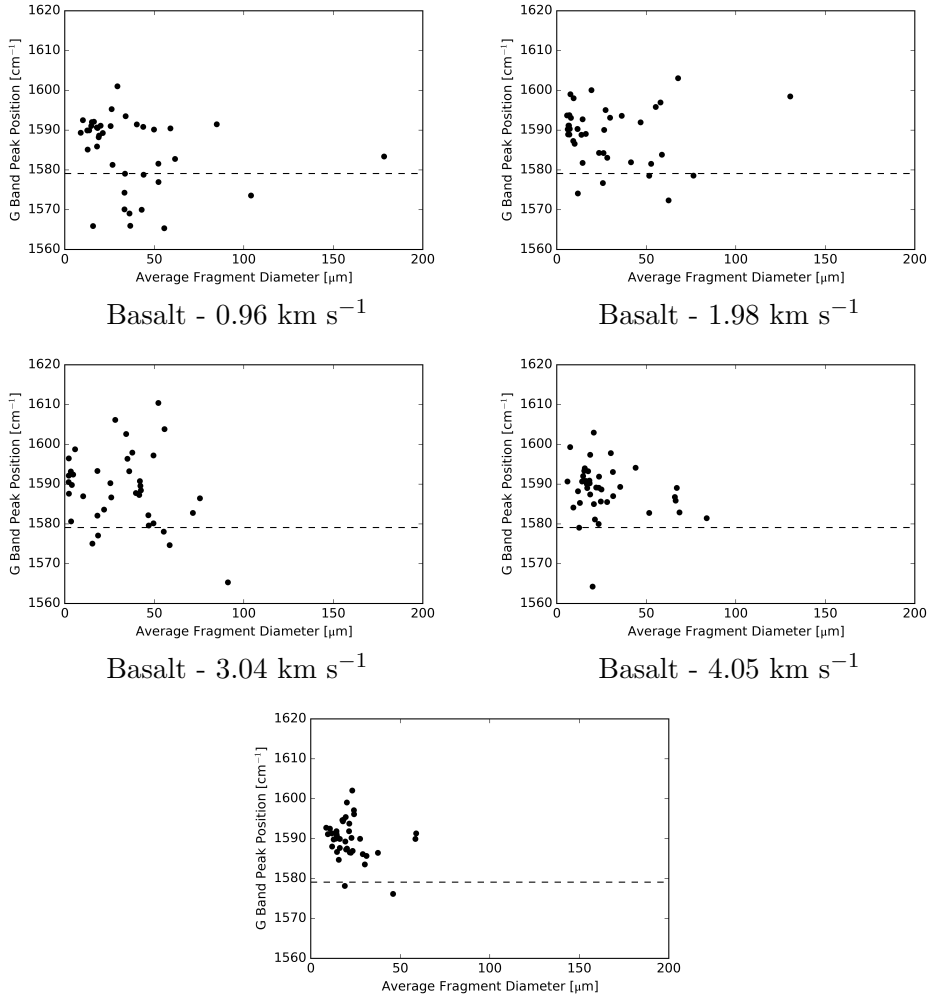

Figure 6.13: Comparison of G band peak position and the average diameter (average of the semi-major and minor axis) of fragments for basalt. The dashed line is the average projectile G band peak position averaged over all projectile spectra. This is 1579.1 cm^{-1} for basalt. There is one data point excluded from the 0.96 km s^{-1} plot which would have been at approximately 250 μm, 1570 cm^{-1}. The reason it is not plotted is due to making the scale of each panel comparable and still being able to discern a pattern without cramping the majority of the data at one end of each plot.

It is not the same for shale (Figure 6.14). At the slower speeds, there are a considerable number of large fragments with G band peak positions around the average projectile G band peak position (the dashed line). The number of larger fragments decreases with increasing shot speed, as shown in Chapter 5. It appears to only be the smaller fragments which have experienced a G band peak position shift. The ma-

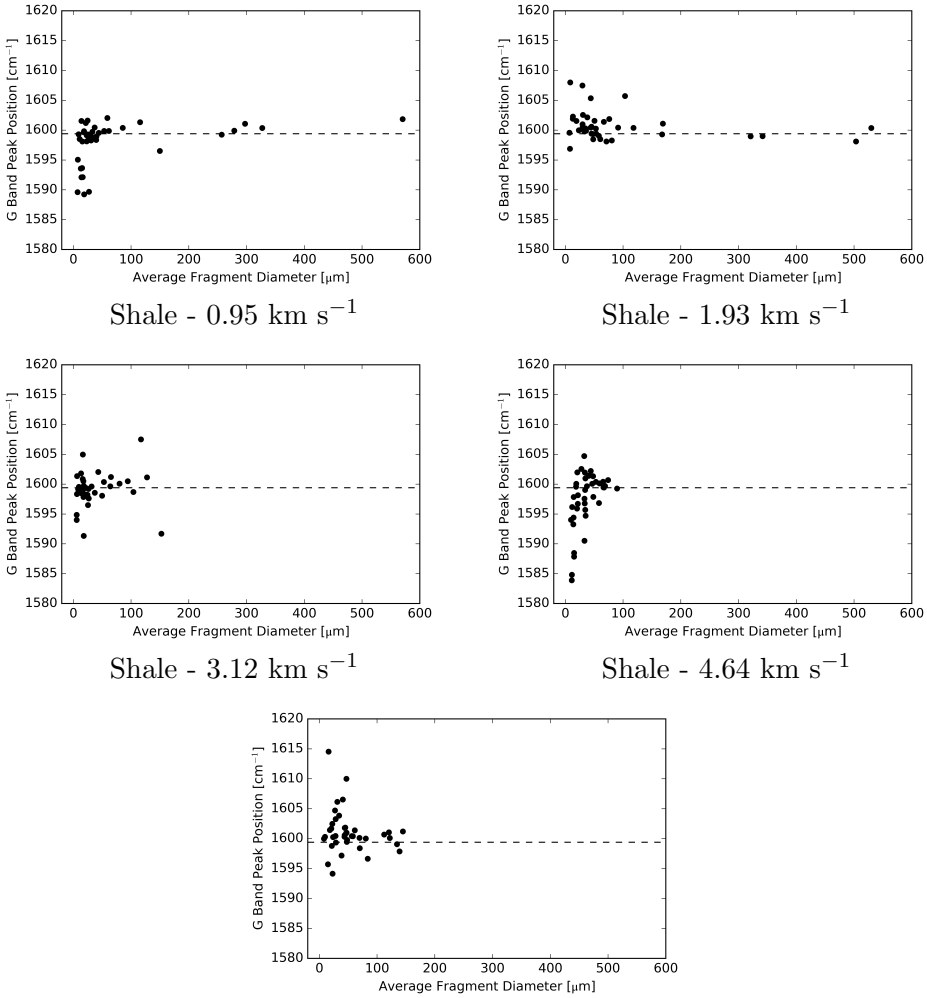

Figure 6.14: Comparison of G band peak position and the average diameter (average of the semi-major and minor axis) of fragments for shale. The dashed line is the average projectile G band peak position averaged over all projectile spectra. This is 1599.4 cm^{-1} for shale.

jority of the largest fragments experience far less of a positive or negative shift than the smaller fragments. The majority of fragments exhibiting a significant shift are all smaller than 100 μm for the slower shots (less than 1.93 km s^{-1}), and smaller than approximately 40 μm for the remaining shots. Both these values are considerably greater than the average fragment size for each shot (see Table 5.3).

For graphite (Figure 6.15), again the number of large fragments decreases with increasing speed. It would appear in every shot for graphite, that the smaller fragments

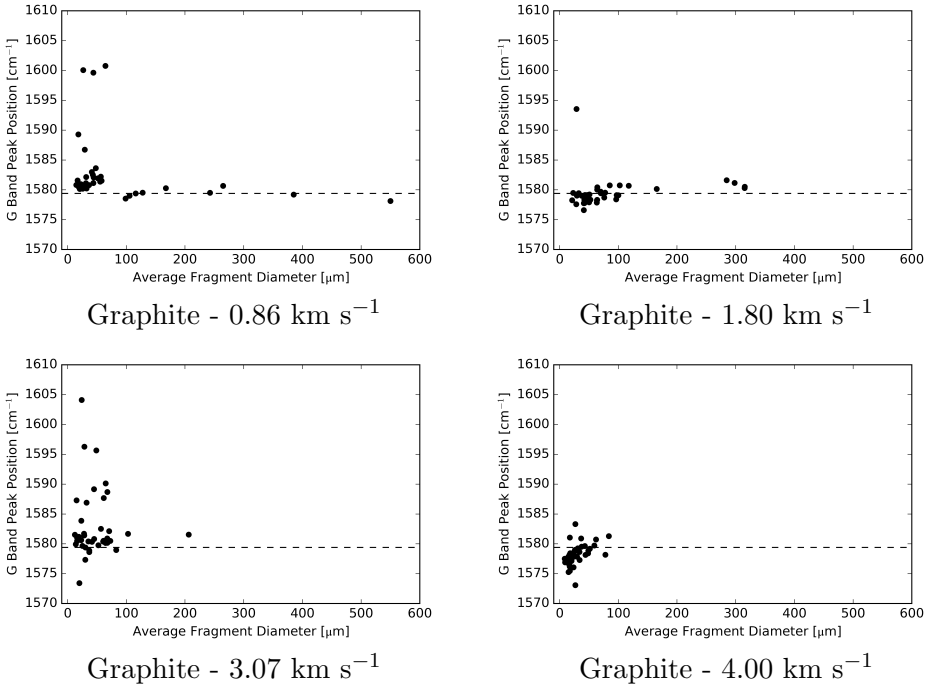

Figure 6.15: Comparison of G band peak position and the average diameter (average of the semi-major and minor axis) of fragments for graphite. The dashed line is the average projectile G band peak position averaged over all projectile spectra. This is 1579.4 cm^{-1} for graphite.

experience a shift, however, sometimes it is upward in wavenumber, and sometimes downwards - but either way it is of low magnitude. Therefore it can be argued that for both shale and graphite, the smaller fragments experience the most significant G band peak position shifts.

D Band Width

In order to determine the full extent of the effect of shock on the carbon D and G bands, the band width (the FWHM) also has to be considered. Figure 6.16 shows the average D band width with the average projectile D band width subtracted for each shot. Therefore, a positive value suggests a broadening post-impacts and a negative value indicates a narrowing of the band width.

For basalt (Figure 6.16a) there appears to be a negative trend with shock pressure.

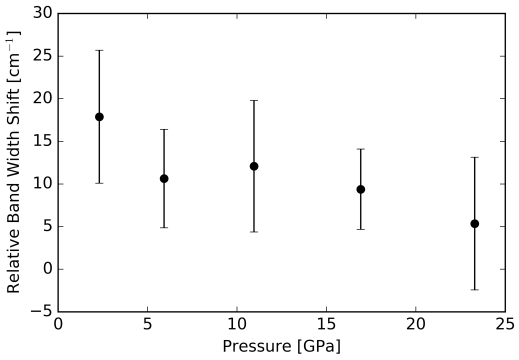

(a) Basalt

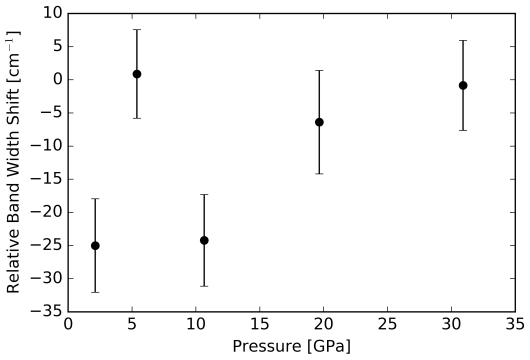

(b) Shale

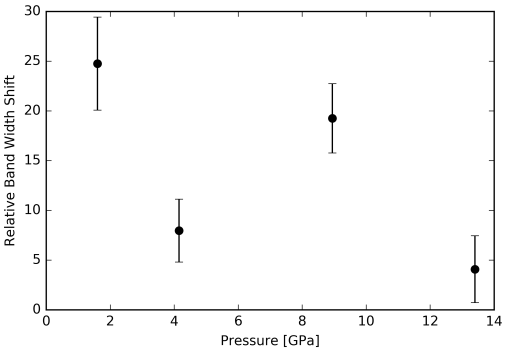

(c) Graphite

Figure 6.16: Relative D band width shift against peak shock pressure, determined using the PIA. The relative shift is the average fragment D band width with the average projectile D band width subtracted from it. Therefore, a positive value would mean the fragment's width is broader.

The D band has become broader as a result of being shocked. However, this broadening effect appears to decrease with increasing shock pressure and, extrapolating, appears negligible above approximately 25 GPa. The maximum relative D band width shift is 17.9 ± 7.8 cm^{-1}. The cause of this decreasing width broadening effect could be due to increasing fractions of the most significantly shocked material being destroyed at the increasing shock pressures, or it could be a shock annealing effect. Internal impurities may be destroyed as a result of the impact, and while the material cools slowly it reorganises into a more strong/purer sample resulting in a reduced broadening effect. Shock annealing has been observed before, an example is Rubin (2006*a*) where it was noted that annealing in three EL chondrites erased shock effects in pyroxene, producing grains with sharp optical extinction. In addition, Rubin (2006*b*) observed the creation of

mosaicized olivines. Furthermore, annealing as a result of shock pressure was observed in obsidian and its fused glass. This occurred at peak shock pressures greater than 25 GPa and resulted in a density reduction (Shimoda et al. 2004). Zion et al. (2017) investigated the annealing effect on Raman spectra of monolayer graphene samples irradiated with various doses of radiation. When annealing at temperatures below 500 °C there was a significant decrease in both the D band (attributed to defects) and the 2D band (at 2700 cm^{-1}, attributed to intact lattice structure). This is explained by annealing-induced enhanced doping (adding impurities). Further annealing in a vacuum at a temperature up to 1000 °C led to a significant increase in the 2D band and a continuous decrease in the D band. This suggests evidence for the partial removal of the defects and restoration of the damaged lattice (Zion et al. 2017).

Although having a larger degree of scatter, graphite also appears to suggest that there is initially a large effect, but with increasing shock pressure the broadening effect decreases in magnitude (see Figure 6.16c). The same explanation for the D band width of basalt would be applicable here.

The shale data is scattered and has no identifiable trend. The effect of shock pressure on the D band width appears to be a narrowing effect for two shots (2.12 and 10.3 GPa). The relative width change for these two shots are both approximately -25 cm^{-1}. The remaining three data points do not show any effect of shock.

G Band Width

Figure 6.17 shows the average fragment G band width with the average projectile G band width subtracted for each shot. Therefore, a positive value suggests a broadening post-impacts and a negative value indicates a narrowing of the band width.

For basalt (Figure 6.17a), the data appears to be scattered with negative values. No trend is discernible and the data seem to lie on an average value of -12.9 cm^{-1}. The G band spectra for basalt thus appear to experience a band narrowing. This is contrary

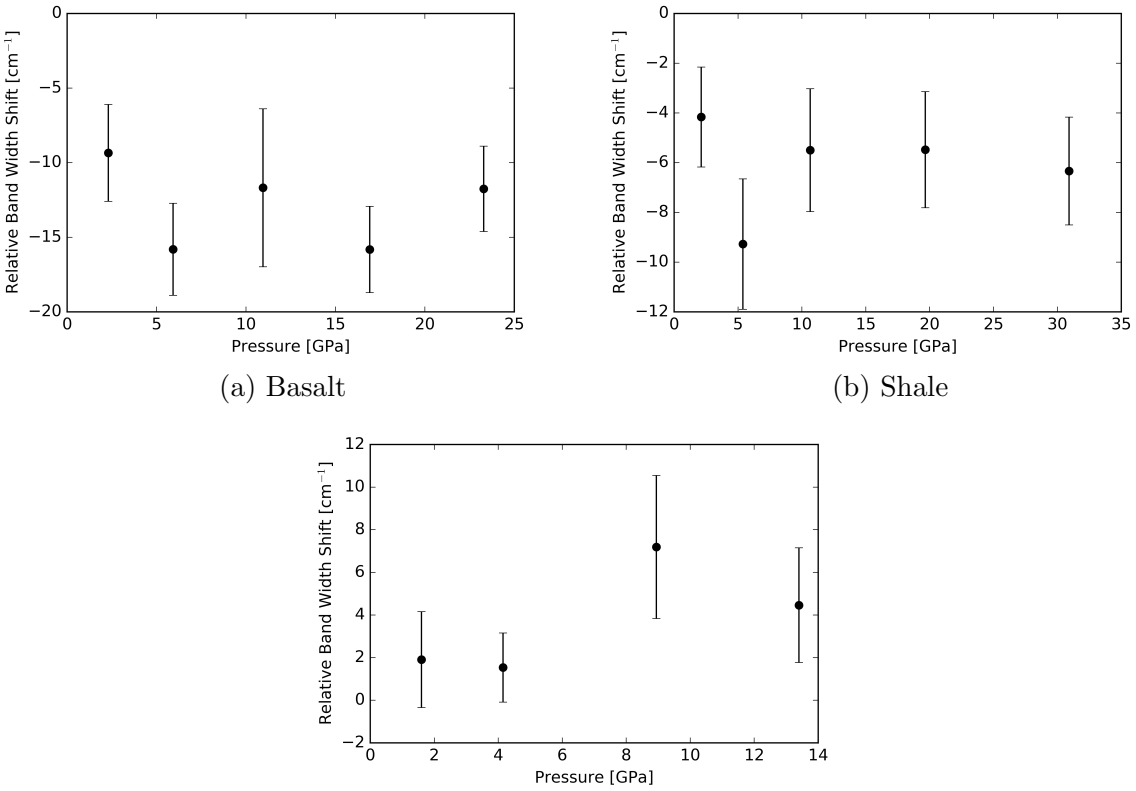

(a) Basalt

(b) Shale

(c) Graphite

Figure 6.17: Relative G band width shift against peak shock pressure determined using the PIA. The relative shift in the average fragment width with the average projectile width subtracted from it. Therefore, a positive value would mean the fragment's width is broader.

to what was thought would happen. Possibly this is an annealing effect as mentioned in a prior discussion. This annealing effect is causing internal impurities to be removed from the crystalline structure, hence leading to the bands becoming narrower.

For shale (Figure 6.17b), there is also possibly a negative trend. However, the values appear to lay scattered around an average value of -6.2 cm^{-1}. It would seem that for every shot, a band narrowing effect is occurring. A possible cause of this could again be shock annealing, as discussed previously. The absolute narrowing of shale G band width is 8.1%, whereas for basalt it is 12.2%. This suggests that the G band spectra for basalt have experienced that most significant narrowing effect. Determining this percentage shift takes into account that the G band widths for the basalt spectra are

wider than shales.

By contrast, for graphite, it would appear that the fragment spectra from the two shots at higher pressure experienced a G band broadening effect. These G band spectra were broadened by 7.2 ± 3.4 and 4.5 ± 2.7 cm^{-1} respectively. For the lower shock pressures, there was no observable effect. The absolute broadening effect for the G band of graphite across all shots is 17.6%. In comparison to basalt and shale, this is the largest shift and is a broadening rather than a narrowing effect. The broadening effect seen for the G band of graphite is due to the well-ordered crystalline structure being distorted by the interaction of the shock wave, causing a strain to the lattice.

D2 Band Width

As for the D and G band widths, Figure 6.18 shows the average D2 band width for graphite with the average projectile D2 band subtracted for each shot.

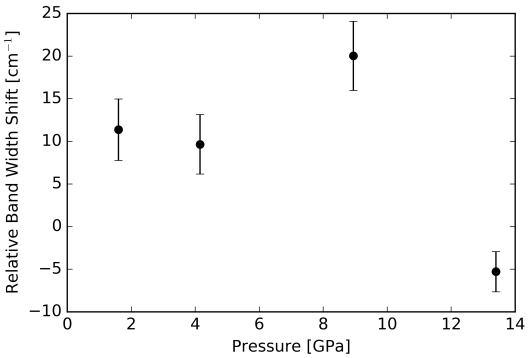

Figure 6.18: Relative D2 band width shift for graphite against peak shock pressure, determined using the PIA. The relative shift if the average fragment width with the average projectile width subtracted from it.

From Figure 6.18 it would appear that the D2 band width in the graphite carbon spectra has a scattered result. The fragments in all shots experienced a change, however, in three shots it was a broadening effect and in the final shot, it was a small narrowing effect (if any). This scatter could be due to the natural variation in the raw sample. From Figure 6.9, the D2 band width had a range of 40 cm^{-1}. When considering this in

the interpretation of the results, the largest shift seen in Figure 6.18 is approximately 20 cm^{-1}, this is well within the range of the raw sample. Although it is hoped that this is accounted for by averaging the data.

Band Separation

Another aspect of the D, G and D2 bands of Raman spectroscopy is the separation between the D and G, and between the G and D2. Figure 6.19 shows the separation between the D and G band and how it changes with peak shock pressure. For this, the average fragment D-G band separation has had the average projectile D-G band separation subtracted. The average projectile D-G band separation for basalt, shale and graphite is 240.8 ± 1.25, 263.7 ± 0.63 and 231.5 ± 0.13 cm^{-1} respectively.

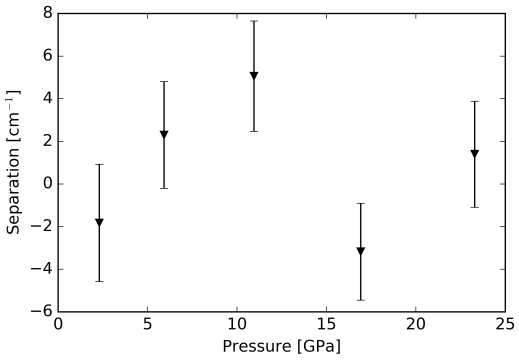

(a) Basalt

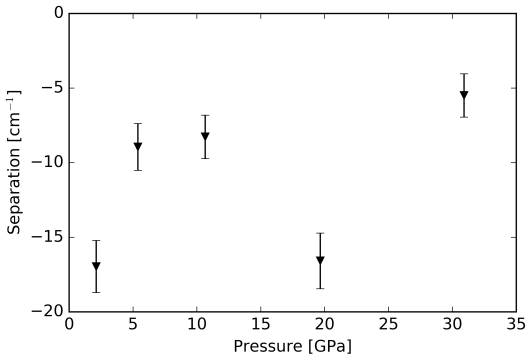

(b) Shale

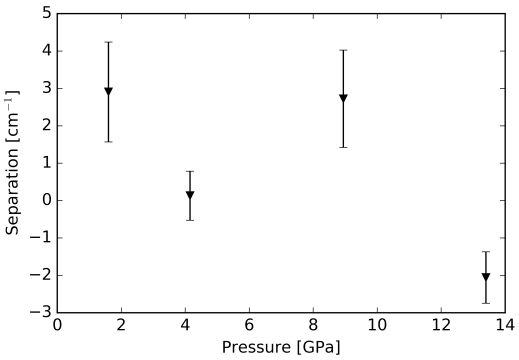

(c) Graphite

Figure 6.19: D and G band separation versus peak shock pressure determined using the PIA. This is the average fragment peak separation for each shot with the average peak separation for every projectile subtracted from it.

For basalt (Figure 6.19a), the data appears scattered around zero. Therefore there would seem to be no effect of shock pressure upon the D-G band separation. There are two data points which appear to suggest an effect on the D-G band separation at 10.9 and 16.9 GPa. However, one suggests the bands are moving further apart (10.9 GPa) and the other, closer together (16.9 GPa). The scatter is thus likely due to the natural variance of the raw sample.

For shale (Figure 6.19b), again the data appear scattered. However, the scatter is not around zero but -11.3 cm^{-1}. Therefore, it would appear that the shock pressure effect to the D-G separation for the shale spectra moves them closer together.

For graphite (Figure 6.19c), the data is also scattered. Three data points do suggest an effect of shock pressure upon the D-G separation, however. Both data points at 1.60 and 8.94 GPa suggests a shift further apart, and at 13.4 GPa a shift closer together. As before, given the low magnitude of the effect the scatter is likely a result of the variation in the raw sample.

Figure 6.20 shows the separation between the G and D2 band and how it changes with peak shock pressure for graphite. For this, the average fragment G-D2 band separation has had the average projectile G-D2 band separation subtracted. The average G-D2 band projectile separation is 36.6 ± 0.21 cm^{-1} for graphite.

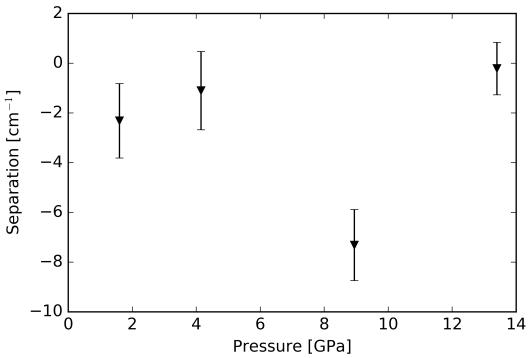

Figure 6.20: G and D2 band separation for graphite versus peak shock pressure determined using the PIA. This is the average fragment peak separation for each shot with the average peak separation for every projectile subtracted from it.

From Figure 6.20 it seems there is no trend. The figure would suggest that the two bands appear closer together but is not that significant with just one data point showing a large effect. As the bands are being shifted closer together, it could suggest that there would be significant difficulty in determining the G and D2 bands apart, especially if their width became broader. This could lead to misinterpretation of spectra.

R1 and R2 Ratios

The effect of shock pressure on the structural organisation of the samples is looked at next. To recap, the larger the R1 and R2 values, the more structurally disorganised the material is. Furthermore, R1 is a better determination of structural organisation when it is greater than 1. R2 is better for values of R1 less than 1. Figure 6.21, 6.22 and 6.23 are a comparison of the R2 values (Equation 6.2) with the R1 values (Equation 6.1) for each shot in this chapter.

For basalt (Figure 6.21) it would seem that for the projectile the data lays along a similar trend. For the lower speeds (0.96, 1.98 and 3.04 km s^{-1}), the fragment values seem to be quite close to the projectile with relatively little scatter around them. However, there is a tendency to higher R2 values in the fragments, which shows up most clearly at 4.05 km s^{-1}. This means the D band area is increasing, or conversely, the area of the G band is decreasing. This means there is increasing disorder. Looking at the 4.96 km s^{-1} shot (Figure 6.21e), the projectile data is in an unusually compact region of R1 v.s. R2, whereas the fragment data is distributed as before.

For shale (Figure 6.22) the projectile data points lay clustered together and on a similar trend line comparable to that in basalt. The fragment data appears to be scattered for the 0.95 km s^{-1} shot. For this shot and the 1.93 km s^{-1} shot, the R2 values have increased. For the 3.12 km s^{-1} shot, there is an increase in both R1 and R2 values. For the 4.64 km s^{-1} shot, there appears to be an increase and decrease in both higher R1 and R2 values. The lower values, meaning more organised, could be fragments at the rear of the projectile meaning they didn't experience significant shock

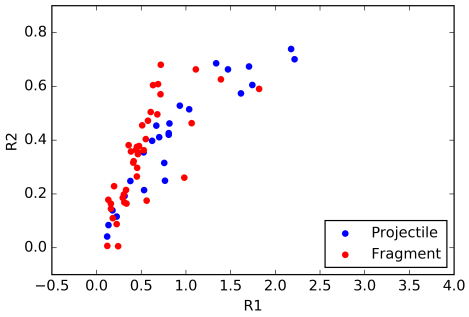

(a) Basalt - 0.96 km s^{-1}

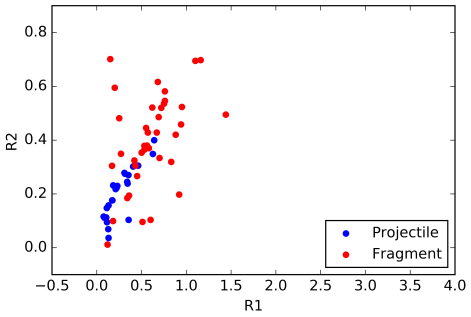

(b) Basalt - 1.98 km s^{-1}

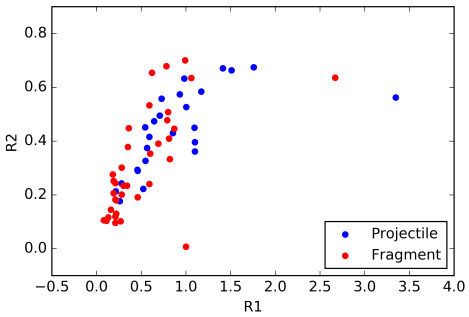

(c) Basalt - 3.04 km s^{-1}

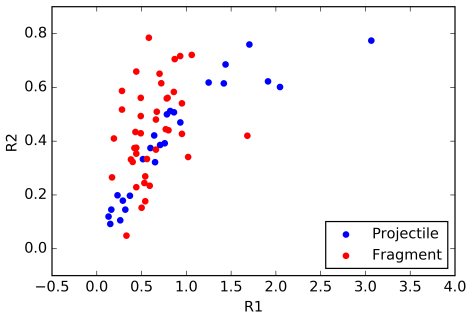

(d) Basalt - 4.05 km s^{-1}

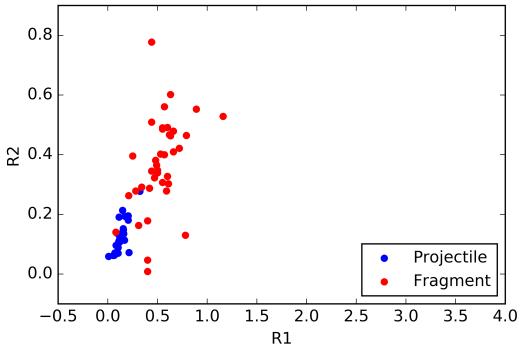

(e) Basalt - 4.96 km s^{-1}

Figure 6.21: R2 versus R1 values for each shot of basalt. The greater the R1 and R2 values are the more disorganised the structure of the material is. There is one data point excluded from the 1.98 km s^{-1} shot at approximately R1 = 5, R2 = 0.5. This was excluded to allow the data to all be plotted on appropriate scaled figures.

pressures. Therefore, these data points would be very similar to the projectile data points. Finally, for the 6.13 km s^{-1} shot, a greater number of projectile data points have much higher R2 values than the other shots. For this projectile, there was an increase in the R2 values mostly (some also had increased R1 values). The R2 values in

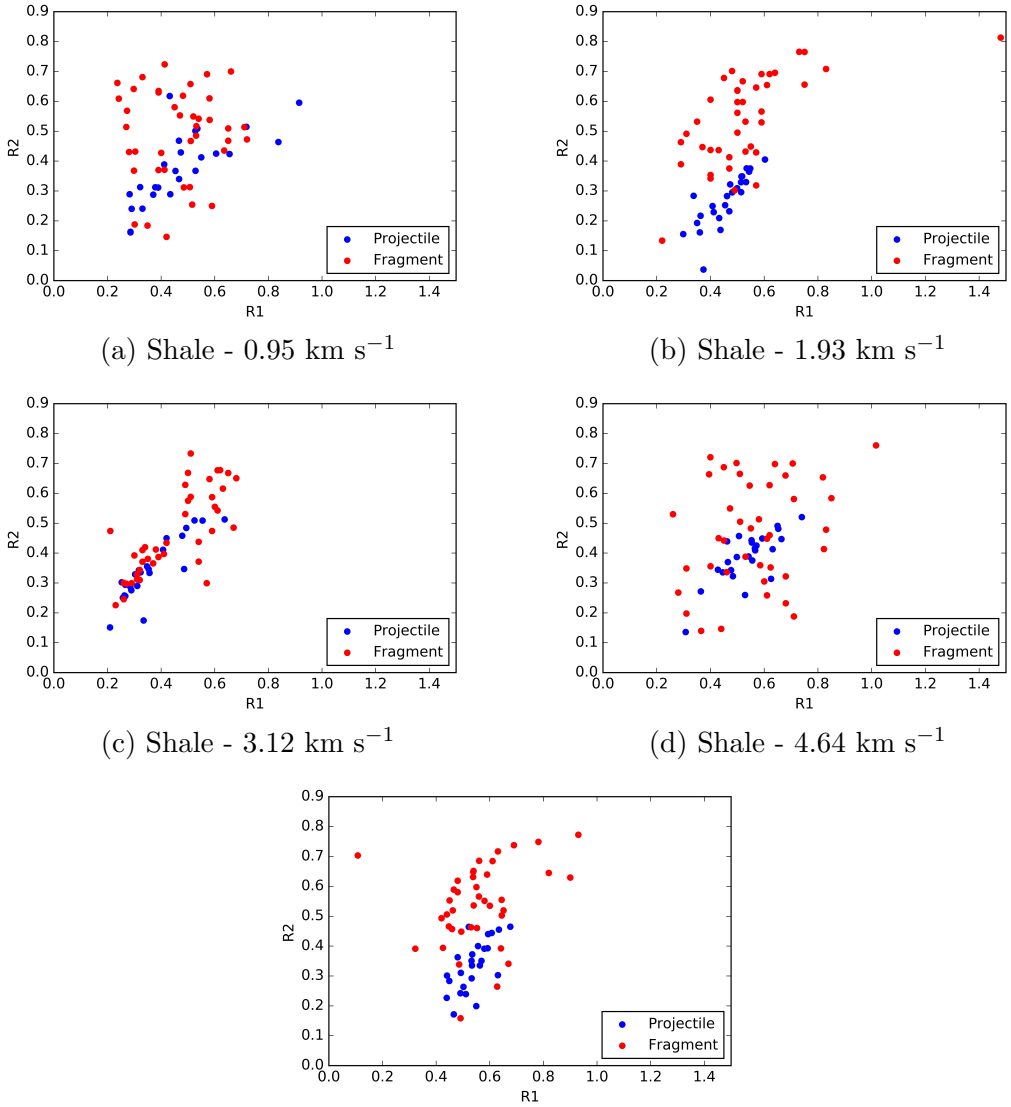

(a) Shale - 0.95 km s^{-1}

(b) Shale - 1.93 km s^{-1}

(c) Shale - 3.12 km s^{-1}

(d) Shale - 4.64 km s^{-1}

(e) Shale - 6.13 km s^{-1}

Figure 6.22: R2 versus R1 values for each shot of shale. The greater the R1 and R2 values are the more disorganised the structure of the material is.

each shot seem to be no greater than the previous shot speed. Possibly to get further structural disorganisation higher peak shock pressures, and hence a greater speed (or different target material), are required. Overall, at most speeds, there was an increase in R2 with little change in R1.

In Figure 6.23 the data are shown for graphite. The projectile data points lay relatively close together with a similar trend of R1 and R2 increasing linearly together,

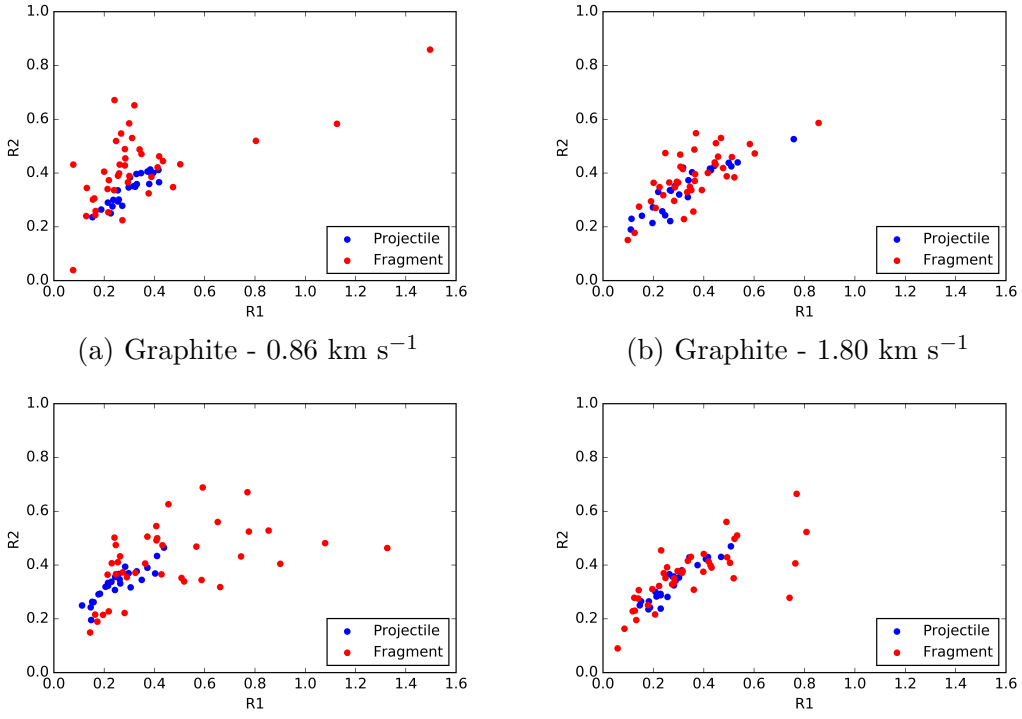

(a) Graphite - 0.86 km s^{-1}

(b) Graphite - 1.80 km s^{-1}

(c) Graphite - 3.07 km s^{-1}

(d) Graphite - 4.00 km s^{-1}

Figure 6.23: R2 versus R1 values for each shot of graphite. The greater the R1 and R2 values are the more disorganised the structure of the material is. There are two data points excluded from the 3.07 km s^{-1} shot at approximately R1 = 2.2 and 4.3, and R2 = 0.7 and 0.9 respectively. These were excluded to allow the data to all be plotted on appropriate scaled figures.

as for basalt and shale in Figure 6.21 and 6.22. However, they are clustered at a lower R1 value than the projectile data for basalt and shale. This would be due to graphite being more ordered. The fragment R1 and R2 values are both higher than the majority of the projectile values although the effects are small at 4.00 km s^{-1}. This suggests that impacting the graphite causes structural disorganisation.

Overall, Figure 6.21, 6.22 and 6.23 suggest that there is negligible difference between projectile and fragment R1 and R2 values for shots less than 4 km s^{-1}. Whereas for the shots greater than this speed there is a small difference occurring.

To investigate further, Figure 6.24 shows the plots for all the R2 and R1 values for each material across every shot.

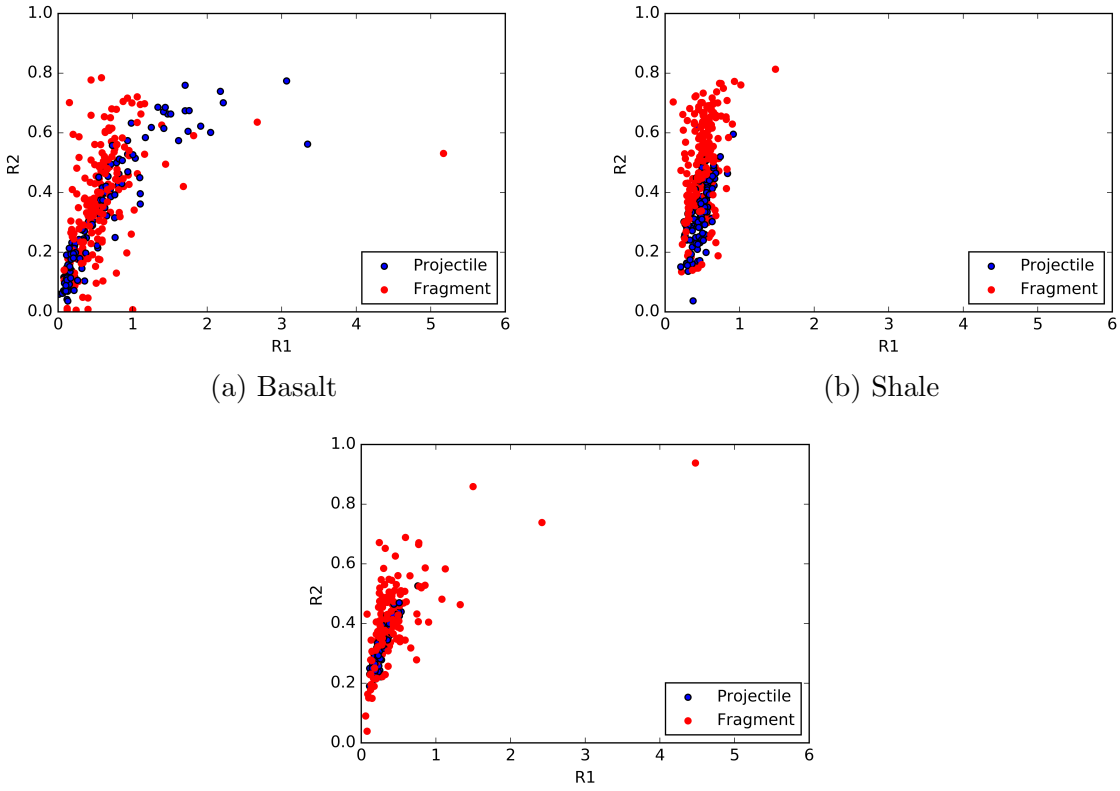

(a) Basalt

(b) Shale

(c) Graphite

Figure 6.24: All R2 values versus all R1 values for basalt, shale and graphite. Larger R1 and R2 values means more structural disorganisation.

Comparing each projectile's R1 and R2 values, it would seem that graphite is the most homogeneous in structural organisation, as expected. This is due to the projectile R1 and R2 values being low. Shale appears to be the next most structurally organised, with basalt being the least.

Looking at the effect of the shock pressure on the fragment's spectra, all materials suggest that there is an increase in R2 value. Shale appears to have the least increase in R1 value, basalt being the second least, whereas graphite has a few fragments with increased R1 values. The main group of the fragment data for basalt have no greater R1 and R2 values than approximately 1.2 and 0.7 respectively. The same for shale and graphite are approximately (R1:R2) 0.8:0.8 and 1.0:0.7 respectively. Therefore, basalt has the largest R1 value and shale has the largest R2 value.

To look closer at how the values of R1 and R2 change with peak shock pressure, Figure 6.25 and 6.26 show the average R1 and R2 fragment value with the average projectile R1 and R2 values subtracted against peak shock pressure.

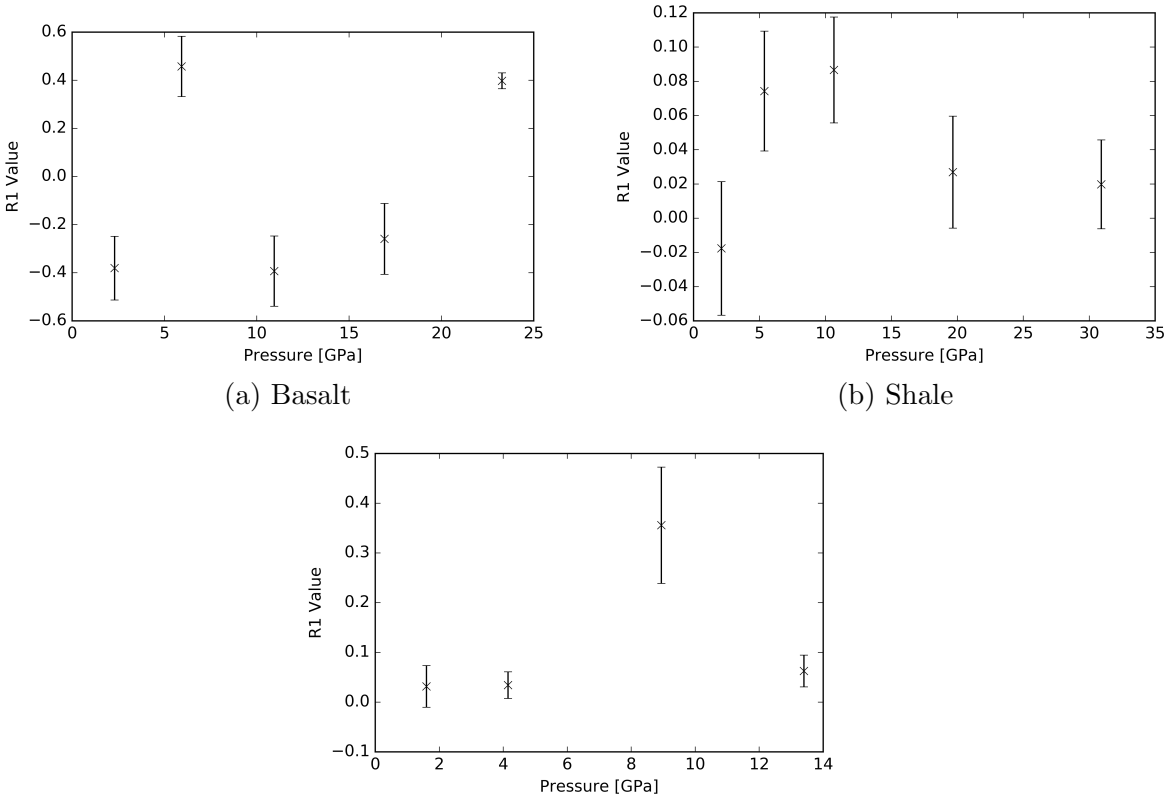

(a) Basalt

(b) Shale

(c) Graphite

Figure 6.25: R1 values for basalt, shale and graphite versus peak shock pressure. The peak shock pressure was determined using the PIA. Negative means a lower fragments R1 value, while positive means higher fragment R1 value. The error bars represent the errors on the mean.

For basalt (Figure 6.25a), the R1 values appear both above and below the projectile R1 values (positive and negative). For the 0.96, 3.04 and 4.05 km s^{-1} (2.3, 10.9 and 16.9 GPa) shots, the R1 value is negative suggesting post-impact/fragment R1 value is lower than the projectile R1 value implying it has become more structurally organised, with the opposite for the other two shots. This scatter could be as a result of the difficulty in acquiring decent D band spectra for basalt. Seeing as the R1 value relies on the D band amplitude, poor D band spectra would bias the results and cause scatter.

For both shale and graphite most fragment R1 values are greater than their corresponding projectile R1 values (positive difference), although for three shots in shale and two in graphite the shifts are not significant due the error bars crossing or meeting zero. Nonetheless, the increase suggests increased structural disorganisation. For both shale and graphite there appears to be no trend with peak shock pressure. Possibly these shock regimes generate insufficient pressures to produce noticeable differences between projectile and fragment R1 values.

A possible explanation for the large error bars and high mean fragment R1 value in Figure 6.25c at 8.94 GPa, is that a greater proportion of fragment spectra are of fragments closer to the front of the projectile upon impact. This means that they have experienced a greater proportion of this pressure, and hence have been affected more. This could be an indication that this shot has produced anomalous results. Although it had been hoped that taking 40 fragment spectra per shot would have minimized the effect of this. However in order to determine this either more fragments from the shots would need Raman analysis, or further shots at a range of speeds would be required.

For the average R2 values (Figure 6.26), again basalt is scattered with the R2 values being greater and less than zero (their projectile R2 values). One shot suggest no significant effect as the error bars cross zero (16.9 GPa). As stated before, this scatter is probably due to the D band spectra being poor for basalt but it could be also due to the variability in the raw sample.

Again for shale and graphite, fragment R2 values are greater than their average projectile R2 values, with the exception of the 2.1 GPa Shale shot. The results suggest, as with the R1 values, that the structural order is more disorganised post shot. However, due to the scatter there doesn't seem to be a clear trend with peak shock pressure.

The shock effects seen here on the carbon Raman spectra is expected to be similar when scaled up to larger impacts. Wehrenberg et al. (2017) states that twinning and related lattice effects occur on time scales of picoseconds for shocks. Any changes that arrive from such mechanical defects will have arisen from the shock wave passage, and

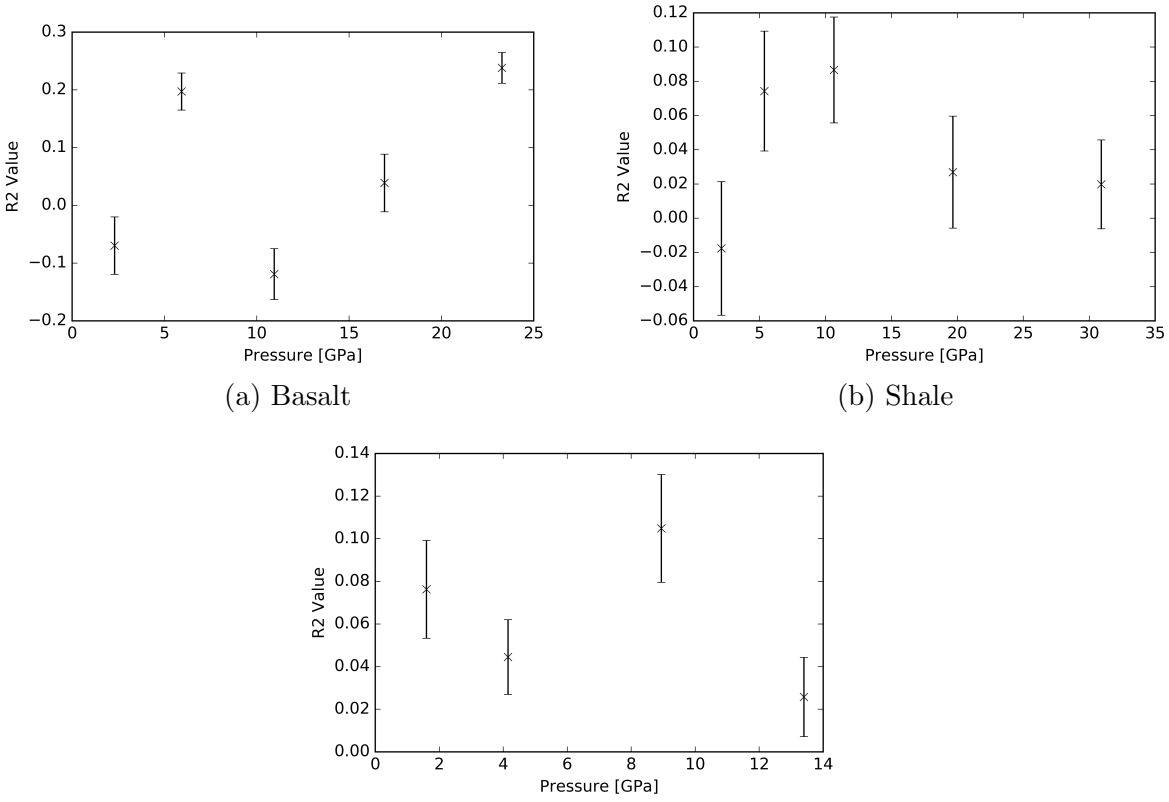

(a) Basalt

(b) Shale

(c) Graphite

Figure 6.26: R2 values for basalt, shale and graphite versus peak shock pressure. The peak shock pressure was determined using the PIA. Negative means a lower fragments R2 value, while positive means higher fragment R2 value. The errors bars represent the error on the mean.

hence the duration of how long it stays shocked is not relevant. However, any melting effects take time, so longer scale homogenisation of materials due to melt and separation out can depend on long time scales. This means that any effect due to the generation of mechanical defects is shock related, and the passage of the shock in these experiments is of sufficient duration for these to occur. However, any more general effect due to heating and melting will depend on the shock duration, elevated temperatures reached and how long that is sustained.

6.3.2 A Comparison of G Band Width and G Band Peak Position - Thermal Maturity

Comparing the G band width with the G band peak position indicates the thermal maturity of carbon in a sample. Thermal maturity stands for the diagenetic changes of organic matter contained in a rock which generates hydrocarbons. It is a primary factor that determines whether a source can produce oil, gas, or condensates (Beyssac et al. 2002a, 2002b). Plotting these two attributes of the G band gives a good view of what happens to the G band post impact regarding any thermal processing. The direction of increasing thermal maturity is shown in Figure 6.27.

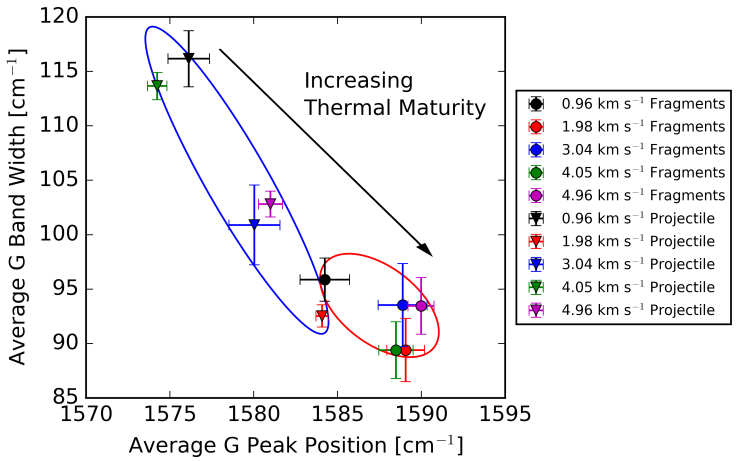

Figure 6.27: The G band width versus the G band peak position for basalt. This is an indication of the thermal maturity of carbonaceous materials in geological samples. The blue ellipse encloses the projectile data and the red ellipse that of the fragments. The arrow denotes the direction of increasing thermal maturity.

From Figure 6.27 it is clear that the basalt fragments have experienced a shift to higher G band peak position and a narrowing of the G band. The projectiles (in the blue ellipse) are spread over a wider range of widths and peak positions, whereas the fragments (in the red circle) are spread over a far smaller range. Looking at each individual shot, every fragment mean spectrum is narrower and shifted to higher band peak position than the projectile counterpart. The 4.96 km s^{-1} shot has the highest peak position (approximately 1590 cm^{-1}) but has not experienced the largest relative

peak position shift. The largest peak position shift appears to be the 4.05 km s^{-1} shot. This shot has also experienced the largest relative narrowing of the G band, with the next greatest narrowing being the 0.96 km s^{-1} shot. The shifting to a higher peak position is thought to be attributed to the strain on the carbon aromatic rings. The narrowing of the G band width is possibly due to impurities being destroyed in the fraction of a microsecond during impact. Overall, it would appear that there has been an increase in thermal maturity for basalt.

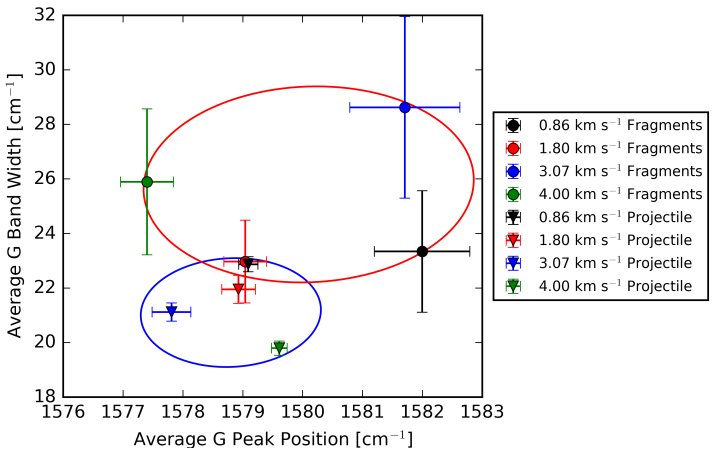

Figure 6.28: The average G band width versus the average G band peak position for graphite. This is an indication of the thermal maturity of carbonaceous materials in geological samples. The blue ellipse encloses the projectile data and the red ellipse that of the fragments.

From Figure 6.28 it would seem that graphite fragments have experienced a shift to a higher G band peak position, and the G band width has also become broader. The peak shift and width broadening are possibly due to the strain on the crystalline lattice causing a greater disorder in the system. Looking at the figure on a shot by shot basis, all but the 4.00 km s^{-1} shot are broader and to a higher peak position. For this particular shot, it would appear that the fragments G band spectra did become larger, but there was a shift to lower wavenumbers for the peak position. The scatter could be due to the natural variance of the raw sample. Overall, it would seem that graphite has not experienced an increase in thermal maturity.

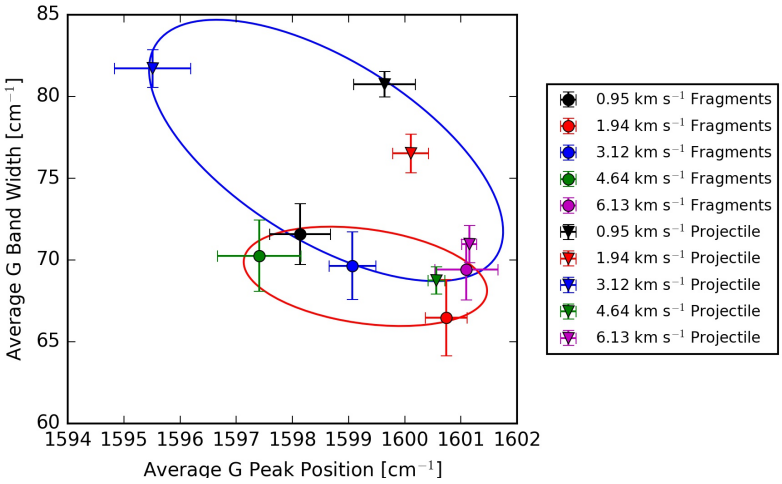

Figure 6.29: The average G band width versus the average G band peak position for shale. This is an indication of the thermal maturity of carbonaceous materials in geological samples. The blue ellipse encloses the projectile data and the red ellipse that of the fragments.

For shale (Figure 6.29) it would seem that the major effect on the fragment G band spectra was a narrowing. There were only two shots where the fragments were shifted to a higher peak position (1.94 and 3.12 km s^{-1}). The rest were shifted to lower peak position. Furthermore, one shot (4.64 km s^{-1}) had the fragment G band spectra broadening. For the impact effect on the thermal maturity of shale, Figure 6.29 would suggest that impacting has not increased the thermal maturity.

6.3.3 In-plane Graphite Crystallite Size of Polycrystalline Materials

The in-plane graphite crystallite size of materials consisting of many crystalline parts which are randomly oriented with respect to each other (polycrystalline), is given by:

$$La = 4.4(\frac{I_G}{I_D}) \tag{6.3}$$

where $I_{G,D}$ is the intensity of the G or D band peak respectively and the units for La are nm (Knight & White 1989, Jehlička et al. 2003). The constant of 4.4 is the C-C bond force constant with a 514.5 nm excitation laser. This is wavelength dependent. The laser used in this work had a 532 nm wavelength. This means that this value used is not the exact value. However, a wavelength difference of 17.5 nm shouldn't cause a significant difference to this number.

Figure 6.30 (basalt), 6.31 (shale) and 6.32 (graphite) are a comparison of the graphite crystallite size with G band peak positions for each shot.

For basalt (Figure 6.30) it would appear that in addition to the previous section's findings of the G band shifting to higher wavenumbers, the smaller in-plane graphite crystallite sizes appear to be shifted the most. This is most apparent in all but the 0.96 km s^{-1} shot. The reason it may not be apparent in that shot could be due to the low shock pressures.

For shale (Figure 6.31) there appears to be no significant difference between projectiles and fragments. Although there is no significant difference in the in-plane graphite crystallite size with increasing impact speed, there does appear to be a slight shift to different peak positions, as shown in past sections. A possible reason for not getting higher shifts could be due to the presence of a D2 band. At the highest peak position, they would be closely situated.

For graphite, in Figure 6.32 there would appear to be a similar pattern to that for basalt. The small in-plane graphite crystallite sizes are the ones to exhibit a G band peak position shift to higher wavenumbers. The larger La fragments do not exhibit this behaviour. This suggests that there could be an in-plane graphite crystallite size-G band shift relation.

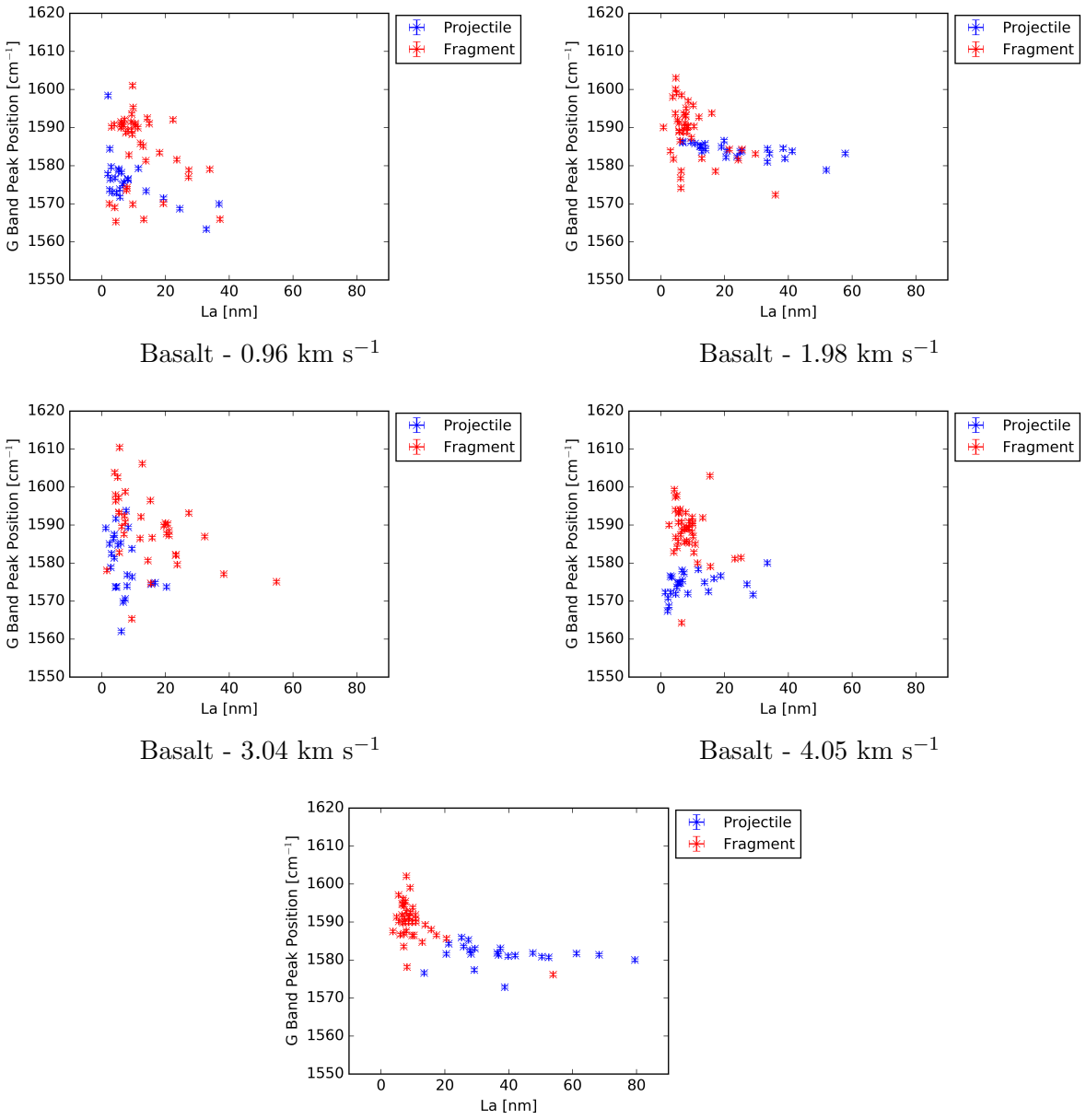

Basalt - 0.96 km s^{-1}

Basalt - 1.98 km s^{-1}

Basalt - 3.04 km s^{-1}

Basalt - 4.05 km s^{-1}

Basalt - 4.96 km s^{-1}

Figure 6.30: Comparison of G band peak position and the in-plane graphite crystalline size of polycrystalline materials for basalt. The error bars represent the spectral resolution of the Raman Spectrometer (0.3 cm^{-1}).

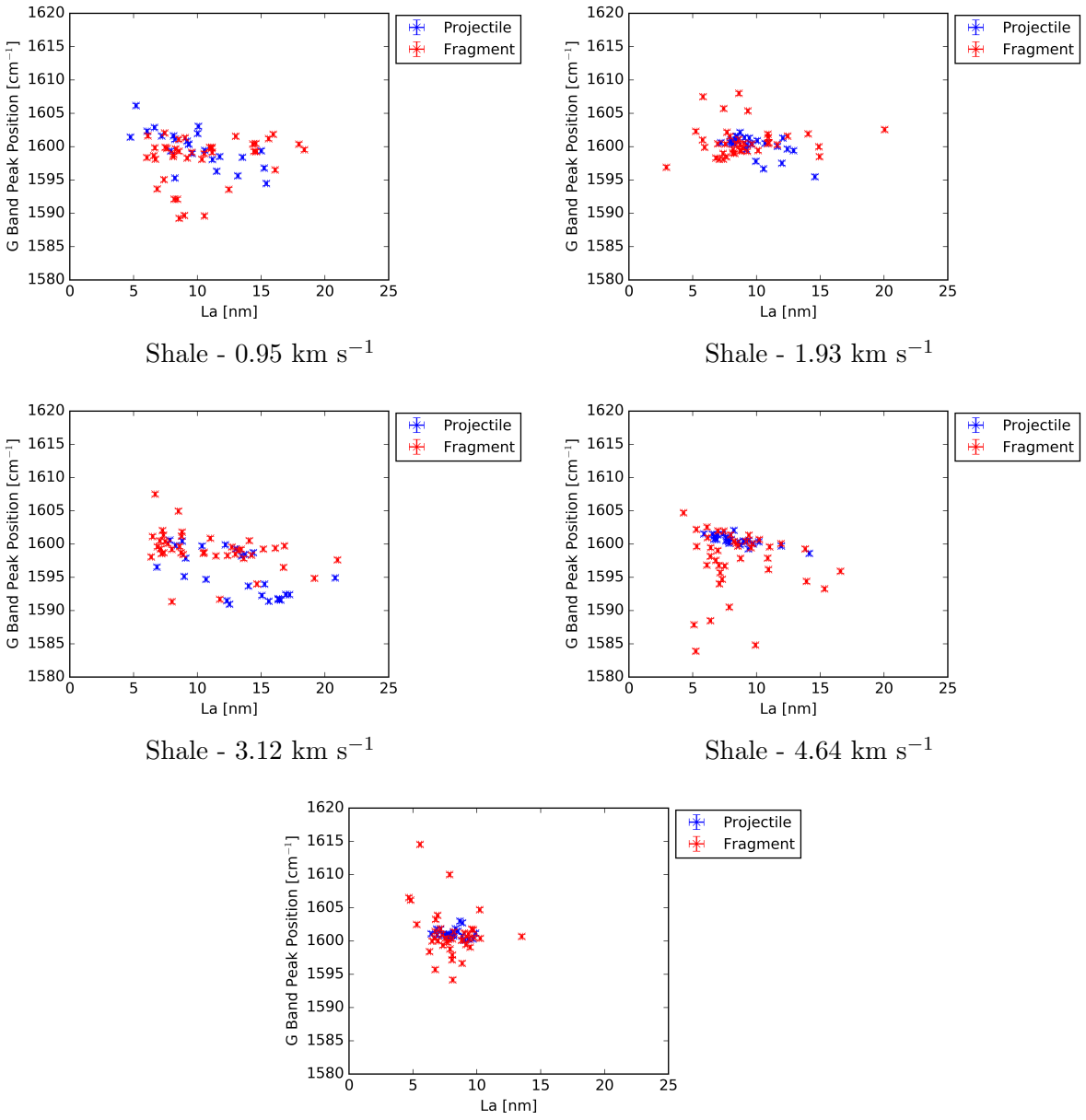

Shale - 0.95 km s^{-1}

Shale - 1.93 km s^{-1}

Shale - 3.12 km s^{-1}

Shale - 4.64 km s^{-1}

Shale - 6.13 km s^{-1}

Figure 6.31: Comparison of G band peak position and the in-plane graphite crystalline size of polycrystalline materials for shale. The error bars represent the spectral resolution of the Raman Spectrometer (0.3 cm^{-1}).

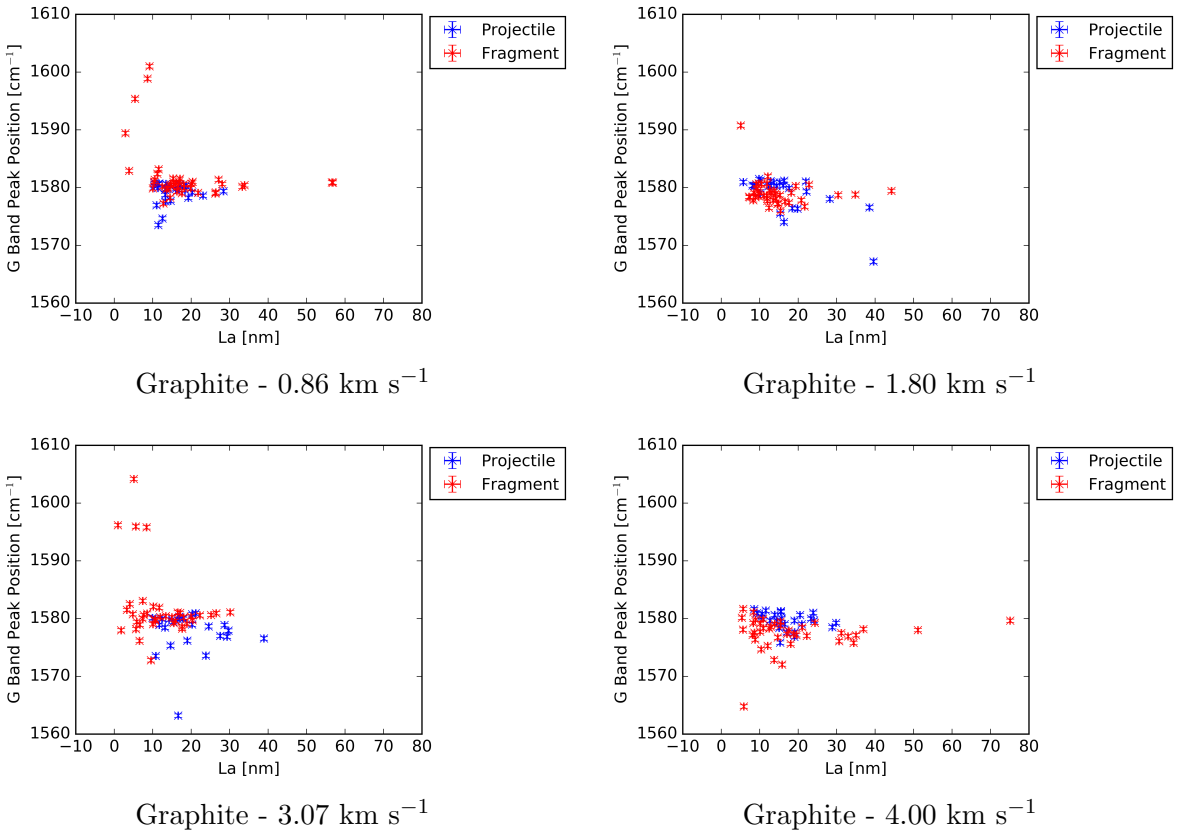

Figure 6.32: Comparison of G band peak position and the in-plane graphite crystalline size of polycrystalline materials for graphite. The error bars represent the spectral resolution of the Raman Spectrometer (0.3 cm^{-1}).

6.4 Implications for ExoMars 2020

One of the primary objectives for the ExoMars 2020 rover is the detection of extraterrestrial life. One method planned to achieve this goal is to use Raman spectroscopy (Rull et al. 2017). An important need to help this goal is the improvement of analytical techniques to identify an unambiguous signal of life. Currently, there is significant difficulty in identifying whether carbonaceous materials are biogenic or abiogenic. The difficulty is that both have very similar Raman spectral attributes. Therefore identification of the biogenicity of carbonaceous materials using Raman spectroscopy is usually accompanied by a visual identification.

In order to improve Raman spectroscopy as a method for life detection, Bower et al. (2013) acquired spectra for a range of microfossils and well-characterised meteorite samples as abiotic controls. Unfortunately, Bower et al. (2013) were unable to unambiguously identify biotic carbon from abiotic carbon, but did make useful steps for the improvement of this method. They suggest, for example, the comparison of the R1 value and the D band width to define the complexity of the carbonaceous material (i.e. highly complex organic materials (high compositional complexity) versus graphite (low compositional complexity)) the sample was derived from. Additionally, the clustering of microfossil samples in certain areas of a plot of G band peak position against G band width was held to be indicative.

The area where ExoMarx 2020 is likely to land could have some shocked rocks. It is possible, therefore, that some carbon bands analysed during the mission could be affected by the shock process.

Figure 6.34 is a comparison of the G band width with the G band peak position for basalt, shale and graphite. Alongside these is Figure 2 from Bower et al. (2013), where they plotted the spectral data for the microfossils and meteorites. What Bower et al. (2013) found was that microfossils samples predominantly clusters in the ellipse in Figure 6.33. This is represented by the green ellipse in Figure 6.34a, 6.34b and 6.34c.

The polygon in Figure 6.33 contains the crystalline graphite. This is represented by the black ellipse in Figure 6.34a, 6.34b and 6.34c.

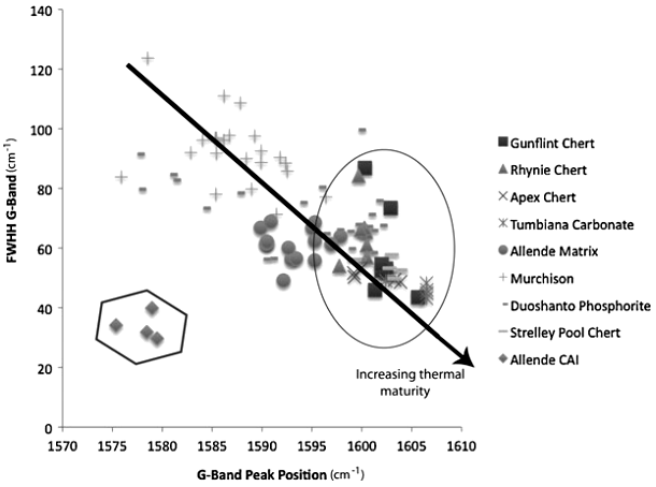

Figure 6.33: Figure from Bower et al. (2013) comparing the G band width with the G band peak position - an indication of the thermal maturity of carbonaceous materials. The arrow is in the direction of increasing thermal maturity. Microfossils cluster in the ellipse and crystalline graphite in the polygon.

From Figure 6.34a, basalt would appear to increase in thermal maturity enough for some fragment data points to lie in the circle where the microfossils cluster. Given that basalt contains abiogenic carbon this could suggest that, if analysed by the ExoMars 2020 rover, it could be misinterpreted as possibly being biogenic carbon. As impacting basalt increases the thermal maturity of the carbon, impacting basalt at higher shock pressures, like that of an asteroid onto the Martian surface, could shift the data even further into the green circle in Figure 6.34b.

For shale (Figure 6.34b) the projectile data is mostly within the microfossils cluster circle suggesting it could be biogenic carbon. This would make sense as shale is a sedimentary rock where hydrocarbons are extracted. Impacting the material appears to shift the bulk of the data further into the green circle. This improves the likelihood of a similar spectra material being identified as possibly biogenic carbon.

For graphite (Figure 6.34c) the projectile and fragment data both lie very close to the black circle indicating crystalline graphite. Impacting the graphite doesn't appear

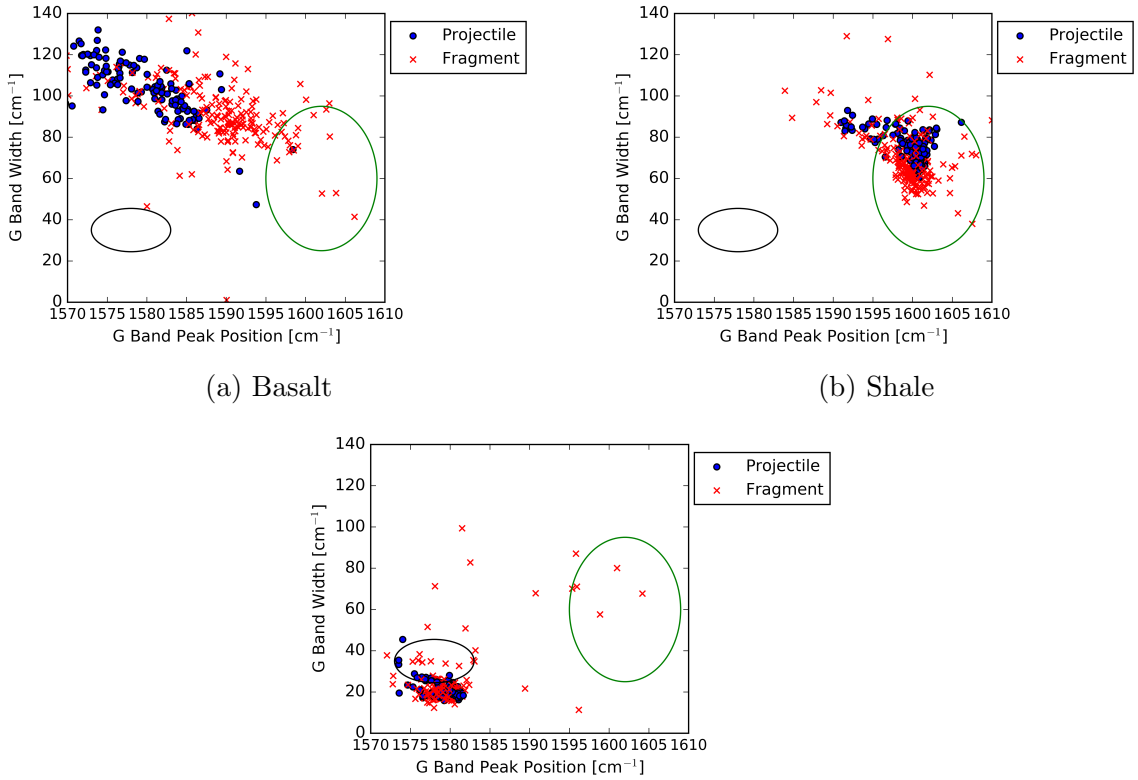

(a) Basalt

(b) Shale

(c) Graphite

Figure 6.34: Comparison of the G band width with the G band peak position - an indication of the thermal maturity of carbonaceous materials. From Bower et al. (2013) work in Figure 6.33, the microfossils generally cluster in the green ellipse and the crystalline graphite in the black ellipse in (a), (b) and (c).

to change its location in the plot. It does, however, introduce some scatter, with some fragment data lying within the green circle. This scatter suggests a loss of order for those fragments.

Figure 6.36 are a comparison of the D band width and the R1 value for basalt, shale and graphite. Figure 6.35 is Figure 4 from Bower et al. (2013), where they plotted the spectral data for the microfossils and meteorites. By plotting the D band width and the R1 values of their samples, Bower et al. (2013) has shown that the materials cluster into different groups that link with the precursor carbonaceous material (enclosed in each shape in Figure 6.35). The groups denote the carbonaceous compositional complexity, i.e. highly complex organic materials (high compositional complexity) versus

graphite (low compositional complexity). In Figure 6.36a the rectangles contains samples where the precursor carbonaceous material was compositionally complex, $\sim 27 > T < \sim 150°C$ (highly complex organic materials). This is represented by the green rectangle in 6.36a, 6.36b and 6.36c. The polygon contains samples where the precursor materials may have been less compositionally complex and hydrothermally overprinted, $\sim 300 > T < \sim 1000°C$. This is represented by the black rectangle in 6.36a, 6.36b and 6.36c. The ellipse in Figure 6.35 contains the purely crystalline graphite carbon, $T > 1000°C$, represented by the cyan rectangle in 6.36a, 6.36b and 6.36c (low compositional complexity).

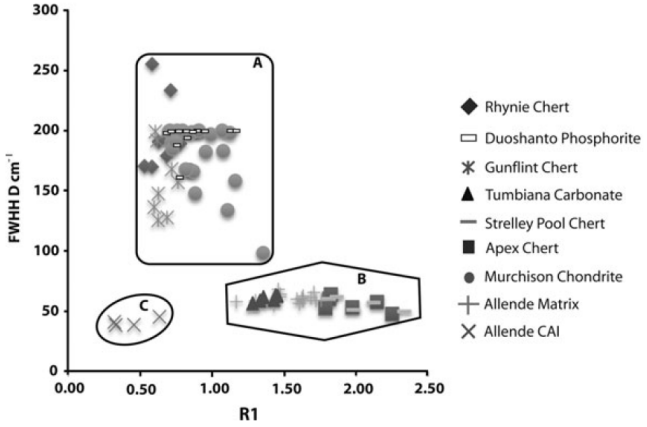

Figure 6.35: Figure 4 from Bower et al. (2013) comparing the D band width with the R1 value. The rectangle contains samples where the precursor carbonaceous material was compositionally complex (highly complex organic material), $\sim 27 > T < \sim 150°C$. The polygon contains samples where the precursor materials may have been less compositionally complex and hydrothermally overprinted, $\sim 300 > T < \sim 1000°C$. The ellipse contains the purely crystalline graphite carbon, $T > 1000°C$.

In Figure 6.36a, basalt lies in the corner of the green box and slightly towards the cyan box. The projectile data also has some points near the black box. The green box is where the precursor carbonaceous material was compositionally complex. The basalt data does appear to have more scatter than the shale and graphite data. Furthermore, impacting the basalt doesn't appear to shift the bulk of the data and doesn't increase the R1 value sufficiently enough to cause too much issue if this material was being identified. However, at higher peak shock pressure this may not be the same.

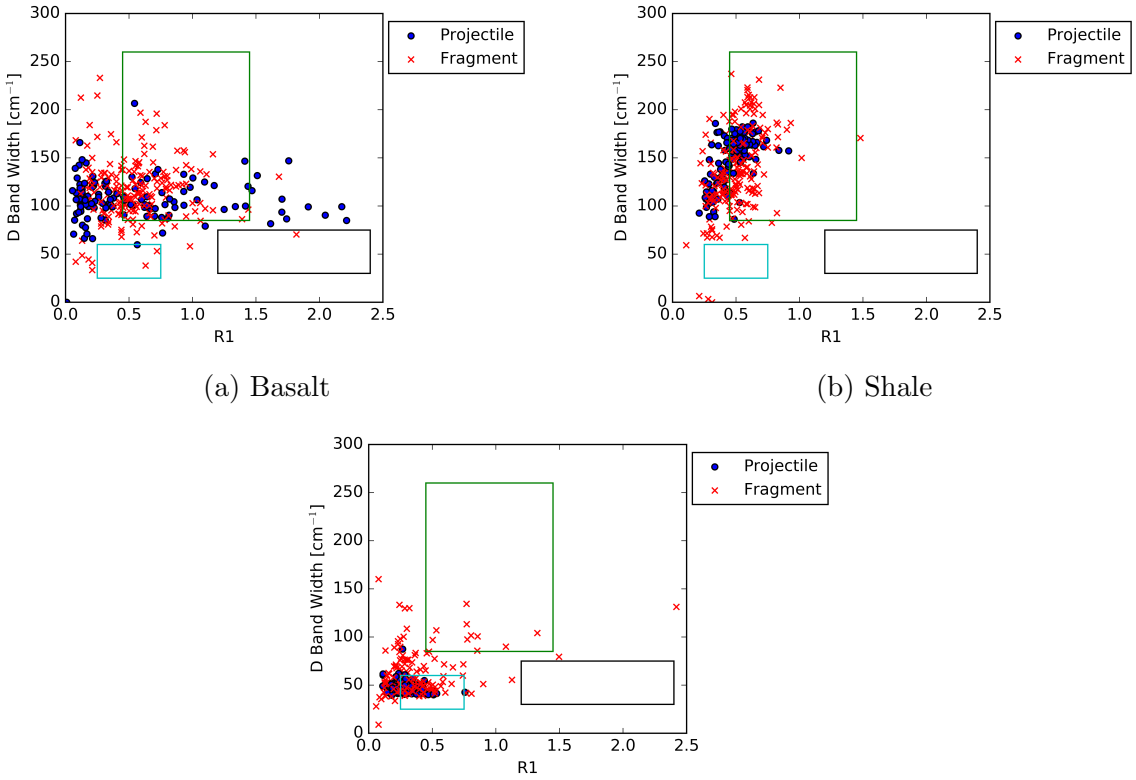

(a) Basalt

(b) Shale

(c) Graphite

Figure 6.36: Comparison of the D band width with the R1 value. The data from this work is plotted on the same axis shown in Figure 6.35. However, the green rectangle contains samples where the precursor carbonaceous material was compositionally complex (highly complex organic material), ∼27 > T < ∼150°C. The black rectangle contains samples where the precursor materials may have been less compositionally complex and hydrothermally overprinted, ∼300 > T < ∼1000°C. The cyan rectangle contains the purely crystalline graphite carbon, T > 1000°C.

For shale (Figure 6.36b) the fragment data seems to be shifting to lower D band widths. Possibly at higher peak shock pressures, this could shift down into the crystalline graphite carbon area (the cyan box).

For graphite (Figure 6.36c) the projectile and fragment data appear mostly in the same location of the plot although not quite fully overlapping that of Bower et al. (2013) for graphite. However, there does seem to be an increase in the D band width for some fragment spectra and a greater range of R1 values. This has shifted them into another location of the plot, which could lead to their compositional complexity

being misinterpreted by missions such as ExoMars. Possibly increasing the peak shock pressure would lead to more data points in the green box in Figure 6.36d.

It would appear that shocked carbon spectra could be misinterpreted as biotic when it is not, due to a misinterpretation of the compositional complexity. Although we still lack the ability to unambiguously identify biogenic carbon from abiogenic carbon this work also needs to be considered when attempting to make this distinction on rocks that could have been subjected to shock.

6.5 Chapter Conclusions

This chapter has discussed the second experiment in this thesis. In this experiment, 1.5 mm cubed projectiles of basalt, shale and graphite were fired onto water at speeds between 0.86 and 6.13 km s^{-1}. For the basalt shots the peak shock pressure range was 2.30 to 23.3 GPa, for shale it was 2.12 to 30.9 GPa, and for graphite, it was 1.60 to 13.4 GPa. The Raman spectra of 40 random separate fragments filtered out from the impacted water were acquired. These spectra were compared to the projectile Raman spectra. The shock pressure effect on the D, G and D2 band peak position, width and separation were analysed. Furthermore, the structural organisation, fragment size effects and the in-plane graphite crystallite size were investigated and implications were drawn. A summary of the findings from this chapter are:

- There was no trend for the shift of the D band peak position. However, basalt and shale had an average shift over all shots of 8.3 and 11.2 cm^{-1}. There was no observable shift for graphite.
- There was no significant trend for the G band peak position. The average shifts across all shots for basalt were 9.0 cm^{-1}. Shale exhibited no average shift as the results were scattered around 0 cm^{-1}. However, four out of five shots did exhibit a significant shift, but these were both positive and negative values. The same is

seen for graphite, two shots suggested a shift to higher wavenumbers and one to lower.

- The peak position for the D2 band in the graphite data suggests that it moves to lower wavenumbers at the highest peak shock pressures. However, there is no trend with shock pressure.

- Result for shale and graphite suggest that it was the smaller fragment sizes that experienced the most peak position shift of the G band. While the larger fragments had peak positions similar to the projectile pre-shot. Results for basalt did not suggest any size effect.

- For the D band spectra for basalt and graphite there appeared to be an initial band width broadening effect. However, as peak shock pressure increased the degree of broadening decreased. This is thought to be due to the destruction of the fragments which would have experienced the most shock via vaporising or melting, or the break down of impurities due to the shock (an annealing effect). Shale seems to suggest a narrowing effect at low peak shock pressure. However, three of five shots don't show an effect of shock pressure on the width of the D band.

- For the G band width, basalt and shale (which have the broadest projectile G band width) displayed a narrowing effect. Whereas, graphite (which has the narrowest projectile G band widths) exhibited a broadening effect with increasing peak shock pressure. Basalt and shale exhibit an absolute narrowing of 12.2% and 8.1%, whereas graphite exhibits an absolute broadening of 17.6%.

- For shale, the D-G band separation appears to suggest that the bands are moving closer together. This is not the case for basalt and graphite.

- The G and D2 band for graphite could be moving closer together. This could lead to difficulties in interpreting carbon spectra and could explain the degree of

scatter for the shale results. Which could also be explained by the variation in the raw sample.

- All materials displayed an increased structural disorder after impact, as shown by plotting the R2 values against the R1 values.
- For basalt, the G band peak position is shifted to higher wavenumbers and the width narrowed. For graphite, the G band peak position is shifted to higher wavenumbers but the width became broader, and for shale, the G band width became narrower and the shift was scattered.
- For basalt, it was clearly seen that the smaller in-plane graphite crystallites experienced the most shift. In addition, as shot speed increased so did the degree of peak position shift on the smallest graphite crystallites. For graphite and shale it appeared that the smallest graphite crystallites experienced the most shock, however, there was no increase in the number of these crystallites with increasing shot speed.

This work has suggested a possibility of misinterpreting a sample when attempting to determine whether it contains biogenic carbon. Although we cannot unambiguously make this distinction, it is important that the shock effects to a sample are taken into account for missions such as the ExoMars 2020 rover. Finally, there is a possibility of an additional misinterpretation of the compositional complexity of carbonaceous materials when identifying using the D band width and the R1 value of the sample.

Chapter 7

Static Pressure Effects on Carbon Raman Spectra

Most of this thesis is concerned with shock effects on samples. However, it is possible to raise samples to high pressures with static loading.

Diamond anvil cells are used to investigate the static pressure effects in-situ on a sample at pressures up to 10 GPa (Pugh 2017). Such cells can be designed to permit Raman studies of the sample whilst it is in the cell under high pressure. Static loading of samples is performed to investigate the graphitisation of rocks. Research into the static loading of a sample has been discussed in Section 2.6.2 of this thesis.

To recap, Zerda et al. (2000) found that for highly oriented pyrolytic graphite (HOPG), increasing the static pressure from 0 to 5 GPa shifted the G band from approximately 1570 to 1595 cm^{-1} (a shift of 25 wavenumbers). Zerda et al. (2000) also found that if a single crystal of HOPG fragmented into multiple crystallites the D band appears in the Raman spectra. By comparison, carbon black shifted by 25 cm^{-1} when the static pressure was at 3.5 GPa. The suggestion for the cause of these shifts in Raman band peak position is the pressure modifying the intermolecular potential (Zerda et al. 2000). This shift to higher wavenumbers has also been reported by Huang

et al. (2010) and Lu et al. (2012).

In this chapter, static pressure experiments are discussed. Shale and graphite samples were placed in a diamond anvil cell and put under static pressures up to 3.53 and 3.59 GPa respectively. This was done to investigate the effects on the G band in these samples' spectra.

7.1 Methodology

In order to determine the effects of static pressure on the carbon bands, a diamond anvil cell was used in the laboratory at Kent. This cell used diamonds to provide the pressure, resulting in the D band of carbon being obscured by the Raman diamond line, meaning that it could not be measured. There are other types of anvil cell which would allow the measurement of the carbon D band (e.g. sapphire), but these were not available in our laboratory.

The premise of a diamond anvil cell is by tightening two screws the diamonds move closer together (Figure 7.1). In between the two diamonds, there is a gasket and in the centre of this gasket, there is a hydraulic fluid containing the sample and powdered ruby. The two diamonds push on the hydraulic fluid causing pressure to increase hydrostatically for the sample and powdered ruby.

The powdered ruby is used as a method for determining the pressure within the cell during compression (see Pugh (2017) for an example of this). Ruby has two distinct peaks at 1367 cm^{-1} (R1) and 1397 cm^{-1} (R2). Using Equation 7.1 the static pressure in GPa can be determined based on the shift of the second peak of ruby (R2) compared to the original R2 position at ambient pressure. In Figure 7.2 we show the Raman spectrum of ruby. The spectra of the ruby were obtained using the red (633 nm) laser built into the Raman spectrometer. Once the required pressure was obtained, the green (532 nm) laser was then used to acquire the sample spectrum in-situ.

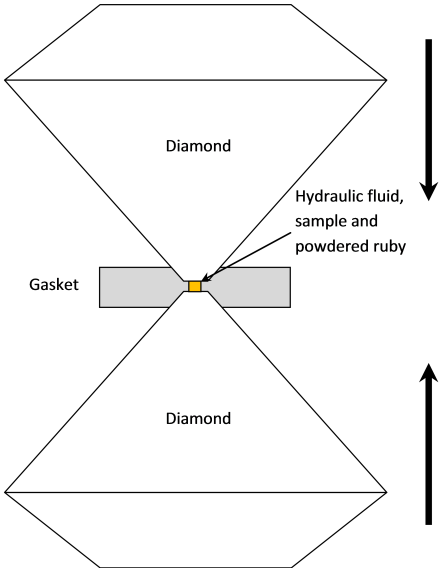

Figure 7.1: Schematic of the diamond anvil cell. In the centre of the gasket and in the middle of the two diamonds is the hydraulic fluid containing the powdered ruby and sample. The thickness of the gasket and the diameter of the hole in the gasket are 180-200 μm and 400 μm respectively.

$$P = 248.4 \left(\frac{\lambda}{\lambda_0} \right)^{6.665}, \tag{7.1}$$

where λ and λ_o are the current and initial wavelength of the R2 peak position and P is the pressure in GPa.

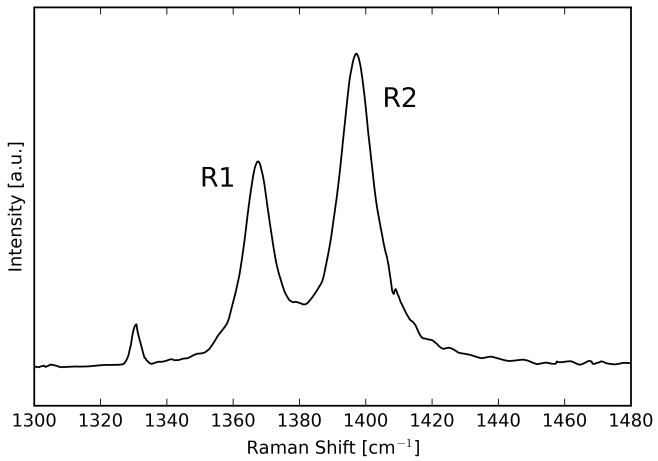

Figure 7.2: Spectra of powdered ruby. R1 and R2 are at approximately 1367 and 1397 cm^{-1} respectively.

Both graphite and shale had two runs completed in order to determine the reliability of the results. These runs were of separate samples. The G carbon band in the basalt was too weak to be observed during this experiment. This is due to a combination of the carbon bands generally being low in intensity (see Appendix E) for all basalt samples and the attenuation of the laser light by the top diamond. Therefore there are no results for basalt.

7.2 Results and Discussion

Figure 7.3 shows the spectra for the second run of graphite at increasing static pressures. The peak shifts from approximately 1580 cm^{-1} up to just over 1590 cm^{-1} over a pressure change of 0 to 3.23 GPa. For example Raman spectra for shale and graphite see Appendix E.2.

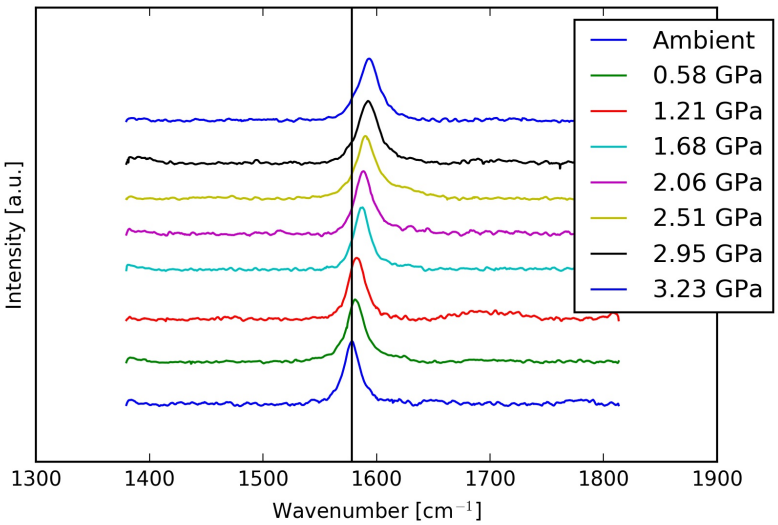

Figure 7.3: Spectra of the G band in graphite v.s. increasing static pressure in the experiments here.

It is evident in Figure 7.3 that the peak position of the G band is shifting to higher wavenumbers as static pressure increases. This is better seen in Figure 7.4. In this figure, both runs for the G band peak positions for shale and graphite are shown

against pressure.

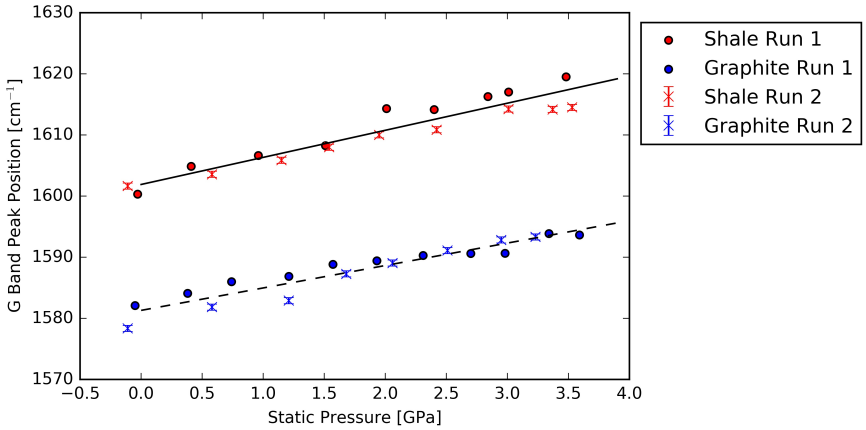

Figure 7.4: G band peak position for shale and graphite v.s. static pressure in these experiments. The R^2 values for shale (solid line) and graphite (dashed line) are $R^2 = 0.9489$, and $R^2 = 0.9515$ respectively. The error bars represent a spectra resolution of 0.5 cm^{-1}. This is the same for every data point and is hence not shown on the run 1 data.

All runs are shown in Figure 7.4 and show the G band peak position shifting to higher wavenumbers linearly with pressure. Additionally, the two runs for both materials appear to agree with each other with relatively little variation. The fitted trend lines have R^2 values close to 1, suggesting that they are a good fit. Shale appears to be increasing in shift at a faster rate than graphite.

The equations of the trend line for shale is:

$$G\,band\,Position = (4.4 \pm 0.4)P + (1601.9 \pm 0.8), \tag{7.2}$$

with R^2=0.9489, and for graphite:

$$G\,band\,Position = (3.7 \pm 0.3)P + (1581.3 \pm 0.6), \tag{7.3}$$

with R^2=0.9515 and where P is the static pressure in GPa.

These results are in agreement in regard to the direction of the shift with past work in the literature (Zerda et al. 2000, Huang et al. 2010, Lu et al. 2012). Table 7.1 displays

a comparison of the results from the literature and this work. Using the values from Table 7.1 and the fits in Figure 7.4, the results here can be compared with those from the literature.

The results for graphite agree with the results for kerogen from Huang et al. (2010) which are determined by an equation of fit to their data (graphite G band position shift at 9.0 GPa is 32.2 cm^{-1}). However, the peak shift at 3.6 GPa differ slightly as the shift reduces to 13.2 cm^{-1} compared with 15.0 $\pm$ 0.5 cm^{-1} from this work. Whereas, the G band peak position shift for shale is too high at this pressure. The shale results here are in good agreement with the single highly oriented pyrolytic graphite crystal from Zerda et al. (2000) (shale G band position shift at 4.3 GPa = 20.6). However, the G band peak position shift for graphite is slightly lower at this pressure. Neither shale or graphite agree with G peak maximum shift for the single walled nano tubes (SWNT). In general, all of these shifts are thought to be due to the pressure affecting the equilibrium spacing between nuclei (bond length), this distorts the electron cloud and leads to a stiffness which results in a difference in the scatter from the carbon aromatic rings (Lucazeau 2003).

Table 7.1: Comparison of the static pressure effects on the G band for different samples. HOPG stands for Highly Oriented Pyrolytic Graphite, and SWNT stands for Single Walled Nano Tubes.

Sample Material	Max Pressure [GPa]	G Peak Max Shift [cm^{-1}]	Trend	Reference
Single HOPG crystal	4.3	21.5	Linear	Zerda et al. (2000)
Kerogen	9.0	33.0	Linear	Huang et al. (2010)
SWNT	4.2	33.0	Two Linear	Lu et al. (2012)
Shale	3.5	19.2	Linear	This Work
Graphite	3.6	15.0	Linear	This Work

Figure 7.5 displays the results for the G band width (FWHM) with increasing static pressure. As pressure exceeds 2 GPa, it appears that the G band becomes broader with increasing static pressure. Lu et al. (2012) found for SWNT that between 0 and 5 GPa the G band width changed linearly with pressure. With a total change of 34 cm^{-1},

i.e. $\sim$7 cm^{-1} per GPa had increased. After 5 GPa, the rate of increase decreases until it becomes zero (total width change of approximately 54 cm^{-1}) at approximately 15 GPa. At 3 GPa the G band width of the SWNT changed by 21 cm^{-1}. Comparing this to the maximum changes of the samples in this experiment (seen in Table 7.3) it is far greater.

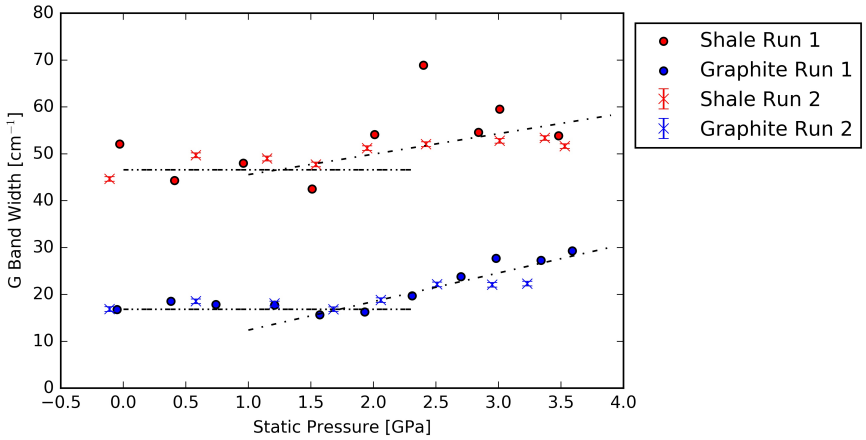

Figure 7.5: G band width for shale and graphite against static pressure. The dot dash lines are to point out a possible trend, where the data is constant until 2 GPa, and then increases. The error bars represent a spectra resolution of 0.5 cm^{-1}. This is the same for every data point and is hence not shown on the run 2 data.

For graphite and shale, the data here is constant up to 2 GPa and then there is an increase. This is shown on Figure 7.5 by the dot-dash lines, and is not seen in Lu et al. (2012). In the data here, run 1 (shale) shows a large degree of scatter around the underlying trend. The outlier in run 1 (shale) at approximately 2.5 GPa, is from a spectrum with a low signal, and is therefore more uncertain.

Table 7.2: Fitting parameters for the G band width for shale and graphite when less than 2 GPa and greater than 2 GPa. From the shale fit, the data point at approximately 2.5 GPa has been excluded. Furthermore, the fit for the shale and graphite data < 2 GPa is the average of the data with the error being the error on the mean.

	<2 GPa	>2 GPa
Shale	48.3 ± 1.2	(4.4 ± 1.5)P+(41.2±4.0)
Graphite	17.3 ± 0.3	(6.1 ± 1.5)P+(6.3±4.4)

Table 7.2 shows the fits for the two sections of the data in Figure 7.5, <2 GPa and

>2 GPa. The fits for the data <2 GPa is the mean over the data range and the errors are the error on the mean. For the data >2 GPa, a linear trend has been fitted.

Both the shifting to higher wavenumbers, and broadening of the G band are due to a change in intermolecular potentials (Zerda et al. 2000).

Table 7.3: Table of the shifts in the individual values for G band peak position and G band width for shale and graphite. This is determined by taking the values for band position and band width at maximum pressure for each run and subtracting the values at ambient pressure. The errors shown here involve the spectral resolution for the configuration of the Raman spectrometer.

	Max Static Pressure [GPa]	ΔG Band Peak Position [cm^{-1}]	ΔG Band Width [cm^{-1}]
Shale			
Run 1	3.48	19.2 ± 0.4	1.8 ± 0.4
Run 2	3.53	12.9 ± 0.4	7.0 ± 0.4
Graphite			
Run 1	3.59	11.6 ± 0.4	12.5 ± 0.4
Run 2	3.23	15.0 ± 0.4	5.4 ± 0.4

The change in the G band peak position and G band width at each run's maximum pressure (with respect to the ambient samples) are displayed in Table 7.3. In terms of peak position, both shale and graphite show similar magnitudes of shift on average. There is a difference in the G band widths between the two materials. For shale, the G band is considerably broader than the G band for graphite, even without any loading. Ignoring the first run for shale, due to the scatter in the data, at approximately 3.5 GPa the G band has broadened by 7.0 cm^{-1}. Whereas for graphite at approximately 3.5 GPa, the G band has broadened by 12.5 cm^{-1}. In absolute terms, shale and graphite have broadened by approximately 16% and 75% respectively. Therefore, the G band for graphite has experienced a considerably larger G band width broadening effect than for shale.

7.2.1 Comparison

In order to investigate the effect of static versus shock pressure on the carbon G band of the samples, the results from the static and shock pressure experiments are compared in Table 7.4. It should be noted, however, that the results from shock experiments are the permanent shifts after release back to ambient pressure. Whereas, the static pressure results are in-situ.

Table 7.4: Comparison of the shock pressure results from Chapter 6, and the static pressure results from this chapter. For the shock experiment, as well as giving results at the maximum pressure observed (Max Pressure), data are also given at an intermediate point (Comparable Pressure) similar to maximum pressure in the static experiments. This is done in order to compare the values. It must be noted that the shock pressure results are post application of pressure, whereas the static pressure results are in-situ.

	Max Pressure [GPa]	Comparable Pressure [GPa]	G Band Shift Direction	G Peak Max Shift [cm^{-1}]	G Width Shift Direction	G Width Max Shift [cm^{-1}]
Shock Pressure						
Basalt	23.3	-	Higher	10.9	Narrower	-11.8
Shale	30.9	-	Higher	1.70	Narrower	-6.34
Graphite	13.4	-	Lower	-1.46	Broader	4.46
Basalt	-	5.90	Higher	10.0	Narrower	-15.8
Shale	-	5.34	Higher	1.34	Narrower	-9.27
Graphite	-	4.15	No Shift	0.18	Broader	1.54
Static Pressure						
Basalt	-	-	-	-	-	-
Shale	3.53	-	Higher	19.2	Broader	7.00
Graphite	3.59	-	Higher	15.0	Broader	12.5

It would seem that there are differences when comparing the two maximum pressure results. However, this is not reasonable as a comparison. Therefore, the results for shock pressures near the maximum static pressure are also displayed in Table 7.4 (called 'Comparable Pressure'). However, this isn't a good direct comparison as the shock pressure results are post the application of pressure, whereas the static pressure is in-situ. Despite this the two situations will be compared.

For shale, the G band peak position shift for both shock and static pressure was to higher wavenumbers. The static pressure shift is approximately fourteen times larger than the shift due to shock pressure.

For the shale shock pressure results, the G band width became narrower. Whereas for the static pressure results, the band became broader. The shock narrowing effect experienced by shale could be as a result of an annealing effect whereby the structure has some imperfections removed. Whereas for static pressure, the G band width would be getting broader due to an increase in structural disorganisation. Zerda et al. (2000) observed that the intensity of the D band increased slightly up to a static pressure of around 10 GPa. This would suggest that their sample was becoming increasingly structurally disorganised. This may be also explain the results of this study.

For graphite, there appears to be no resultant shift after shocking to 4.15 GPa. However, there is a 15 cm^{-1} shift for the G band peak position due to static pressure. The G band width for graphite in both pressure scenarios became broader. The magnitude of the width change for static pressure is near eight times that of shock pressure. Thus for both the G band peak position and width, there was a greater change in the static pressure.

As stated, a major difference between these two situations is for shock pressure we are taking spectra post effect, whereas for static pressure the spectra are acquired in-situ. It is often thought that shock pressure creates a lasting effect, unlike static pressure effect changes are removed again after release back to lower pressure. To examine if spectra are altered/unaltered after release from a static pressure, we compare specimens before and after static loading (see Table 7.5). In Table 7.5 we do not show data from the first graphite run because the sample was lost after the pressure was released in the cell. Table 7.5 suggests that after the release of static pressure the spectra did not return to original values.

From Table 7.5, both shale runs appear to return to lower wavenumber than when at ambient pressure. Whereas graphite returns to a higher wavenumber. For shale run 1, the G band peak positions are close, suggesting it could have possibly returned to the sample conditions prior to the static pressure experiment. However, the other two (shale run 2, and graphite run 2) appear to have experienced a permanent effect on the

Table 7.5: The G band peak position and band width for three static pressure runs when returned to ambient pressure. The error on the ambient and return data is the spectral resolution when fitting. The peak static pressure for Shale Run 1 and 2, and Graphite Run 2 are 3.48, 3.53 and 3.23 GPa respectively.

	G Peak Position [cm^{-1}]	G Width [cm^{-1}]
Shale Run 1		
Ambient	1601.5 ±0.5	52.1 ±0.5
Return	1600.3 ±0.5	50.3 ±0.5
Change	1.2 ±0.7	1.8 ±0.7
Shale Run 2		
Ambient	1601.6 ±0.5	44.6 ±0.5
Return	1597.3 ±0.5	54.5 ±0.5
Change	4.3 ±0.7	-9.9 ±0.7
Graphite Run 2		
Ambient	1578.3 ±0.5	16.9 ±0.5
Return	1580.2 ±0.5	18.7 ±0.5
Change	-1.9 ±0.7	-1.8 ±0.7

G band peak position.

For the G band width, both shale run 2 and graphite run 2 remained broader than when at ambient pressure. Whereas shale run 1 returned to a narrower width. Again permanent changes appear to have occurred to the G band width for both samples.

7.3 Chapter Conclusion

This chapter has discussed the static pressure effects on shale and graphite. Unfortunately, basalt could not be used as the G band intensities were too low to be determined. Furthermore, the D band could not be analysed due to the diamond line masking it, and, the D2 band in the graphite was not intense enough to determine. Despite these limitations, useful data were obtained.

The static pressure within the cell was determined by observing the shift of the ruby peaks. This relative shift of the R2 peak (1397 cm^{-1}) is calibrated to determine the static pressure within the cell (Equation 7.1). There were two runs each for shale and graphite. The maximum pressures obtained for the two materials were 3.59 and 3.53

GPa for graphite and shale respectively. The findings of this chapter can be summarised as follows:

- Both shale and graphite's G band peak position increased linearly with static pressure. The maximum change in G band peak position for shale was 19.2 cm^{-1} and for graphite 15.0 cm^{-1}, at 3.48 and 3.23 GPa respectively.
- The G band width increased (became broader) with static pressure for both materials. For shale, one run exhibited some scatter whilst the other appears to show a similar trend to graphite. For both graphite and shale, the band width doesn't seem to show an increase until approximately 2 GPa. From there onwards, it appears to increase linearly.
- In comparison to the shock pressure results for the two materials, there was no full agreement. For shale, the G band shift direction was the same, whereas the band width were opposites. For graphite, the G band width was the same. Whereas for static pressure, the G band peak position was shifted to higher wavenumbers, and for shock pressure, there was no shift.
- The magnitudes of the G band peak position shift between the two pressure scenarios were very different, with the shock pressure being a significantly lower magnitude than the static pressure.
- It was also found that no sample returned to the exact G band peak position and width after the removal of the static pressure. The closest was within 1.2 cm^{-1}. For G peak position, both shale runs returned to positions below the ambient pressure position, and graphite was above. For the G band width, shale run 2 and graphite were broader than at ambient, and shale run 1 was narrower.

Overall we can say that the irreversible changes in the Raman spectra after shock, are significantly less than the change that occurs in loaded samples at similar pressures, or even at shock pressure some five or six times greater. This is expected as the

static pressure results here are taken when the sample is under pressure and the shock pressure results are post the application of pressure. Releasing the sample, allowing the pressure to return to ambient, allows the sample's molecules to return to/towards (if there is a residual effect then it wouldn't return to the exact configuration) their original configuration.

Chapter 8

Temperature Effects on Carbon Raman Spectra

The previous chapter in this thesis discussed the influence of static pressure on the Raman spectra of shale and graphite samples. Another well known and important way of causing a change to the carbon D and G bands is temperature. This is investigated in this chapter.

Changes to Raman spectra reflect an underlying change to the sample. In this case, graphitisation is very important. There are three significant factors contributing to graphitisation. These are; static pressure, temperature and time scale. Of these, the temperature is deemed to be the most important (Beyssac et al. 2002a, Beyssac et al. 2002b). Huang et al. (2010) looked into the static pressure and temperature effects upon kerogen. They found that the influence on the D and G band peak positions were in the opposite directions for the two effects. Static pressure shifted the peak positions to higher wavenumbers, whereas, temperature shifted to lower (Huang et al. 2010). Furthermore, Huang et al. (2010) estimated the relative effect of temperature and pressure on the shift of each band by determining a coefficient (dT/dP). This value was found to be 3.9 $\times 10^{-3}$ and 6.8 $\times 10^{-3}$ °C GPa^{-1} for D and G bands respectively. The

interpretation of this suggests that for the maximum pressure at which a metamorphic rock is formed (1 GPa), the relative shift of the D and G band caused is countered by temperatures of 256 and 147 °C for the D and G band respectively (Huang et al. 2010). A discussion of this is in Chapter 2.

In this chapter, the effects of temperature on the carbon D and G bands for basalt, shale, and graphite samples are explored. In order to investigate the effects of temperature, the samples were heated up to 773 K and, for scientific curiosity, cooled to 173 K.

8.1 Methodology

A Linkam temperature stage (see Figure 8.1) was used in order to investigate the temperature effects on the carbon D, G and D2 bands in Raman spectroscopy for basalt, shale, and graphite. The temperature stage has a liquid nitrogen pump in order to lower the temperature of samples down to around 173 K and a heating element to heat a sample to approximately 773 K.

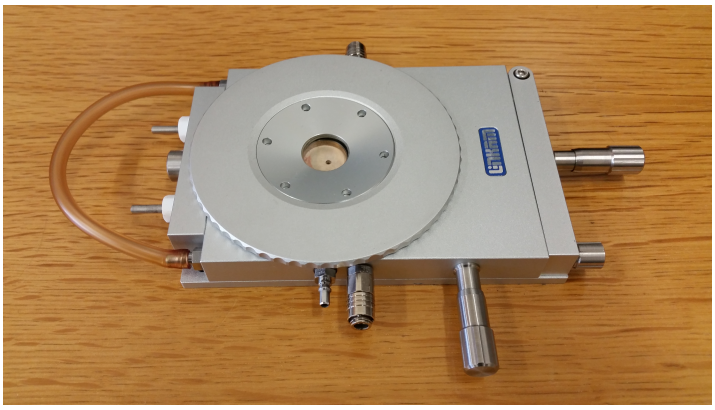

Figure 8.1: Image of Linkam temperature stage used in this experiment. The stage is 14 by 10 cm in size.

The 532 nm (green) laser was used in the Raman spectrometer to acquire spectra of the samples, along with a 25% neutral density filter (blocking 75% of laser light) and a dwell time of 5 seconds at 8 accumulations. This means that each spectrum had 80

seconds acquisition time due to two spectral ranges. The reason an overall continuous dwell time of 40 seconds is not used is to avoid introducing any laser heating effects that may lead to burning of the sample.

Each temperature map is split into heating and cooling due to laboratory constraints. For each run (8 runs in total, 1 automated and 3 manual spot check for both heating and cooling runs) a separate sample was used. Therefore, hot and cold runs were never run on the exact same sample material.

For the automated temperature maps, the temperature was altered in increments of 10 K. For hot temperature work, the temperature range was from 303 to 773 K. For cold temperature work, the range was 303 K down to 173 K. At each increment, the sample was held at the temperature for one hour to ensure a stable temperature throughout the whole of the sample. Due to the time constraints, each sample experienced the automated temperature experiment once.

To compare the automated method to one with increased user control, spot checks were performed. These were performed at 173, 213, 253, room temperature, 393, 493, 583, 683 and 773 K. The temperatures were held constant for one hour, as in the automated mapped results. This was repeated three times for three separate samples for the two separate temperature experiments (hot and cold).

8.2 Results and Discussion

Before discussing the results for each band, when analysing the data there appeared to be a considerable amount of scattering in the automated mapped results compared to the spot check data. Figure 8.2 shows the D band peak position against temperature for the automated mapped data and the spot check data. For both basalt and shale, the mapped data appears scattered to a higher degree than for graphite. This is something that occurred throughout the experiment. For some aspects of the spectra, the degree of scattering increased for temperature greater than approximately 500 K.

The spot check data has a lesser degree of scatter. It was noted when performing the spot checks that at higher temperatures there was difficulty in the laser focusing due to the hot/cold air, something that could be accounted for by a user, but not when automated. Furthermore, the heating experiment ran for approximately 2 days. Over this time the laser could have possibly drifted out of calibration which would have introduced further scatter. These factors combined with the D band for basalt being naturally low in intensity meant that the automated mapping was not as reliable as the spot check data. Hence, for the remainder of this chapter only the spot check data shall be discussed. The plots for both the automatically mapped and spot check data can be seen in Appendix A.

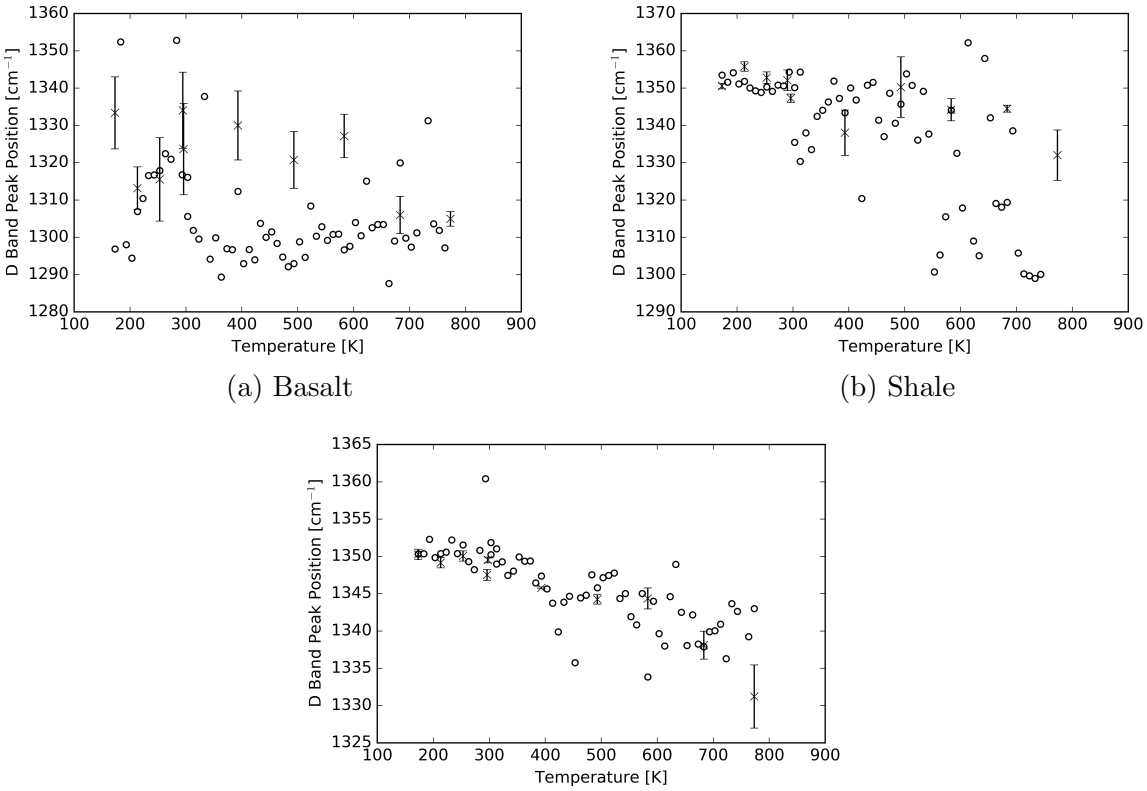

(a) Basalt

(b) Shale

(c) Graphite

Figure 8.2: D band peak position for basalt, shale and graphite against temperature. The black crosses show the results for the spot checks and open circles the data from automated runs. The error bars are the error on the mean value.

Appendix E.3 contains some example spectra for basalt, shale and graphite whilst

being cooled and heated. For basalt, the signal to noise ratio (SNR) is high, especially for the cooling spectra (Figure E.9). This would be due to a mix of the basalt sample not having strong carbon bands, the laser being attenuated through the temperature stage and effects of temperature on the focusing of the laser. Looking at the cooling example spectra, the SNR is very high and it is difficult to clearly make out the D and G band. For heating (Figure E.10), the SNR is better, however, the D band is still masked in some of the spectra.

For shale and graphite, the SNR is better than for the basalt spectra. This is due to the carbon bands in these materials being stronger. For the cooling spectra of shale (Figure E.11), the D band appears to exhibit quite a bit of variation. This could be as a result of a change in the material or difficulties in acquiring spectra at the coldest temperatures. The same is not seen for the graphite sample being cooled (Figure E.13). This is possibly due to the D band being stronger (meaning more counts and lower SNR) in the graphite sample. The heating of the shale sample (Figure E.12) has a better SNR than the cooling spectra. The G band does not exhibit much variation, whereas the D band does change in amplitude. The heating of the graphite sample (Figure E.14) has the best SNR. The D band in the spectra does exhibit some variation in amplitude, with it being at its lowest at the highest temperatures. The G band of graphite does have some variation in band width (FWHM), however, they are mostly similar.

Figure 8.3 shows the graphite spot check data and how it changes with hot and cold temperatures. The two vertical black lines refer to the position of the D and G band at room temperature (296 K).

It is clear that heating causes the G band to shift to lower wavenumbers, whereas cooling shifts it to higher wavenumbers. This shift in position is due to the temperature change affecting the population of different energy levels for each normal mode and because of the non-equidistance in energy of these levels, the average position of the atom is altered (Lucazeau 2003). The D band appears to almost become unresolvable due to becoming very broad and low intensity when heated. This suggests that the

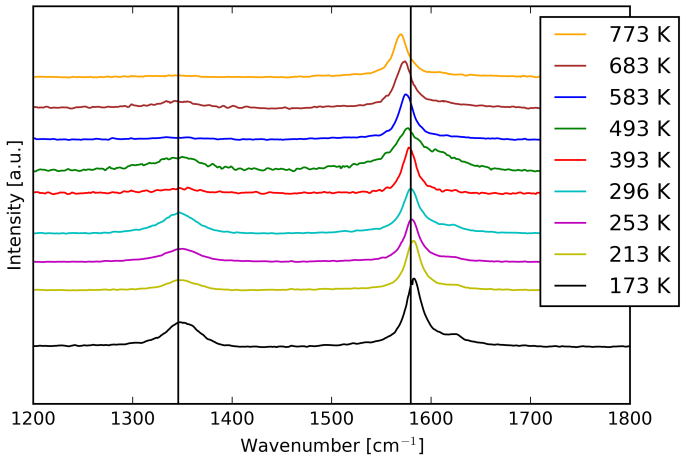

Figure 8.3: Graphite spot check spectra v.s. increasing temperature. The temperature ranges from 173 to 773 K. The two vertical black lines refer to the D and G band peak position for the spectra at room temperature (296 K).

sample becomes more structurally organised. The reverse is seen when cooling, the D band shifts to higher wavenumbers and has a greater intensity, suggesting an increase in structural disorder. The changes to the D, G and D2 bands shall be discussed in depth in the next section.

8.2.1 Effects on the D, G and D2 Bands

This section discusses the results of the effects of temperature on the D, G and D2 bands. In particular, it looks at the changes in band peak position, band width, R1 value and R2 value. In all cases, the spectra were fitted using LapSpec6 software and the relevant data processed as in previous chapters.

D Band Peak Position

Figure 8.4 shows the D band peak position versus temperature for basalt, shale, and graphite.

For the D band peak position for basalt (Figure 8.4a), there seems to be a negative

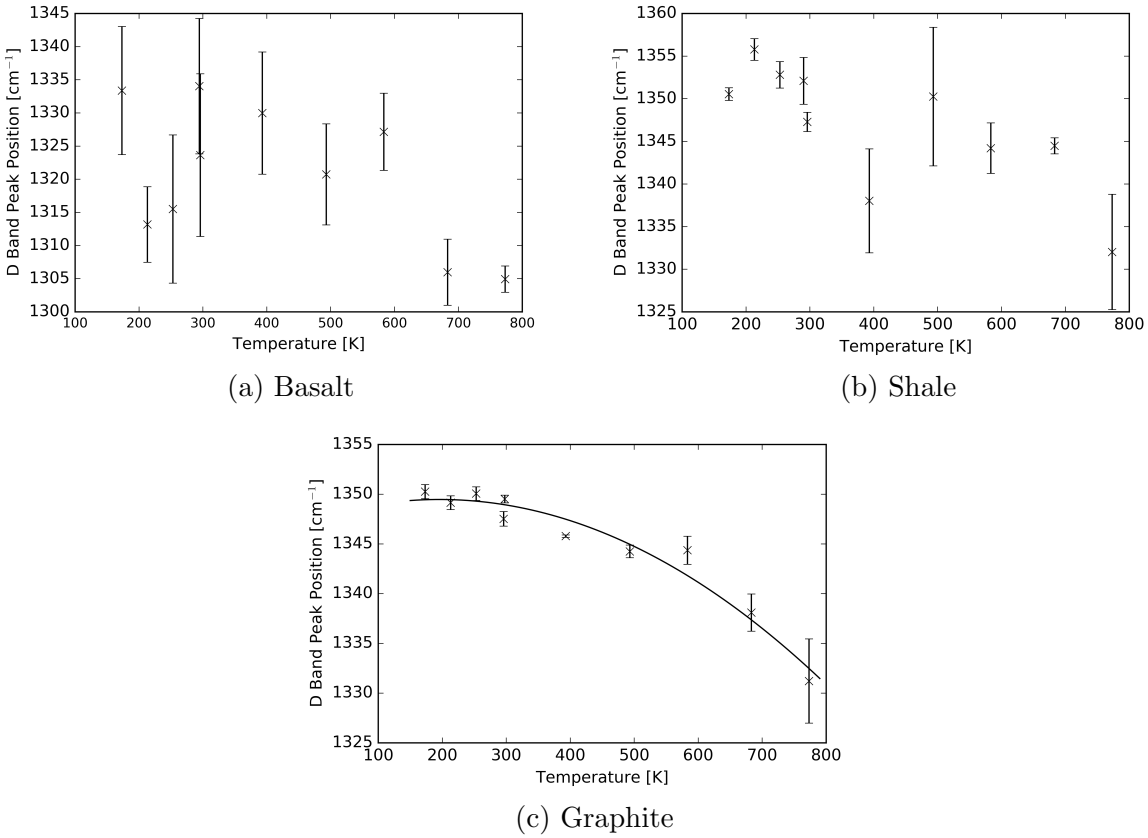

(a) Basalt

(b) Shale

(c) Graphite

Figure 8.4: D band peak position for basalt, shale and graphite against temperature. The error bars represent the error on the mean.

trend, meaning when heated, the D band peak position shifts to lower wavenumbers, and when cooled it moves to higher wavenumbers. However, there is significant scatter in the data and most data points have large error bars. This is due to the natural variation in the raw sample as basalt is not a homogeneous carbonaceous material (see Appendix E). The carbon in basalt could be in the form of calcite, carbonates or graphite. If it is in the form of graphite, it could be non-homogeneously distributed and lead to similar trends between the two materials. However, for each run to be graphite is unlikely. The error bars at room temperature do overlap suggesting that the two experiments can be joined together. Interestingly, the smallest error bars are at the hottest temperature. Possibly the carbonaceous material is becoming more structured, hence less variable, due to heating.

For shale (Figure 8.4b), it would appear that the D band peak position is again shifting to lower wavenumbers at higher temperatures and to higher wavenumbers at lower temperatures. However, as for the basalt results, the data are scattered. Both the error bars and the scatter is less in comparison to the basalt results. This could be due to the shale having a greater homogeneity due to less variation in the raw sample. The room temperature data points are not overlapping. However, the difference between the two is very small (<1 cm^{-1}). The total shift, from 173 to 773 K, is approximately 19 cm^{-1}.

For graphite (Figure 8.4c), there would appear to be a polynomial trend with temperature, with far less scatter than for basalt and shale. The error bars on the data point are also small. Both of these factors are due to the homogeneity of the sample, which has a low variation of the raw sample. The two room temperature data points are also near, being separated by less than a wavenumber. Interestingly the largest error bar is at the hottest temperature. This could be due to the heat in the temperature stage causing issues when trying to acquire spectra.

The graphite data in Figure 8.4 has been fitted with a polynomial trend line. The equation and the correlation coefficient are:

$$D = -(5.1 \pm 1.5) \times 10^{-5} T^2 + (0.02 \pm 0.01)T + (1348 \pm 3), \tag{8.1}$$

with $R^2 = 0.9533$, D the D band peak position in cm^{-1} and T the temperature in kelvin.

G Band Peak Position

Figure 8.5 shows the G band peak position against temperature for basalt, shale, and graphite.

For basalt (Figure 8.5a), the G band peak position shifts to lower peak positions between 173 and 393 K, whereas between 393 and 773 K the peak position increases.

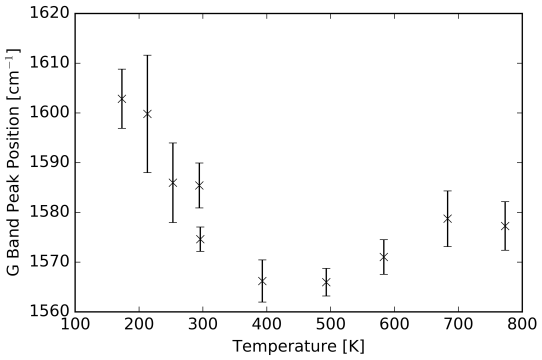

(a) Basalt

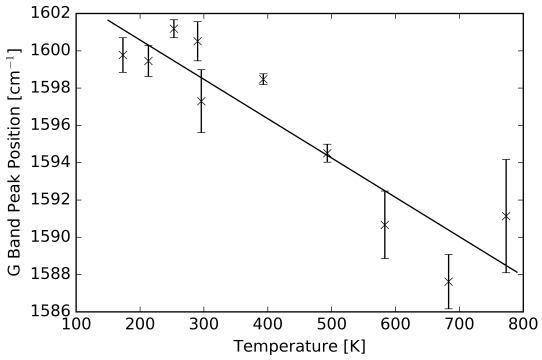

(b) Shale

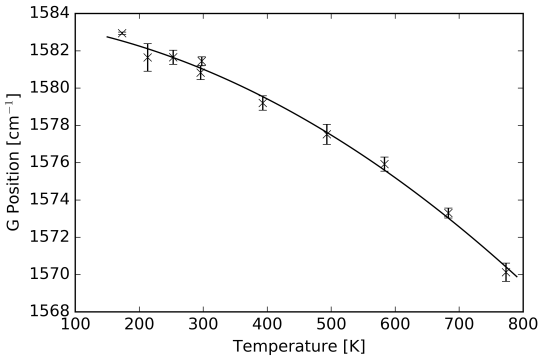

(c) Graphite

Figure 8.5: G band peak position for basalt, shale and graphite against temperature. The error bars represent the error on the mean.

Possibly the G band peak position cannot shift lower than a particular value and the trend is to a constant value at temperature >400 K. As the raw G band peak position in basalt is the lowest in magnitude in comparison to shale and graphite, possibly we do not see this same effect for shale or graphite. The error bars are reasonably significant due to the natural variation in the raw sample. The two room temperature data points do not overlap. However, they are within a few wavenumbers. The reason they are not overlapping could be due to the natural variation in the raw sample.

For shale (Figure 8.5b) it would seem that there is a negative linear trend with increasing temperature. Thus heating the shale sample above room temperature causes the G band peak position to shift to lower wavenumbers, and cooling it shifts it to higher wavenumbers. Some of the error bars are large, this is most likely due to the

homogeneity of the raw sample. Furthermore, the two room temperature data points do not overlap but they are close. Again the largest error bar is at the hottest temperature, this is due to the hot air in the temperature stage affecting the spectra acquisition. The total peak position shift from the coldest to the hottest temperature is approximately 9 cm^{-1} over 600 K.

For graphite (Figure 8.5c) there is a clear negative trend with increasing temperature. The low amount of scatter in the data is likely due to graphite having much more intense bands than basalt and shale, and graphite being the most homogeneous. Between the lowest and highest temperature, there has been a G band peak shift of approximately 13 cm^{-1} over 600 K. This shift in the G band peak position is due to the weakening of these modes. The two room temperature data points overlap, suggesting that there is a good reliability that the two separate maps can be seen as one data set.

The shale and graphite data in Figure 8.5 have been fitted with a linear and polynomial trend lines respectively. The equations and the correlation coefficients are, for shale:

$$G = -(0.021 \pm 0.003)T + (1605 \pm 2), \tag{8.2}$$

with $R^2 = 0.8424$. For graphite:

$$G = -(1.7 \pm 3.9) \times 10^{-5}T^2 - (0.004 \pm 0.004)T + (1584 \pm 1), \tag{8.3}$$

with $R^2 = 0.9938$. For both equations G is the G band peak position in cm^{-1} and T is the temperature in kelvin.

From the correlation coefficients, it is evident that graphite has a very good fit, and shale a decent fit.

D2 Band Peak Position

The D2 band is only present in the graphite spectra, as discussed in Chapter 6. Hence, Figure 8.6 only shows the D2 band peak position with temperature for graphite.

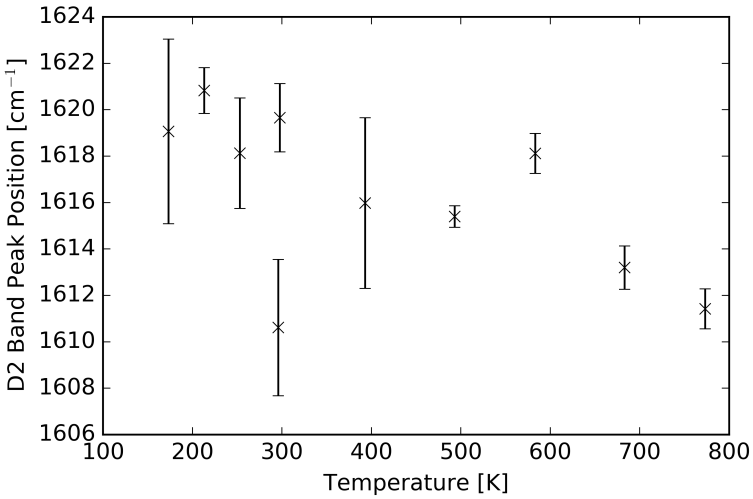

Figure 8.6: D2 band peak position for graphite against temperature. The error bars represent the error on the mean.

Figure 8.6 appears to suggest a negative trend of D2 peak position with increasing temperature. Just like the other bands, heating causes the band to shift to lower wavenumbers, and cooling to higher. However, the results for the D2 band position against temperature appear to be scattered. This scatter is most probably due to the low intensity of the D2 band. Compared to the D and G, the D2 band was just a small shoulder peak. Equally, this could be the cause of the separation between the two room temperature data points of approximately 4 cm^{-1}.

D Band Width

Figure 8.7 shows the D band width (FWHM) versus temperature for basalt, shale and graphite.

The data for the D band width versus temperature for basalt and shale appears to be scattered (Figure 8.7a and 8.7b) around approximately 91 and 98 cm^{-1} respectively.

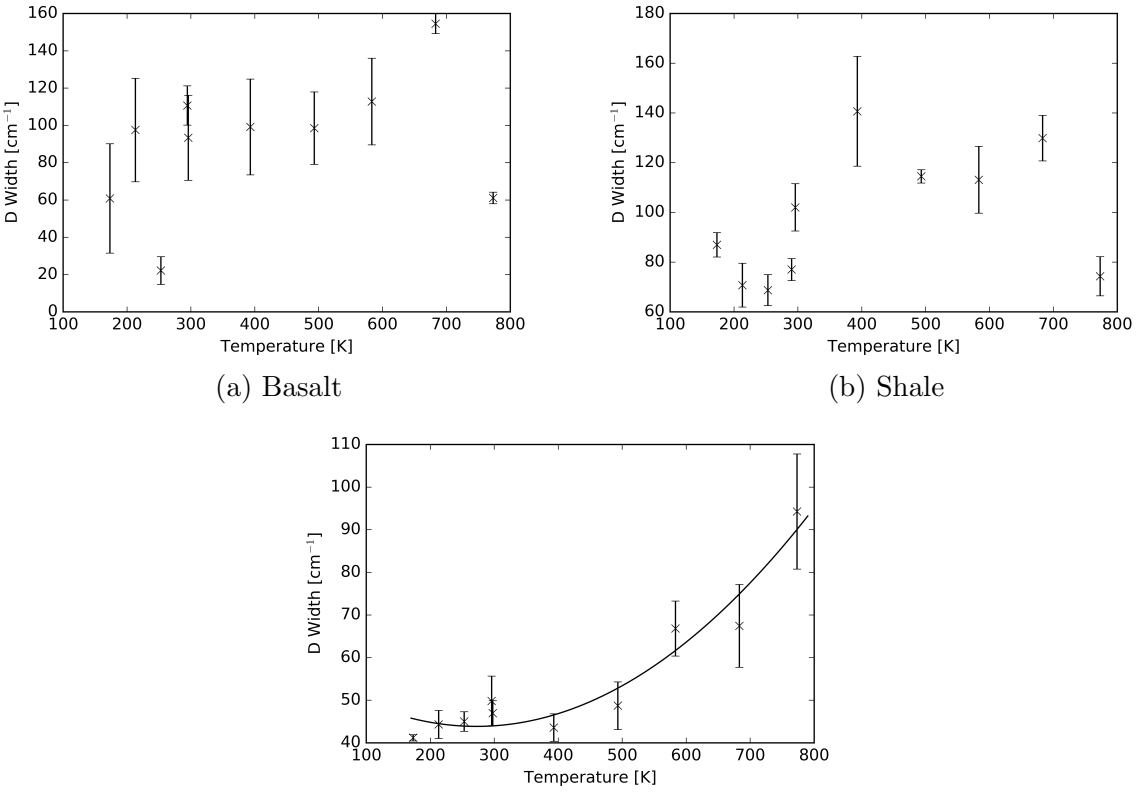

(a) Basalt

(b) Shale

(c) Graphite

Figure 8.7: D band width for basalt, shale and graphite against temperature. The error bars are the errors on the mean.

The scatter and the error bar sizes could be due to the natural variation in the raw sample. For basalt, the two room temperature data points overlap, whereas, for shale, they do not and are separated by approximately 10 cm^{-1}. For both, it would appear that the bands in the cold data sets are narrower and the heated are broader. However, this is not significant enough to suggest a trend.

The D band width in graphite, however, appears to broaden with increasing temperature. From 493 K up to 773 K, the width broadens significantly. At temperatures lower than 493 K, the width does not change much, remaining roughly constant at approximately 46 cm^{-1}. The reason for the variation in band half-width due to temperature is due to the decay of a given phonon into two or three phonons (Lucazeau 2003). For both temperature and pressure, the phonon density of states is a critical

parameter and temperature affects its population, whereas pressure changes its form (Lucazeau 2003). The two room temperature data points overlap, suggesting that the two maps lead into each other. The error bars are greatest at the higher temperature. This could be due to the hot temperatures causing the laser to fluctuate in focus leading to an effect on the band width.

The graphite data has been fitted with a polynomial function. The equation and the correlation coefficient are:

$$D\,Width = (1.8 \pm 0.5) \times 10^{-4} T^2 - (0.10 \pm 0.05) T + (57.5 \pm 10.3), \qquad (8.4)$$

with $R^2 = 0.9235$. Where $D\,Width$ refers to the D band width in cm^{-1} and T to the temperature of the sample in kelvin.

G Band Width

Figure 8.8 shows the G band width versus temperature for basalt, shale and graphite.

For basalt (Figure 8.8a) the G band width appears scattered around approximately 121 cm^{-1} for the temperature between 300 and 773 K. For the cooling temperature experiment, the G band appears to become narrower. The error bars for the hot temperature data points are narrower than the cold temperature. The cold temperature data error bars are typically nearly 20 cm^{-1}. This suggests a lot of variability. Possibly collecting more data with more cold temperature experiment runs would show that the G band does not narrow as significantly as suggested here. The cross over data points at 300 K, where the two temperature maps cross, shows a discrepancy between the two basalt temperature experiments. This could be due to the natural variation of the raw sample. However, it does throw into question the validity of the pattern seen in Figure 8.8a.

For shale (Figure 8.8b) there is a positive trend of the G band width with temperature. Heating the shale broadens the G band, whereas cooling narrows it. The error

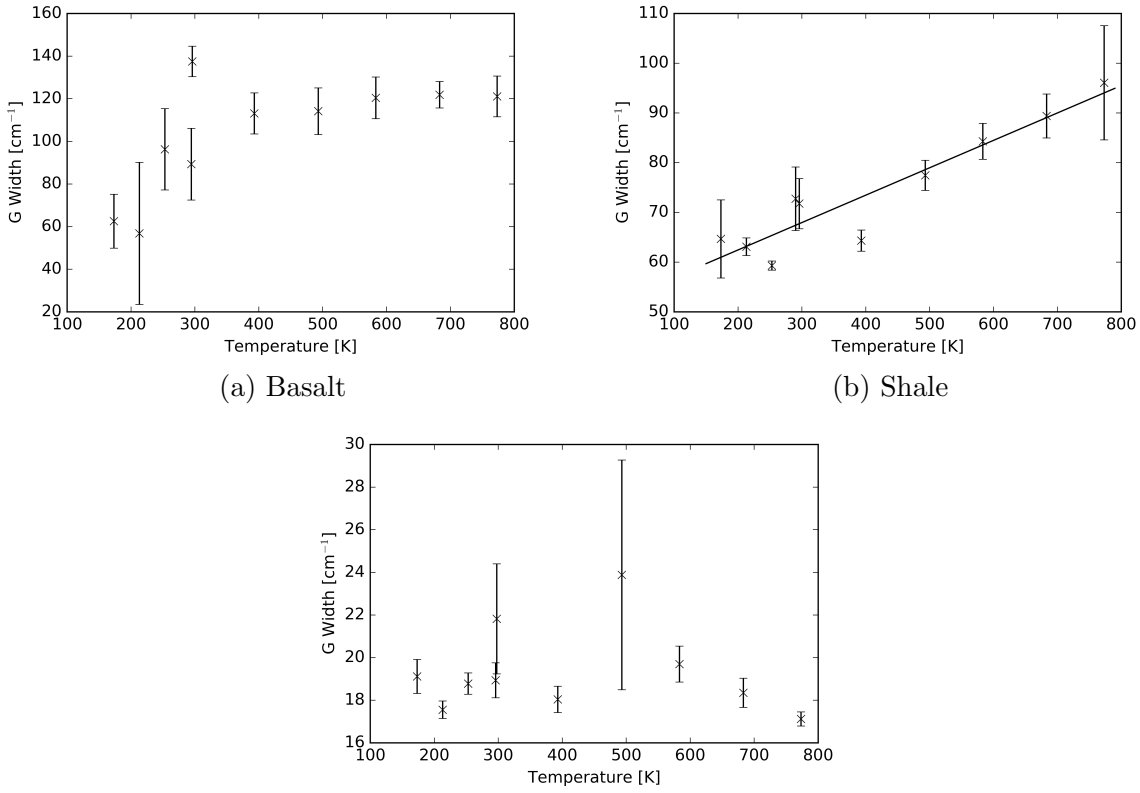

(a) Basalt

(b) Shale

(c) Graphite

Figure 8.8: G band width for basalt, shale and graphite against temperature. The error bars represent the error on the mean.

bars are mostly small, with the hottest and coldest data points as the most interesting exceptions. At these temperatures, the acquisition of the spectra may be affected by the conditions resulting in larger error bars. The room temperature data appears to overlap adding plausibility that these two experiment's data can be joined together. The equation and correlation coefficient for the linear trend plotted in Figure 8.8b is:

$$GWidth = (0.055 \pm 0.01)T + (51.4 \pm 3.5), \tag{8.5}$$

with $R^2 = 0.8696$. Where $GWidth$ refers to the G band width in cm^{-1} and T to the temperature of the sample in kelvin. However, the fit to this data is not that great due to the scatter.

For graphite, it appears the G band width remains constant throughout the whole

temperature range at approximately 18 cm^{-1}. However, there are two points that lie apart from the rest. These points are also accompanied by large error bars suggesting that they could include anomalous results. However, in order to determine this, the whole temperature range would need to be re-tested.

D2 Band Width

Figure 8.9 shows the D2 band width versus temperature for graphite.

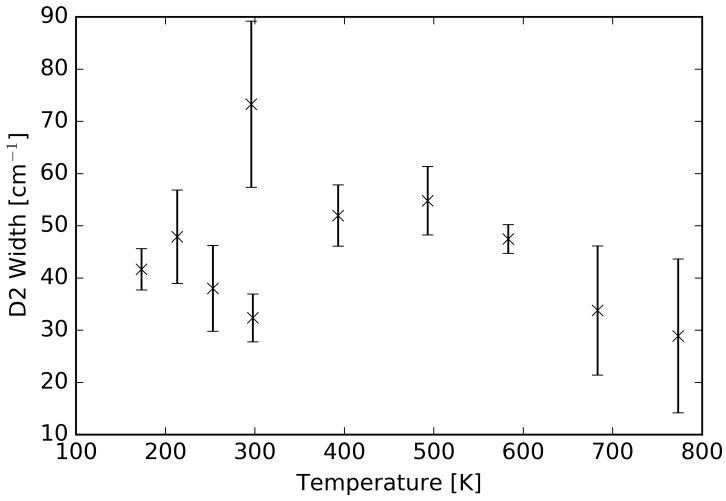

Figure 8.9: D2 band width for graphite against temperature. The error bars represent the error on the mean.

There appears to be no trend in Figure 8.9, as the data is scattered around 45 cm^{-1}. The error bars on the data are also quite big, with the majority being greater than 10 cm^{-1}. This equates to nearly a quarter of the band's width in some cases. The reason these are so large could be due to the difficulties of resolving the D2 band in the spectra. As this is a weak shoulder band, it is naturally tough to resolve. The addition of the Linkam temperature stage increased this difficulty.

R1 Value

Figure 8.10 displays the results for the R1 value, which is the ratio of the D and G band intensities (Equation 6.1), against temperature. The R1 value is an indicator of the structural organisation of carbonaceous materials. A high value of R1 suggests that the sample is more structurally disorganised.

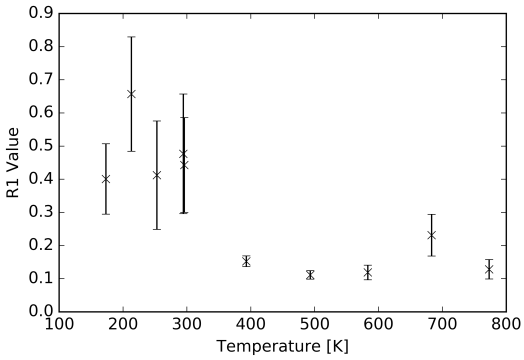

(a) Basalt

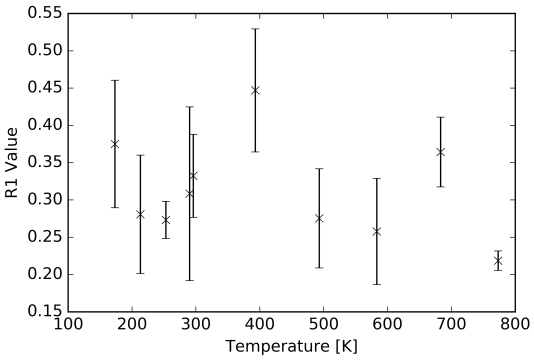

(b) Shale

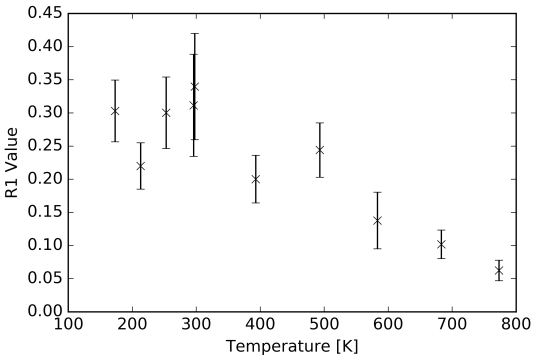

(c) Graphite

Figure 8.10: Ratio of D and G band amplitude (R1 value) for basalt, shale and graphite against temperature. The error bars represent the errors on the mean.

For basalt (Figure 8.10a) the R1 value appears to be constant for temperatures between 393 and 773 K, and higher in value for room temperature and below. For the majority of the hot temperature experiments, the R1 value is approximately 0.1. This is very low and it is related to poor D band spectra of low intensity. It could suggest that heating the sample increases the structural organisation. For the cold temperature experiment, the R1 values are similar to the room temperature value. Interestingly the

room temperature data points overlap suggesting that the two temperature experiments are relatable. The largest error bars are on the cold temperature experiment data. This suggests a greater degree of variation in the results. This could be due to the natural variation in the raw sample. A possible reason why the error bars are much smaller for the heated results could be that heating the sample lowered the natural variability of the raw sample, as both room temperature data points had large error bars. Some possible mineral phases containing carbon in the basalt sample would be calcite, carbonates and graphite. Although graphite would be non-homogeneously distributed, it is a possible reason for the similarity between the trends seen for basalt and graphite in Figure 8.10. Meaning that the basalt carbon bands being analysed could be graphitic in nature in this case.

The R1 values for shale (Figure 8.10b) exhibit no trend, and are scattered around 0.31. The scatter and large error bars could be due to the variation in the raw sample. The two room temperature data point do overlap, suggesting that the two temperature experiments are relatable.

For graphite (Figure 8.10c), although there is significant scatter, the R1 value appears to decrease with increasing temperature, falling from 0.30 ± 0.05 at 173 K to 0.06 ± 0.02 at 773 K. This suggests that the carbonaceous material is increasing in structural organisation due to heating. Additionally, the two room temperature results overlap suggesting that the two separate experiments are relatable. Finally, the error bars on the data, although smaller than basalt and shale, could be due to the natural variation in the raw sample. Although the peak position and width aren't particularly varying, the intensities could be.

R2 Value

Figure 8.11 displays the results for the R2 value, which is the ratio of the D and D + G + D2 band areas (Equation 6.2), against temperature. The R2 value is an indicator to the structural organisation of carbonaceous materials. A high value of R2 suggests

that the sample is more structurally disorganised.

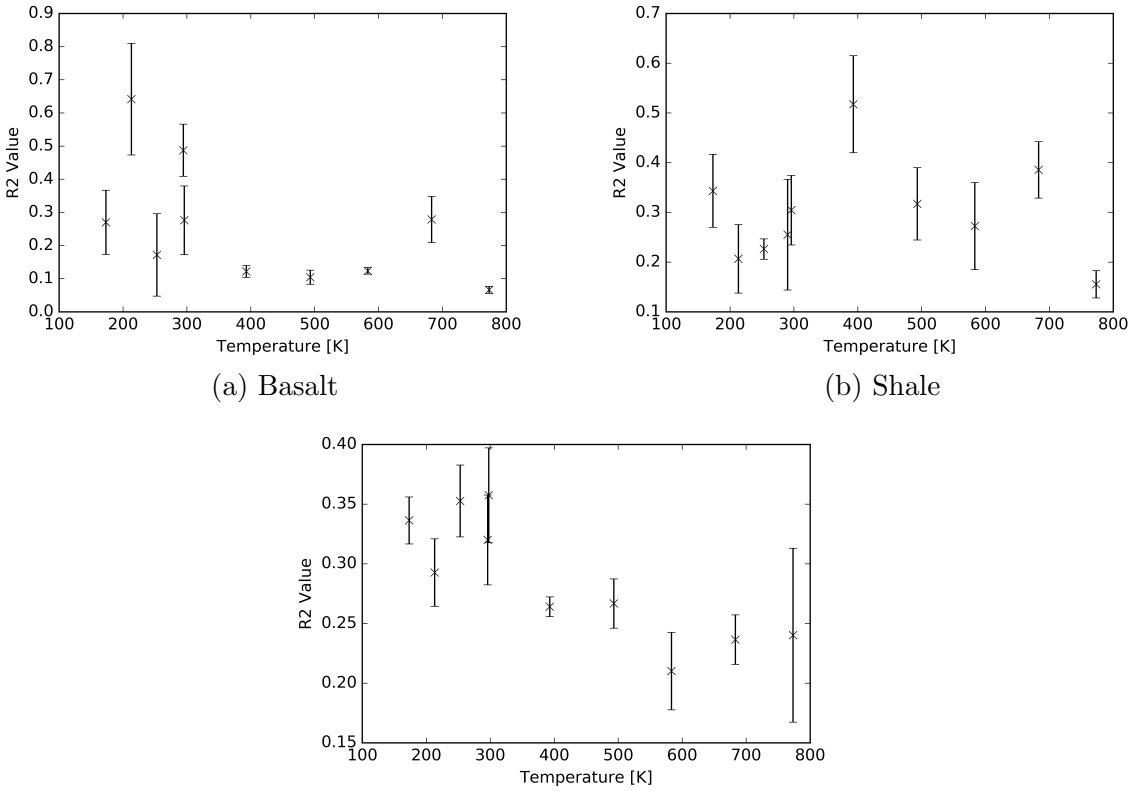

(a) Basalt

(b) Shale

(c) Graphite

Figure 8.11: Ratio of D and G band areas (R2 value) for basalt, shale and graphite against temperature. The error bars represent the error on the mean.

For the R2 value for the basalt spectra (Figure 8.11a), the pattern appears to be similar to Figure 8.10a. The R2 values remain relatively constant during the heating experiments. Whereas, during the cooling experiment the values are scattered around the room temperature data points. As with the R1 value, the constant R2 values are associated with low-intensity D bands at high temperatures. Unlike the R1 value, the two room temperature data points do not overlap. This could be due to the variation of the raw sample. Which, for basalt, was very large.

Again, the R2 values for shale (Figure 8.11b) are similar to the R1 values. Overall there is no trend and the data is scattered around 0.30. The error bars on the majority of data points are large. This could be due to the natural variation in the raw sample,

which has also masked any possible trend. The two room temperature data points do overlap, suggesting the two experiments are relatable.

For graphite (Figure 8.11c), the R2 value appears to decrease with increasing temperature, falling from 0.34 ± 0.02 at 173 K to 0.24 ± 0.07 at 773 K. This suggests that the carbonaceous material is increasing in structural order. As both R1 and R2 exhibited this trend it would appear that heating graphite increases the structural order of the carbonaceous material. Additionally, the room temperature data points overlap, suggesting that it is a reasonable suggestion that the two sets of data can be joined. The error bars on the data are similar in size to that of the R1 values, however, the final data point, at 773 K, has significantly larger error bars. This could suggest that there is an anomalous result and explain why it is higher than the previous data point.

Return to Room Temperature

In addition to how the attributes of the bands are affected by temperature, it is of interest to determine if there has been any permanent alteration. Table 8.1 shows the results for the spectra once they had returned to ambient (room) temperature after being heated. The values displayed are the average differences (before heating minus after heating) for each sample's spot check.

For the D band results, none of the D band widths for any sample suggests a significant permanent change due to the size of the errors on the mean. However, the D band peak positions for each sample do suggest a permanent shift to higher wavenumbers. The difference before and after for basalt is very large and is accompanied by a large error. The reasons this could be so large would be due to the large variation in the raw material and the fact that the D band, for basalt, was often very low in intensity. Although each sample had spectra obtained from the same region during heating and post-heating, across the three samples there could still be large variation as each sample is different areas of the rock. The fluctuation in the raw sample, as shown in Chapter 6, for basalt is very large suggesting a wide range of values and hence large differences.

Table 8.1: The average D band, G band, D2 band and R1 and R2 differences of the samples when returned to room (ambient) temperature. The difference is the sample pre temperature experiment result minus that of the sample after the temperature experiment.

	D Band Peak Position [cm^{-1}]	D Width [cm^{-1}]	G Band Peak Position [cm^{-1}]	G Width [cm^{-1}]	D2 Band Peak Position [cm^{-1}]	D2 Width [cm^{-1}]	R1 Value	R2 Value
Basalt								
Difference	-37.96	-58.09	-26.69	42.42	-	-	0.31	0.09
Error	± 15.33	± 77.49	± 4.33	± 9.84	-	-	± 0.18	± 0.15
Shale								
Difference	-6.69	-9.21	-3.98	-7.31	-	-	-0.06	-0.06
Error	± 2.19	± 17.07	± 3.36	± 6.51	-	-	± 0.08	± 0.09
Graphite								
Difference	-2.69	4.48	-0.39	-1.25	-7.54	43.24	0.15	0.10
Error	± 1.05	± 7.52	± 0.71	± 2.24	± 4.80	± 20.71	± 0.11	± 0.08

For shale and graphite, both had a significantly lower difference than for basalt. However, between the two, shale appears to have experienced a greater permanent effect of heating.

For the G band results, neither the peak position or width for graphite appeared to experience a permanent alteration. For basalt and shale peak positions, basalt experienced the greatest permanent change, both being shifted to higher wavenumbers. This large difference, and for the basalt G band width, could be due to the variation of the raw sample while comparing the six different samples. For shale, the error on the G band peak position is very large in comparison to the difference, so the shifting to a higher wavenumber could be a little less than a wavenumber if any. For the G band widths, basalt's narrowed and shale's broadened. This opposite effect could due to the initial widths of the two samples. The average basalt and shale G band width before heating were 71.8 and 137.5 cm^{-1} respectively. Possibly the widths are changing to an intermediate point due to a change in structural order.

The D2 band in the graphite samples appears to have a permanent peak position shift to higher wavenumbers and a narrowing. Both of these results could be due to the structural order increasing, hence, the band shifting, becoming narrower and less

intense. If this is occurring then it should be evident in the R1 and R2 value results discussed next.

For the R1 value, basalt and graphite barely suggest a permanent change due to the size of the errors. The same can be seen for the R2 values. It appears that shale's structural order has definitely not permanently changed, this agrees with the results in Figure 8.10b and 8.11b. Graphite possibly suggests that there has been an increase in structural order, despite the large errors both ratio values decreased. While basalt only had one ratio value change but by a considerable amount. Therefore, heating the sample to 773 K has not permanently changed the structure of the samples, however, it does suggest possibly the beginning of a change, which may be more evident at higher temperatures.

8.2.2 Comparison

The following tables display the comparison data for the shock pressure, static pressure and temperature experiments. The tables are split into the D band, G band and R1/R2 values. In each situation, the maximum condition (e.g. hottest temperature, or highest peak shock pressure) has the ambient condition (for temperature experiment this is preheating) subtracted as a comparison.

Table 8.2 displays the comparison results for the D band. Note that due to using a diamond anvil cell to create the static pressure, during the static pressure experiments no D band information was obtained for the samples.

Interestingly for the D band, the shock pressure and temperature results oppose each other in shift direction. These results could suggest that the flash heating effect, which occurs during a hypervelocity impact, could counteract the effects of shock pressure. Where shock pressure effect appears to be shifting to higher wavenumbers, the temperature effect is shifting to lower. This could mean that the magnitude of the shift being observed in the shock pressure results could be lower due to temperature effects.

Table 8.2: Comparison data for the D band peak position and width for the shock pressure, static pressure and temperature experiments. In each experiment, the results shown are the shifts at the highest condition (e.g. hottest temperature, or highest peak shock pressure) compared to the ambient condition.

		D Band Shift Direction	D Peak Max Shift [cm^{-1}]	D Width Shift Direction	D Width Max Shift [cm^{-1}]
Shock Pressure	Basalt	Higher	9.49	Broader	5.36
	Shale	Higher	7.12	Narrower	-0.80
	Graphite	Higher	0.60	Broader	4.09
Static Pressure	Basalt	-	-	-	-
	Shale	-	-	-	-
	Graphite	-	-	-	-
Temperature	Basalt	Lower	-18.7	Narrower	-32.2
	Shale	Lower	-15.3	Narrower	-27.7
	Graphite	Lower	-16.3	Broader	44.4

The magnitude of the three temperature experiment shifts are similar, whereas the shock pressure shifts for graphite are considerably different to basalt and shale. This difference could be due to the peak shock pressure experienced in the samples fasted shot speed, which for graphite was slower than basalt and shale.

For the D band widths, shale and graphite are in agreement with regards to width change direction. Comparing the result for basalt, it would appear that the temperature and shock pressure experiments contradict in width direction. For these materials, the magnitudes of the change in the D band width for the temperature experiments are significantly larger than for the shock pressure experiments. This suggests that the temperature has had a greater effect on these materials than shock pressure.

In Table 8.3 the results for the G band are discussed. The results for the basalt G band in the static pressure experiment cannot be shown as the samples would not give a signal from within the diamond anvil cell.

For the G band peak position, both shock pressure and temperature experiments for basalt agreed in shift direction. Whereas for shale, both the shock and static pressure experiments disagreed with temperature in shift direction, and for graphite,

Table 8.3: Comparison data for the G band peak position and width for the shock pressure, static pressure and temperature experiments. In each experiment, the results shown are the shifts at the higher condition (e.g. hottest temperature, or highest peak shock pressure).

		G Band Shift Direction	G Peak Max Shift [cm^{-1}]	G Width Shift Direction	G Width Max Shift [cm^{-1}]
Shock Pressure	Basalt	Higher	10.9	Narrower	-11.8
	Shale	Higher	1.70	Narrower	-6.34
	Graphite	Lower	-1.46	Broader	4.46
Static Pressure	Basalt	-	-	-	-
	Shale	Higher	19.2	Broader	7.00
	Graphite	Higher	15.0	Broader	12.5
Temperature	Basalt	Higher	2.66	Broader	31.7
	Shale	Lower	-6.16	Broader	24.3
	Graphite	Lower	-10.7	Narrower	-1.81

the shock pressure and temperature shift directions agreed but disagreed with the static pressure. Possibly for shale, the flash heating during impact could be leading to the observed shock pressure effect being lowered. This could also be a similar explanation for why the G band in graphite has shifted to a lower wavenumber. The maximum peak shock pressure experienced by graphite is more than 10 GPa less than basalt and shale. Possibly this lower pressure may be counter balanced by the temperature effects leading to it being negative. Interestingly, the D band peak position for graphite was also low in comparison to basalt and shale.

For the G band width, the basalt temperature and shock pressure effects are the reverse. Whereas for shale, the shock pressure band width change is opposite to the effects from static pressure and temperature. For graphite, the shock and static pressure results are in the opposite direction to the temperature results. Comparing the magnitudes of the shift, it could be possible that the broadening of the graphite spectra due to pressure could be affected by the flash heating during impact, due to the static pressure effects being greater than the shock pressure effects.

Table 8.4 displays the results for the R1 and R2 values across the three experiments. Again, due to the D band not being observed in the static pressure experiment, there

Table 8.4: Comparison data for the R1 and R2 values for the shock pressure, static pressure and temperature experiments. In each experiment, the results shown are the shifts at the highest condition (e.g. hottest temperature, or higher peak shock pressure).

		R1 Value Shift Direction	R1 Max Shift	R2 Value Shift Direction	R2 Max Shift
Shock Pressure	Basalt	Decrease	-0.087	Increase	0.047
	Shale	Increase	0.080	Increase	0.200
	Graphite	Increase	0.052	Increase	0.023
Static Pressure	Basalt	-	-	-	-
	Shale	-	-	-	-
	Graphite	-	-	-	-
Temperature	Basalt	Decrease	-0.315	Decrease	-0.210
	Shale	Decrease	-0.114	Decrease	-0.149
	Graphite	Decrease	-0.249	Decrease	-0.080

are no R1 and R2 value results. Once more, the temperature and shock pressure results are mostly in opposite directions. Suggesting that heating the samples increase the structural order and shocking the samples decreases it. An exception to this is the R1 values for basalt, which in both experiments suggest the same direction shift. A possible cause of this could be due to the difficulty in getting adequate D band spectra.

The reason why pressure and temperature effects are in reverse is due to what is happening physically in these two conditions. Applying pressure to a sample decreases the bond lengths and results in a stiffening of the bonds, leading to the peak position shifting to higher wavenumbers. When a sample is heated the population of different energy levels change and the modes weaken, resulting in an effect in the average position of the atom and a shifting in the peak position to lower wavenumbers (Lucazeau 2003, Huang et al. 2010).

Considering that in the slowest shot (around 1 km s^{-1}) the peak flash heating temperature may reach around 400 K (within the temperature experiment range), and that at the fastest speeds it could reach as high as 3,000 K, there could be a considerable temperature effect at work on the Raman spectra during a hypervelocity impact. An important difference to note is the time scales. During a hypervelocity impact, the samples can experience very high temperatures but only for a fraction of a

microsecond, whereas, in these temperature experiments, the samples were at elevated temperatures for hours. The shock duration does not have an effect on the Raman spectra (Wehrenberg et al. 2017).

8.3 Chapter Conclusions

This chapter has discussed an investigation into the effects of cooling and heating upon the D and G Raman bands in basalt, shale and graphite. The minimum temperature investigated was 173 K (-100 °C), and the maximum was 773 K (500 °C). A summary of the findings from this chapter are:

- Shale and graphite suggest a negative trend of D band peak position with temperature. Cooling shifts the D band to higher wavenumbers, and heating to lower. The same trend is seen for the G and D2 band peak position, however, for the G band, the data is less scattered.
- For basalt and shale, the D band width doesn't change much with temperature, remaining mostly constant. However, for graphite, the D band width increases with increasing temperature.
- For shale, although the G band width data is scattered, it suggests a positive trend with temperature, suggesting that heating the sample causes the G band to broaden. For graphite, the width of the G band remains mostly constant at 18 cm^{-1}. For basalt, it is constant during heating, but narrows during cooling. The D2 band width is scattered around 45 cm^{-1}. For both the D and G band, the variation in the band half-widths is due to the decay of a given phonon into two of three phonons (Lucazeau 2003).
- For graphite, the R1 and R2 value decreases with increasing temperature. This suggests that the carbonaceous material becomes more structurally ordered.

- Post heating, none of the sample's D bands returned to the preheating locations, whereas all the sample's D band widths did. Additionally, both basalt and shale experienced permanent effects to the G band peak position and width.

- The R1 and R2 values for graphite appear to remain lower than before heating, suggesting that there has been permanent structural ordering to the sample.

- For the majority of band attributes, temperature appears to have the reversed direction shift effect to the band peak position and width compared to pressure. The reason for this is due to pressure affecting the equilibrium spacing between nuclei (the bond length), distorting the electron cloud and hence the restoring forces resulting in a stiffening of the bonds. This shifts the peak position to higher wavenumbers. Whereas, temperature affects the population of the different energy levels and weakens the modes, this in turn effects the average position of the atom (Lucazeau 2003, Huang et al. 2010), shifting the peak position to lower wavenumber when heating. This could suggest that the magnitude of shift seen post hypervelocity impact could be low due to a flash heating effect.

Overall, it would appear that the effects of temperature are mostly in reverse to the effect of pressure. Implying that the shock pressure effect was less than the static loading effect. During an impact, the projectile would experience flash heating, which could be affecting the shock pressure effect on the Raman spectra.

Chapter 9

Capture Effects of Olivine Grains in Fine Grained Mineral Assemblages Fired into Aerogel

In 2006, NASA's Stardust spacecraft returned successfully from its mission to collect material from the coma of the Jupiter-Family Comet 81P/Wild2 (Brownlee et al. 2006). It is estimated that it collected thousands of cometary dust particles, approximately 1 – 300 μm in size and totalling approximately 3 x10^{-4} g in mass (Brownlee et al. 2006, Hörz et al. 2006). These dust particles were collected using aluminium foils and SiO_2 aerogel blocks whilst Stardust was passing the comet at a relative speed of 6.1 km s^{-1}. Aerogel is a low density, highly porous medium which has the ability to capture small impacting grains relatively intact (Hörz et al. 2006). The specific aerogel used on Stardust was transparent and had a density gradient of 5 mg cc^{-1} at the front face rising to 50 mg cc^{-1} at the rear. Aerogel is a very useful capture material as it leads to a low pressure impact spread along the length of a track formed as the grain decelerates. The resulting captured grain at the end of the track is referred to as the terminal grain (for a review of the use of aerogel in dust capture in space see Burchell, Graham & Kearsley 2006). The capture process in aerogel is thought to involve a low

shock pressure of ≤300 MPa (Trigo-Rodriguez et al. 2008) and can heat samples to over 1,000 °C for a brief period of a microsecond (see Naguchi et al. 2007 and Leroux 2012). Furthermore, it has been shown that 10 μm sized terminal grain particles remain unmelted and relatively unaltered after capture (e.g. Leroux 2012).

One of the most abundant minerals in the Solar System is Olivine ($(Mg^{+2}, Fe^{+2})_2 SiO_4$). The Raman spectrum of olivine is easily recognisable with a doublet at around 820 and 850 cm^{-1}, referred to as P1 and P2 respectively (Figure 9.1). This doublet represents the internal stretching vibrational modes of the SiO_4 ionic group. The height of the P1 and P2 doublet are a function of the crystal orientation (Chopelas 1991). Furthermore, it has been observed that the exact position of these peaks systematically varies with the olivine composition (Kuebler et al. 2006, Ishibashi et al. 2012).

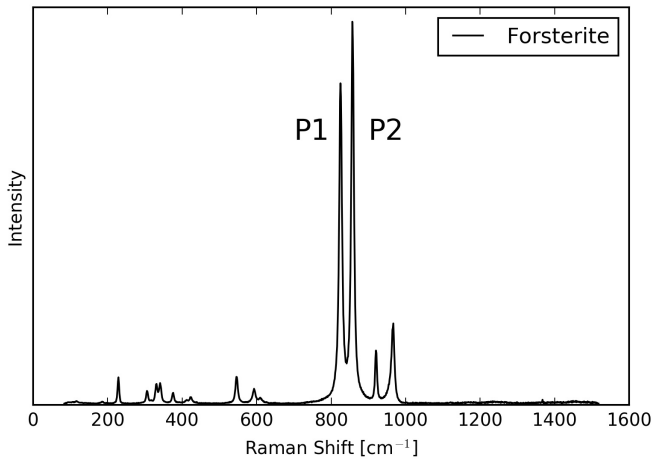

Figure 9.1: Characteristic olivine spectra with doublet peaks P1 (∼820 cm^{-1}) and P2 (∼850 cm^{-1}). Sample from the RRUFF spectral database - http://rruff.info/forsterite/display=default/.

Olivine has two end-members: forsterite (magnesium rich) and fayalite (iron rich). The term Fo content refers to the percentage of magnesium in the olivine. For example olivine with an Fo content of Fo_{90} has a ratio of 90:10 of magnesium:iron. In contrast the Fa content denotes how iron rich the olivine is. From Kuebler et al. (2006) the following equations determine the Fo content from the Raman spectra of a sample of

olivine:

$$Fo(P1) = y_1 + a_1 x_1 + b_1 x_1^2, \tag{9.1}$$

$$Fo(P2) = y_2 + a_2 x_2 + b_2 x_2^2, \tag{9.2}$$

$$Fo(P1\&P2) = y_3 + a_3 x_1 + b_3 x_2 + c_3 x_1^2 + d_3 x_2^2, \tag{9.3}$$

where $x_{1,2}$ refers to the peak position of P1 or P2 (in cm^{-1}) and the rest are constants shown in Table 9.1.

Table 9.1: Table of values for constants in Equation 9.1, 9.2 and 9.3 (Kuebler et al. 2006).

	Equation		
Constants	9.1	9.2	9.3
y_i	-484679.0451	-38847.12569	-206232.989
a_i	1172.726064	86.9086353	80.19039778
b_i	-0.709225968	-0.048381694	399.3502311
c_i			-0.042436391
d_i			-0.235797345

Foster et al. (2014) demonstrated a permanent shift of the olivine doublet peaks for single grains. However, Harriss & Burchell (2016) showed that the shifts only occur at higher impact speeds ($>\sim$5 km s^{-1}) and that the direction of the shift was found to be twice the magnitude of the work by Foster et al. (2014). The issue that arises is that given this shift, any attempt to find the Fo content as per Kuebler et al. (2006), will be flawed unless the shock effect is allowed for. For a full review see Chapter 2.

The presence of single grains of olivine would be a rare occurrence in space, so this chapter investigates the shock effects on mineral assemblages being captured in aerogel. This would allow use of Raman spectroscopy to determine Fo content of fine olivine grains inside larger assemblages captured by Stardust.

9.1 Methodology

9.1.1 Sample Material

For this work, the meteorite NWA 10256 CR2 (carbonaceous) was used. This was chosen as a good analogue to the material captured by the Stardust mission as it contains olivines with varied Fe content. The sample was analysed at the University of Leicester by SEM-EDX using a Phillips XL30 ESEM, both in thin section and in powdered form. The CR2 chondrite meteorite was found to consist of 58% chondrules, with many greater than 1 mm in diameter. It is mostly composed of pyroxenes ($En_{89-98}Wo_{0-1}Fs_{1-10}$) and olivines ($Fo_{91-99}$) (Hicks et al. 2017). The chondrules are surrounded by a matrix of fayalitic olivines (Fo_{34-50}), Fe-sulfides, Fe-Ni-metals and Fe-oxides (Hicks et al. 2017).

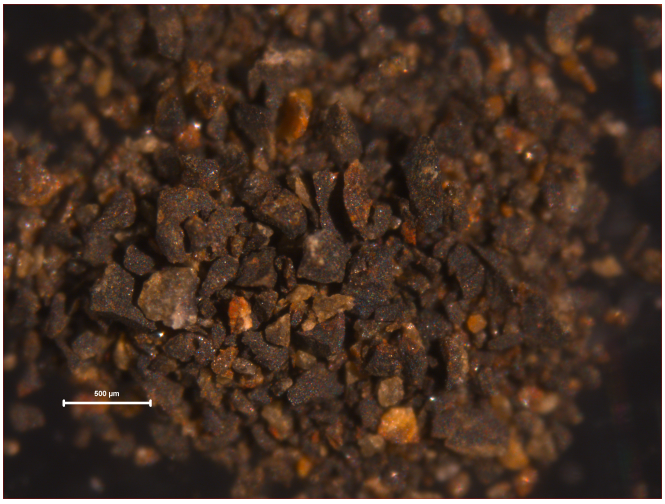

Figure 9.2: Microscope image of some raw CR2 grains before shooting.

The material from the interior of the meteorite was ground into a powder with a grain size of 25 – 200 μm. In order to establish the content of the powders before firing, the University of Kent's Raman spectrometer was used. The 532 nm (green) laser (same as in Chapter 6, 7, 8) was used to acquire the Raman spectra. Due to the small size of the grains used the 532 nm laser was used at a low power to ensure there were no laser heating effects on the grains; Hibbert & Price (2014) have shown that this can be a potential problem in the interpretation of Raman spectra.

9.1.2 The LGG and Shot Regime

The powdered meteorite was fired using the University of Kent's Two-stage Light Gas Gun (LGG) (for a discussion on how the gun operates see Chapter 3). The difference in the shots completed for this chapter, to those in other chapters, was the pressure inside the gun chamber, which was < 0.1 mbar, and the target material. A lower pressure was used as there was no water being used in the shot. Three shots were performed, with speeds of 6.10, 6.20 and 6.28 km s^{-1}, i.e. comparable to the Stardust mission capture speeds.

The target material was aerogel with a density gradient of 25 mg cm^{-3} at the front face and rising to 55 mg cm^{-3} at the rear. Each block was 30 mm thick. As a result of the transparent nature of aerogel, the Raman spectra of the terminal grains can be obtained in-situ without extraction from the aerogel (Burchell et al. 2001). The track lengths were measured using a Leica microscope.

9.2 Results and Discussion

9.2.1 Raman Characterisation

In order to appropriately characterise the powdered CR2 carbonaceous chondrite sample before shooting, 120 separate spectra were acquired from separate grains. As expected, this suggested that the sample consisted of mostly olivine and enstatite (Mg-rich end member of pyroxene). However, hematite was also found. To guarantee the correct identification of these minerals, comparative spectra from the RRUFF online database (Lafuente et al. 2015) were used. The RRUFF database contains high quality spectra data from well characterised materials. In Figure 9.3 we show example spectra for each mineral relevant to this work.

Of the 120 spectra, approximately 47% were olivine, 46% were enstatite and 7%

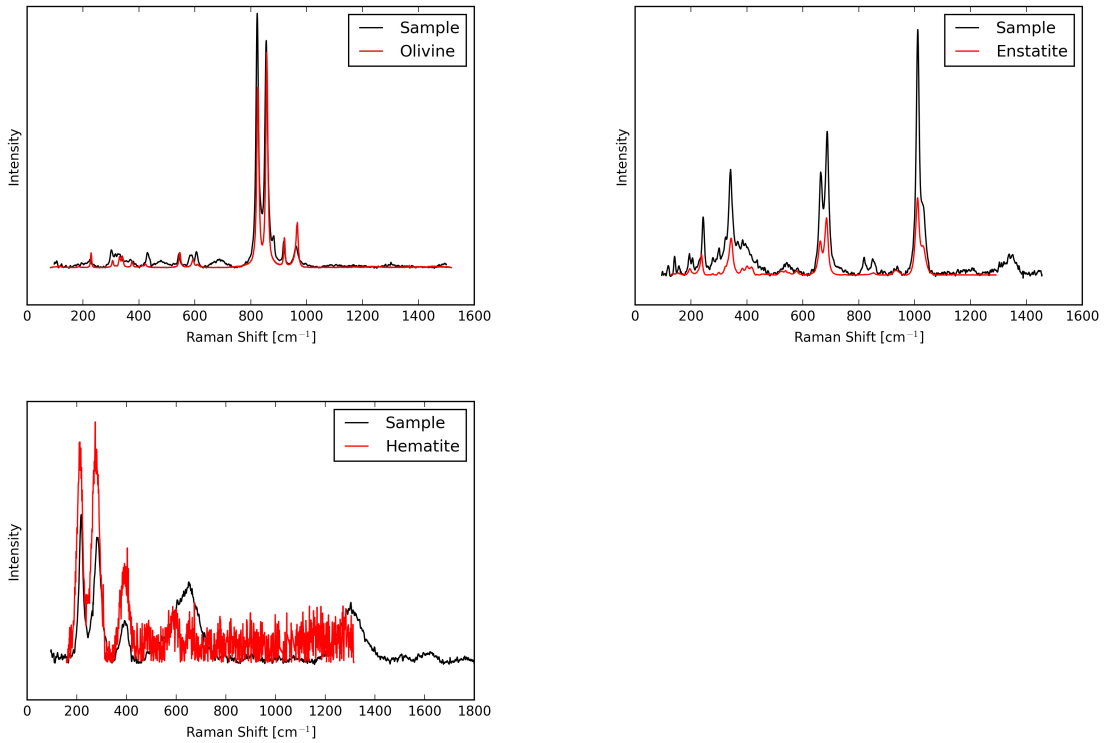

Figure 9.3: Example spectra (black) of each mineral from the CR2 meteorite with accompanying comparison spectra (red).

were hematite. In order to determine the chemistry of the olivine spectra, Equation 9.3 was used. Performing this splits the olivines into three Fo groups - Fo_{43-57} (7% of spectra), Fo_{70-82} (29% of spectra) and Fo_{88-99} (64% of spectra), see Figure 9.4. This was unexpected in that the elemental analysis at Leicester had only indicated the presence of Fo_{34-50} and Fo_{91-99}. The appearance of a group with Fo_{70-82} was, therefore, a surprise, but was confirmed by its repeated presence (29% of spectra).

The comparative spectrum for the hematite sample is not the standard spectrum (Figure 9.3). The comparative spectrum used (RRUFF ID: R070240) has a measured chemistry of $(Fe^{3+}_{1.97}\ Al_{0.02}\ Mn^{3+}_{0.01})\ O_3$ and was confirmed as hematite by X-ray diffraction and chemical analysis. This sample was collected from the Moshgai, Gobi Desert in Mongolia (Lafuente et al. 2015). The broadness of the spectral peaks in this reference spectrum is due to the sample being poorly crystalline and matches the observed peak widths in our laboratory grains. Thus, the hematite grains in the meteorite sample are

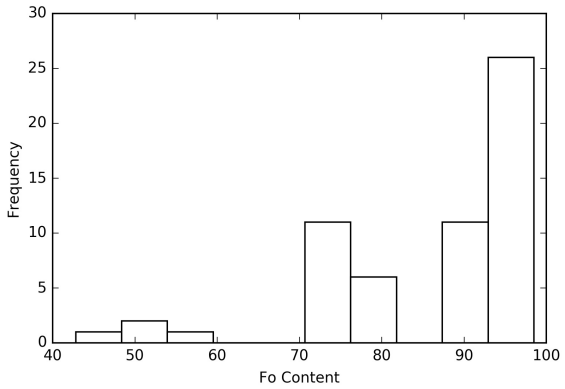

Figure 9.4: Fo content for the pre-shot characterised olivine samples. This shows the sample splits into three groups - Fo_{43-57}, Fo_{70-82} and Fo_{88-99}.

also poorly crystalline.

9.2.2 Olivine Capture

From the three shots, there were 52 observable grains. Figure 9.5 is an image of a track and terminal grain. Generally, between 15 and 20 particles were captured per shot with a broad variation in track lengths (0.82 – 21.3 mm) and terminal grain sizes (diameter 6.28 – 74.4 μm). One grain passed through the aerogel block and into the back plate.

Figure 9.5: Image of terminal grain and capture track. The grain entered the block of aerogel at the right side of the image. An arrow indicates the terminal grain.

Raman spectroscopy was performed on all these grains in situ. We found significant issues in acquiring strong spectra due to substantial fluorescing, and the depth of the locations within the aerogel block meaning there was difficulty focusing upon them. Despite this, six grains produced olivine spectra. Of these grains, five terminal grains were found in a single shot and one in another. The spectra were fitted using LabSpec6 to find the peak positions and Equation 9.3 was then used to determine their Fo content.

Figure 9.6 is a plot of the terminal grain's Fo content. In Figure 9.6 the red, black and blue lines in the figure represent the boundaries of the three Fo groups discussed in the previous section.

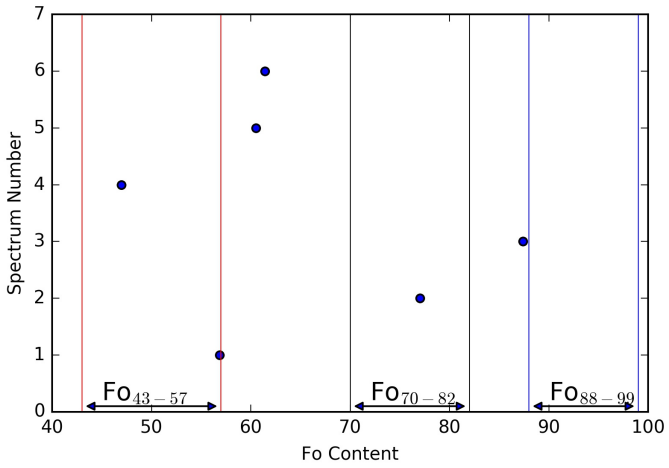

Figure 9.6: The Fo conetent for each olivine spectra captured in aerogel. The two red lines refer to the boundaries of the Fo_{43-57} group, the black for the Fo_{70-82} group and the blue for the Fo_{88-99} group. Each grain is shown separately on the vertical axis.

In Figure 9.6 there appear to be three spectra that have a Fo content outside the three characterised groups (Spectra 3, 5 and 6). This suggests that these spectra have been altered upon capture in the aerogel. Foster et al. (2014) have shown that the capture in aerogel results in a shift to a lower wavenumber for both peaks P1 and P2. Therefore, we deduce that Spectrum 3 has been shifted down from the Fo_{88-99} and Spectra 5 and 6 have been shifted down from the Fo_{70-82} group. It is, of course, possible that a larger shift occurred and these grains also originated from the Fo_{88-99} group. These alterations are as a result of the capture process in aerogel. It is possible that the other spectra have been shifted, e.g. Spectrum 1 could have come from a higher Fo band and been shifted downward, but they cannot be positively demonstrated by Raman spectra.

In order to determine an estimate of the peak shift for Spectra 3, 5 and 6 we assumed that they have shifted from the mean Fo content peak position of the pre-shot spectra in the bands to their immediate right in Figure 9.6. This comparison suggests a shift

downward for Spectrum 3, 5 and 6 of 1.21, 1.56 and 1.48 cm^{-1} for P1 and 1.81, 3.40 and 3.21 cm^{-1} for P2.

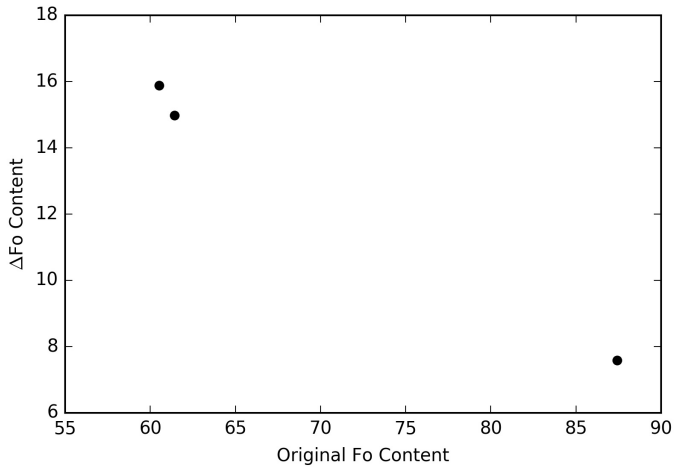

Figure 9.7: Magnitude of the difference in Fo content from the measured captured grain to the mean Fo content of the Fo group vs. captured grain Fo content.

Figure 9.7 shows the magnitude of the change in measured Fo content versus the original Fo content. It would suggest that the lower original Fo content has a greater change. This is due to the P2 peak experiencing a greater shift, suggesting that the shock/heating is causing the peaks to move closer together. This agrees with the separation in the peak position corresponding to the different Fo content (see Figure 9 in Foster et al. 2014). It has been shown that San Carlos olivine (Fo_{92}) can experience up to 10 cm^{-1} in shift, to the left corresponding to ΔFo of approximately 25, when captured in aerogel (Foster et al. 2014). This shift is greater than that experienced by the Fo_{88-99} olivines in this work ($\Delta Fo \approx 8$). This difference could be due to the olivines being a constituent of the mineral assemblage, or that it is from a small grain.

9.2.3 Other Minerals

In Figure 9.8 we show the Raman spectra of the other minerals found in the terminal grains. In Figure 9.8a we compare the enstatite captured spectra to a reference sample

from the RRUFF database (RRUFF ID: R070641). Interestingly, it would appear that some of the spectra experienced far greater capture alterations than both olivine and hematite in that the peaks broaden significantly. This appears to be in contradiction with Burchell et al. 2006 who suggest enstatite experiences less alteration as a result of capture. It appears that along with a possible peak shift, the peaks have widened indicating a break-down of crystallinity, both due to shock and/or heat effects. An additional reason for the broadening of the enstatite peaks could be due to the surface being partially melted and therefore the spectra are suggesting some glassification of the mineral surface.

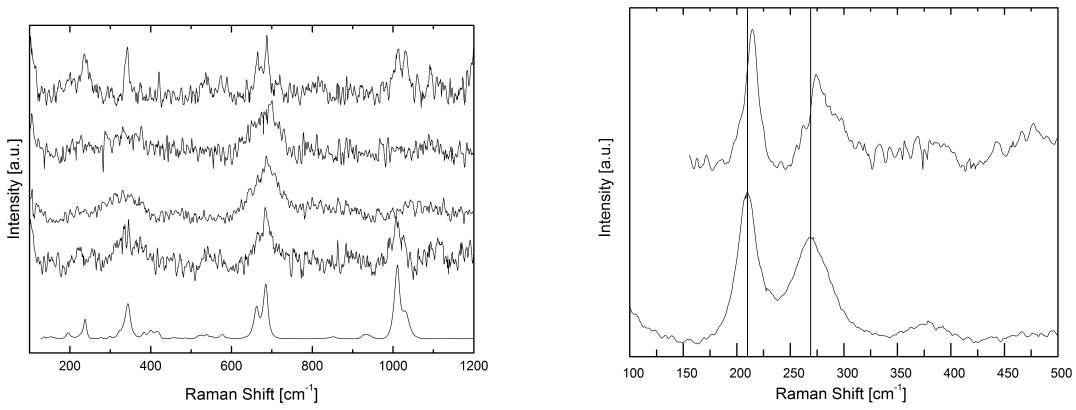

(a) (b)

Figure 9.8: (a) Top four spectra are of possible enstatite captured grains with the bottom being a reference enstatite spectrum from the RRUFF database. (b) Top spectrum is hematite that has been captured in aerogel, the bottom is a hematite spectrum from the pre-shot meteorite.

One spectrum of hematite was observed, see Figure 9.8b. The proportion in which we find olivine:enstatite:hematite (6:4:1) are within statistics comparative with those in the raw sample (47:46:7, or approximately 5:5:1). In Figure 9.8b there appears to be a peak shift of approximately +4 cm^{-1} for both peaks due to the shock and heating effects during capture. Unlike the olivine, the shift is to higher wavenumbers. Previous experiments firing 10 μm grains of hematite into aerogel at 6 km s^{-1}, displayed a downwards shift in the Raman spectra (see Figure 9.9, taken from Bridges et al. 2010),

the opposite to the shift observed here.

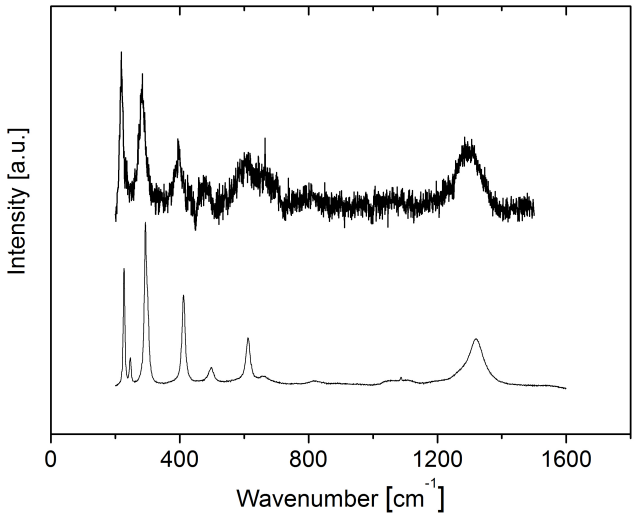

Figure 9.9: 10 μm hematite grain after capture in aerogel (density 30 kg m^{-3}) at 6.1 km s^{-1}. The bottom spectrum is a comparison raw grain. This figure has been taken from Bridges et al. (2010).

Figure 9.9 is taken from Bridges et al. (2010) and shows a Raman spectrum from 10 μm captured hematite grain fired at 6 km s^{-1} into aerogel compared with that from a raw grain. It is evident that the whole spectrum of the captured grain has been shifted to lower wavenumbers (by a few wavenumbers) and the individual peaks increased in width. The reason why these two results may not be agreeing could be due to the initial chemical composition of the hematite pre-shot. Much like the olivine, where the ratio of magnesium and iron relates to the doublet peak position, the initial chemistry of the two pre-shot hematite may mean that their peak positions are at different locations. However, the differences in peak position could be as a result of the production of hematite from magnetite as the sample is heated. This has been shown to lead to similar shifts and broadening (Shebanova & Lazor 2003).

9.3 Chapter Conclusions

This chapter discusses the capture effects on a carbonaceous chondrite (CR2) meteorite when fired into aerogel at speeds between 6.1 and 6.3 km s^{-1}. The goal was to determine the capture effects on olivine when it was a constituent of a mineral assemblage. Here is a summary of the findings from this chapter:

- Three examples of shifted olivine spectra are detected. An estimate of the shift for the peaks P1 and P2 for the three spectra are 1.21, 1.56 and 1.48 cm^{-1} and 1.81, 3.40 and 3.21 cm^{-1}, both to lower wavenumbers, respectively.
- However, the magnitude of these shifts are not in full agreement with past work (Foster et al. 2014). The magnitude is lower than in Foster et al. (2014) which could be as a result of being a constituent of a mineral assemblage. This could mean that the shock wave is propagating differently through the inhomogeneous material. This would affect the olivine differently in comparison to when it is a singular grain.
- Given that the position of P1 and P2 are used to determine the relative Mg/Fe content of the olivine, these results indicate that there may be uncertainties in the Mg/Fe content of the olivines found by Stardust if identified by Raman spectroscopy. Further, the correction suggested by Foster et al. (2014) may over correct the Fo content.
- We also identified other minerals in the sample (enstatite and hematite), and see changes to their spectra as well. Both capture effects on these materials do not agree with past work (Burchell et al. 2006, Bridges et al. 2010). In the case of enstatite, the shift in the Raman spectra were in the same direction, but of greater magnitude than in previous work. For the hematite, the shift was in the opposite direction to previous work.

Final conclusions and future work

Conclusions

The work conducted in this thesis was investigating the fragmentation of the impacting projectiles and the effect of shock pressure, static pressure and temperature on the carbon D and G bands in Raman spectroscopy. Further work has looked into the capture effect upon olivine as a constituent of a mineral assemblage. The following section shall briefly outline the findings from the completed work.

Chapter 5 discussed the fragmentation of basalt and shale projectiles. In this experiment basalt and shale was filed into approximately 1.5 mm cubes. The projectiles were fired into water at speeds between 0.39 and 6.13 km s^{-1} using the University of Kent's Two-stage Light Gas Gun. This produced peak shock pressures of up to 30.9 GPa. The water, containing the fragmented projectile, was then filtered through a 0.1 μm filter membrane. These filters were then mapped using a SEM at $\times$95 magnification, producing over 900 fields of view. From here, ImageJ was used to analyse the fragments. Over 400,000 fragments were measured in each shot. The ratio of the semi-minor to semi-major axis of each fragment was investigated. Cumulative fragment size distributions were generated and fitted with three power laws in the form of $N(> S) = aS^b$. The gradient b was shown to get steeper with increasing impact speed. An approximation for the total mass retained of the projectile was also determined. From this, it was possible to estimate impactor percentage survival at different Solar

System impact scenarios. The ratio of the mass of the largest fragment to the mass of the projectile was also plotted against the projectile energy density. From this, the catastrophic disruption energy density of basalt and shale were found. Finally, from this work, it was possible to determine information about possible impactors applicable to many Solar System impact events. Specific examples of impacts on Vesta and Ceres were explored, and showed that significant fractions of a basalt-like impactor can be retrieved at the impact site. Furthermore, this work is directly significant to the impacts of micrometeorite and millimetre sized impactors on airless bodies. Giving information regarding the mixing on asteroids surfaces.

Chapter 6 discussed the shock pressure effects on the D, G and D2 carbon bands present in the basalt, shale and, an additional material, graphite. The method from Chapter 5 was used in order to shock the materials. The peak shock pressure range for basalt, shale and graphite was 2.30 to 23.3 GPa, 2.12 to 30.9 GPa, and 1.60 to 13.4 GPa respectively. Before shooting, each projectile was mapped using the 532 nm Raman laser on one projectile face. From this map, 25 spectra were used to characterise the projectile material. Post shot, Raman spectra of 40 random separate fragments were obtained. These spectra were compared to the projectile spectra. There was considerable difficulty in acquiring good D band spectra for basalt, and it did appear that the variation in the raw material spectra could have led to scatter in the results. Therefore, limited trends could be ascertained. Upon analysis of the R1 and R2 values, it would seem that shocking the material did generally increase the structural disorder. Furthermore, it seemed that the smaller in-plane graphite crystallites experienced the most G band peak position shift. Finally, this work suggests that there could be a possibility of misinterpreting a sample when attempting to determine whether it is biogenic carbon if the sample is from a shocked area.

Chapter 7 and 8 discussed the static pressure and temperature effects on the D and G carbon bands in the sample materials. In order to produce static pressure on the sample materials a diamond anvil cell was used, and to investigate hot and

cold temperature effects a Linkam temperature stage was used. Samples experienced a static pressure up to 3.59 GPa, and a temperature range of 173 to 773 K (-100 to 500 °C). The G band peak position appeared to shift to higher wavenumbers with increasing static pressure. The width of the G band doesn't appear to change until approximately 2 GPa, where it broadens. No observations of the D band could be obtained due to the diamond Raman line. Heating the sample materials appears to shift both band peak positions to lower wavenumbers. The widths of the bands didn't change much with temperature. Furthermore, heating the sample appears to increase the structural order of the materials. Interestingly, it would seem that the effects of pressure and temperature generally shift the band positions in opposite directions. The effects of shock pressure were to a lower degree than static pressure. Possibly, as a hypervelocity impact includes shock pressure and flash heating effects, it could explain why a lesser shift is observed from the shock pressure results. Or this could be due to the spectra from the static pressure experiments being obtained in-situ whereas, the residual afterwards is analysed in the shock testing.

Chapter 9 discussed the capture effects on a ground carbonaceous chondrite (CR2) meteorite fired into aerogel at speeds between 6.1 and 6.3 km s^{-1}. This was done in order to determine the capture effects on olivine when it is a constituent of a mineral assemblage. The P1 and P2 peaks of olivine both shifted to lower wavenumbers. The magnitude of these shifts were lower than reported in past work (Foster et al. 2014). This could suggest that the shock wave is propagating differently through the inhomogeneous material. As the peak positions of P1 and P2 are related to the relative Mg/Fe content of the olivine, this work indicates that there may be uncertainties in the Mg/Fe content of the olivine found by NASA's Stardust mission, if identified by Raman spectroscopy.

Future work

Building on the work in this thesis there are a multitude of possible different investigations that could be conducted in the future. This section shall discuss some of these.

Projectile Fragmentation

Chapter 5 looked into the fragmentation of projectiles impacting at angles of normal incidence. This is highly unlikely to occur in Solar System impacts. The most probable impact angle is 45°. Therefore, it would be important to investigate the effects of impact angle on the fragmentation of the projectile. The same investigations can be conducted as in Chapter 5 and directly compared. This would give much better insight into projectile survival after hypervelocity impacts onto Solar System bodies.

To explore projectile fragmentation further, it would be interesting to use the same methods seen in Chapter 5 to investigate the impact effects on other projectile materials which are analogous to different types of potential impactors in the Solar System. Work of this nature has already begun with copper (comparing to the Deep Impact Mission), for example, (see McDermott et al. 2016). This work only looked at fragments greater than 10 μm in size, so it could be interesting to look at sizes less than this using the method from this thesis.

Furthermore, it would also be interesting to compare experimental projectile fragmentation with hydrocode simulations to draw comparisons.

Effects on the Carbon D and G band for a Target Material

Some interesting comparative work that could be conducted, would be to fire molybdenum spheres onto targets of basalt, shale and graphite. The molybdenum spheres are

a good projectiles for this experiment as they do not have a Raman signature. They can also be fired as a buck shot resulting in multiple craters meaning multiple results can be drawn from one shot. The resultant craters could then be mapped using the Raman spectrometer, and the shift to the D, G and D2 bands could be analysed. It is important to note that the surface of the crater will need to be lightly washed to remove the carbon gun debris fired by the gun. Firing onto the materials as a target allows for the impacted material to be directly compared to the raw material in the local area, possibly reducing the effect of the variation in the raw sample spectra. However, there still will be some sample variation (non-homogeneous nature) effects to contend with.

Impact Effects on Spectra of Other Materials

The impact effects upon other materials can also be investigated. For example the impact effects on minerals such as pyroxenes (e.g. enstatite), magnetite and olivine, or upon biological materials. Reports on the impact effects upon the olivine doublet are noted by Chapter 9 (or Wickham-Eade et al. 2017, accepted), Foster et al. (2014), Harriss & Burchell (2016) and Avdellidou et al. (2016). These investigations can be conducted with the projectile impacting water, aluminium foils, or aerogel, or it can be the target material. The capture effects on minerals and biological materials can have implications for possible future space missions, e.g. Hyabusa 2.

Pressure versus Temperature

It would be interesting to constrain the role of temperature on the effect on Raman spectra during a hypervelocity impact. To do this a gem quality material needs to be subjected to a range of shock pressures. Separate samples should then be put under static pressure, using a diamond anvil cell, to see how the shifts of the peaks compare to the shocked conditions. The temperature effects upon another separate sample can be investigated using a Linkam temperature stage. The shifts can then be compared

to possibly constrain the effects of flash heating upon the Raman spectra of a sample during a hypervelocity impact. In addition to this, hydrocode models can be used to estimate the peak temperature during each impact to see if there is any overlap.

Final Remarks

To conclude, the effects of hypervelocity impacts are extensive and much of it unknown. Although increasing computational power enhances impact models, hypervelocity impact experiments are still vital to the understanding of the processes occurring. The effect hypervelocity impacts have on the evolution of the surfaces of planetary bodies and fields in Astrobiology will continue to display many great advancements, answering many important mysteries. For now, hopefully, this thesis has added one more small piece to a very big puzzle.

Bibliography

Abernethy, F. A. J., Verchovsky, A. B., Starkey, N. A., Anand, M., Franchi, I. A. & Grady, M. M. (1928), 'Stable isotope analysis of carbon and nitrogen in angrites', *Nature* **121**, 501–502.

A'Hearn, M. F., Belton, M. J. S., Delamere, W. A., Kissel, K. P., McFadden, L. A., Meech, K. J., Melosh, H. J., Schultz, P. H., Sunshine, J. M., Thomas, P. C., Veverka, J., Yeomans, D. K., Baca, M. W., Busko, I., Crockett, C. J., Collins, S. M., Desnoyer, M., Eberhardy, C. A., Ernst, C. M., Farnham, T. L., Feaga, L., Groussin, O., Hampton, D., Ipatov, S. I., Li, J.-Y., Lindler, D., Lisse, C. M., Mastrodemos, N., Owen Jr, W. M., Richardson, J. E., Wellnitz, D. D., & White, R. L. (2005), 'Deep Impact: Excavating Comet Tempel 1', *Science* **310**, 258–264.

Ahrens, T. J. & O'Keefe, J. D. (1972), 'Shock melting and vaporization of Lunar rocks and minerals', *Moon* **4**, 214–249.

Altwegg, K., Balsiger, H., Bar-Nun, A., Berthelier, J. J., Bieler, A., Bochsler, P., Briois, C., Calmonte, U., Combi, M., De Keyser, J., Eberhardt, P., Fiethe, B., Fuselier, S., Gase, S., Gombosi, T. I., Hansen, K. C., Hassig, M., Jackel, A., Kopp, E., Korth, A., LeRoy, L., Mall, U., Marty, B., Mousis, O., Neefs, E., Owen, T., Reme, H., Rubin, M., Semon, T., Tzou, C. Y., Waite, H. & Wurz, P. (2015), '67P/Churyumov-Gerasimenko, a Jupiter family comet with a high D/H ratio', *Science* **347**, 1–3.

Anderson, T. L. (1991), *Fracture Mechanics: Fundamentals and Applications*, CRC Press, Boca Raton, USA.

Armstrong, J. C. (2010), 'Distribution of impact locations an velocities of Earth meteorites on the Moon', *Earth Moon Planets* **107**, 43–54.

Arvidson, R. E., Ashley, J. W., Bell III, J. F., Chojnacki, M., Cohen, J., Economou, T. E., Farrand, W. H., Fergason, R., Fleischer, I., Geissler, P., Gellert, R., Golombek, M. P., Grotzinger, J. P., Guinness, E. A., Heberle, R. M., Herkenhoff, K. E., Herman, J. A., Iagnemma, K. D., Jolliff, B. L., Johnson, J. R., Klingelhofer, G., Knoll, A. H., Knudson, A. T., Li, R., McLennan, S. M., Mittlefehldt, D. W., Morris, R. V., Parker, T. J., Rice, M. S., Schroder, C., Soderblom, L. A., Squyres, S. W., Sullivan, R. J. & Wolff, M. J. (2011), 'Opportunity Mars Rover mission: Overview and selected results from Purgatory ripple to traverses to Endeavour crater', *Journal of Geophysical Research* **116**, E00F15.

Asay, J. R. & Shahinpoor, M. (1993), *High-pressure shock compression of solids*, Springer-Verlag, Berlin, GER.

Attrep, M., Orth, C. J. & Quintana, L. R. (1991), Chemical fractionation of siderophile elements in impactites from Australian meteorite craters, *in* '22nd LPSC, page 22'.

Avdellidou, C., Price, M. C., Delbo, M., Ioannidis, P. & Cole, M. J. (2016), 'Survival of the impactor during hypervelocity collisions I. An analogue for low porosity targets', *Monthly Notices of the Royal Astronomical Society* **456**, 2957–2965.

Banwell, C. N. (1983), *Fundamentals of molecular spectroscopy*, McGraw-Hill Book Company, Berkshire, UK.

Baratoux, D. & Reimold, W. U. (2016), 'The current state of knowledge about shatter cones: Introduction to the special issure', *Meteoritics and Planetary Science* **51**, 1389–1434.

Benz, W. & Asphaug, E. (1999), 'Catastrophic disruption revisited', *Icarus* **142**, 5–20.

Beyssac, O., Goffe, B., Chopin, C. & Rouzaud, J. N. (2002), 'Raman spectra of carbonaceous material in metasediments: a new geothermometer', *Journal of Metamorphic Geology* **20**, 859–871.

Beyssac, O., Goffe, B., Petitet, J. P., Froigneux, E., Moreau, M. & Rouzaud, J. N. (2003), 'On the characterization of disordered and heterogeneous carbonaceous materials by Raman spectroscopy', *Spectrochimica Acta Part A* **59**, 2267–2276.

Beyssac, O., Rouzaud, J. N., Goffe, B., Brunet, F. & Chopin, C. (2002), 'Graphitization in a high-pressure, low-temperature metamorphic gradient: a Raman microspectroscopy and HRTEM study', *Contributions to Mineralogy and Petrology* **143**, 19–31.

Bischoff, A., Horstmann, M., Pack, A., Laubenstein, M. & Haberer, S. (2010), 'Asteroid 2008 TC3-Almahata Sitta: A spectacular breccia containing many different ureilitic and chondritic lithologies', *Meteoritics and Planetary Science* **45**, 1638–1656.

Bland, P. A., Artemieva, N. A., Collins, G. S., Bottke, W. F., Bussey, D. B. J. & Joy, K. H. (2008), Asteroids on the Moon: Projectile survival during low velocity impact, *in* '39th LPSC, abstract: 2045'.

Bockelée-Morvan, D., Crovisier, J., Mumma, M. J. & Weaver, H. A. (2004), 'The composition of cometary volatiles', *Comets II* **75**, 391–423.

Bogner, A., Jouneau, P. H., Tholet, G., Basset, D. & Gauthier, C. (2007), 'A history of scanning electron microscopy developments: Towards 'wet-STEM' imaging', *Micron* **38**, 390–401.

Boslough, M. B. & Asay, J. R. (1992), *High-pressure Shock Compression of Solids - Ch. 2: Basic principles of shock compression*, Springer-Verlag, New York, USA.

Bottke, W. F., Durda, D. D., Nesvorny, D., Jedicke, R., Morbidelli, A., Vokrouhlicky, D. & Levison, H. (2005), 'The fossilized size distribution of the main asteroid belt', *Icarus* **175**, 111–140.

Bottke, W. F., Nolan, M. C., Greenberg, R. & Kolvoord, R. A. (1994), 'Velocity distribution among colliding asteroids', *Icarus* **107**, 255–268.

Bowden, S. A., Court, R. W., Milner, D., Lindgren, P., Crawford, I. A., Parnell, J. & Burchell, M. J. (2008), 'The thermal alteration by pyrolysis of the organic component

of small projectiles of mudrock during capture at hypervelocity', *Journal of Analytical and Applied Pyrolysis* **82**, 312–314.

Bower, D. M., Steele, A., Fries, M. D. & Kater, L. (2013), 'Micro Raman spectroscopy of carbonaceous material in microfossils and meteorites: Improving a method for life detection', *Astrobiology* **13**, 103–113.

Bridges, J. C., Burchell, M. J., Changela, H. G., Foster, N. J., Creighton, J. A., Carpenter, J. D., Gurman, S. J., Franchi, I. A. & Busemann, H. (2010), 'Iron oxides in comet 81P/Wild 2', *Meteoritics and Planetary Science* **45**, 55–72.

Brolly, C., Parnell, J. & Bowden, S. (2016), 'Raman spectroscopy: Caution when interpreting organic carbon from oxidising enviroments', *Planetary and Space Science* **121**, 53–59.

Brownlee, D. E. & et al. (2006), 'Comet 81P/Wild 2 under a microscope', *Science* **314**(5806), 1711–1716.

Buchwald, V. F. (1975), *Hand of Iron Meteorites*, University of california Press, Berkeley, CA.

Bucio, L., Rosales, I., Thions, C., Soullard, J. & Orozco, E. (2015), 'Phase transition induced by shock copression of gypsum mineral: X–ray and micro–Raman analysis', *High Pressure Research* **35**, 355–362.

Bunch, T. E. & Cassidy, W. A. (1972), 'Petrographic and electron microprobe study of the Monturaqui impactite', *Contributions to Mineralogy and Petrology* **36**, 95–112.

Burchell, M. J. (2015), *Shocked rocks: impacts form the laboratory to the Solar System, in Planetary Mineralogy*, European Mineralogical Union (EMU) and the Mineralogical Society of Great Britain and Ireland, London, UK.

Burchell, M. J., Bowden, S. A., Cole, M., Price, M. C. & Parnell, J. (2014), 'Survival of organic materials in hypervelocity impacts of ice on sand, ice and water in the laboratory', *Astrobiology* **14**, 473–485.

Burchell, M. J., Cole, M. J., McDonnell, J. A. M. & Zarnecki, J. C. (1999), 'Hypervelocity impact studies using the 2 MV Van de Graaf accelerator and two-stage light gas gun of the University of Kent at Canterbury', *Measurement Science and Technology* **10**, 41–51.

Burchell, M. J., Cole, M. J., Price, M. C. & Kearsley, A. T. (2012), 'Experimental investigation of impacts by solar cell secondary ejecta on silica aerogel and aluminium foil: Iimplications for the Stardust interstellar dust collector', *Meteoritics and Planetary Sciance* **47**, 671–683.

Burchell, M. J., Cole, M. J., Ramkissoon, N. K., Wozniakiewicz, P. J., Price, M. C. & Foing, B. (2015), 'SMART-1 end of life shallow regolith impact simulations', *Meteoritics and Planetary Science* **50**, 1436–1448.

Burchell, M. J., Creighton, J. A. & Kearsley, A. T. (2001), 'Capture of paticles in hypervelocity impacts in aerogel', *Meteoritics and Planetary Science* **36**, 209–211.

Burchell, M. J., Foster, N. J., Kearsley, A. T. & Creighton, J. A. (2008), 'Indentification of mineral impactors in hypervelocity impact craters in aluminium by Raman spectroscopy of residues', *Meteoritics and Planetary Science* **43**, 135–142.

Burchell, M. J., Graham, G. & Kearsley, A. (2006), 'Cosmic dust collection in aerogel', *Annual Review of Earth and Planetary Science* **34**, 385–418.

Burchell, M. J., Harriss, K. H., Price, M. C. & Yolland, L. (2017), 'Survival of fossilised diatoms and forams in hypervelocity impacts with peak shock pressures in the 119 GPa range', *Icarus* **290**, 81–88.

Burchell, M. J. & Kearsley, A. T. (2009), 'Short-period Jupiter family comets after Stardust', *Planetary and Space Science* **57**, 1146–1161.

Burchell, M. J., Mann, J., Creighton, J. A., Kearsley, A. T. & Franchi, I. A. (2006), 'Indentification of minerals and meteoritic materials via Raman techniques after capture in hypervelocity impacts on aerogel', *Meteoritics and Planetary Science* **41**, 217–232.

Burchell, M. J., McDermott, K. H., Price, M. C. & Yolland, L. J. (2014), 'Survival of fossils under extreme shocks induced by hypervelocity impacts', *Philosophical Transactions of the Royal Society A* **372**, 2–15.

Burchell, M. J., Robin-Williams, R. & Foing, B. (2010), 'The SMART-1 lunar impace', *Icarus* **207**, 28–38.

Canup, R. & Asphaug, E. (2001), 'Origin of the moon in a giant impact near the end of the earth's formation', *Nature* **412**, 708–712.

Chao, E. C. T., Shoemaker, E. M. & Madsen, B. M. (1960), 'First natural occurrence of coesite', *Science* **132**, 220–222.

Chopelas, A. (1991), 'Single crystal Raman spectra of forsterite, fayalite, and monticellite', *American Mineralogist* **76**, 1100–1109.

Coes, L. (1953), 'A new dense crystalline silica', *Science* **118**, 131–132.

Courreges-Lacoste, G. B., Ahlers, B. & Perez, F. R. (2007), 'Combined raman spectrometer/laser-induced spectrometer for the next esa mission to breakdown mars', *Spectrochimica Acta Part A-Molecular and Biomolecular Spectroscopy* **68**, 1023–1028.

Court, R. W., Sephton, M. A., Parnell, J. & Gilmour, I. (2007), 'Raman spectroscopy of irradiated organic matter', *Geochimica et Cosmochimica Acta* **71**, 2547–2568.

Crozier, W. D. & Hume, W. (1957), 'High-velovity, Light-Gas Gun', *Journal of Applied Physics* **28**, 892–894.

Daly, R. T. & Schultz, P. H. (2013), Experimental studies into the survival and state of the projectile, *in* '44th LPSC, abstract: 2240'.

Daly, R. T. & Schultz, P. H. (2014), How much of the impactor (and its water) ends up in Vesta's regolith?, *in* '45th LPSC, abstract: 2070'.

Daly, R. T. & Schultz, P. H. (2015*a*), New constraints on the delivery of impactors to icy bodies: implications for Ceres, *in* '46th LPSC, abstract: 1792'.

Daly, R. T. & Schultz, P. H. (2015*b*), 'Predictions for impactor contamination on ceres based on hypervelocity impact experiments', *Geophysical Research Letters* **42**, 7890–7898.

Daly, R. T. & Schultz, P. H. (2016), 'Delivering a projectile component to the Vestan regolith', *Icarus* **264**, 9–19.

DeMeo, F. E., Binzel, R. P., Slivan, S. M. & Bus, S. J. (2009), 'An extension of the bus asteroid taxonomy into the near-infrared', *Icarus* **202**, 160–180.

Dense, M. R. (1968), *Shock zoning at Canadian craters: petrography and structural implications, in Shock Metamorphism of Natural Materials*, Mono Book Corp, Baltimore, USA.

Deuysch, A., Poelchau, M. H. & Kenkmann, T. (2015), *Impact metamorphism in terrestrial and experimental cratering events, in Planetary Mineralogy*, European Mineralogical Union (EMU) and the Mineralogical Society of Great Britain and Ireland, London, UK.

Doolan, C. J. (2001), 'A two-stage light gas gun for the study of high speed impact in propellants', *Department of Defence* **Salisbury, Technical Report**, 1092.

Durda, D. D., Bottke Jr, W. F., Nesvorny, D., Enke, B. L., Merline, W. J., Asphaug, E. & Richardson, D. C. (2007), 'Size-frequency distributions of fragments from SPH/N-body simulations of asteroid impacts: comparison with observed asteroid families', *Icarus* **186**, 498–516.

Durda, D. D., Greenberg, R. & Jedicke, R. (1998), 'Collisional models and scaling laws: A new interpretation of the shape of the main-belt asteroid size distribution', *Icarus* **135**, 431–440.

Elkins-Tanton, L. T. (2006), *Asteroids, meteorites and comets*, Chealsea House, New York, USA.

ESA (2016*a*), 'The ExoMars rover instrument suite', `http://exploration.esa.int/jump.cfm?oid=45103`. Accessed: 06/09/2016.

ESA (2016*b*), 'Oxia Planum', `http://exploration.esa.int/jump.cfm?oid=54724`. Accessed: 06/09/2016.

Fairen, A. G., Dohm, J. M., Baker, V. R., Thompson, S. D., Mahaney, W. C., Herkenhoff, K. E., Rodriguez, J. A. P., Davila, A. F., Schulze-Makuch, D., El Maarry, M. R., Uceda, E. R., Amils, R., Miyamoto, H., Kim, K. J., Anderson, R. C. & McKay, C. P. (2011), 'Meteorites at Meridiani Planum provide evidence for significant amounts of surface and near-surface water on early Mars', *Meteoritics and Planetary Science* **46**, 1832–1841.

Farrell-Turner, S., Reimold, W. U., Nieuwoudt, M. & Erasmus, R. M. (2005), 'Raman spectrocopy of olivine in dunite experimentally shocked to pressures betwen 5 and 56 GPa', *Meteoritics and Planetary Science* **40**, 1311–1327.

Fendyke, S., Price, M. C. & Burchell, M. J. (2013), 'Hydrocode modelling of hypervelocity impacts on ice', *Advances in Space Research* **52**, 705–714.

Ferrari, A. C. (2007), 'Raman spectroscopy of graphene and graphite: Disorder, electron-phonon coupling, doping and nonadiabatic effects', *Solid State Communications* **143**, 47–57.

Ferrari, A. C. & Basko, D. M. (2013), 'Raman spectroscopy as a versatile tool for studying the properties of graphene', *Nature Nanotechnology* **8**, 235–246.

Ferrari, A. C. & Robertson, J. (2000), 'Interpretatino of Raman spectra of disordered and amorphous carbon', *Physical Review B* **61**, 14095–14107.

Flandes, A. & Maravilla, D. (2004), 'Dust escape mechanism from Io', *Advances in Space Research* **34**, 2251–2255.

Fornasier, S., Lantz, C., Barucci, M. A. & Lazzarin, M. (2014), 'Aqueous alterations on main belt primitive asteroids: Results from visible spectroscopy', *Icarus* **233**, 163–178.

Foster, N., Wozniakiewicz, P. J., Price, M. C., Kearsley, A. T. & Burchell, M. J. (2014), 'Identification by Raman spectroscopy of Mg–Fe content of olivine samples after impact at 6 km s^{-1} onto aluminium foil and aerogel: In the laboratory and in Wild–2 cometary samples', *Geochimica et Cosmochimica Acta* **121**, 1–14.

French, B. M. & Koeberl, C. (2010), 'The convincing identification of terrestrial meteorite impact structures: What work, what does't, and why', *Earch Science Reviews* **98**, 123–170.

Fries, M., Burchell, M. J., Kearsley, A. & Steele, A. (2009), 'Capture effects in carbonaceous material: A Stardust analogue study', *Meteoritics and Planetary Science* **44**, 1465–1474.

Fujiwara, A., Kawaguchi, J., Yeomans, D. K., Abe, M., Mukai, T., Okada, T., Saito, J., Yano, H., Yoshikawa, M., Scheeres, D. J., Barnouin-Jha, O., Cheng, A. F., Demura, H., Gaskell, R. W., Hirata, N., Ikeda, H., Kominato, T., Miyamoto, H., Nakamura, A. M., Nakamura, R., Sasaki, S. & Uesugi, K. (2006), 'The rubble-pile asteroid Itokawa as observed by Hayabusa', *Science* **312**, 1330–1334.

Gault, D. E. & Heitowit, E. D. (1963), 'The partition of energy for hypervelocity impact craters formed in rock', *Sixth Hypervelocity Impact Symposium* **1**, 419–456.

Gault, D. E., Quaide, W. L. & Oberbeck, V. R. (1968), *Impact cratering mechanics and structures, in Shock Metatmorphism of Natural Materials*, Mono Book Corp, Baltimore, USA.

Gault, D. E. & Wedekind, J. A. (1978), Experimental studies of oblique impact, *in* '9th LPSC, page 374'.

Gingold, R. A. & Monaghan, J. J. (1977), 'Smoothed particle hydrodynamics - Theory

and application to non-spherical stars', *Monthly Notices of the Royal Astronomical Society* **181**, 375–389.

Goderis, S., Paquay, F. & Claeys, P. (2013), *Impact cratering processes and products - Projectile identification in terrestrial impact structures and ejecta material*, Blackwell Publishing Ltd.

Goldstein, J. I., Newbury, D. E., Echlin, P., Joy, D. C. & Lifshin, E. (1981), *Scanning electron microscopy and X-ray microanalysis*, Plenum Press, New York, USA.

Grady, M. M., Verchovsky, A. B. & Wright, I. P. (2004), 'Magmatic carbon in Martian meteorites: Attempts to constrain the carbon cycle on Mars', *International Journal of Astrobiology* **3**, 117–124.

Grady, M. M., Wright, I. P. & Pillinger, C. T. (1997), 'Carbon in howardite, eucrite and diogenite basaltic achondrites', *Meteoritics and Planetary Science* **32**, 863–868.

Grieve, R. A. F., Dence, M. R. & Robertson, P. B. (1977), *Cratering processes; as interpreted from the occurrences of impact melts, in Impact and Explosion Cratering*, Pargamon Press, New York, USA.

Griffith, A. A. (1921), 'The phenomena of rupture and flow in solids', *Philosophical Transactions of the Royal Astronomical Society of London, Series A* **221**, 163–198.

Grün, E., Baghul, H. A., Balogh, A., Bame, S. J., Fechtig, H., Forsyth, R., Manner, M. S., Horany, M., Kissel, J., Lindblab, B. A., Linkert, D., Linkert, G., Mann, I., McDonnell, J. A. M., Morfill, G. E., Phillips, J. L., Polanskey, C., Schwehm, G., Siddique, N., Staubach, P., Svestka, J. & Taylor, A. (1993), 'Discovery of Jovian dust streams and interstellar grains by the Ulysses spacecraft', *Nature* **362**, 428–430.

Gurov, E. P. (1998), 'The group of Macha craters in Western Yakutai', *Planetary and Space Science* **46**, 323–328.

Gurov, E. P., Gurova, E. P. & Rakitskaya, R. B. (1995), 'Impact diamonds in the craters of the Ukrainian shield', *Meteoritics* **30**, 515–516.

Harriss, K. H. & Burchell, M. J. (2016), 'A study of the observed shift in the peak position of olivine Raman spectra as a result of shock induced by hypervelocity impacts', *Meteoritics and Planetary Science* **51**, 1289–1300.

Hartogh, P., Lis, D. C., Bockelee-Morvan, D., de Val-Borro, M., Biver, N., Kuppers, M., Bergin, E. A., Crovisier, J., Rengel, M., Moreno, R., Szutowicz, S. & Blake, G. A. (2011), 'Ocean-like water in the jupiter-family comet 103P/Hartley 2', *Nature* **478**, 218–220.

Hayhurst, C. J. & Clegg, R. A. (1997), 'Cylindrically symmetric SPH simulations of hypervelocity impacts on thin plates', *International Journal of Impact Engineering* **20**, 337–348.

Hibbert, R. & Price, M. C. (2014), Charaterisation of Raman spectra of high purity olivine as a function of temperature and shock history: preparation for ExoMars, *in* '45th LPSC, abstract: 1350'.

Hicks, L. J., MacArthur, J. L., Bridges, J. C., Price, M. C., Wickham-Eade, J. E., Burchell, M. J., Hansford, G. M., Butterworth, A. L., Gurman, S. J. & Baker, S. H. (2017), 'Magnetite in comet Wild 2: evidence for parent body aqueous alteration', *Meteoritics and Planetary Science* **52**, 2075–2096.

Hirata, N. & Ishiguro, M. (2011), Properties and possible origin of black boulder on the asteroid Itokawa, *in* '42nd LPSC, abstract: 1821'.

Hitachi (2013), 'Let's familiarize ourselves with the SEM!'. Accessed: 03.10.2016.

Holsapple, K., Giblin, I., Housen, K., Nakamua, A. & Ryan, E. (2002), 'Asteroid impacts: Laboratory experiments and scaling laws', *Asteroids III* **1**, 443–461.

Hörz, F. & et al. (2006), 'Impact features on Stardust: implications for comet 81P/Wild2 dust', *Science* **314**, 1716–1719.

Housen, K. R. & Holsapple, K. A. (2011), 'Ejecta from impact craters', *Icarus* **211**, 856–875.

Huang, E.-. P., Haung, E., Yu, S.-. C., Chen, Y.-. H., Lee, J.-. H. & Fang, J.-. N. (2010), 'In situ Raman spectroscopy on kerogen at high temperatures and high pressures', *Physics and Chemistry of Minerals* **37**, 593–600.

Hughes, D. W. & Williams, I. P. (2000), 'The velocity distribution of periodic comets and stream meteoroids', *Monthly Notices of the Royal Astronomical Society* **315**, 629–634.

Hutchinson, I. B., Parnell, J., Edwards, H. G. M., Jehlicka, J., Marshall, C. P., Harris, L. V. & Ingley, R. (2014), 'Potential for analysis of carbonaceous matter on Mars using Raman spectroscopy', *Planetary and Space Science* **103**, 184–190.

Isbell, W. M. (2005), *Shock Waves: Measuring the Dynamic Response of Materials*, Imperial College Press, UK.

Ishibashi, H., Arakawa, M., Yamamoto, J. & Kagi, H. (2012), 'Precise determination of Mg/Fe ratios applicable to terrestrial olivine samples using Raman spectroscopy', *Journal of Raman Spectroscopy* **43**, 331–337.

Ivanov, B. A. & Melosh, H. J. (2013), 'Two-dimensional numberical modelling of the Rheasilvia impact formation', *Journal of Geophysical Research Planets* **118**, 1545–1557.

Jaumann, R., Williams, D. S., Buczkowski, D. L., Yingst, R. A., Preusker, F., Hiesinger, H., Schmedemann, N., Kneissl, T., Vincent, J. B., Blewett, D. T., Buratti, B. J., Carsenty, U., Denevi, B. W., De Sanctis, M. C., Garry, W. B., Keller, H. U., Kersten, E., Krohn, K., Li, J. Y., Marchi, S., Matz, K. D., McCord, T. B., McSween, H. Y., Mest, S. C., Mittlefehldt, D. W., Mottola, S., Nathues, A., Neukum, G., O'Brien, D. P., Pieters, C. M., Prettyman, T. H., Raymond, C. A., Roatsch, T., Russell, C. T., Schenk, P., Schmidt, B. E., Scholten, F., Stephan, K., Sykes, M. V., Tricarico, P., Wagner, R., Zuber, M. T. & Sierks, H. (2012), 'Vesta's shape and morphology', *Science* **336**, 687–690.

Jeanloz, R., Ahrens, T. J., Lally, J. S., Nord Jr, G. L., Christie, J. M. & Heuer, A. H. (1977), 'Shock-produced olivine glass: First observation', *Science* **29**, 457–459.

Jedicke, R., Larsen, J. & Spahr, T. (2002), 'Observational selection effects in asteroid surveys', *Asteroids III* **1**, 71–87.

Jeffers, S. V., Manley, S. P., Bailey, M. E. & Asher, D. J. (2001), 'Near-Earth object velocity distributions and consequences for the Chicxulub impactor', *Monthly Notice of the Royal Astronomical Society* **327**, 126–132.

Jehlička, J., Urban, O. & Pokorný (2003), 'Raman spectroscopy of carbon and solid bitumens in sedimentary and metamorphic rocks', *Spectrochimica Acta Part A* **59**, 2341–2352.

Jenniskens, P. & et al. (2009), 'The impact and recovery of asteroid 2008 TC3', *Nature* **458**, 485–488.

Joy, K. H., Zolensky, M. E., Nagashima, K., Huss, G. R., Kent Ross, D., McKay, D. S. & Kring, D. A. (2012), 'Direct detection of projectile relics from the end of the lunar basin-forming epoch', *Science* **336**, 1426–1429.

Kenkmann, T., Poelchau, M. H., Trullenque, G., Hoerth, T., Schafer, F., Thoma, K. & Deutsch, A. (2012), 'Shatter cones formed in a MEMIN impact cratering experiment', *75th Annual Meeting of the Meteoritical Society, abstract: 5092* .

Kessler, D. J. (1981), 'Derivation of the collision probability between orbiting objects: The lifetimes of Jupiter's outer moons', *Icarus* **48**, 39–48.

Kieffer, S. W. & Simonds, C. H. (1980), 'The role of volatiles and lithology in the impact cratering process', *Reviews of Geophysics and Space Physics* **18**, 143–181.

Kieffler, S. W., Phakey, P. P. & Christie, J. M. (1976), 'Shock processes in porous quartzite: transmission electron microscope observations and theory', *Contributions to Mineralogy and Petrology* **59**, 41–93.

Knight, D. S. & White, W. B. (1989), 'Characterization of diamond films by Raman spectroscopy', *Journal of Material Research* **4**, 385–393.

Koblitz, J. (2000), 'Metbase 5.0'. CD-ROM, accessed: 15.11.2016.

Konhauser, K. O. (1998), 'Diversity of bacterial iron mineralization', *Earth Science Reviews* **43**, 91–121.

Krinsley, D. H., Pye, K., Boggs Jr, S. & Tovey, N. K. (1998), *Backscatttered scanning electron microscopy and image analysis and sedementary rocks*, Cambridge University Press, Cambridge, UK.

Kuebler, K. E., Jolliff, B. L., Wang, A. & Haskin, L. (2006), 'Extracting olivine (Fo-Fa) compositions from Raman spectra peak position', *Geochimica et Cosmochimica Acta* **70**, 6201–6222.

Kupchella, R., Stowe, D., Weiss, M., Pan, H. & Cogar, J. (2015), 'SPH Modelling improvements for hypervelocity impacts', *Procedia Engineering* **103**, 326–333.

Kyte, F. T. (1998), 'A meteorite from the Creaceous/Tertiary boundary', *Nature* **396**, 237–239.

Lafuente, B., Downs, R. T., Yang, H. & Stone, N. (2015), 'The power of databases: the RRUFF project'.

Lamy, L. L., Toth, I., Fernández, Y. R. & Weaver, H. A. (2004), 'The sizes, shapes, albedos and colors of cometary nuclei', *Comets II* **1**, 223–264.

Lardner, D. (1853), 'On the classification of comets and the distribution of their orbits in space', *MNRAS* **13**, 188–191.

Leliwa-Kopystynski, J., Burchell, M. J. & Wlodarczyk, I. (2009), 'The impact origin of Eunomia and Themis families', *Meteoritics and Planetary Science* **44**, 1929–1935.

Leroux, H. (2012), 'Fine-grained material of 81P/Wild2 in interaction with the Stardust aerogel', *Meteoritics and Planetary Science* **47**, 613–622.

Love, S. G. & Ahrens, T. J. (1996), 'Catastrophic impacts on gravity dominated asteroids', *Icarus* **124**, 141–155.

Lu, S., Yao, M., Li, Q., Iv, H., Liu, D., Liu, B., Liu, R., Jiang, L., Yoa, Z., Liu, Z., Zou, B. & Cui, T. Liu, B. (2012), 'Exploring the possible interlinked structures in single–wall carbon nanotubes under pressure by Raman spectroscopy', *Journal of Raman Spectroscopy* **44**, 176–182.

Lucazeau, G. (2003), 'Effects of pressure and temperature on Raman spectra od solids: anharmonicity', *Journal of Raman Spectroscopy* **34**, 478–496.

Luque, F. J., Pasteris, J. D., Wopenka, B., Rodas, M. & Barrenechea, J. F. (1998), 'Natural fluid-deposited graphite: minerological charateristics and mechanisms of formation', *American Journal of Science* **298**, 471–498.

Macdonald, A. M. & Wyeth, P. (2006), 'On the use of photobleaching to reduce fluorescence background in Raman spectroscopy to improve the reliability of pigment identification on painted textiles', *Journal of Raman Spectroscopy* **37**, 830–835.

MacPherson, C. G., Hilton, D. R., Newman, S. & Mattey, D. P. (1999), 'Carbon dioxide, c13 to c12 ratio and water variability in natural basaltic glasses: A study comparing stepped heating and FTIR spectroscopic techniques', *Geochimica et Cosmochimica Acta* **63**, 1805–1813.

Maier, W. D., Andreoli, M. A. G., McDonald, I., Higgins, M. D., Boyce, A. J., Shukolyukov, A., Lugmair, G. W., Ashwal, L. D. Graser, P., Ripley, E. M. & Hart, R. J. (2006), 'Dicovery of a 25 cm asteroid clast in the giant morokweng impact crater, south africa', *Nature* **441**, 203–206.

Marchi, S., McSween, H. Y., O'Brien, D. P., Schenk, P., De Sanctis, M. C., Gaskell, R., Jaumann, R., Mottola, S., Preusker, F., Raymond, C. A., Roatsch, T. & Russell, C. T. (2012), 'The violent collisional history of asteroid 4 Vesta', *Science* **336**, 690–694.

Marshall, C. P., Edwards, H. G. M. & Jehlicka, J. (2010), 'Understanding the application of Raman spectroscopy to the detection of traces of life', *Astrobiology* **10**, 229–243.

McDermott, K. H., Price, M. C., Cole, M. J. & Burchell, M. J. (2016), 'Survivability of copper projectiles during hypervelocity impacts in porous ice: A laboratory investigation of the survivability of projectiles impacting comets or other bodies', *Icarus* **268**, 102–117.

Melosh, H. J. (1989), *Impact Cratering: A geological process*, Oxford University Press, UK.

Melosh, H. J. (2013), *Impact Cratering Processes and Products*, Blackwell Publishing Ltd, chapter 2: The contact and compression stage of impact cratering., pp. 32–42.

Melosh, H. J. & Ivanov, B. A. (1999), 'Impact crater collapse', *Annual Review of Earth and Planetary Science* **27**, 385–415.

Michikami, T., Moriguchi, K., Hasegawa, S. & Fujiwara, A. (2007), 'Ejecta velocity distribution from impact cratering experiments on porous and low strength targets', *Plenetary and Space Science* **55**, 70–88.

Mittlefehldt, D. W., See, T. H. & Hörz, F. (1992*a*), 'Dissemination and fractionation fo projectile materials in the impact melts from Wabar crater, Saudi Arabia', *Meteoritics* **27**, 361–370.

Mittlefehldt, D. W., See, T. H. & Hörz, F. (1992*b*), Projectile dissemination in impact melts from Meteor crater, Arizon, *in* '23rd LPSC, page 919'.

Morbidelli, A., Chambers, J., Lunine, J. I., Petit, J. M., Robert, F., Valsecchi, G. B. & Cyr, K. E. (2000), 'Source regions and timescales for the delivery of water to the earth', *Meteoritics and Planetary Science* **35**, 1309–1320.

Morgan, J. W., Ganapathy, R. & Anders, E. (1975), Meteoritic material in four terrestrial meteortic craters, *in* '6th Lunar Planetary Conference, page 1609'.

Moritoh, T., Kawai, N., Nakamua, K. G., Kondo, K. & Katayama, M. (2003), 'Hypervelocity inpact experiments up to 9 km/s by a compact multi-stage light gas gun', *International Journal of Impact Engineering* **29**, 459–467.

Morris, A. J. W. & Burchell, M. J. (2017), 'Laboratory tests of catastrophic disruption of rotating bodies', *Icarus* **296**, 91–98.

Morris, A. J. W., Price, M. C., Cole, M. J., Kearsley, A. T. & Burchell, M. J. (2011), Cratering efficiency in rocks as a function of rock temperature, *in* '42nd LPSC, abstract: 1943'.

Nagaoka, H., Takasawa, S., Nakamura, A. M. & Sangen, K. (2014), 'Degree of impactor fragmentation under collision with a regolith surface Laboratory impact experiments of rock projectiles', *Meteoritics and Planetary Science* **49**, 69–79.

Naguchi, T., Nakamura, T., Okudaira, K., Yano, H., Sugita, S. & Burchell, M. J. (2007), 'Thermal alteration of hydrated minerals during hypervelocity capture into silica aerogel at the flyby speed of Stardust', *Meteoritics and Planetary Science* **42**, 357–372.

NASA (2014*a*), 'Curiosity finds iron meteorite on mars', `https://www.nasa.gov/jpl/msl/pia18387`. Accessed: 21/12/2017.

NASA (2014*b*), 'Scanning habitable enviroments with raman and luminescence for organics and chemicals (SHERLOC)', `http://mars.nasa.gov/mars2020/mission/instruments/sherloc/for-scientists/`. Accessed: 10/08/2016.

NASA-JPL (2016), 'Dawn', `http://dawn.jpl.nasa.gov/`. Accessed: 13/10/2016.

Norton, O. R. & Chitwood, L. A. (2008), *Field Guide to Meteors and Meteorites*, Springer, London, UK.

O'Brien, D. P. & Sykes, M. V. (2011), 'The origin and evolution of the asteroid belt - Implications for Vesta and Ceres', *Space Science Review* **163**, 41–61.

O'Keefe, J. D. & Ahrens, T. J. (1982), 'Cometary and meteorite swarm impact on planetary surfaces', *Journal of Geophysical Research* **103**, 6668–6680.

Öpik, E. J. (1976), *Interplanetary encounters: close-range gravitational interactions*, Elsevier Scientific Publishing, Amsterdam.

Osinski, G. R. (2007), 'Impact metamorphism of CaCO3 bearing sandstones at the Haughton structure, Canada', *Meteoritics and Planetary Science* **42**, 1945–1960.

Osinski, G. R. & Pierazzo, E. (2013), *Impact Cratering: processes and products*, Wiley-Blackwell, West Sussex, UK.

Osinski, G. R., Tornabene, L. L. & Grieve, R. A. F. (2011), 'Impact ejecta emplacement on the terrestrial planets', *Earth and Planetary Science Letters* **310**, 167–181.

Palomba, E., Longobardo, A., De Sanctis, M. C., Zambon, F., Tosi, F., Ammannito, E., Capaccioni, F., Frigeri, A., Capria, M. T., Cloutis, E. A., Jaumann, R., Combe, J.-P., Raymond, C. A. & Russell, C. T. (2014), 'Composition and mineralogy of dark material units on vesta', *Icarus* **240**, 58–72.

Parnell, J., Bowden, S. A., Lindgren, P., Burchell, M. J., Milner, D., Price, M. C., Baldwin, C. & Crawford, I. A. (2010), 'The preservation of fossil biomarkers during hypervelocity impact experiments using organic rich siltstones as both projectiles and targets', *Meteoritics and Planetary Science* **45**, 1340–1358.

Pasek, M. A. (2015), 'Phosphorus as a lunar volatile', *Icarus* **255**, 18–23.

Philipp, S. L., Afsar, F. & Gudmundsson, A. (2013), 'Effects of mechanical layering on hydrofracture emplacement and fluid transport in reservoirs', *Frontiers in Earth Science* **1**, 1–19.

Piekutowski, A. J. (1995), 'Fragmentation of a sphere initiated by hypervelocity impact with a thin sheet', *International Journal of Impact Engineering* **17**, 627–638.

Pierazzo, E. & Melosh, H. J. (2000), 'Hydrocode modeling of oblique impacts: The fate of the projectile', *Meteoritics and Planetary Science* **35**, 117–130.

Potter, R. W. K. & Collins, S. (2013), 'Numerical modeling of asteroid survivability and possible scenarios for the Morokweng crater-forming impact', *Meteoritics and Planetary Science* **48**, 744–757.

Pugh, E. (2017), 'Cryogenic loading of Argon pressure medium in Diamond Anvil Cells with in-situ pressure determination', *Review of Scientific Instruments* **88**.

Rabinowitz, D., Bowell, E., Showmaker, E. & Muinonen, K. (1994), *Hazards due to comets and asteroids*, University of Arizona Press, Tucson.

Raman, C. V. & Krishnan, K. S. (1928), 'A new type of secondary radiation', *Nature* **121**, 501–502.

Reddy, V., Le Corre, L., O'Brien, D. P., Nathues, A., Cloutis, E. A., Durda, D. D., Bottke, W. F., Bhatt, M. U., Nesvorny, D., Buczkowski, D., Scully, J. E. C., Palmer, E. M., Sierks, H., Mann, P. J., Becker, K. J., Beck, A. W., Mittlefehldt, D., Li, J.-Y., Gaskell, R., Russell, C. T., Geffey, M. J., McSween, H. Y., McCord, T. B., Combe, J.-P. & Blewett, D. (2012), 'Delivery of dark material to Vesta via carbonaceous chondritic impacts', *Icarus* **221**, 544–559.

Reed, S. J. B. (2005), *Electron Microprobe Analysis and Scanning Electron Microscopy in Geology*, Cambridge University Press, Cambridge, UK.

Reich, S. & Thomsen, C. (2004), 'Raman spectroscopy of graphite', *Philosophical Transactions: Mathematical, Physical and Engineering Sciences* **362**, 2271–2288.

Robert, F. (2003), 'The D/H ratio in chondrites', *Space Science Reviews* **106**, 87–101.

Rubin, A. E. (2006*a*), 'Shock and annealing in EL chondrites', *69th Annual Meteoritical Society Meeting* **69**, 5274.

Rubin, A. E. (2006*b*), 'Shock, post-shock annealing, and post-annealing shock in ureilites', *Meteoritics and Planetary Science* **41**, 125–133.

Rull, F., Maurice, S., Diaz, E., Lopez, G., Catala, A. & the RLS Team (2013), Raman laser spectrometer (RLS) for ExoMars 2018 rover mission: currect status and science operation mode on powdered samples, *in* '44th LPSC, abstract: 3110'.

Rull, F. & et al. (2017), 'The Raman Laser Spectrometer for the ExoMars rover mission to Mars', *Astrobiology* **17**, 627–654.

Sakai, H., Des Marais, D. J., Ueda, A. & Moore, J. G. (1984), 'Concentrations and isotope ratios of carbon, nitrogen and sulfur in ocean-floor basalt', *Geochimica et Cosmochimica Acta* **48**, 2433–2441.

Schneider, H. & Hornemann, U. (1977), 'Preliminary data on the shock-induced high-pressure transformation of olivine', *Earth and Planetary Science Letters* **36**, 322–324.

Schultz, P. H. (1988), 'Cratering on Mercury: A relook', *Mercury* **1**, 274–335.

Schultz, P. H. & Gault, D. E. (1984), Effects of projectile deformation on crater efficiency and morphology, *in* '15th LPSC, page 730'.

Schultz, P. H. & Gault, D. E. (1990*a*), 'Decapitated impactors in the laboratory and on the planets', *21st Lunar and Planetary Science Conference* pp. 1099–1100.

Schultz, P. H. & Gault, D. E. (1990*b*), 'Prolonged global catastrophes from oblique impacts', *Geological Society of America Special Paper* **247**, 239–261.

Schultz, P. H., Koeberl, C. & Bunch, T. (1994), 'Ground truth for oblique impact processes: new insight from the Rio Cuarto, Argentina, crater field', *Geology* **22**, 889–892.

Schultz, R. A. (1993), 'Brittle strength of basaltic rock masses with applications to Venus', *Geophysical Research Planets* **98**, 10883–10895.

SCRes (2004), 'What is Raman Spectroscopy', `http://www.sicklecellinfo.net/raman.htm`. Accessed: 12/12/2016.

Shebanova, O. N. & Lazor, P. (2003), 'Raman study of magnetite (Fe3O4): laser-induced thermal effects and oxidation', *Journal of Raman Spectroscopy* **34**, 845–852.

Shimoda, K., Okuno, M., Syono, Y., Kikuchi, M., Fukuoka, K., Koyano, M. & Katayama, S. (2004), 'Structural evolutions of an obsidian and its fused glass by shock-wave compression', *Physics and Chemistry of Minerals* **31**, 532–542.

Siebert, F. & Hildebrant, P. (2008), *Chapter 2. Theory of infrared absorption and Raman spectroscopy from Vibrational spectroscopy in life science*, Wiley, West Sussex, UK.

Smekal, A. (1923), 'Zur quantentheorie der dispersion', *Der Naturwissenschaften* **43**, 873–872.

Smith, E. & Dent, G. (2005), *Modern raman spectroscopy: A practical approach*, Wiley, West Sussex, UK.

Steel, D. (1998), 'Distribution and moments of asteroid and comet impact speeds upon the Earth and Mars', *Planetary Space Science* **46**, 473–478.

Stöffler, D., Gault, D. E., Wedekind, J. & Polkowski, G. (1975), 'Experimental hypervelocity impact into quartz sand: distribution and shock metamorphism of ejecta', *Journal of Geophysical Research* **80**, 4062–4077.

Stöffler, D. & Langenhorst, F. (1994), 'Shock metamorphism of quartz in nature and experiment: I. Basic observation and theory', *Meteoritics* **29**, 155–181.

Tan, P. H., Deng, Y. M. & Zhao, Q. (1998), 'Temperature dependent Raman spectra and anomalous Raman phenomenon of highly oriented pyrolytic graphite', *Physical Review Letters B* **58**, 5435–5440.

Taylor, S. R. (1967), 'Composition of meteorite impact glass across the Henbury strewn field', *Geochimica et Cosnochimica Acta* **73**, 4891–4906.

Thomas, P. C., Binzel, R. P., Gaffey, B. H., Zellner, A. D., Storrs, E. & Wells, E. (1997), 'Vesta: spin pole, size, and shape from hst images', *Icarus* **128**, 88–94.

Trigo-Rodriguez, J. M., Dominguez, G., Burchell, M. J., Hörz, F. & Llorca, J. (2008), 'Bublous tracks arising from hypervelocity capture in aerogel', *Meteoritics and Planetary Science* **43**, 75–86.

Tuinstra, F. & Koenig, J. L. (1970), 'Raman spectrum of graphite', *The Journal of Chemical Physics* **53**, 1126–1130.

Vernon-Parry, K. D. (2000), 'Scanning electron microscopy: An introduction', *III-Vs Review* **13**, 40–44.

Veverka, J., Klaasen, K., A'Hearn, M., Belton, M., Brownlee, D., Chesley, S., Clark, B., Economou, T., Farquhar, R., Green, S. F., Groussin, O., Harris, A., Kissel, J., Li, J.-Y., Meech, K., Melosh, H. J., Richardson, J., Schultz, P. H., Silen, J., Sunshine, J. M., Thomas, P., Bhaskaran, S., Bodewits, D., Carcich, B., Cheuvront, A., Farnham, T. L., Sackett, S., Wellnitz, D. & Wolf, A. (2013), 'Deep Impact: Excavating Comet Tempel 1', *Return to Comet Tempel 1: Overview of Stardust-Next results* **222**, 424–435.

Vidano, R. P., Fischbach, D. B., Willis, L. J. & Loehr, T. M. (1981), 'Observation of Raman band shifting with excitation wavelength for carbons and graphites', *Solid State Communications* **39**, 341–348.

Wang, Y., Alsmeyer, D. C. & McCreery, R. L. (1990), 'Raman spectroscopy of carbon materials: structural basis of observed spectra', *Chemistry of Materials* **2**, 557–563.

Wehrenberg, C. E., McGonegle, D., Bolme, C., Higginbotham, A., Lazicki, A., Lee, H. J., Nagler, B., Park, H. S., Remington, B. A., Rudd, R. E., Sliwa, M., Suggit, M., Swift, D., Tavella, F., Zepeda-Ruiz, L. & Wark, J. S. (2017), 'In situ X-ray diffraction measurement of shock-wave-driven twinning and lattice dynamics', *Nature* **550**, 496–499.

Weisberg, M., J. McCoy, T. & N. Krot, A. (2006), 'Systematics and evaluation of meteorite classification', **2**, 19–52.

Weissman, P. R. (1982), 'Geological implications of impacts of large asteroids and comets on the Earth', *Geological Society of America Special Papers* **190**, 15–25.

Weissman, P. R., Asphaug, E. & Lowry, S. C. (2004), 'Structure and density of cometary nuclei', *Comets II* **1**, 337–357.

Westphal, A. J. & et al. (2014), 'Evidence for interstellar origin of seven dust particles collected by the Stardust spacecraft', *Science* **345**, 786–791.

Wickham-Eade, J. E., Burchell, M. J., Price, M. C. & Harriss, K. H. (in review), 'Hypervelocity impact fragmentation of basalt and shale projectiles', *Meteoritics and Planetary Science* .

Wickham-Eade, J. E., Burchell, M. J., Price, M. C., Hicks, L. J., MacArthur, J. L. & Bridges, J. C. (2017), 'Raman identification of olivine grains in fine grained mineral assemblages fired into aerogel', *Procedia Engineering* **204**, 413–420.

Wilk, J. & Kenkmann, T. (2016), 'Formation of shatter cones in MEMIN impact experiments', *Meteoritics and Planetary Science* **51**, 1477–1496.

Winter, R. (2009), *Key concepts of shock hydrodynamics*, Imperial College London, UK.

Wozniakiewicz, P. J., Ishii, H. A., Kearsley, A. T., Burchell, M. J., Bradley, J. P., Price, M. C., Teslich, N., Lee, M. R. & Cole, M. J. (2012), 'Stardust impact analogs: Resolving pre- and postimpact mineralogy in Stardust Al foils', *Meteoritics and Planetary Science* **47**, 708–728.

Wünneman, K., Collins, G. S. & Osinski, G. R. (2008), 'Numberical modelling of impact melt production in porous rocks', *Earth and Planetary Science Letters* **269**, 530–539.

Xie, X., Chen, M., Dai, C., El Goresy, A. & Gillet, P. (2001), 'A comparative study of naturally and experimentally shocked chondrites', *Earth and Planetary Science Letters* **187**, 345–356.

Yue, Z., Johnson, B. C., Minton, D. A., Melosh, H. J., Di, k., Hu, W. & Liu, Y. (2013), 'Projectile remnants in central peaks of lunar impact craters', *Nature Geoscience* **6**, 435–437.

Zahnle, K., Dones, L. & Levison, H. (1998), 'Cratering rates on the Galilean satellites', *Icarus* **136**, 202–222.

Zahnle, K., Schenk, P., Levison, H. & Dones, L. (2003), 'Cratering rates in the outer solar system', *Icarus* **163**, 263–289.

Zahnle, K., Schenk, P., Sobieszczyk, S., Dones, L. & Levison, H. (2001), 'Differential cratering of synchronously rotating satellites by ecliptic comets', *Icarus* **153**, 111–129.

Zerda, T. W., Xu, W., Zerda, A., Zhao, Y. & Von Dreele, R. B. (2000), 'High pressure Raman and neutron scattering study on structure of carbon black particles', *Carbon* **38**, 355–361.

Zha, X. P., Gong, B., Zheng, Y. F. & Chen, Y. X. (2018), 'Precise carbon isotopic ratio analyses of micro amounts of carbonate and non-carbonate in basalt using continuous-flow isotope ratio mass spectrometry', *Rapid Communications in Mass Spectrometry* **32**, 48–56.

Zion, E., Butenko, A., Kaganovskii, Y., Richter, V., Wolfson, L., Sharoni, A., Kogan, E., Kaveh, M. & Shlimak, I. (2017), 'Effect of annealingon Raman spectra of monolayer graphene samples gradually disordered by ion irradiation', *Journal of Applied Physics* **121**, 114301.

Zook, H. A. (2002), 'Spacecraft measurements of the cosmic dust flux', *Accretion of extraterrestrial matter throughout Earth's history* **1**, 75–92.

Appendices

Appendix A

Temperature Experiment Plots

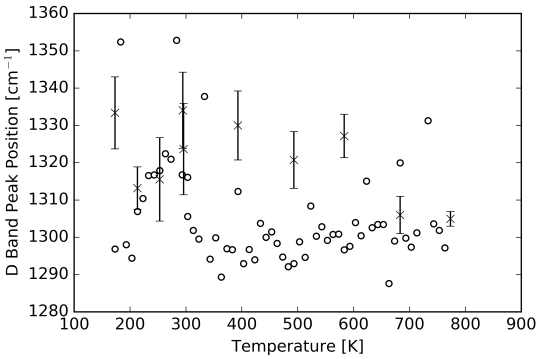

(a) Basalt

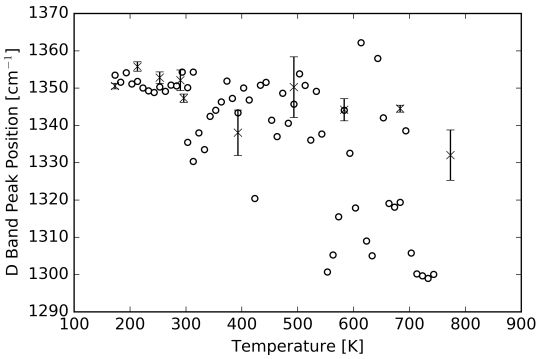

(b) Shale

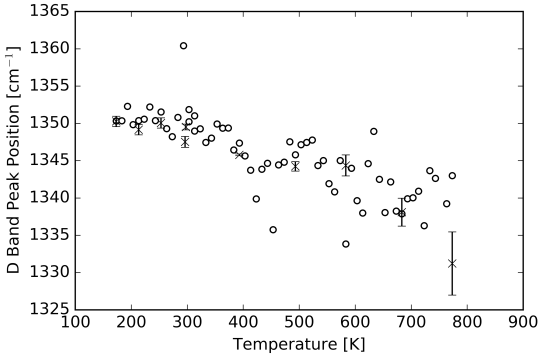

(c) Graphite

Figure A.1: D band peak position for basalt, shale and graphite against temperature, including spot check data. The errors are the error on the mean.

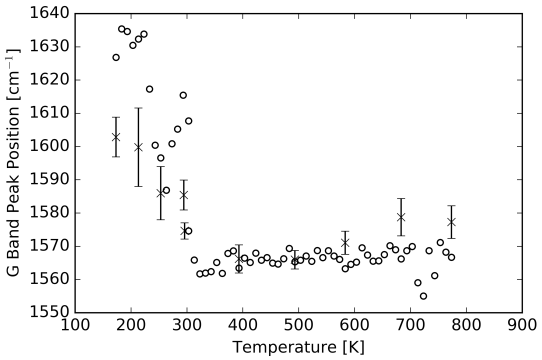

(a) Basalt

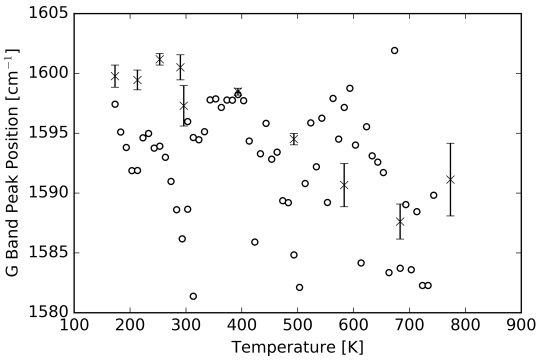

(b) Shale

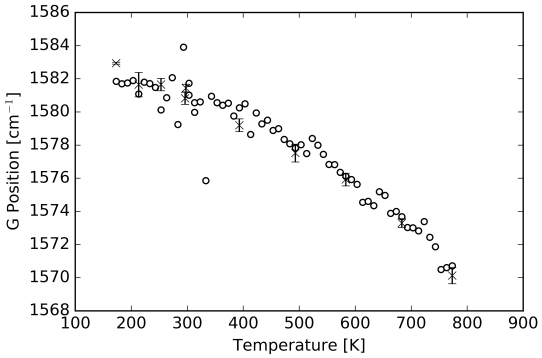

(c) Graphite

Figure A.2: G band peak position for basalt, shale and graphite against temperature, including spot check data. The errors are the error on the mean.

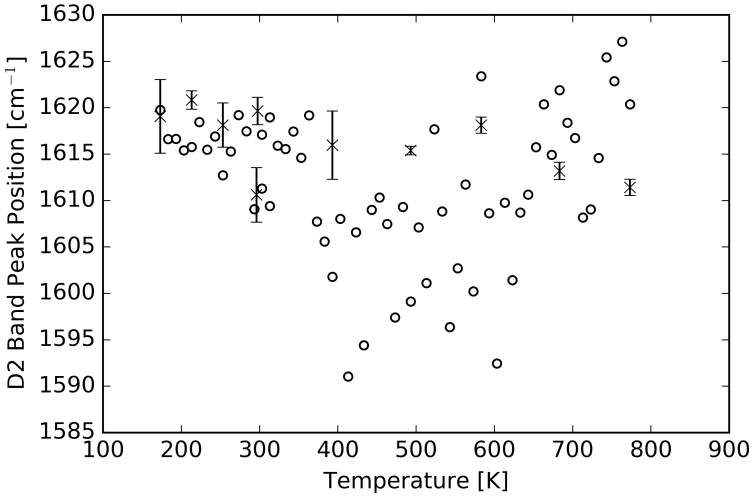

Figure A.3: D2 band peak position for graphite against temperature, including spot check data. The errors are the errors on the mean.

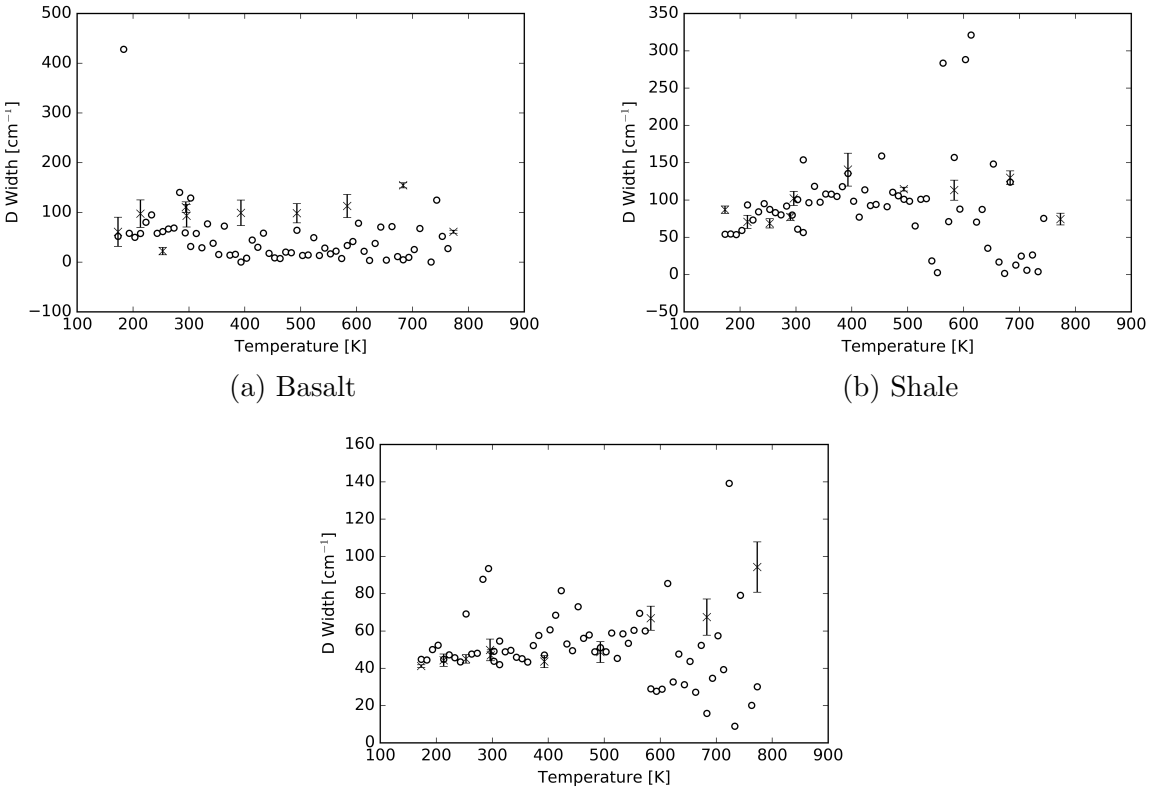

(a) Basalt

(b) Shale

(c) Graphite

Figure A.4: D band width for basalt, shale and graphite against temperature, including spot check data. The errors are the errors on the mean.

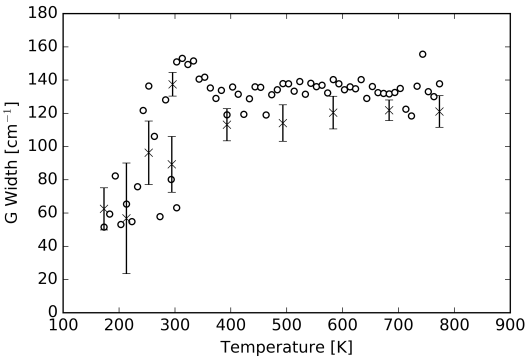

(a) Basalt

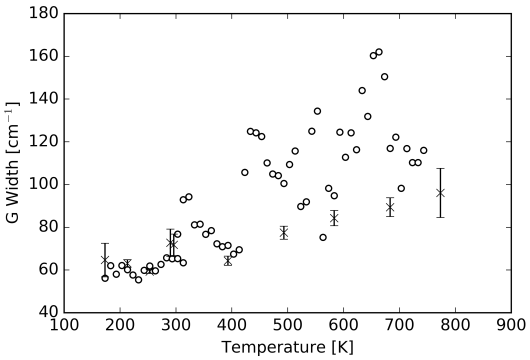

(b) Shale

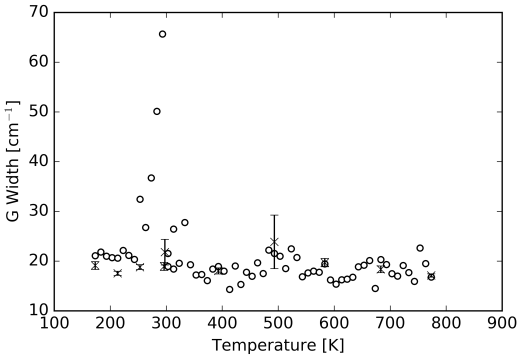

(c) Graphite

Figure A.5: G band width for basalt, shale and graphite against temperature, including spot check data. The errors are the errors on the mean.

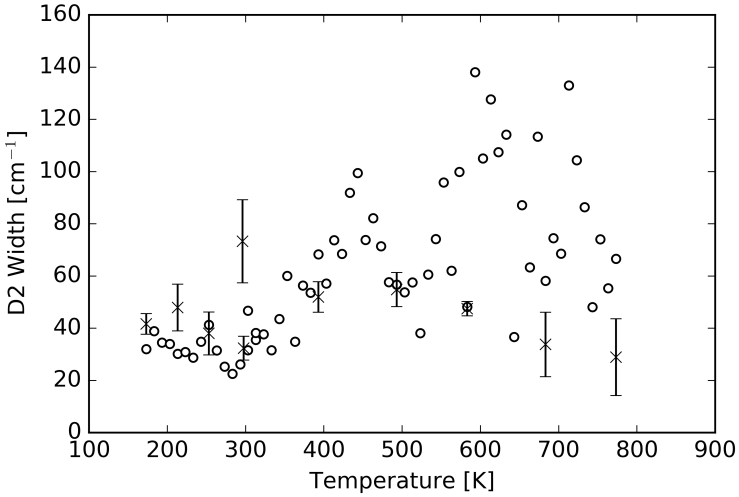

Figure A.6: D2 band width for graphite against temperature, including spot check data. The errors are the errors on the mean.

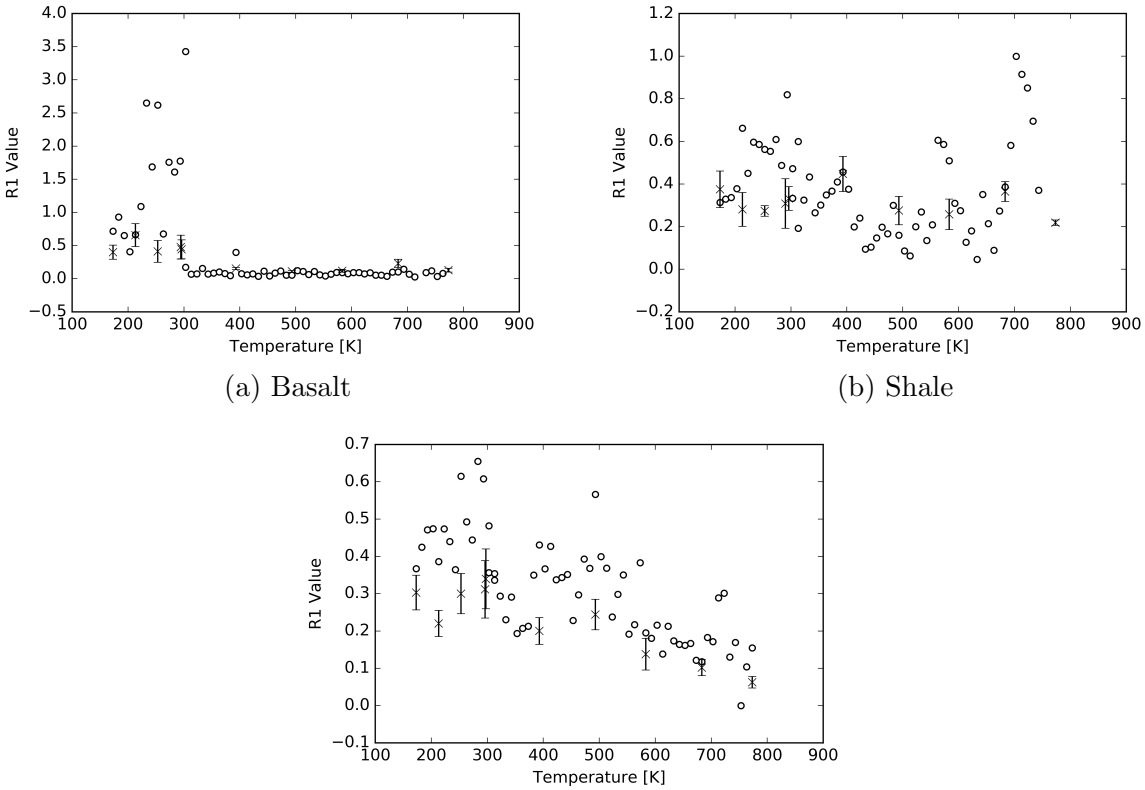

(a) Basalt

(b) Shale

(c) Graphite

Figure A.7: Ratio of D and G band amplitude (R1 value) for basalt, shale and graphite against temperature, including spot check data. The errors are the errors on the mean.

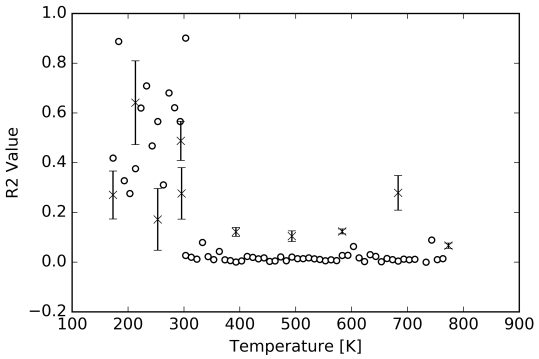

(a) Basalt

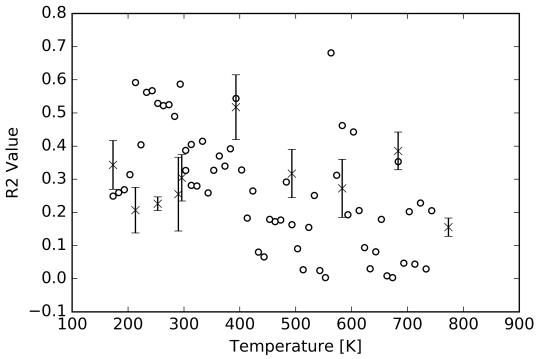

(b) Shale

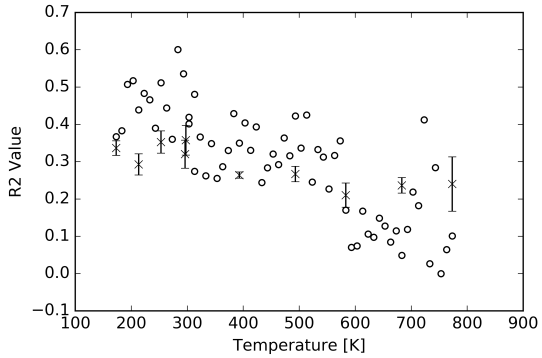

(c) Graphite

Figure A.8: Ratio of D and G band areas (R2 value) for basalt, shale and graphite against temperature, including spot check data. The red data points show the results for the spot check.

Appendix B

Projectile Log and Shot Log

B.1 Projectile Log

Table B.1: Projectiles made for shots. Note some projectiles used in shots in Table B.2 do not appear in this table. * means basalt Sphere.

Date	Number	Material	Dimensions [mm]	Mass [mg]	Raman Mapped	Shot Numbers	Speeds [km s^{-1}]
24/11/14	PreCat	Basalt	1.46 x 1.44 x 1.54	7.8091	No	G271114#1	5.31
02/03/15	PreCat	Basalt	1.55 x 1.54 x 1.49	11.0215	No	S050315#1	0.961
20/04/15	B01	Basalt	1.52 x 1.51 x 1.41	8.0027	Yes	G010515#2	3.04
20/04/15	B02	Basalt	1.51 x 1.51 x 1.52	8.9644	Yes	G200515#1	1.98
12/05/15	B03	Basalt	1.53 x 1.51 x 1.48	9.0036	Yes	G270515#1	4.51
01/06/15	B04	Basalt	1.54 x 1.49 x 1.52	7.8049	Yes	G030616#1	n/a
01/06/15	B05	Basalt	1.54 x 1.52 x 1.38	7.2704	Yes	S050815#1	0.838
08/06/15	B06	Basalt	1.53 x 1.51 x 1.45	8.1406	Yes	S100615#1	0.64
08/06/15	B07	Basalt	1.49 x 1.50 x 1.47	7.4286	Yes	G170615#1	2.02
16/06/15	B08	Basalt	1.52 x 1.52 x 1.54	8.7076	Yes	S240615#1	0.703
22/06/15	B09	Basalt	1.49 x 1.47 x 1.42	7.4325	Yes	G120815#1	6.09
22/06/15	B10	Basalt	1.52 x 1.45 x 1.40	7.2913	Yes	S290615#1	0.514
03/08/15	B11	Basalt	1.45 x 1.47 x 1.42	7.2558	Yes	G100915#1	6.29
03/08/15	B12	Basalt	1.41 x 1.42 x 1.43	6.8172	Yes	G300915#1	n/a

Continued on next page

Table B.1 – *Continued from previous page*

Date	**Number**	**Material**	**Dimensions [mm]**	**Mass [mg]**	**Raman Mapped**	**Shot Numbers**	**Speed [km s^{-1}]**
07/09/15	S01	Shale	1.49 x 1.41 x 1.36	6.4649	Yes	G041115#1	3.12
07/09/15	S02	Shale	1.47 x 1.44 x 1.44	7.1359	Yes	S181115#1	0.95
29/09/15	B13	Basalt	1.49 x 1.45 x 1.41	7.2557	Yes	-	-
29/09/15	B14	Basalt	1.50 x 1.49 x 1.44	7.1040	Yes	G071015#1	n/a
29/09/15	B15	Basalt	1.47 x 1.46 x 1.44	7.0080	Yes	G141015#1	4.05
05/09/15	B16	Basalt	1.50 x 1.49 x 1.48	7.4567	Yes	G041115#2	4.96
05/09/15	B17	Basalt	1.49 x 1.48 x 1.42	7.7528	Yes	G211015#2	6.02
29/10/15	B18	Basalt	1.52 x 1.51 x 1.48	7.8892	Yes	G041115#1	4.92
06/11/15	B19	Basalt	1.48 x 1.47 x 1.40	7.1346	Yes	G131115#1	4.78
06/11/15	B20	Basalt	1.49 x 1.46 x 1.43	7.4325	Yes	S211215#1	0.958
17/11/15	B21	Basalt	1.51 x 1.50 x 1.48	8.8064	Yes	G261115#1	1.95
17/11/15	S03	Shale	1.45 x 1.51 x 1.43	7.4867	Yes	G031215#2	4.64
01/12/15	B22	Basalt	1.49 x 1.48 x 1.46	7.6841	Yes	G101215#1	4.71
04/01/16	S04	Shale	1.50 x 1.48 x 1.47	7.9056	Yes	G130116#1	1.86
11/01/16	S05	Shale	1.50 x 1.47 x 1.46	7.4033	Yes	G130116#2	1.93

Continued on next page

Table B.1 – *Continued from previous page*

Date	Number	Material	Dimensions [mm]	Mass [mg]	Raman Mapped	Shot Numbers	Speed [km s^{-1}]
11/01/16	S06	Shale	1.50 x 1.49 x 1.48	8.2697	Yes	G211015#1	6.10
11/01/16	S07	Shale	1.49 x 1.48 x 1.46	8.0830	Yes	G211015#2	6.13
11/01/16	S08	Shale	1.47 x 1.46 x 1.46	7.5117	Yes	G280116#1	0.386
21/01/16	S09	Shale	1.46 x 1.46 x 1.45	7.1062	Yes	G030216#1	0.591
21/01/16	S10	Shale	1.49 x 1.48 x 1.46	7.6771	Yes	-	-
18/02/16	B23	Basalt	1.51 x 1.51 x 1.50	8.8775	No	S190216#1	0.971
18/02/16	B24	Basalt	1.52 x 1.51 x 1.46	7.7691	No	-	-
24/02/16	B25*	Basalt*	1.50 mm diameter	5.3808	No	G240216#1	n/a
24/02/16	B26*	Basalt*	1.50 mm diameter	5.1431	No	G110516#1	1.98
09/03/16	B27	Basalt	1.47 x 1.43 x 1.41	7.4938	No	S110316#1	0.981
14/03/16	B28	Basalt	1.50 x 1.49 x 1.48	8.2545	No	G170316#1	n/a
30/03/16	B29	Basalt	1.43 x 1.42 x 1.41	7.4240	No	G210416#3	2.01
30/03/16	B30	Basalt	1.47 x 1.45 x 1.38	7.2529	No	S270416#1	0.588
30/03/16	G01	Graphite	1.51 x 1.50 x 1.50	6.1545	Yes	G100616#1	3.07
21/06/16	G02	Graphite	1.50 x 1.52 x 1.50	6.1976	Yes	G130716#1	0.863

Continued on next page

Table B.1 – *Continued from previous page*

Date	**Number**	**Material**	**Dimensions [mm]**	**Mass [mg]**	**Raman Mapped**	**Shot Numbers**	**Speed [km s^{-1}]**
21/06/16	G03	Graphite	1.56 x 1.50 x 1.44	5.6166	Yes	G130716#2	n/a
18/07/16	G04	Graphite	1.53 x 1.45 x 1.45	5.4670	Yes	G200716#2	n/a
18/07/16	G05	Graphite	1.53 x 1.48 x 1.43	5.7500	Yes	G280716#1	n/a
26/07/16	G06	Graphite	1.49 x 1.48 x 1.43	5.6461	Yes	G280716#2	n/a
26/07/16	G07	Graphite	1.51 x 1.50 x 1.43	5.8902	Yes	-	-
24/08/16	G08	Graphite	1.50 x 1.48 x 1.37	5.294	Yes	G080916#1	n/a
24/08/16	G09	Graphite	1.56 x 1.51 x 1.50	6.854	Yes	G140916#1	1.80
24/08/16	G10	Graphite	1.50 x 1.49 x 1.36	5.416	Yes	G280916#1	4.00
24/08/16	B31	Basalt	1.51 x 1.50 x 1.46	7.905	Yes	G140916#2	4.92
24/08/16	B32	Basalt	1.52 x 1.49 x 1.44	7.728	Yes	G140916#3	n/a
12/09/16	G11	Graphite	1.54 x 1.50 x 1.49	6.251	Yes	-	-
13/10/16	S11	Shale	1.48 x 1.46 x 1.44	7.285	Yes	G201016#1	3.22
13/10/16	S12	Shale	1.53 x 1.49 x 1.48	7.937	Yes	G231116#1	n/a
13/10/16	S13	Shale	1.52 x 1.51 x 1.43	8.037	Yes	G301116#1	n/a
13/10/16	S14	Shale	1.50 x 1.49 x 1.49	7.881	Yes	G071216#1	n/a

Continued on next page

Table B.1 – *Continued from previous page*

Date	**Number**	**Material**	**Dimensions [mm]**	**Mass [mg]**	**Raman Mapped**	**Shot Numbers**	**Speed [km s^{-1}]**
28/11/16	B33	Basalt	1.52 x 1.51 x 1.48	-	Yes	-	-
28/11/16	B34	Basalt	1.51 x 1.47 x 1.44	-	-	-	-
12/12/16	S15	Shale	1.48 x 1.47 x 1.41	-	-	-	-
12/12/16	S16	Shale	1.53 x 1.51 x 1.43	-	-	-	-
12/12/16	S17	Shale	1.53 x 1.50 x 1.43	-	-	-	-
12/12/16	S18	Shale	1.53 x 1.51 x 1.33	-	-	-	-
30/01/17	B35	Basalt	1.56 x 1.42 x 1.38	-	Yes	G210617#1	n/a
30/01/17	B36	Basalt	1.50 x 1.51 x 1.50	-	Yes	-	-

B.2 Shot Log

Table B.2: Shot Log for duration of PhD. This includes work not in thesis.

#	Date	Shot Code	Projectile	Target	Speed [km s^{-1}]	PIA [GPa]	Success?	*Notes*
1	31/10/14	G311014#1	Basalt - 1.5mm cube	Water	-	-	No	Projectile lost
2	06/11/14	G061114#1	Basalt - 1.5mm cube	Water	5.32	84.5	Yes	-
3	27/11/14	G271114#1	Basalt - 1.5mm cube	Water	5.31	84.2	Yes	-
4	17/12/14	G171214#1	Shale - 1.5mm cube	Water	4.92	-	Yes	-
5	27/02/15	G270215#1	No projectile	Ice	4.77	-	Yes	Control Shot
6	05/03/15	G050315#1	Basalt - 1.5mm cube	Water	0.961	7.37	Yes	-
7	25/03/15	G250315#1	No projectile	Ice	5.36	-	Yes	Control Shot Redo
8	01/05/15	G010515#2	B01	Water	3.04	35.4	Yes	-
9	20/05/15	G200515#1	B02	Water	1.98	19.1	Yes	Missing Fragments
10	27/05/15	G270515#1	B03	Water	4.51	64.9	Yes	-
11	03/06/15	G030615#1	B04	Water	-	-	No	Broke up
12	10/06/15	G100615#1	B06	Water	0.64	4.50	Yes	-
13	17/06/15	G170615#1	B07	Water	2.02	19.6	Yes	-
14	24/06/15	G240615#1	B08	Water	0.703	5.02	Yes	-
15	29/07/15	G290715#1	B10	Water	0.514	3.48	Yes	-

Continued on next page

Table B.2 – *Continued from previous page*

#	Date	Shot Code	Projectile	Target	Speed [km s^{-1}]	PIA [GPa]	Success?	*Notes*
16	05/08/15	S050815#1	B05	Water	0.838	1.9	Yes	-
17	12/08/15	G120815#1	B09	Water	6.08	32.4	Yes	-
18	10/09/15	S100915#1	None	Ice	0.936	-	Yes	-
19	10/09/15	G100915#1	B11	Water	6.29	34.3	Yes	-
20	30/09/15	G300915#1	B12	Water	-	-	No	Hit something
21	07/10/15	G071015#1	B14	Water	-	-	No	Broke up
22	14/10/15	G141015#1	B15	Water	4.05	16.9	Yes	-
23	21/10/15	G211015#2	B17	Water	6.02	31.9	Yes	-
24	04/11/15	G041115#1	B18	Water	4.92	23.0	Yes	-
25	04/11/15	G041115#2	B16	Water	4.96	23.3	No	Broke up
26	04/11/15	G041115#3	S01	Water	3.12	10.3	Yes	-
27	13/11/15	G131115#1	B19	Water	4.78	-	No	Broke up
28	18/11/15	S181115#1	S02	Water	0.95	2.12	Yes	-
29	26/11/15	G261115#1	B21	Water	1.95	5.80	Yes	-
30	03/12/15	G031215#2	S03	Water	4.64	19.7	Yes	-

Continued on next page

Table B.2 – *Continued from previous page*

#	Date	Shot Code	Projectile	Target	Speed [km s^{-1}]	PIA [GPa]	Success?	*Notes*
31	10/12/15	G101215#1	B22	Water	4.71	21.4	Yes	-
32	21/12/15	S211215#1	B20	Water	0.958	2.29	Yes	-
33	13/01/16	G130116#1	S04	Water	1.86	-	No	Broke up
34	13/01/16	G130116#2	S05	Water	1.93	5.34	Yes	-
35	20/01/16	G200116#1	S06	Water	6.10	-	No	Broke up
36	20/01/16	G200116#2	S07	Water	6.13	30.9	Yes	-
37	28/01/16	G280116#1	S08	Water	0.386	0.74	Yes	-
38	03/02/16	G030216#1	S09	Water	0.591	1.20	Yes	-
39	19/02/16	S190216#1	B23	Water	0.971	0.49	No	15^o impact
40	24/02/16	G240216#1	B25*	Water	-	-	No	Hit something
41	11/03/16	S110316#1	B27	Water	0.981	0.50	Yes	15^o impact
42	17/03/16	G170316#1	B28	Water	-	-	No	Hit something
43	06/04/16	G060416#1	NWA4502 (CV3)	Aerogel	6.55	-	Yes	-
44	13/04/16	G130416#1	CR2 C	Aerogel	6.28	-	Yes	-
45	13/04/16	G130416#2	NWA4502 Ground	Aerogel	6.36	-	Yes	-

Continued on next page

Table B.2 – *Continued from previous page*

#	Date	Shot Code	Projectile	Target	Speed [km s^{-1}]	PIA [GPa]	Success?	*Notes*
46	20/04/16	G200416#1	CR2 B Ground	Aerogel	6.20	-	Yes	-
47	20/04/16	G200416#2	CR2 A	Aerogel	6.10	-	Yes	-
48	20/04/16	G200416#3	B29	Water	2.01	1.12	Yes	15^o impact
49	27/04/16	S270416#1	B30	Water	0.588	0.29	Yes	15^o impact
50	11/05/16	G110516#1	B26*	Water	1.982	5.93	Yes	Basalt sphere
51	10/06/16	G100616#1	G01	Water	3.07	-	Yes	-
52	13/07/16	G130716#1	G02	Water	0.863	-	Yes	-
53	13/07/16	G130716#2	G03	Water	-	-	No	Broke up
54	20/07/16	G200716#2	G04	Water	-	-	No	Broke up
55	28/07/16	G280716#1	G05	Water	-	-	No	Broke up
56	28/07/16	G280716#2	G06	Water	-	-	No	Hit something
57	08/09/16	G080916#1	G08	Water	-	-	No	Broke up
58	14/09/16	G140916#1	G09	Water	1.80	4.15	Yes	-
59	14/09/16	G140916#2	B31	Water	4.92	23.0	Yes	-
60	14/09/16	G140916#3	B32	Water	-	-	No	Broke up

Continued on next page

Table B.2 – *Continued from previous page*

#	Date	Shot Code	Projectile	Target	Speed [km s^{-1}]	PIA [GPa]	Success?	*Notes*
61	28/09/16	G280916#1	G10	Water	4.00	-	Yes	-
62	12/10/16	G121016#1	S10	Water	4.53	-	Yes	-
63	20/10/16	G201016#1	S11	Water	3.22	-	Yes	-
64	23/11/16	G231116#1	S12	Water	-	-	No	Broke up
65	30/11/16	G301116#1	S13	Water	-	-	No	Broke up
66	07/12/16	G071216#1	S14	Water	-	-	No	Broke up
67	21/06/17	G210617#1	B35	Water	-	-	No	Broke up

Appendix C

Abstracts Submitted

This appendix shows the submitted abstracts with J. E. Wickham-Eade being first author.

Can micrometeorites survive impact on the Moon or Vesta? Fragmentation of Basalt Projectiles in Hypervelocity Impacts in the Laboratory

J. E. Wickham-Eade[1] and M. J. Burchell[1]

[1] Centre for Astrophysics and Planetary Science, School of Physical Sciences, University of Kent, Canterbury CT2 7NR, United Kingdom; email: jew9@kent.ac.uk

Introduction: Dust does not stay in space, it can impact bodies. The surfaces of atmosphere-less bodies such as the Moon or asteroids are continuously being bombarded by micrometeorites. But could any macroscopic fractions of micrometeorites survive these impacts? There is evidence from the Moon that this happens (e.g. [1] and references therein). There is also interest from Vesta which shows possible accumulation of non-indigenous material from an impact [2]. It is therefore sensible to ask how much material survives and what its size distribution is. Some recent work on this topic includes [3, 4, 5] and references therein. Here we report on the fragmentation of basalt projectiles impacting water. We compare our results to those expected for impactors on the Moon and Vesta. Regarding the Moon we consider the specific low speed example of impacts from ejecta arising from giant impacts on the Earth.

Method: The Univ. Of Kent's two-stage light-gas gun [6] was used to fire 1.5 mm cubes of basalt into bags of water. The impact speeds range from 0.64 to 6.0 km s^{-1}. The water was then filtered and the filter paper mapped in an SEM (Hitachi S3400N). Automated software was used to find the size of the collected individual fragments. We can extract the size of fragments down to 10 µm in diameter and can find over 100,000 fragments in a typical impact. The Planar Impact Approximation [6] was used to calculate the peak shock pressures.

Results: From these shots we will report on the morphology of the fragments, the fragment size distributions and the retained mass. By determining the shock pressures of a basalt projectile impacting a porous target (analogous of the lunar surface and similarly Vesta) we deduce the retained mass of a small projectile impacting on the Moon or Vesta and the appropriate size distribution of the fragments.

Reference: [1] Joy K.H. et al. 2012. *Science*, 336(6087), 1426–1429. [2] Reddy V., et al., 2012. *Icarus* 221(2), 544–559. [3] McDermott K.W., et al., 2015. "Survivability of copper projectiles during hypervelocity impacts in porous ice: A laboratory investigation of the survivability of projectiles impacting comets or other bodies", *Icarus* accepted. [4] Avdelliou Ch., et al., 2015. "Survival of the impactor during hypervelocity collisions: an analogue for low porosity targets", *MNRAS* accepted. [5] Daly R.T, and Schultz P.H., 2016. Icarus 264, 9–19. [6] Burchell M. et al. (1999) *Measurement Science and Technology*, 10(1), 41–50. [7] Melosh H.J. (1989) *Impact cratering: a geologic process*. Oxford University Press.

FRAGMENTATION OF BASALT AND SHALE PROJECTILES IN HYPERVELOCITY IMPACTS IN THE LABORATORY. J. E. Wickham-Eade[1] and M. J. Burchell[1], [1]Centre for Astronomy and Planetary Sciences, School of Physical Sciences, Ingram Building, University of Kent, Canterbury, Kent CT2 7NH, United Kingdom (jew9@kent.ac.uk).

Introduction: This work focuses on projectile survival in hypervelocity impacts. There have been studies of the projectile dating back to the 1960s, but these are less frequent than other studies. Nevertheless, projectile survival after an impact is of importance for a variety of reasons. For example: Projectile fragments have been recovered from 13 impact sites on Earth (e.g. see Table 15.1 in [1]). It has been suggested that projectile fragments can be present in central peaks in lunar impact craters [2]. The dark material on the surface of Vesta is likely to come from impactors [3]. Non-indigenous materials have been found on the Moon e.g. [4] and so on. Indeed the sub-surface regions at man-made impact sites should also contain impactor material (e.g. the crater on comet 9P/Tempel-1 arising from the Deep Impact mission [5-6]).

Laboratory studies of impactor survival do exist. There are examples such as those of [6-9]. As well as size distributions of fragments, there are reports of analyses of recovered fragments to see if the impact processed their organic content, with particular relevance to astrobiology, e.g. [10-11]. It is no surprise therefore that more studies are now appearing on projectile fragment survival, including [12-13].

Accordingly, here we report on the survival of basalt and shale projectiles fired into water at speeds up to 6 km s^{-1}. In this present work we focus on the fragment size distribution and its evolution vs. impact speed and peak shock pressure.

Method: We used the Univ. of Kent two stage light gas gun [14] to fire 1.5 mm cubes of basalt and shale into bags of water. The impacts studied were at speeds between 0.52 and 6.02 km s^{-1} for basalt and, so far, 0.95, 3.12 and 4.64 km s^{-1} for shale. The water was filtered after the impact to extract the projectile fragments. After extraction, the samples were imaged in a SEM (Hitachi S3400N) and automated software was used to find and size the individual fragments; see Fig. 1 for an example. We can extract and measure fragments down to around 10 μm in size and can find over 100,000 fragments in the higher speed shots. As a check, one sample was measured directly on the SEM by the user to confirm the accuracy of the software method.

We use the Planar Impact Approximation [15] to find peak shock pressures in each impact. This requires a linear shock wave speed relation of the form U = C + Su, with values for C and S for both projectile and target materials. From [15] we take for basalt: C = 2.60 km s^{-1}, S = 1.62 and density 2860 kg m^{-3}, for water, the equivalent values were 2.39 km s^{-1}, 1.33 and 997.9 kg m^{-3} and for shale we used 2.30 km s^{-1}, 1.61 and 2545 kg m^{-3} taken from [16].

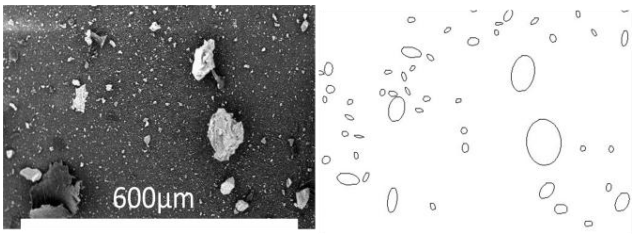

Fig. 1. SEM field of view for fragments at 3.04 km s^{-1} and software oval fit.

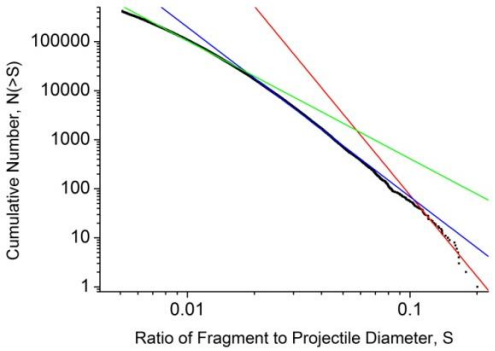

Fig. 2. Example fragment size distributions (FSD) for 0.96 km s^{-1}. The red fit is for large fragments, blue for medium and green for small.

Results: In Fig. 2, we show an example fragment size distribution (normalised to the original projectile diameter) for the impact at 0.96 km s^{-1}. We have fitted the cumulative size distributions with power laws of the form $N(>S) = aS^b$, where N is the number of fragments greater than a given size S. A single power b does not fit the entire size range of fragments recovered from a single shot and so we make 3 fits to each distribution at small, medium and large (normalised) fragment sizes. There is usually a steeper slope (larger b value) at larger fragment sizes, with a smaller slope (lower b value) at smaller sizes. b ranges for basalt and shale from: Small sizes -2.4 to -3.6 and -1.7 to -3.6, Intermediate Sizes -3.5 to -4.2 and -2.9 to -4.3 and at the Largest Sizes -4.4 to -6 and -0.8 to -11 respectively.

The behavior of the fragment size at the very largest sizes depends sharply on impact speed. At the lower speeds the first few largest fragments form a concave shape on the cumulative size distribution in log-log space. This flattens out at an intermediate

speed (3 km s^{-1}, 10.5 GPa) and then becomes convex at higher speeds. This is suggestive of the behavior of the similar cumulative size distributions for fragmented *targets* as they pass from the just disrupted to the heavily disrupted regimes (e.g. see [17-18]). This behaviour also appears to be seen in the shale results.

We used the ratio of the largest axis (a) and an orthogonal axis (b) to characterise each fragment shape. We find that the average mean value over all sizes and speeds of b/a for basalt and shale is 0.60 ± 0.19 and 0.64 ± 0.17 respectively.

We have also estimated the total surviving mass percentage we extract after each impact. This is shown in Fig. 3 vs. peak shock pressure as found by the PIA. We see an initially rapid drop in the surviving mass but this then flattens off at higher speeds and pressures. Given that, due to the small size of the grains, there is not much mass in the very fine size fraction below 10 μm where our sensitivity falls off, the missing mass is likely carried away from the target (by water lost during the impact back along the impact direction where our target holder was not sealed to allow entrance of the projectile) as suggested for example in [19]. Or increasingly amounts of the projectile start to be vaporized. It appears that after our first three shots shale has a similar surviving mass percentage to basalt at low shock pressures, however, at higher shock pressures it has a higher surviving mass percentage.

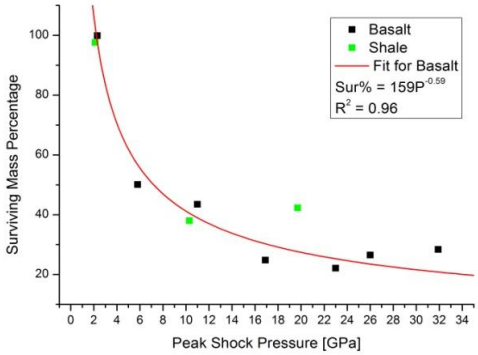

Fig. 3. Surviving mass percentage vs. peak shock pressure.

We have also looked at the relationship of the largest fragment mass ratio $m_{L,p}/M_p$ with the projectile impact energy density Q_p, as suggested in the literature [20][21]. This plotted with previous data [20][21] suggests that over the shot regime there is a change in slope past ~1 km s^{-1}, see Fig. 4. However, the latter part of the shot regime agrees with data of basalt projectiles impacting at non-normal incidence [20]. We calculate that the energy density at which catastrophic disruption of the basalt projectile occurs is (25.1 ± 1.9) x10^4 J kg^{-1}.

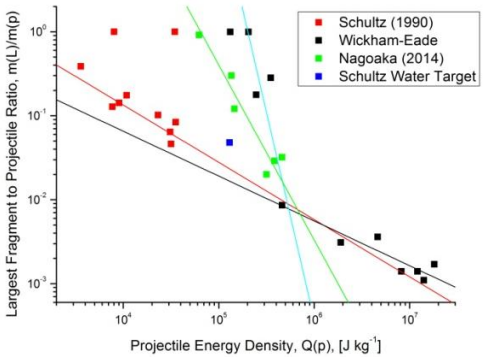

Fig. 4. Largest fragment mass ratio $m_{L,p}/M_p$ vs. projectile impact energy density Q_p.

Conclusions: We have conducted a detailed set of measurements of the fragment size distribution for impacts of basalt and shale on to water in the speed range 0.52 to 6.02 km s^{-1} and 0.95 to 4.64 km s^{-1}, which corresponds to peak shock pressures of 1.1 to 31.9 GPa and 2.1 to 19.7 GPa respectively. The fragment size distribution changes with increasing impact speed, with fewer large fragments in the higher speed shots. However, even at the higher speeds there is significant retention of the projectile material in the target.

Preliminary results for shale indicate a higher disruptive energy and a higher surviving mass fraction at high shock pressures than for basalt.

References: [1] Goderis S. et al. (2013) Chapter 15, 223 – 239, in: *Impact cratering processes and products*. Edited by G.R. Osinski and E. Pierazzo, pub. Wiley-Blackwell. [2] Yue Z. et al. (2013) *Nature Geoscience, 6*, 435–437. [3] Reddy V. et al. (2012) *Icarus, 221(2)*, 544–559. [4] Joy K.H. et al., (2012) *Science, 336(6087)*, 1426–1429. [5] Schultz P.H. et al. (2013) *Icarus, 222*, 502–515. [6] McDermott et al., (2016) Icarus, doi:10.1016/j.icarus.2015.12.037 [7] Schultz P.H. and Gault D.E. (1984) *LPSC XV*, Abstract #730. [8] Hernandez V.S. et al (2006) *IJIE, 32*, 1981–999. [9] Kenkmann T. et al. (2013) *MAPS, 48(1)*, 150–164. [10] Parnell J. et al. (2010) *MAPS, 45*, 1340–1358. [11] Burchell et al. (2014) *Astrobiology, 14(6)*, 473–485. [12] Daly R.T & Schultz P.H. (2015) *GRL, 42*. [13] Daly R.T. & Schultz P.H. (2016) *Icarus, 264*, 9-19. [14] Burchell M. et al. (1999) *Meas. Sci. Tech., 10(1)*, 41–50. [15] Melosh H.J. (1989) *Impact cratering: a geologic process*. OUP. [16] Ahrens J.T. and Johnson M.L. (1995) Chapter 4, 35-44, in: *Rock physics and phase relations*. AGU. [17] Durda D.D. et al. (2007) *Icarus, 186*, 498–516. [18] Leliwa-Kopystynski et al. (2010) *MAPS, 44*, 1929–1935. [19] Burchell M.J. et al. (2012) *MAPS, 47*, 671– 683. [20] Schultz P.H. and Gault D.E. (1990) *Geo. Soc. America, Special Paper 247*. [21] Nagaoka H. et al. (2014) *MAPS, 49*, 69–79.

SHOCK PRESSURE AND TEMPERATURE EFFECTS ON CARBON D AND G BANDS IN RAMAN SPECTROSCOPY FOR BASALT, SHALE AND GRAPHITE. J. E. Wickham-Eade[1] and M. J. Burchell[1], [1]Centre for Astronomy and Planetary Sciences, School of Physical Sciences, Ingram Building, University of Kent, Canterbury, Kent, CT2 7NH, United Kingdom (jew9@kent.ac.uk).

Introduction: The European Space Agency's (ESA) ExoMars Rover mission, to be launched in 2020, plans to investigate the Martian surface and sub-surface for indications of life (biomarkers). One instrument on the rover will be the Raman Laser Spectrometer (RLS), which is a 532 nm (green) laser Raman spectrometer [1]. The University of Kent's Raman Spectrometer is fitted with a 532 nm laser, making it a suitable facility to investigate potential science to come from this instrument.

The Raman spectra of carbon is often identified by the presence of the D (at ~1345 cm^{-1}) and G (at ~1575 cm^{-1}) bands (Fig. 1). Shock effects on spectral peaks have been shown to occur for different minerals [2, 3], e.g. for the mineral olivine impacting on aluminum foils and aerogel [4, 5, 6]. Work involving static pressure and temperature effects on the Raman spectra of carbon have also been conducted [7, 8]. However, the shock pressure and temperature effects on carbon bearing rocks is not well understood. Seeing as carbon is a highly important and abundant element for indications of life it is time that this is investigated.

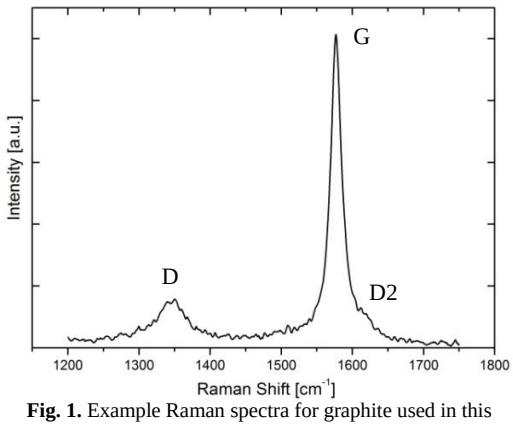

Fig. 1. Example Raman spectra for graphite used in this work. This spectra has had its background fluorescence removed.

Accordingly, here we report on the shock pressure and temperature effects on the carbon bearing rocks basalt, shale and graphite.

Method: The basalt, shale and graphite samples were filed into 1.5 mm cubes. A small area on the face of each projectile was then mapped using the Univ. of Kent's 532 nm laser Raman spectrometer. Next, using the Univ. of Kent two stage light gas gun [9] each projectile was fired into bags of water [10]. The water was filtered after the impact to extract the projectile fragments [10]. The impacts studied were at speeds between 0.96 and 4.96 km s^{-1} for basalt, 0.95 to 6.13 km s^{-1} for shale and for graphite 0.86 and 4.00 km s^{-1}. The spectra of 40 projectile fragments per shot were obtained and compared to the initial projectile spectra.

We use the Planar Impact Approximation (PIA) [11] to determine the peak shock pressure for the shot speeds. The PIA requires a linear shock wave speed relation of the form of U = C + Su, where values for C and S for both the projectile and target are required. For the shot speeds presented the peak shock pressures are between 2.3 to 23.3 GPa for basalt and 2.1 to 30.9 GPa for shale.

The effects of temperature on the D and G carbon Raman bands was investigated using a Linkam Temperature Controlled microscope stage. For basalt, shale and graphite the samples were heated from 303 K up to 773 K in steps of ten degrees. They were held for one hour at each temperature to ensure the sample was uniformly heated. In addition, shale and graphite have been cooled from 303 K down to 173 K using liquid nitrogen.

Results: In Fig. 2, we show a plot of the D and G band peak positions and their changes with temperature. Overall, it suggests that with increasing temperature both the D and G band peak positions shift to lower wavenumbers for shale and graphite, agreeing with carbon bands in the literature [12]. This shift of the band positions signals a weakening of these modes. Similarly, at colder temperatures the peaks are shifted to higher wavenumbers, possibly suggesting that there is a strengthening of these modes. The increasing degree of scatter of D band peak positions past approximately 550 K is due to the reduction in intensity of the band's signal as a result of the heating process. Furthermore, there appears to be considerable differences between the G bands peak positions for the three materials, whereas, for the D band both shale and graphite appear similar.

In Fig. 3, we show a comparison of the average G band width to the average G band peak position before and after shooting for basalt and shale. Traditionally, this is taken as indicating the thermal maturity of a sample. Thermal maturity refers to the extent to heat-driven reactions that alter the composition of organic matter, for example, the

conversion of organic matter in sedimentary rocks to petroleum.

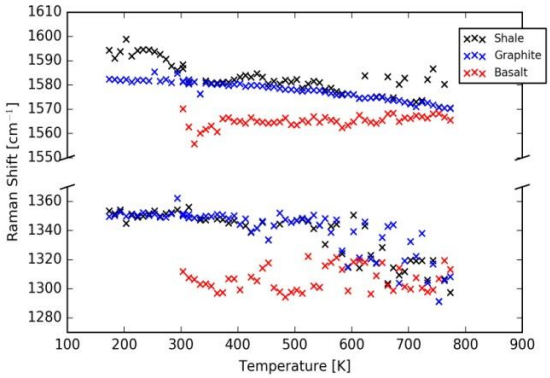

Fig. 2. Carbon D and G band peak position against temperature for shale, graphite and basalt.

Comparing basalt and shale they appear to behave differently post shock. The basalt shows a significant thermal maturity increase. By contrast, the shale appears to have a decreased G band width post-shock with no commensurate change in the overall position.

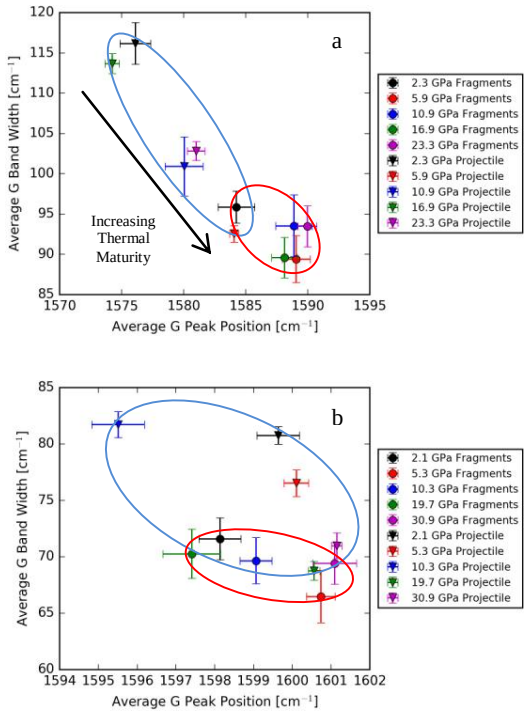

Fig. 3. Plot of the average G band width vs. the average G band peak position for each shot. This relation indicates the thermal maturity of a sample. In this case the two samples are basalt (a) and shale (b). Blue circles are for the projectile before shooting and the red for the fragments.

Furthermore, Fig. 2 and 3 seem to suggest that the effects of heating and the effects of shock pressure on the carbon G band oppose each other with regard to the band position. Further work shall be conducted in order to determine the full effects of heating and shock pressure with the addition of comparing static pressure in order to further understand these effects.

Conclusions: We have conducted a detailed investigation into the effect of shock pressure and temperature on the D and G band of carbon in Raman spectroscopy. The shock pressure ranges for basalt and shale were 2.3 to 23.3 GPa and 2.1 to 30.9 GPa respectively and the temperature ranges were from 173 to 773 K for shale and graphite and from 303 to 773 K for basalt. Temperature alters the D and G band peak positions of carbon in rocks by shifting it to lower wavenumbers at higher temperatures (>303 K) and to higher wavenumbers at lower temperatures (<303 K). This appears to be the opposite for shock pressure where G band peak positions are mostly shifted to higher wavenumbers. Furthermore, shock pressure appears to decrease the width of the carbon G band.

This work suggests that when analyzing carbon in Raman spectra it is important to consider the shock and temperature history of the sample. This is because both the D and G band are significantly affected by these factors.

Acknowledgements: JWE would like the thank the Kent Opportunity Fund for funding his PhD and Mike Cole for operating the Univ. of Kent's two stage light gas gun. MJB would like to that STFC for funding the gun.

References: [1] Rull, F. et al. (2013) *LPSC XLIV*, Abstract #2403. [2] Farrell-Turner, S. et al. (2005) *MAPS, 40*, 1311-1327. [3] Bucio, L. et al. (2015) *High Pressure Res., 35*, 355-362. [4] Foster, N. et al. (2014) *Geochim. Cosmochim. Acta, 121*, 1-14. [5] Hariss, K. H. & Burchell, M. J. (2016) *MAPS, 51*, 1289-1300. [6] Xie, X. et al. (2001) *EPSL, 187*, 345-356. [7] Zerda, T. W. (2000) *Carbon, 39*, 355-361. [8] Beyssac, O. et al. (2002) *J. Metamorph. Geol., 20*, 859-871. [9] Burchell M. J. et al. (1999) *Meas. Sci. Tech., 10(1)*, 41–50. [10] Wickham-Eade, J. E. & Burchell, M. J. (2016) *LPSC XLVII*, Abstract #1235. [11] Melosh H. J. (1989) *Impact cratering: a geologic process*. OUP. [12] Huang, E-. P. et al. (2010) *Phys. Chem. Miner., 37*, 593-600.

Presentation Preference:
__X___ Oral
__X___ Poster

14th Hypervelocity Impact Symposium
April 24th – 28th, 2017
University of Kent, Canterbury, UK

RAMAN IDENTIFICATION OF OLIVINE GRAINS IN FINE GRAINED MINERAL ASSEMBLAGES FIRED INTO AEROGEL

J. E. Wickham-Eade[1], M. J. Burchell[1], M. C. Price[1], L. J. Hicks[2], J. L. MacArthur[2] and J. C. Bridges[2]

[1]Centre for Astrophysics and Planetary Science, School of Physical Sciences, Ingram Building, University of Kent, Canterbury, Kent, CT2 7NH, UK. (jew9@kent.ac.uk),
[2]Space Research Centre, Dept. of Physics & Astronomy, University of Leicester, Leicester, LE1 7RH, UK.

ABSTRACT

Introduction

NASA's Stardust mission (Brownlee et al. 2006) was a sample return mission to collect material from the coma of comet 81P/Wild 2. Material was captured using aluminum foils and SiO_2 aerogel, whilst flying past the comet with a relative speed of 6.1 km s^{-1}. Aerogel is a low density, highly porous medium. The aerogel used for the Stardust mission was transparent and had a density gradient of 5 mg cc^{-1} at the front face rising to 50 mg cc^{-1} at the rear. Aerogel captures materials in a low pressure impact spread along the length of a track formed as the projectile decelerates in the aerogel. The captured grain at the end of its track is known as the terminal grain (see Burchell et al. (2006) for a review of the use of aerogel in dust capture in space). This process is thought to involve low shock pressure of ≤300 MPa according to Trigo-Rodriquez et al. (2008), but can heat the samples to over 1,000 ^{o}C for a brief period of a microsecond.

Olivine ($(Mg^{+2}, Fe^{+2})_2SiO_4$) is a very common mineral found in the Solar System, including in asteroids and comets. Fortunately, olivine has a very distinct Raman spectra with a characteristic doublet at around 820 and 850 cm^{-1}, referred to as P1 and P2 respectively. The effects of single grains of olivine being captured in aerogel and on aluminum foil at 6 km s^{-1} was investigated by Foster et al. (2014). The authors found a permanent shift of the olivine

doublet peaks in the captured samples on comparison to the original un-shocked samples. It was concluded that this was due to strain on the olivine crystal lattice caused by the effect of impact. Subsequently, Harriss and Burchell (2016) looked at olivine impacts onto aluminum foil at a range of speeds (1 – 6 km s^{-1}) and showed that the shifts in P1 and P2 only occurred at the higher speeds.

Taken together, these results suggest that olivine experiences capture effects when fired as a single grain into aerogel. However, in space, the presence of impactors consisting of single grains would be rare. Therefore, this work is looking into the capture effects on olivine in aerogel where the olivine is a constituent of a fine grained multi-mineral assemblage. Our results inform a project to analyse carbonaceous chondrite powders shot into aerogel at 6 k ms^{-1}. The results are helping us to refine the closest chondrite analogues to the Comet Wild2 parental material (Hicks et al. 2017).

Method

Our starting material was the NWA 10256 CR2 (carbonaceous) chondrite. This was analysed by SEM-EDX using a Phillips XL30 ESEM at the University of Leicester both in thin section and in powdered form. Material from the interior of the meteorite was ground into a powder with a grain size of 25 - 200 µm. These powders were fired into aerogel with a density gradient of 25 – 55 mg cm^{-3} using the University of Kent's Two-Stage Light Gas Gun (Burchell et al. 1999). The shot speeds were between 6.1 – 6.3 km s^{-1}, i.e. comparable to the Stardust mission. The samples where characterized before shooting using the University of Kent's Raman spectrometer. A 532 nm (green) laser, similar to the laser to be used on ExoMars, was used to acquire the spectra. Low power was used to ensure there was no laser heating affects to the grains, as it this can be a potential problem (Hibbert and Price 2014).

Due to the transparent nature of aerogel, spectra of the terminal grains were obtained without them needing to be removed from the aerogel.

Results and Discussion

The Raman characterizing of the material pre-shot showed that it was a mix of predominately pyroxene and olivine. The captured material in the aerogel exhibited a broad variation in track lengths (0.82 – 21.3 mm) and terminal grain sizes (average diameter 6.28 – 74.4 µm). Here we analyse data from two shots. Of these shots, six terminal olivine grains were found in one (CR2 B) and only one in another (CR2 C). Comparing the average peak positions for the olivine doublet, there was a shift of 1.88 ± 0.28 cm^{-1} for P1 to the left (i.e. to a lower wavenumber), and the width of P1 broadened by 2.11 ± 0.07 cm^{-1}. The width for P2 became narrower by 2.25 ± 1.24 cm^{-1}, and no shift was observed for the P2 peak (the average shift was to the left but was only 0.07 ± 0.88 cm^{-1}, i.e. not significant). Figure 1 is a graphical representation of a characteristic olivine spectrum before shooting and the spectra of the six terminal grains found after capture from the CR2 B shot. These alterations in peak position and width would be as a result of the shock and heating effect on the crystalline lattice.

From Figure 1 it is clear the one terminal grain (top spectrum in Figure 1) containing olivine experienced a far more significant shift than the others. A potential cause of this significant shift may be due to a differing degree of shock being experienced by a sub-grain during the capture process, when inside a larger assemblage depending on its location inside the whole grain. When results from this work are compared with past work we are seeing a shift in the same direction however a different magnitude, especially for the P2 peak. This could be as a result of the olivine being a constituent of the mineral assemblage or of the small size of the sub-grains.

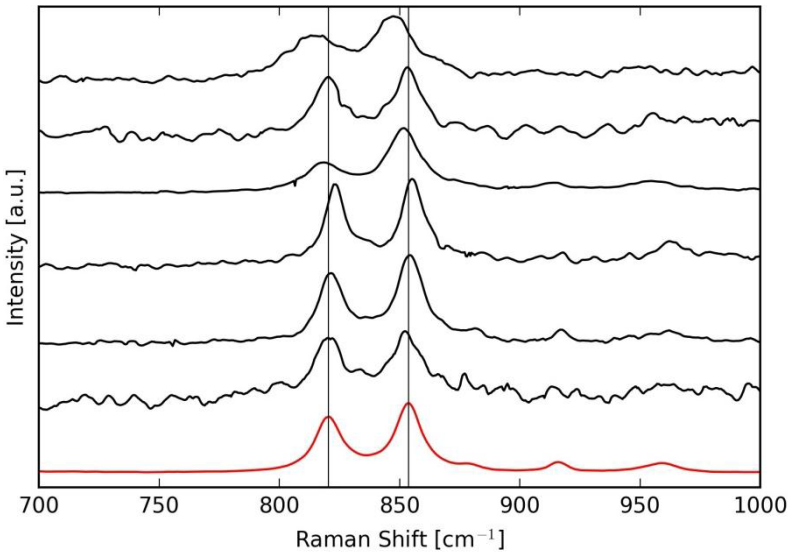

Figure 1. Olivine spectra from the CR2 B shot. In red is the spectrum from an un-shot sample of the CR2 meteorite. In black are the spectra for the six terminal grains captured in the aerogel at 6 km s^{-1}.

Conclusion

A carbonaceous chondrite (CR2) meteorite was fired into aerogel at speeds between 6.1 – 6.3 km s^{-1} in order to investigate the capture effects on olivine. The peak position of the P1 doublet was shifted, whereas the peak of P2 was not. This isn't in full agreement with past work (Foster et al. 2014; Harriss and Burchell 2016). This result could be due to the olivine being a part of the mixture of minerals meaning the shock wave propagates differently to material consisting of one mineral, or the small size of the sub-grains compared to the single grains used in past work. Given that the positions of P1 and P2 are used to determine the relative Mg/Fe content of the olivine, these results indicate that there may be uncertainties in the Mg/Fe content of the olivines found by Stardust if identified with Raman spectroscopy.

References

• Burchell et al. (1999) Meas. Sci. Tech.10, 41-51. • Burchell et al. (2006) Ann. Rev. Earth Planet. Sci. 34, 385–418. • Brownlee et al. (2006) Science 314, 1711-1716. • Foster et al.

(2014) Gechim. Cosmochim. Acta. 121, 1-14. • Harriss and Burchell (2016) MAPS, 51, 1289-1300. • Hibbert and Price (2014) LPSC XLV, abstract #1350. • Hicks L.J. et al. (2017) MAPS, (in review). • Trigo-Rodriquez et al. (2008) Icarus, 128, 88-94.

Appendix D

Codes

D.1 Matlab Scripts

Script for gun shot residue removal from fragment distribution

This Matlab script was used to remove the gun shot residue data from the projectile fragment data. It reads in both unprocessed and control data. It then puts them into a histogram with a 0.1 μm bin size. The two histograms are then subtracted and the resultant data is written out to the file opened in the first line.

```
%Distribution Subtraction Code
tic;

clear all;

%Change for new shot data
FID = fopen('Sub_synth_2kms_SphereDiam_FFP.txt','w');

dist = importdata('synth_2kms_SphereDiam.txt');
controldist = importdata('Control_SphereDiam_FFP.txt');

max = max(controldist);

distcut1 = dist(dist<max);
```

```
misdis = dist(dist>max)

edges = [10.1:0.1:max];

[h_dist, bins] = hist(distcut1,edges);
bincount1 = histc(distcut1,edges);
[h_controldist, bins2] = hist(controldist,edges);
bincount2 = histc(controldist,edges);

histo = h_dist - h_controldist;
bincount = bincount1 - bincount2;

%Removes Negative Numbers
histo(histo<0)=0;

g = size(histo);

for a = 1:g(2)
        data = repmat(bins(a:a),histo(a:a),1);
        fprintf(FID,'%2.5f\t\n',data);
end

fprintf('Done!\n');
fclose(FID);

toc
```

D.2 Python Scripts

Script for Raman Data Analysing of Shock Pressure Results

This example script is for the shocked graphite spectra. It reads, sorts and processes the data for it to be plotted. It also determines the error on the mean, standard deviation and combined error for the data. This script is the same for the basalt and shale spectra.

```
# -*- coding: utf-8 -*-
"""
Created on Thu Jun 29 12:09:47 2017
```

```
@author: Jamie
"""

import numpy as np
import pylab as plt
from matplotlib.patches import Ellipse

########Data Type Setting############

mydtype = np.dtype([('Num',int),('DPos',float),('DAmp',float),('DWidth',float),
('DArea',float),('GPos',float),('GAmp',float),
('GWidth',float),('GArea',float),('D2Pos',float),('D2Amp',float),
('D2Width',float),('D2Area',float),('R1',float),('R2',float)])
mydtype2 = np.dtype([('Num',int),('DPos',float),
('DAmp',float),('DWidth',float),('GPos',float),('GAmp',float),('GWidth',float),
('Ratio',float)])
mydtype3 = np.dtype([('Speed',float),('Pressure',float)])

##################################

#########Reading Data############

Frag3 = np.genfromtxt('S01Frag3120ms.txt',dtype=mydtype,
usecols=[0,1,2,3,4,5,6,7,8,9,10,11,12,13,14],delimiter='\t',skip_header=1)
Proj3 = np.genfromtxt('S01Proj3120ms.txt',dtype=mydtype,
usecols=[0,1,2,3,4,5,6,7,8,9,10,11,12,13,14],delimiter='\t',skip_header=1)
Frag2 = np.genfromtxt('S05Frag1940ms.txt',dtype=mydtype,
usecols=[0,1,2,3,4,5,6,7,8,9,10,11,12,13,14],delimiter='\t',skip_header=1)
Proj2 = np.genfromtxt('S05Proj1940ms.txt',dtype=mydtype,
usecols=[0,1,2,3,4,5,6,7,8,9,10,11,12,13,14],delimiter='\t',skip_header=1)
Frag4 = np.genfromtxt('S03Frag4640ms.txt',dtype=mydtype,
usecols=[0,1,2,3,4,5,6,7,8,9,10,11,12,13,14],delimiter='\t',skip_header=1)
Proj4 = np.genfromtxt('S03Proj4640ms.txt',dtype=mydtype,
usecols=[0,1,2,3,4,5,6,7,8,9,10,11,12,13,14],delimiter='\t',skip_header=1)
Frag6 = np.genfromtxt('S07Frag6130ms.txt',dtype=mydtype,
usecols=[0,1,2,3,4,5,6,7,8,9,10,11,12,13,14],delimiter='\t',skip_header=1)
Proj6 = np.genfromtxt('S07Proj6130ms.txt',dtype=mydtype,
usecols=[0,1,2,3,4,5,6,7,8,9,10,11,12,13,14],delimiter='\t',skip_header=1)
Frag1 = np.genfromtxt('S02Frag950ms.txt',dtype=mydtype,
usecols=[0,1,2,3,4,5,6,7,8,9,10,11,12,13,14],delimiter='\t',skip_header=1)
Proj1 = np.genfromtxt('S02Proj950ms.txt',dtype=mydtype,
```

```
usecols=[0,1,2,3,4,5,6,7,8,9,10,11,12,13,14],delimiter='\t',skip_header=1)

data = np.genfromtxt('SpeedPressure.txt',dtype=mydtype3,delimiter='\t',
skip_header=1)

##################################

#######Computing Averages#########

lt = [Frag1,Frag2,Frag3,Frag4,Frag6]

AvDiam = []
AvDPos = []
AvDAmp = []
AvDWidth = []
AvGPos = []
AvGAmp = []
AvGWidth = []
AvD2Pos = []
AvD2Amp = []
AvD2Width = []
AvR1 = []
AvR2 = []

StdGPos = []
StdDPos = []
StdD2Pos = []
StdGWidth = []
StdDWidth = []
StdD2Width = []
StdR1 = []
StdR2 = []

for i in lt:
    FragAv = np.nanmean(i['DPos'])
    AvDPos.append(FragAv)
    FragAv = np.nanmean(i['DAmp'])
    AvDAmp.append(FragAv)
    FragAv = np.nanmean(i['DWidth'])
    AvDWidth.append(FragAv)
    FragAv = np.nanstd(i['DWidth'])
```

```
        StdDWidth.append(FragAv)
        FragAv = np.nanmean(i['GPos'])
        AvGPos.append(FragAv)
        FragStd = np.nanstd(i['GPos'])
        StdGPos.append(FragStd)
        FragStd = np.nanstd(i['DPos'])
        StdDPos.append(FragStd)
        FragStd = np.nanstd(i['D2Pos'])
        StdD2Pos.append(FragStd)
        FragAv = np.nanmean(i['GAmp'])
        AvGAmp.append(FragAv)
        FragAv = np.nanmean(i['GWidth'])
        AvGWidth.append(FragAv)
        FragStd = np.nanstd(i['GWidth'])
        StdGWidth.append(FragStd)
        FragAv = np.nanmean(i['D2Pos'])
        AvD2Pos.append(FragAv)
        FragAv = np.nanmean(i['D2Amp'])
        AvD2Amp.append(FragAv)
        FragAv = np.nanmean(i['D2Width'])
        AvD2Width.append(FragAv)
        FragAv = np.nanstd(i['D2Width'])
        StdD2Width.append(FragAv)
        FragAv = np.nanmean(i['R1'])
        AvR1.append(FragAv)
        FragAv = np.nanstd(i['R1'])
        StdR1.append(FragAv)
        FragAv = np.nanmean(i['R2'])
        AvR2.append(FragAv)
        FragAv = np.nanstd(i['R2'])
        StdR2.append(FragAv)

lt2 = [Proj1, Proj2, Proj3, Proj4, Proj6]

AvDPosP = []
AvDAmpP = []
AvDWidthP = []
AvGPosP = []
AvGAmpP = []
AvGWidthP = []
AvD2PosP = []
```

```
AvD2AmpP = []
AvD2WidthP = []
AvR1P = []
AvR2P = []

StdGPosP = []
StdDPosP = []
StdD2PosP = []
StdGWidthP = []
StdDWidthP = []
StdD2WidthP = []
StdR1P = []
StdR2P = []

for i in lt2:
    FragAv = np.nanmean(i['DPos'])
    AvDPosP.append(FragAv)
    FragAv = np.nanmean(i['DAmp'])
    AvDAmpP.append(FragAv)
    FragAv = np.nanmean(i['DWidth'])
    AvDWidthP.append(FragAv)
    FragAv = np.nanstd(i['DWidth'])
    StdDWidthP.append(FragAv)
    FragAv = np.nanmean(i['GPos'])
    AvGPosP.append(FragAv)
    FragStd = np.nanstd(i['GPos'])
    StdGPosP.append(FragStd)
    FragStd = np.nanstd(i['DPos'])
    StdDPosP.append(FragStd)
    FragStd = np.nanstd(i['D2Pos'])
    StdD2PosP.append(FragStd)
    FragAv = np.nanmean(i['GAmp'])
    AvGAmpP.append(FragAv)
    FragAv = np.nanmean(i['GWidth'])
    AvGWidthP.append(FragAv)
    FragStd = np.nanstd(i['GWidth'])
    StdGWidthP.append(FragStd)
    FragAv = np.nanmean(i['D2Pos'])
    AvD2PosP.append(FragAv)
    FragAv = np.nanmean(i['D2Amp'])
    AvD2AmpP.append(FragAv)
```

```
    FragAv = np.nanmean(i['D2Width'])
    AvD2WidthP.append(FragAv)
    FragAv = np.nanstd(i['D2Width'])
    StdD2WidthP.append(FragAv)
    FragAv = np.nanmean(i['R1'])
    AvR1P.append(FragAv)
    FragAv = np.nanstd(i['R1'])
    StdR1P.append(FragAv)
    FragAv = np.nanmean(i['R2'])
    AvR2P.append(FragAv)
    FragAv = np.nanstd(i['R2'])
    StdR2P.append(FragAv)

##################################

ProjAvDPos = np.mean(AvDPosP)
ProjAvDAmp = np.mean(AvDAmpP)
ProjAvDWidth = np.mean(AvDWidthP)
ProjAvGPos = np.mean(AvGPosP)
ProjAvGWidth = np.mean(AvGWidthP)
#ProjAvDPos = np.mean(AvDPosP)
ProjAvD2Pos = np.mean(AvD2PosP)
ProjAvD2Amp = np.mean(AvD2AmpP)
ProjAvD2Width = np.mean(AvD2WidthP)
ProjAvR1 = np.mean(AvR1P)
ProjAvR2 = np.mean(AvR2P)

#######Calculate Errors###########

lt3 = [0,1,2,3,4]

FWHMGPos = [StdGPos[m] * 2.36 for m in lt3]
FWHMGPosP = [StdGPosP[m] * 2.36 for m in lt3]

FWHMGWidth = [StdGWidth[m] * 2.36 for m in lt3]
FWHMGWidthP = [StdGWidthP[m] * 2.36 for m in lt3]

ErrGPos = [StdGPos[m]/np.sqrt(40) for m in lt3]
ErrDPos = [StdDPos[m]/np.sqrt(40) for m in lt3]
ErrD2Pos = [StdD2Pos[m]/np.sqrt(40) for m in lt3]
```

```
ErrGWidth = [StdGWidth[m]/np.sqrt(40) for m in lt3]
ErrDWidth = [StdDWidth[m]/np.sqrt(40) for m in lt3]
ErrD2Width = [StdD2Width[m]/np.sqrt(40) for m in lt3]

ErrR1 = [StdR1[m]/np.sqrt(40) for m in lt3]
ErrR2 = [StdR2[m]/np.sqrt(40) for m in lt3]

ErrGPosP = [StdGPosP[m]/np.sqrt(25) for m in lt3]
ErrDPosP = [StdDPosP[m]/np.sqrt(25) for m in lt3]
ErrD2PosP = [StdD2PosP[m]/np.sqrt(25) for m in lt3]

ErrGWidthP = [StdGWidthP[m]/np.sqrt(25) for m in lt3]
ErrDWidthP = [StdDWidthP[m]/np.sqrt(25) for m in lt3]
ErrD2WidthP = [StdD2WidthP[m]/np.sqrt(25) for m in lt3]

ErrR1P = [StdR1P[m]/np.sqrt(25) for m in lt3]
ErrR2P = [StdR2P[m]/np.sqrt(25) for m in lt3]

####La####

La1 = 4.35 * Frag1['GAmp']/Frag1['DAmp']
La1P = 4.35 * Proj1['GAmp']/Proj1['DAmp']

La2 = 4.35 * Frag2['GAmp']/Frag2['DAmp']
La2P = 4.35 * Proj2['GAmp']/Proj2['DAmp']

La3 = 4.35 * Frag3['GAmp']/Frag3['DAmp']
La3P = 4.35 * Proj3['GAmp']/Proj3['DAmp']

La4 = 4.35 * Frag4['GAmp']/Frag4['DAmp']
La4P = 4.35 * Proj4['GAmp']/Proj4['DAmp']

La5 = 4.35 * Frag6['GAmp']/Frag6['DAmp']
La5P = 4.35 * Proj6['GAmp']/Proj6['DAmp']


##########Subtracting##############

DGSep = [x - y for x, y in zip(AvGPos, AvDPos)]
DGSepP = [x - y for x, y in zip(AvGPosP, AvDPosP)]
```

```
GD2Sep = [x - y for x, y in zip(AvD2Pos, AvGPos)]
GD2SepP = [x - y for x, y in zip(AvD2PosP, AvGPosP)]

DeltaADGSep = [np.sqrt(x**2 + y**2) for x, y in zip(ErrGPos, ErrDPos)]
DeltaADGSepP = [np.sqrt(x**2 + y**2) for x, y in zip(ErrGPosP, ErrDPosP)]

DeltaAGD2Sep = [np.sqrt(x**2 + y**2) for x, y in zip(ErrGPos, ErrD2Pos)]
DeltaAGD2SepP = [np.sqrt(x**2 + y**2) for x, y in zip(ErrGPosP, ErrD2PosP)]

DPosSub = [x - y for x, y in zip(AvDPos, AvDPosP)]
DAmpSub = [x - y for x, y in zip(AvDAmp, AvDAmpP)]
DWidthSub = [x - y for x, y in zip(AvDWidth, AvDWidthP)]
GPosSub = [x - y for x, y in zip(AvGPos, AvGPosP)]
GAmpSub = [x - y for x, y in zip(AvGAmp, AvGAmpP)]
GWidthSub = [x - y for x, y in zip(AvGWidth, AvGWidthP)]

DeltaA = [np.sqrt(x**2 + y**2) for x, y in zip(ErrGPosP, ErrGPos)]
DeltaAD = [np.sqrt(x**2 + y**2) for x, y in zip(ErrDPosP, ErrDPos)]
DeltaAD2 = [np.sqrt(x**2 + y**2) for x, y in zip(ErrD2PosP, ErrD2Pos)]

DeltaADWidth = [np.sqrt(x**2 + y**2) for x, y in zip(ErrDWidthP, ErrDWidth)]
DeltaAGWidth = [np.sqrt(x**2 + y**2) for x, y in zip(ErrGWidthP, ErrGWidth)]
DeltaAD2Width = [np.sqrt(x**2 + y**2) for x, y in zip(ErrD2WidthP, ErrD2Width)]

DeltaAR1 = [np.sqrt(x**2 + y**2) for x, y in zip(ErrR1P, ErrR1)]
DeltaAR2 = [np.sqrt(x**2 + y**2) for x, y in zip(ErrR2P, ErrR2)]

DPosSubAv = AvDPos - ProjAvDPos
GPosSubAv = AvGPos - ProjAvGPos
D2PosSubAv = AvD2Pos - ProjAvD2Pos

DWidthSubAv = AvDWidth - ProjAvDWidth
GWidthSubAv = AvGWidth - ProjAvGWidth
D2WidthSubAv = AvD2Width - ProjAvD2Width

R1SubAv = AvR1 - ProjAvR1
R2SubAv = AvR2 - ProjAvR2
```

Appendix E

Example Raman Spectra

E.1 Shock Pressure Experiment

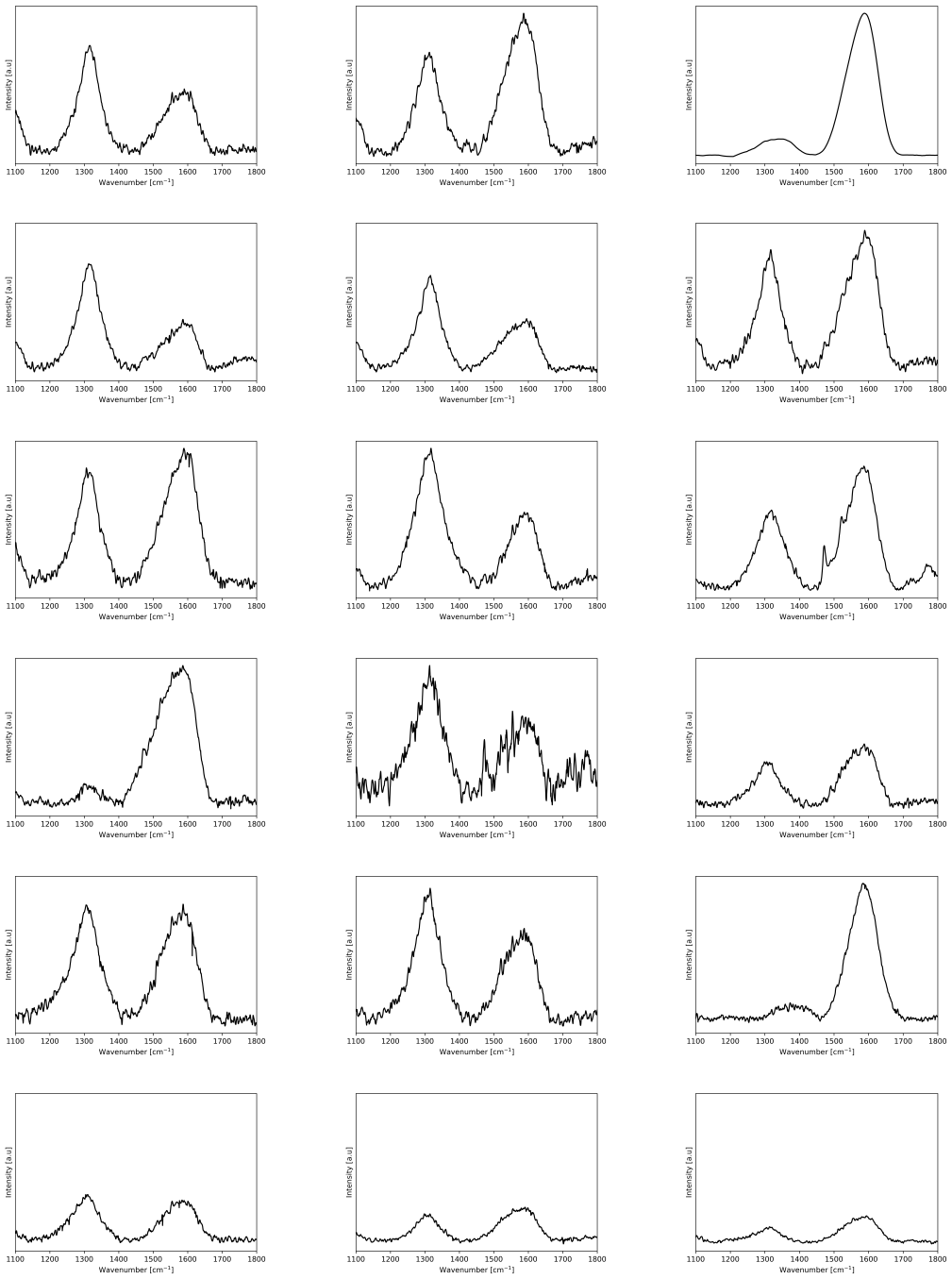

Figure E.1: Example Raman spectra of the basalt projectiles before shooting.

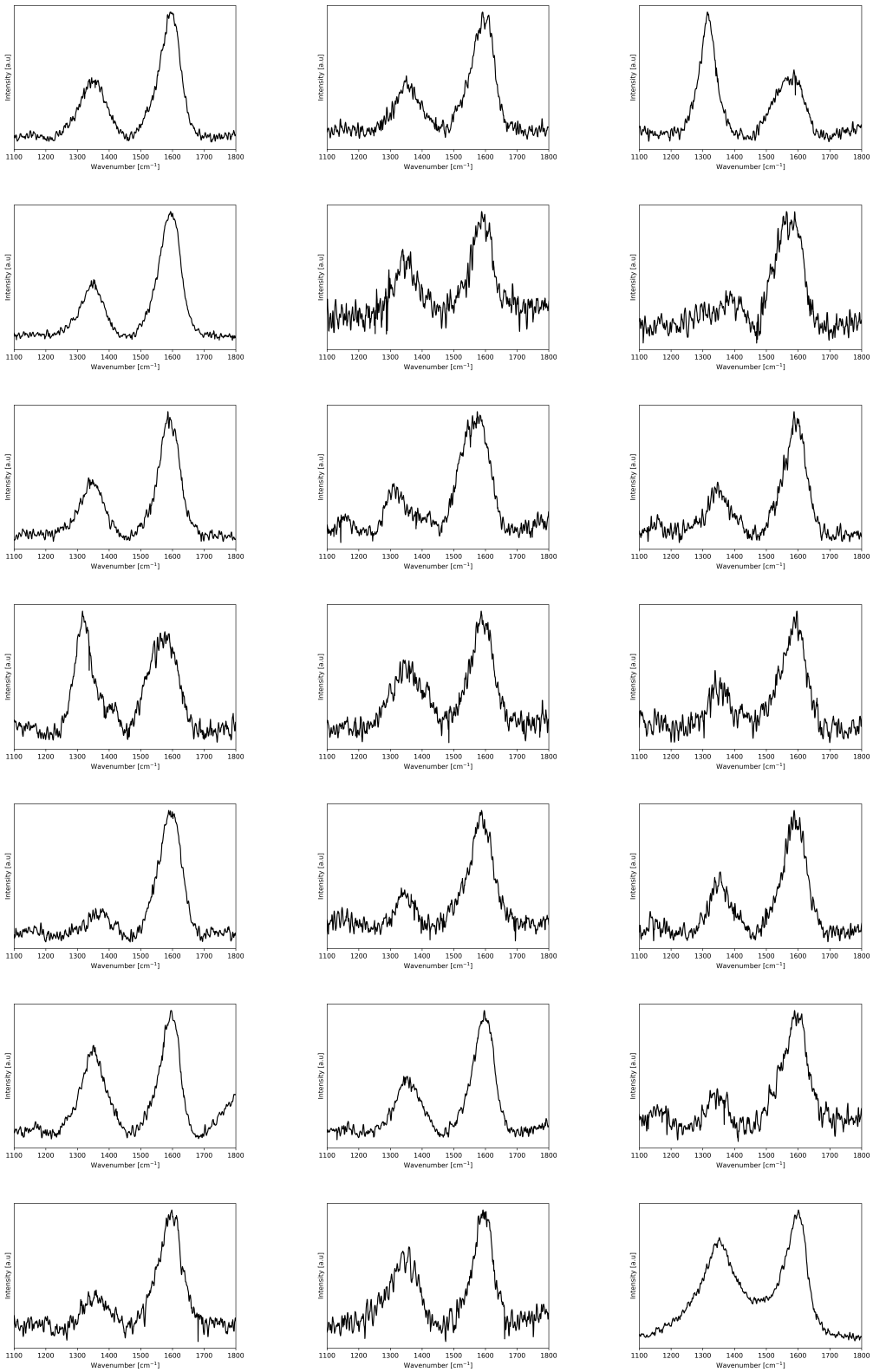

Figure E.2: Example Raman spectra of basalt fragments post-impacting.

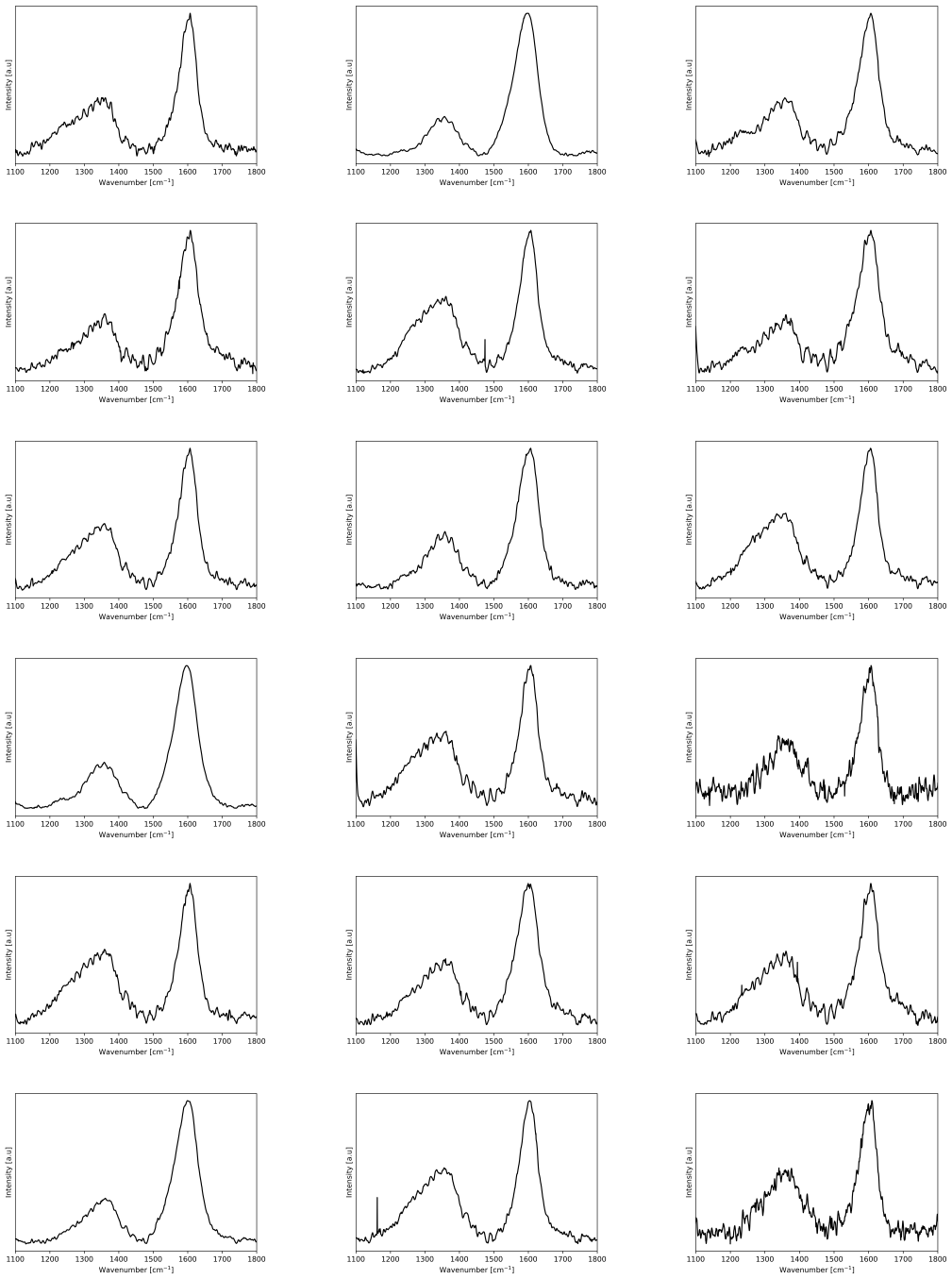

Figure E.3: Example Raman spectra of the shale projectiles before shooting.

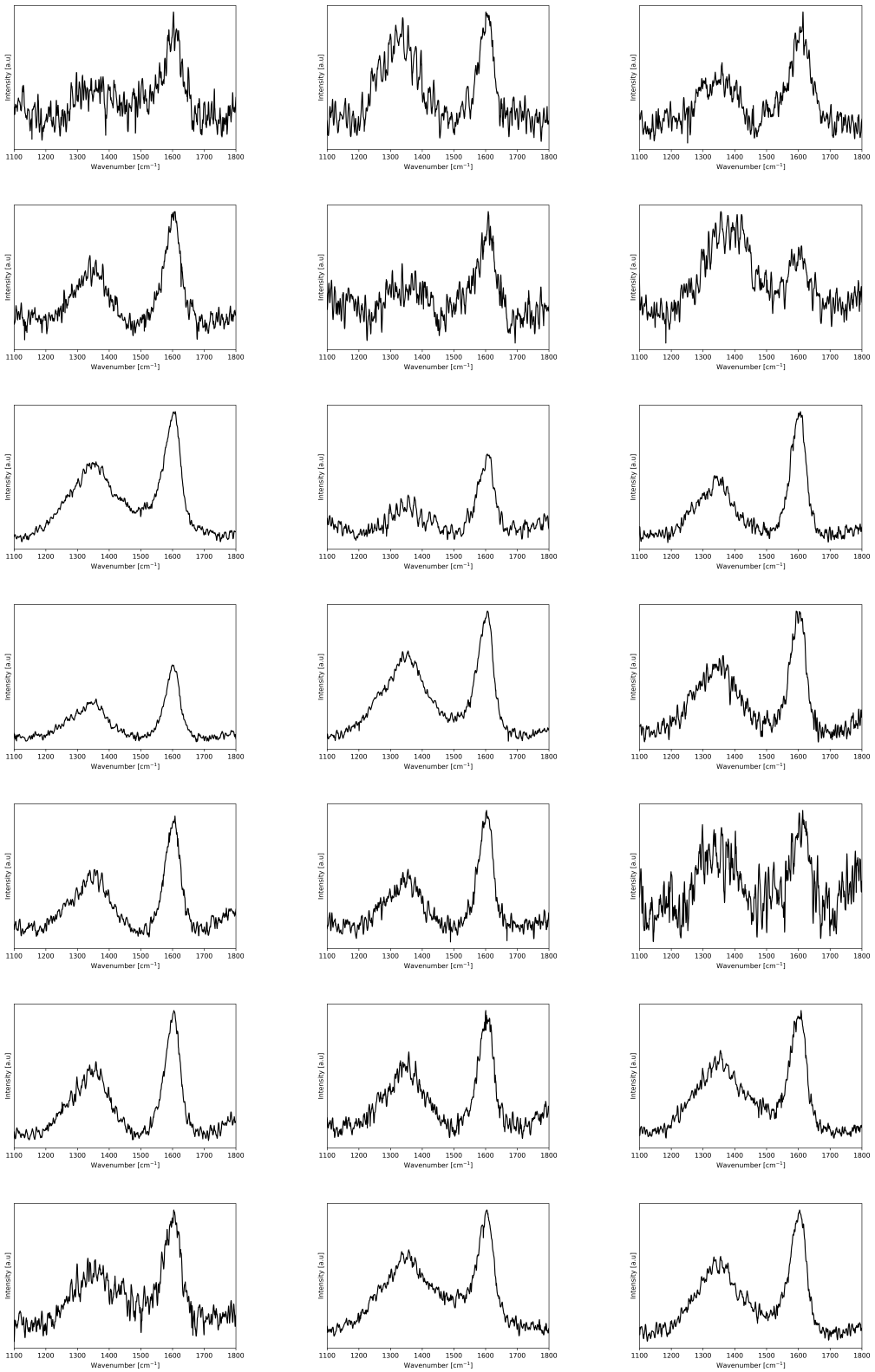

Figure E.4: Example Raman spectra of shale fragments post-impacting.

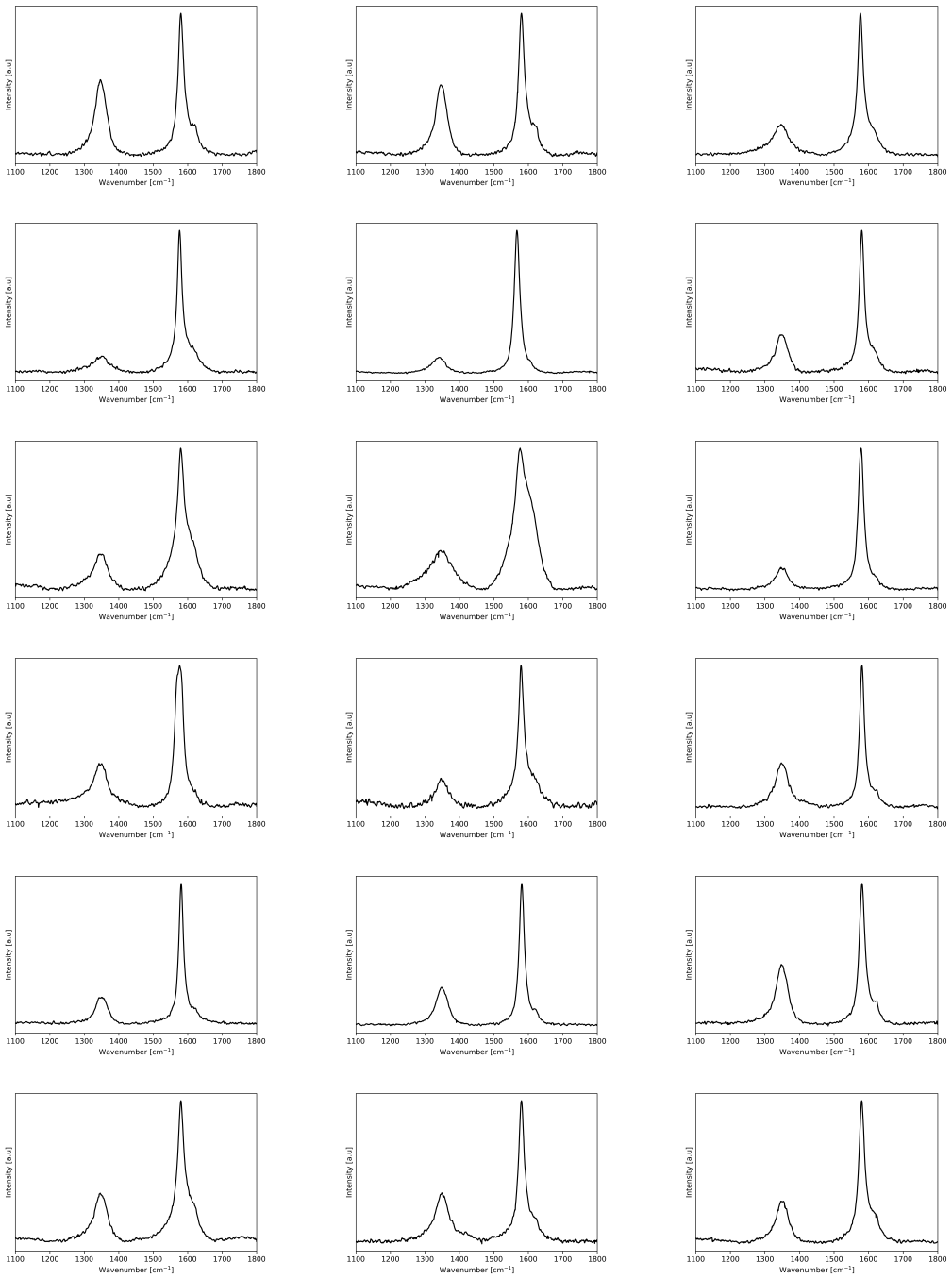

Figure E.5: Raman spectra of the graphite projectiles before shooting.

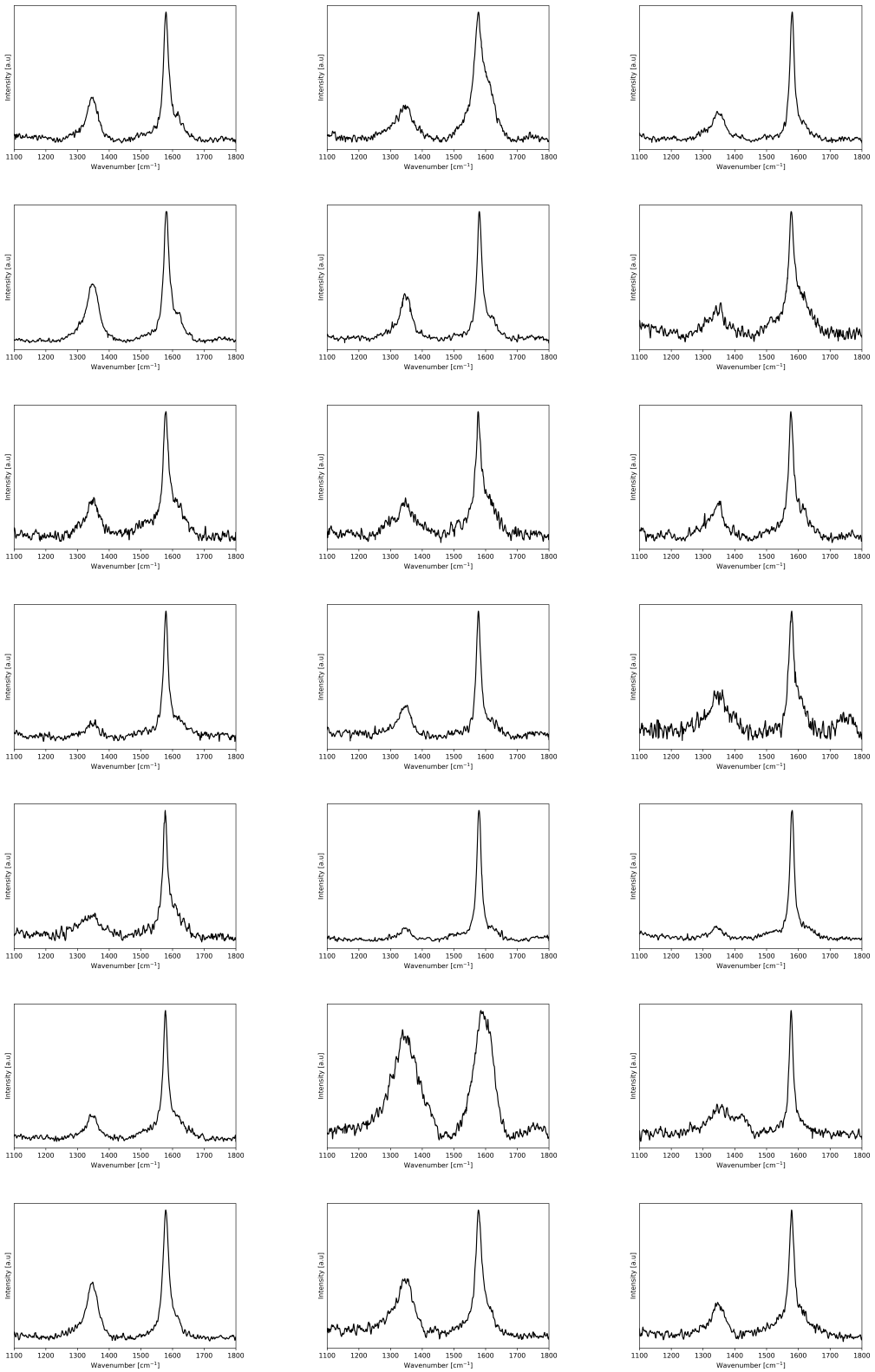

Figure E.6: Example Raman spectra of graphite fragments post-impacting.

E.2 Static Pressure Experiment

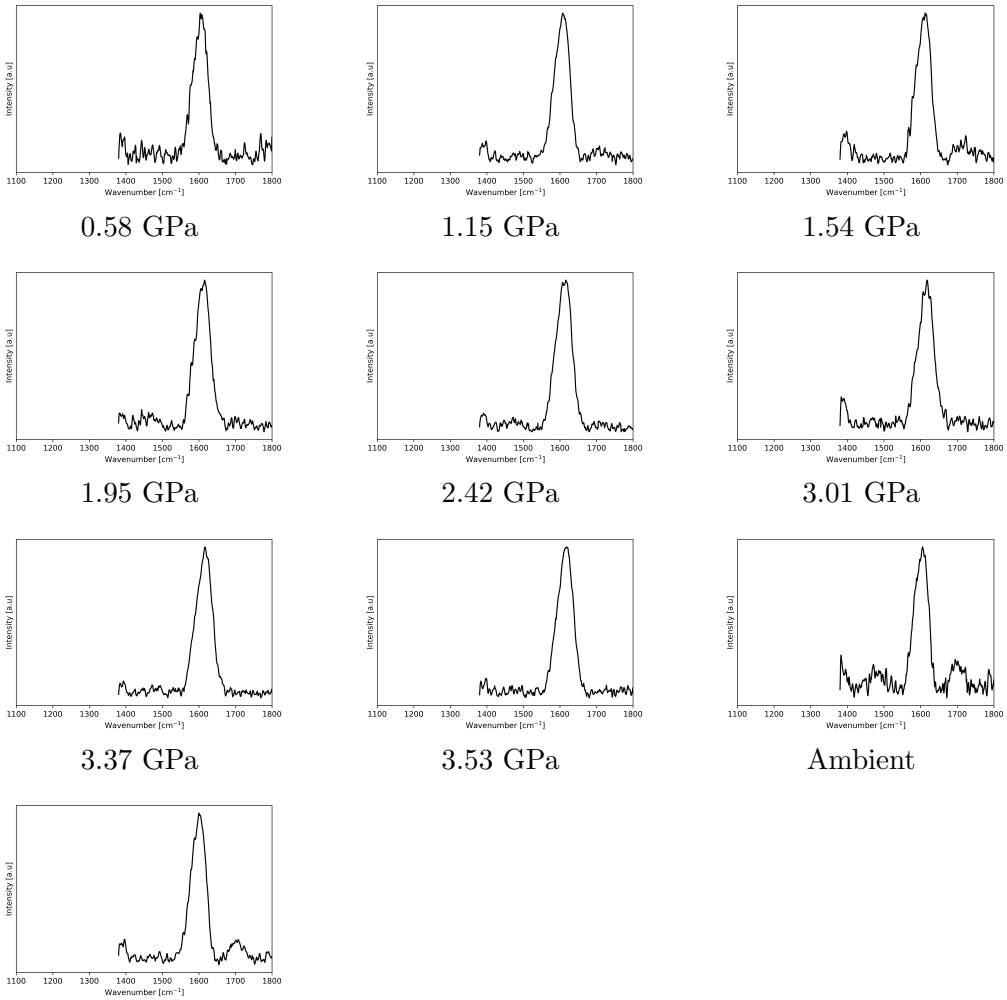

Figure E.7: Raman spectra of the shale sample during compression.

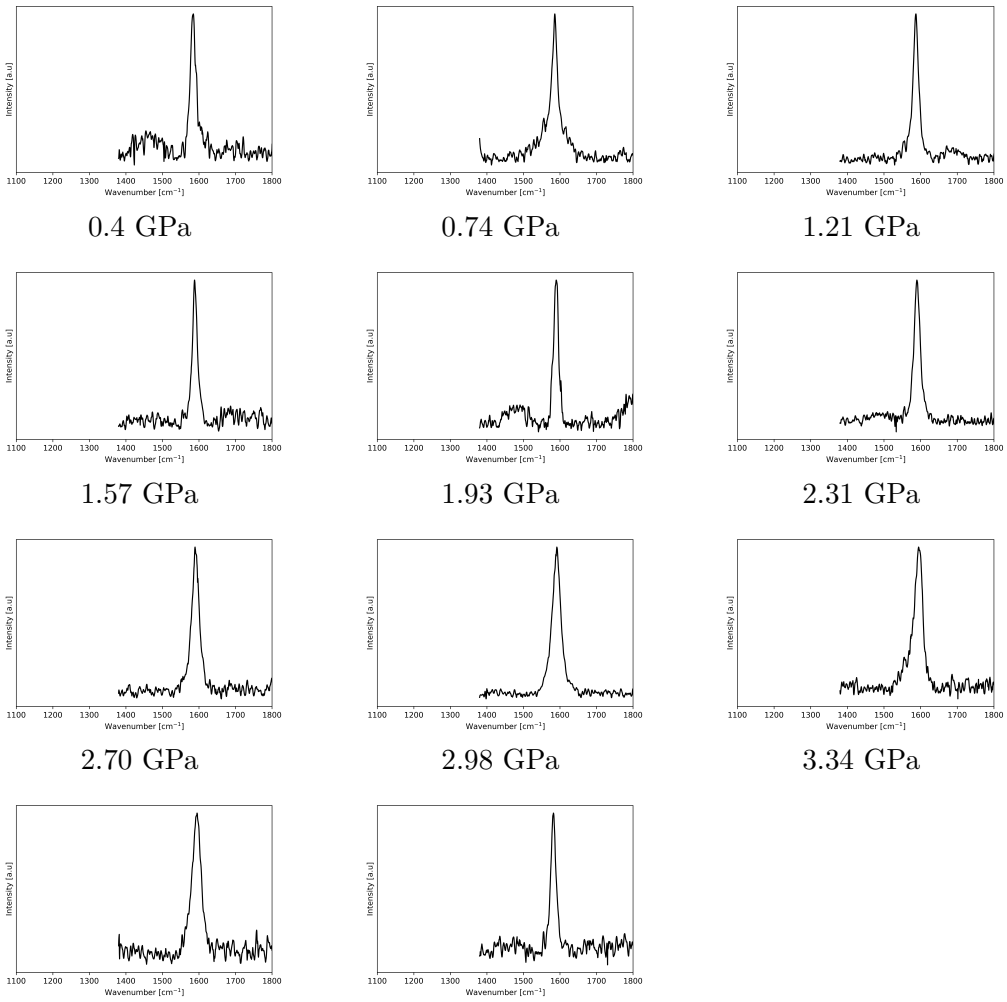

Figure E.8: Raman spectra of the graphite sample during compression.

E.3 Temperature Experiment

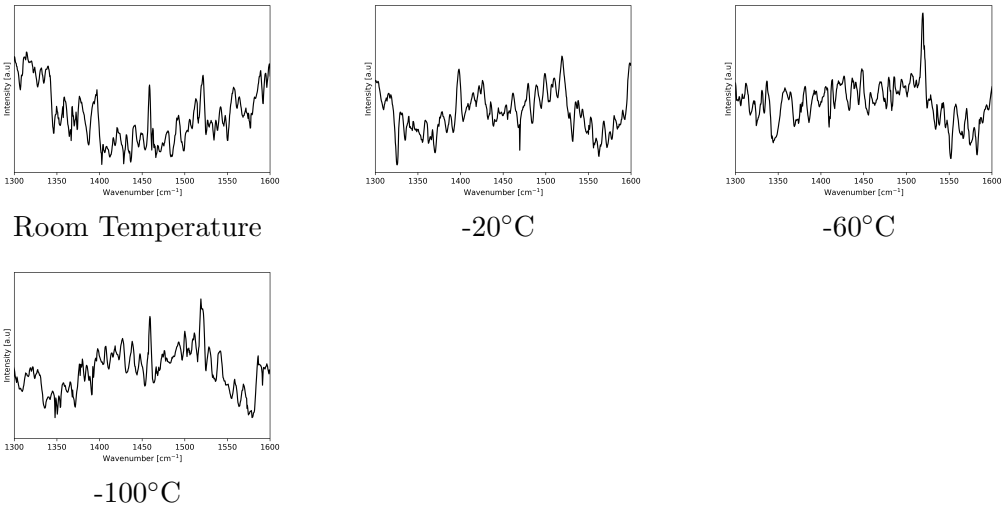

Figure E.9: Raman spectra of the basalt sample during cooling.

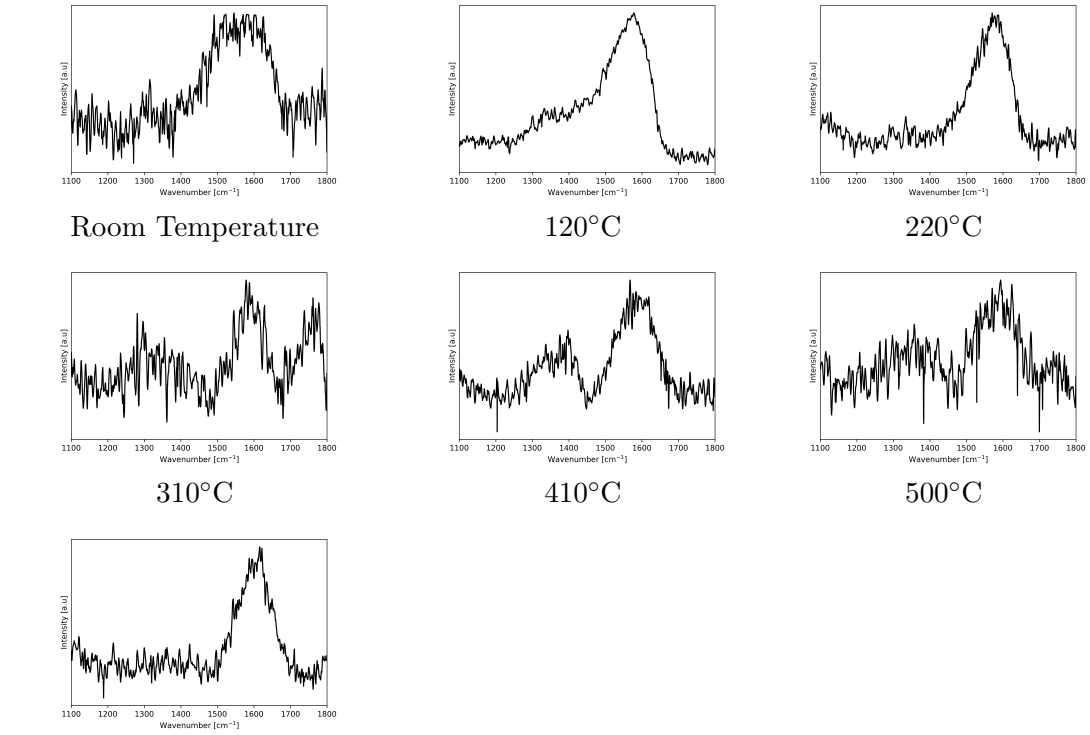

Figure E.10: Raman spectra of the basalt sample during heating.

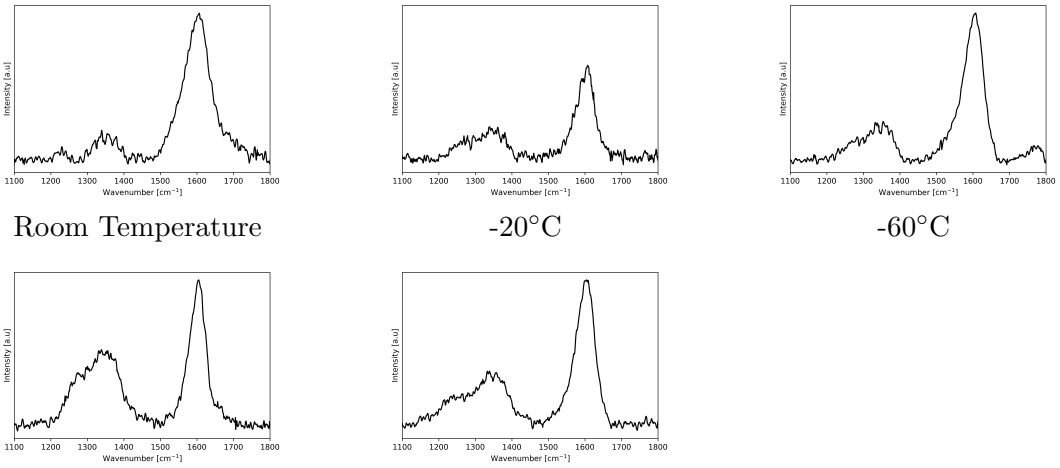

Figure E.11: Raman spectra of the shale sample during cooling.

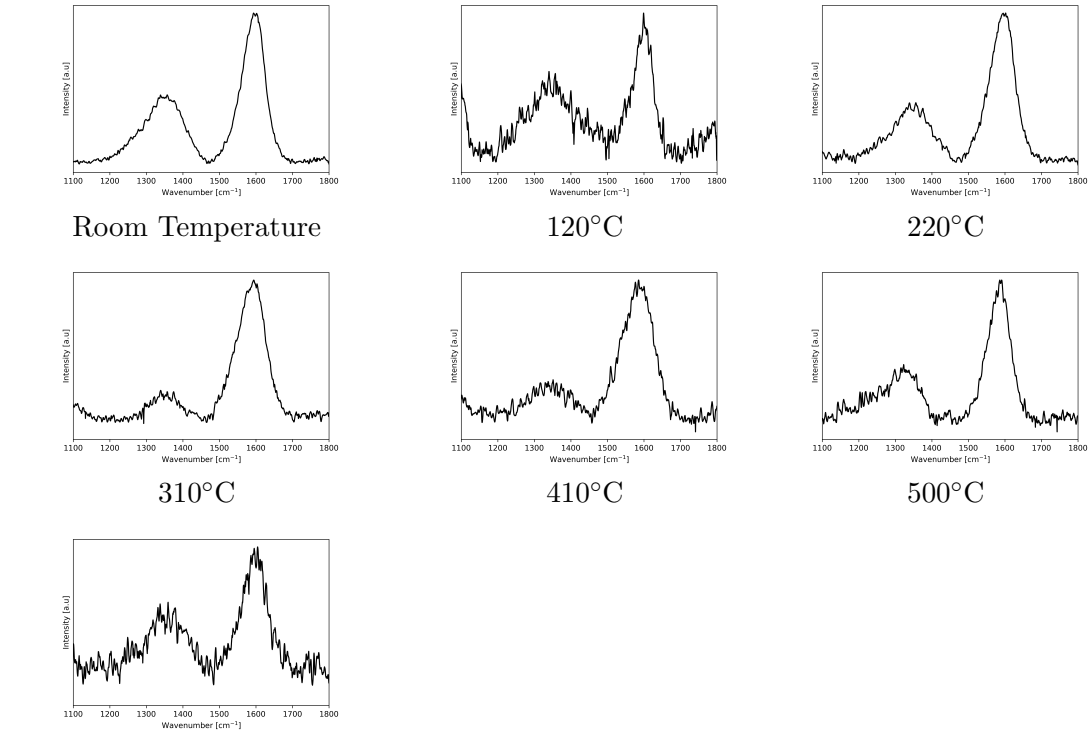

Figure E.12: Raman spectra of the shale sample during heating.

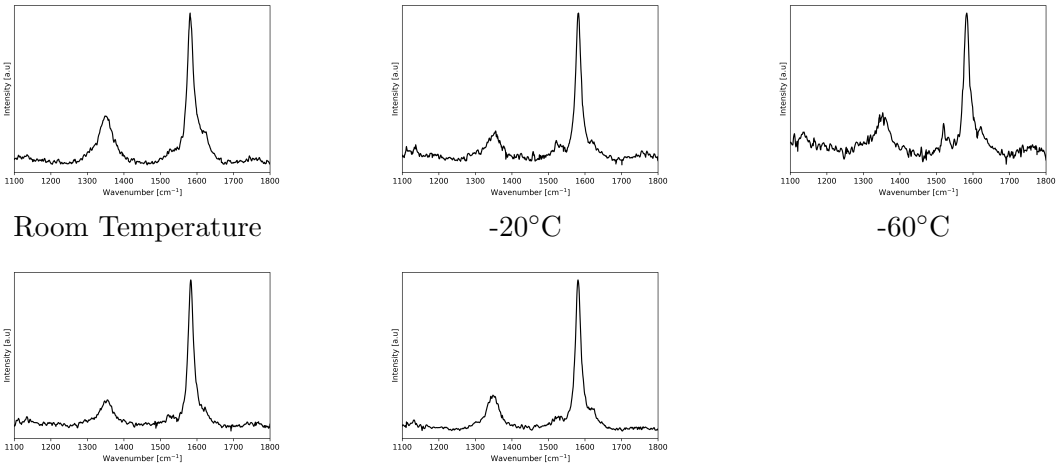

Figure E.13: Raman spectra of one run of graphite during cooling.

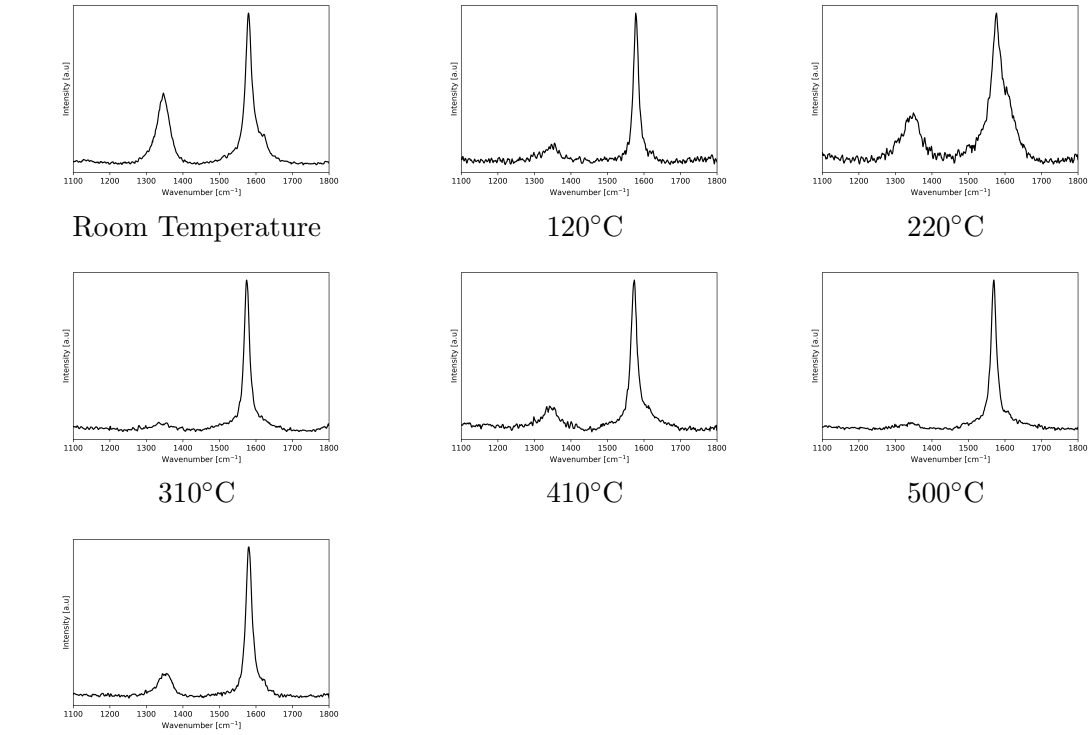

Figure E.14: Raman spectra of the graphite sample during heating.